A Computational Model for Z-Pinch Plasma Channels

Osman Yasar

February 1990

UWFDM-823

Ph.D. thesis.

FUSION TECHNOLOGY INSTITUTE

UNIVERSITY OF WISCONSIN

MADISON WISCONSIN

A Computational Model for Z-Pinch Plasma Channels

Osman Yasar

Fusion Technology Institute
University of Wisconsin
1500 Engineering Drive
Madison, WI 53706

http://fti.neep.wisc.edu

February 1990

UWFDM-823

Ph.D. thesis.

A COMPUTATIONAL MODEL FOR Z-PINCH PLASMA CHANNELS

by

OSMAN YASAR

A thesis submitted in partial fulfillment of the requirements for the degree of

DOCTOR OF PHILOSOPHY

(Nuclear Engineering and Engineering Physics)

at the

UNIVERSITY OF WISCONSIN - MADISON

1989

To my wife, Bedriye.

Abstract

An adaptive grid finite difference scheme has been derived for simulating non-linear and unsteady one dimensional (planar,cylindrical and spherical) fluid flow by adapting to steep gradients in different physical quantities. The scheme is applied to z-pinch plasma channels that are used for ion beam transport in Light Ion Beam Fusion Reactor designs. The axial plasma is subject to joule heating caused by the discharge current ($\sim 100kA$) that is used to create azimuthal magnetic fields to confine an ion beam current of $\sim 0.5MA$. The radiation emitted by the plasma seems to be vitally important for analyzing the formation of channels, requiring accurate methods that treat radiative transfer coupled to magnetohydrodynamics.

The channel formation and ion beam injection is studied by simulations with what we call a 1-D Adaptive Radiation Magnetohydrodynamics (ARMHD) computer code developed for the purpose of this thesis research. ARMHD models the plasma with single-fluid MHD equations, and therefore does not distinguish between the electrons and ions. It solves for the radiation field intensity through the *radiative transfer equation* using a multigroup discrete ordinate S_N method. The governing equations are hyperbolic conservation laws (PDEs) transformed to an adaptive grid reference frame that moves in time to follow the high gradients in the solutions. An explicit procedure based on the equidistribution principle is used to move the grid

system to avoid the implicit coupling between the physical equations and the grid system.

Adaptive gridding seems to be most effective in flows with high gradient regions. Typical quantities which have been tried for adaption are *density, momentum, temperature, electrical resistivity* or any combination of two of these. For z-pinch plasma channel simulations, the adaption on *temperature-momentum* proves to be better in terms of the high mesh concentration it provides throughout the channel, where other quantities besides the temperature and momentum are also varying. Also, the mesh spacing in the channel provided with the adaptive gridding seems to be about two times smaller than what was obtained with a lagrangian scheme using the same number of mesh points.

Applications of ARMHD indicate the feasibility of using argon and nitrogen for plasma channels. These were ruled out in favor of helium by earlier calculations using a radiative diffusion model. ARMHD calculations treat the thin plasma in the channel more accurately than the diffusion approximation, leading to this different conclusion.

Approved:

Date

Professor Gregory A. Moses

Nuclear Engineering and Engineering Physics

Acknowledgement

I would like to express my sincere appreciations to my thesis advisor Professor Gregory A. Moses for his support and encouragement throughout the course of this research. His patience, understanding, guidance as well as the computing environment he has provided were essential in completing this work. I would also like to thank him for the support and guidance he has given to me to complete my graduate study in computer sciences.

Many thanks go to staff scientists Dr. Robert Peterson and Dr. Joe MacFarlane for their stimulating discussions. My fellow graduate student Kim Simmons has been most supportive and encouraging throughout my graduate study at UW-Madison. His generosity and frankness makes him a unique friend and I consider myself lucky for having him as my office-mate for past three years. Makarem Hussein, Hesham Khater, Joan Casas, Doug Roberts, Mary Kulas, Ping Wang, Tim Tautges and former students Dr. Elafify and Dr. Henderson also deserve acknowledgement for their friendship and informative discussions.

I am also grateful to many teachers I have had in both engineering and computer sciences. Special thanks go to Professors Moses, Plohr, Strikwerda, Parter, Conrad, Emmert, Solomon, Landweber and Livny, whose lectures constituted in one way or another a milestone for my research and study in general.

Finally, I would like to express my sincere thanks to my wife, Bedriye, for the sacrifices she has made and the hardships she has gone through for my graduate study in addition to her own. Her endurance during the past four years represents a debt that I can only try to repay. Our parents deserve special thanks for their continued support in the furtherance of our education. They have surely looked forward to this time. Many thanks to Meggy and John for their warm welcome during our early days here, and to Goknur, Sakman, Yazici and Erkal families for making our stay in Madison an enjoyable one.

Financial support provided by Sandia National Laboratory, San Diego Supercomputer Center and Kernforschungszentrum - Karlsruhe (GERMANY) is sincerely appreciated.

Contents

List of Figures

List of Tables

Chapter 1

Introduction

Z-pinch plasma channels are important to the design of Light Ion Beam Inertial Confinement Fusion (ICF) Reactors and near term experiments. In these applications, such as the Laboratory Microfusion Facility (LMF) and Light Ion Beam Reactor (LIBRA), high intensity ion beams are used to ablatively implode a target to achieve extremely high densities and to shock heat deuterium-tritium (D-T) fuel to temperatures sufficiently high to have a thermonuclear burn [2].

Light ion beams ($Z \leq 6$), with their high charge to mass ratio and high current densities, cannot propagate over large distances in a vacuum without significant beam divergence. The standard solution of this is to charge and current neutralize the beams so that their mutual electrostatic repulsion and tendency to pinch is removed. This involves filling the region between

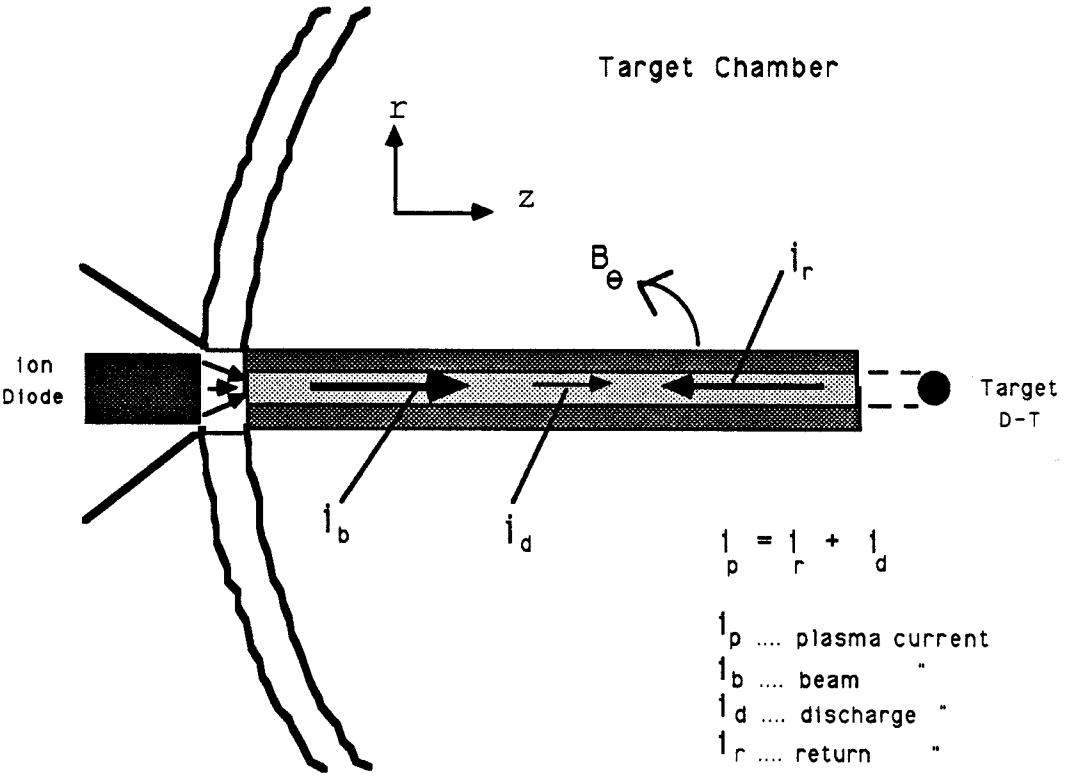

Figure 1.1: Schematic of beam propagating plasma channel in LIB fusion.

the diode (the place where ions are formed) and the target with an ionized medium. One method of doing this, first proposed by Yonas [3], is to fill the standoff region with gas and strike a discharge along the path from the diode to the target. The discharge in the gas provides the required charge neutralization and confines the ions as they propagate. This confinement is due to the magnetic field produced by the discharge current. The ionized gas (plasma) responds to the ion beam with a *return current* in the opposite direction to current neutralize it. Figure 1.1 shows a schematic diagram of a z-pinch plasma channel.

The idea of using ion beams as drivers in the ICF studies emerged as an alternative to laser fusion because of the low efficiency and high cost of the laser drivers. The attention to ion beam drivers was split into Heavy Ion Beam (HIB) [4] and Light Ion Beam (LIB) [5] applications. Even though both have their promising futures, the LIB fusion appears to be less expensive in terms of technology. Some LIB designs include LIBRA [5], UTLIF [6], ADLIB [7] and EAGLE [8]. Among these, the LIBRA study is a self-consistent conceptual design of a commercial fusion power reactor. It is a 330 MWe power plant with a direct capital cost of \$2200/kWe. A major goal of the study is to understand the potential of light ion fusion as the basis for small yet economically attractive power reactors. This is done by completing a self-consistent point design, evaluating its cost, and cost scaling the design to different power levels. A schematic of the LIBRA design is shown

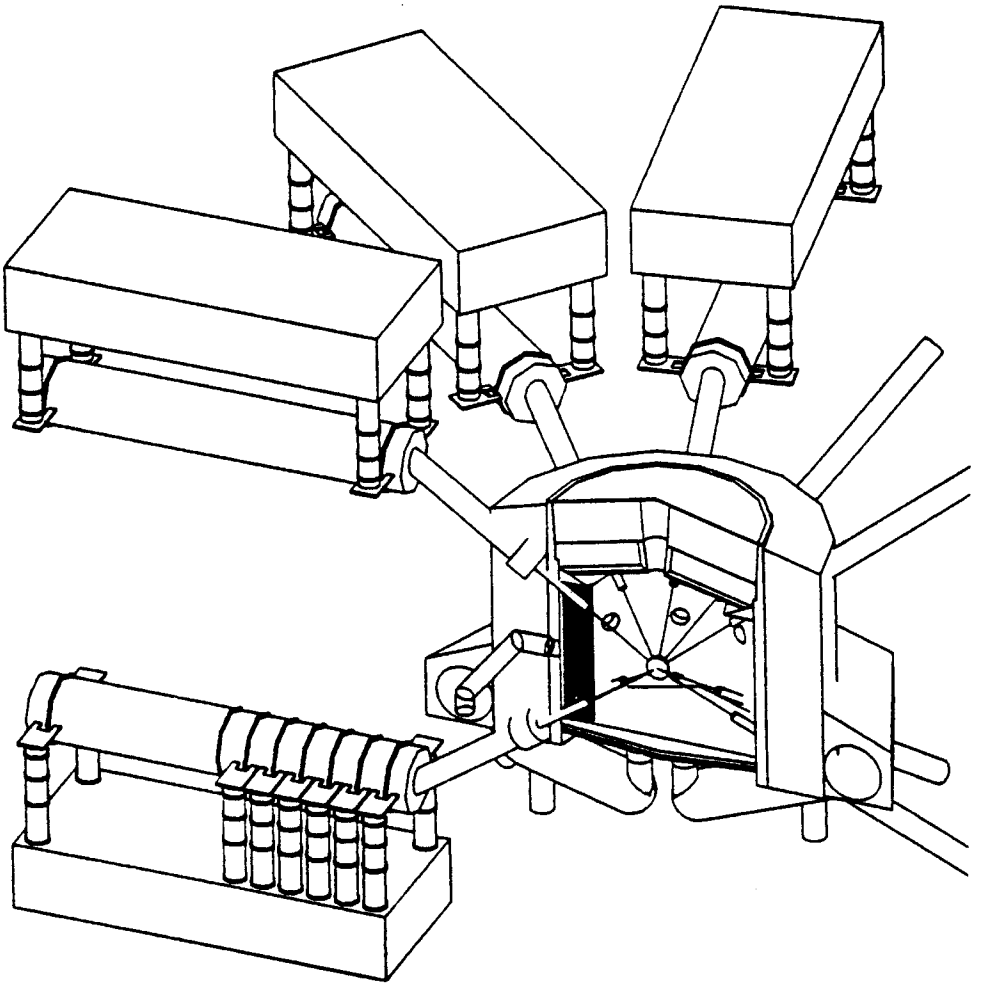

Figure 1.2: LIBRA reactor design [9].

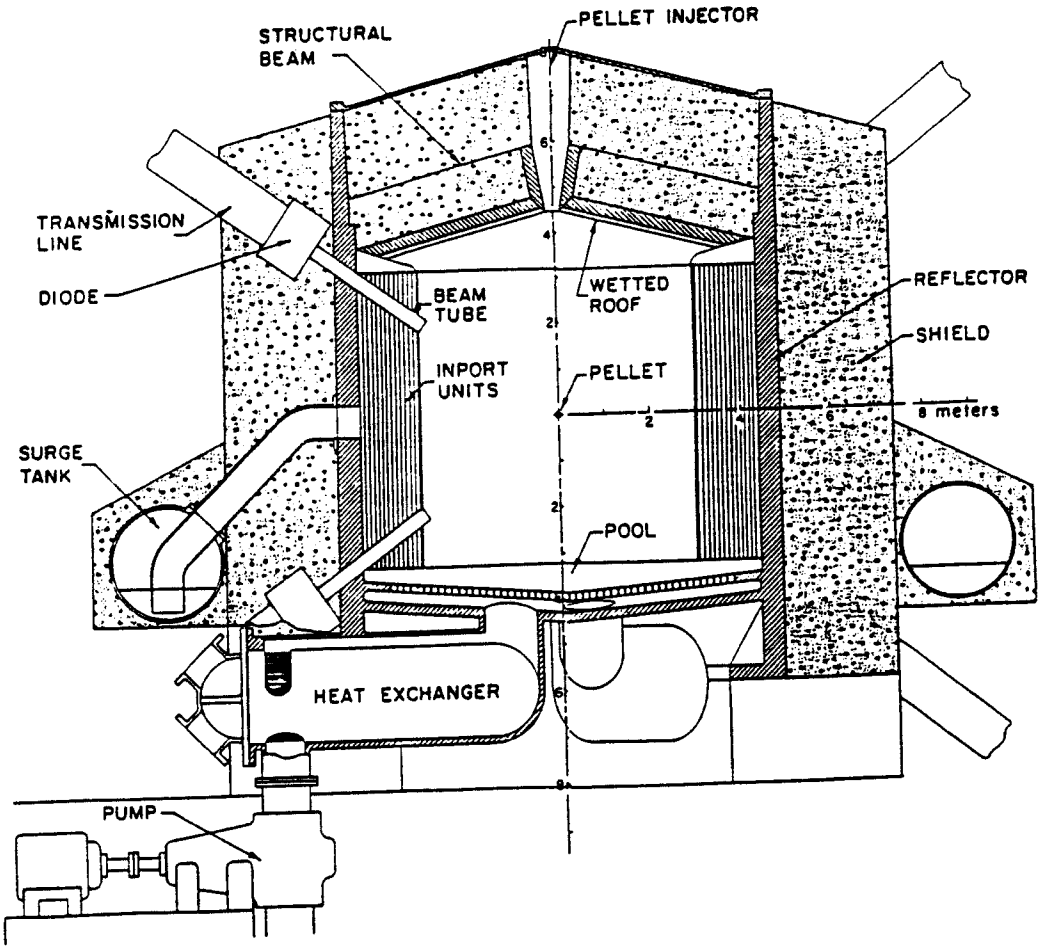

Figure 1.3: Cross section of LIBRA target chamber [9].

in Figure 1.2 and a cross section of the reactor chamber is shown in Figure 1.3. Fusion targets are imploded by 4 MJ shaped pulses of 30 MeV Li ions at a rate of 3 Hz. The high intensity part of the ion pulse is delivered by 16 diodes through 16 separate free-standing z-pinch plasma channels formed in 100 torr of helium with trace amounts of lithium [9].

The efficient transport of ion beams for LIBRA requires the design parameters shown in Table 1.1. Channels are $\sim$ 6 meters long with a radius of 0.5 cm. Channels enter the target chamber along two cones, 35° above and below the horizontal plane containing the target. For each channel, there is a return channel to return the discharge current that leaves the target chamber through the top. To be useful and efficient, the channel parameters at the time of beam injection must meet a variety of competing conditions [10]. The density in the channel must be low enough to minimize beam collisional losses, but high enough to prevent the beam from expanding it via the Lorentz force produced by the plasma return current induced by the beam. Its temperature must be high enough to provide good neutralization of the beam current and to minimize the energy lost by the return current heating the channel. Its radius must be small enough to maintain the beam fluence (power/area) transmission efficiency. Finally, the channel magnetic field just before beam injection must be high enough to confine the ions with the highest expected energies and injection angles.

The study of plasma channel transport has been aided by a considerable

Table 1.1: LIBRA Parameters [9].

General	Net electric power	331 MW
	Gross electric power	441 MW
	Thermal power	1160 MW
	Recirc. power fraction	0.25
	Driver efficiency	0.23
	Target gain	80
	Fusion gain	18.4
	Direct capital cost	$2200/kW
Lithium Ion Beams	Energy	25-35 MeV
	Number high/low power	16/2
	Peak power on target	400 TW
	Pulse compression ratio	5
	Pulse length on target	9 ns
	Current/channel	0.3 MA
	Entering on target	1.1 MA
	Energy transport eff.	0.63
Laser-Guided, Free Standing Channels	Length	5.4 meters
	Radius	0.5 cm
	Peak B-field	27 kG
	Peak current	100 kA
	Rise time	1 μs
	Voltage drop	1 MV

body of theoretical work. It needs efforts in both direct numerical simulation and experimental verification. The work by Freeman, Baker and Cook [10] represents the most complete set of simulations of the development of an optimized propagation channel. In addition to these researchers, Watrous, Moses and Peterson [11] contributed to this issue by further developing an optimized plasma channel. Several computer codes (ZPINCH [11], ION [12], WINDOW [13]) were written at UW-Madison to study ion beam formation and propagation. Among these, ZPINCH [11,14] is used to simulate the channel formation. It is a 1-D lagrangian radiation magnetohydrodynamics code and was developed by making extensive modifications and additions to an existing radiation hydrodynamics code, MF-FIRE [15].

Lagrangian grid schemes have often been used to model this type of problem. In these schemes, the mass of each computational cell is constant because the cell boundaries move at the fluid velocity (i.e., there is no mass flux across the cell boundary). Typical plasma channel simulations by ZPINCH indicate a blast wave character of the discharge plasma while it is interacting with the magnetic field. The nature of the z-discharge plasma channel problem creates steep gradients in density, temperature and electrical conductivity which one would like to resolve. Being a lagrangian code, ZPINCH automatically resolves only density gradients as shown in Figure 1.4 [1]. Yet because the density is low in the region where the temperature (and hence the conductivity) peaks, the mesh in this region will be elongated. This

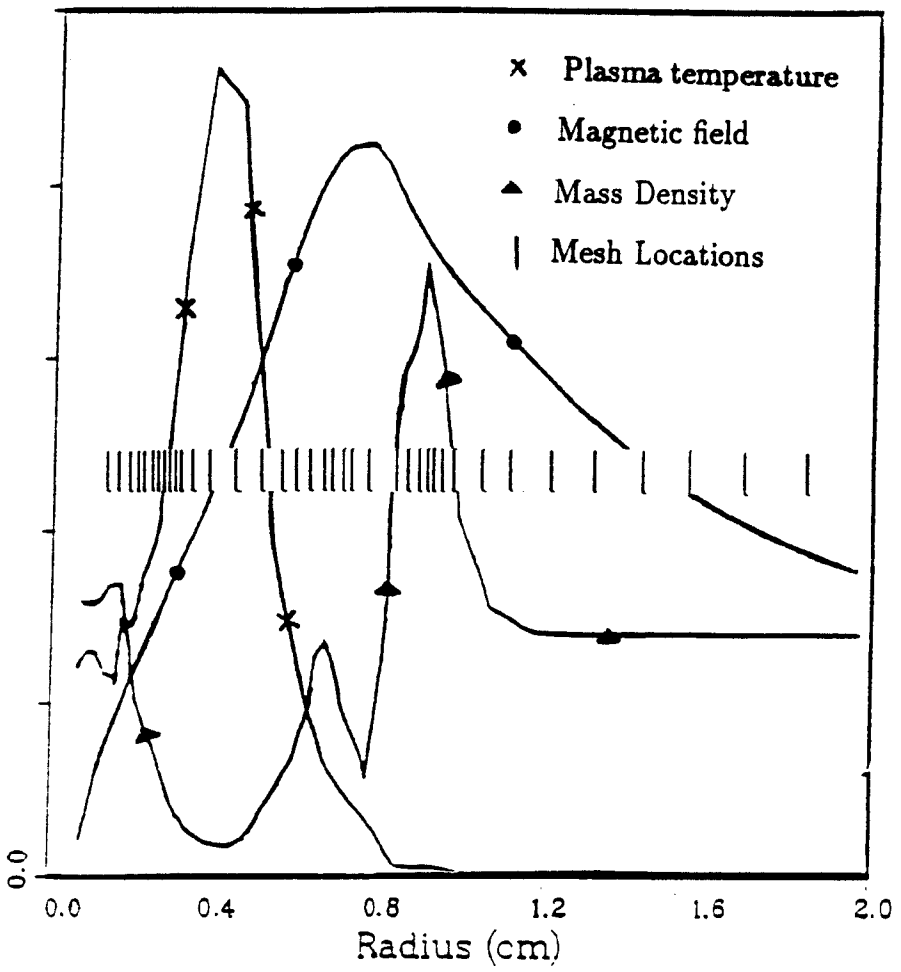

Figure 1.4: Temperature, density and magnetic field profiles of the plasma channel by ZPINCH [1].

effect will tend to smear the temperature and magnetic field gradients in space, thus losing the resolution (accuracy) needed to follow this non-linear conduction problem.

The weakness of the ZPINCH code is not only the grid system. There are some other issues in it that need to be improved. The plasma in the channel is dense and hot and it radiates. There exists a population of photons that interact with the plasma. ZPINCH treats the radiation with a diffusion approximation. However, the mean free path of x-rays in most of the plasmas (argon,helium) used for z-pinch channels is much larger than the physical dimensions of the channel. Hence, the diffusion approximation of radiation hydrodynamics (RHD) simply is inadequate for such applications. Moses and Peterson [17] have indicated this inadequacy in published results when they included the radiation effects in the channel simulations .

In the past two decades, finite difference numerical methods to solve partial differential equations (PDE) have been developed quite significantly. Advances have been made in grid generation, computer technology as well as in numerical methods. The complexity of the problems, though, has also grown and far more computer resources are needed to handle the increased complexity. Thus, one is faced with finite computer resources (memory and CPU time) and must worry about the problems of how many grid points to use and where to place them to get a more accurate solution. The complexity of such problems arouses the interest to develop techniques for constructing

adaptive grid systems by which the solution of the differential equation is obtained on an arbitrarily moving grid system. Mesh points move in such a way that they concentrate in places where needed. The updated grid point positions are determined by some measure of the quality of the numerical solution [18,19].

Because of the tremendous potential adaptive gridding has for reducing computational costs while maintaining the same level of accuracy, it is a forefront area in **computational physics**. The need for it is basically due to two concerns; better accuracy and minimizing the number of the mesh points. The accuracy concern arises from the fact that more challenging simulation problems are highly time-dependent (unsteady) and have regions of high gradients. One would like to have a sufficient number of mesh points at these high gradient regions while trying to keep the total number of mesh points at a minimum. The adaptive mesh systems solve this dilemma and cluster the points where needed in the space domain while just requiring a reasonable amount of mesh points. The mesh distribution is changed as the solution develops in time.

Therefore, problems with high gradient regions benefit the most from adaptive mesh systems. In fact, for some problems there exist multigradient regions, even of different quantities (density and temperature) and they may occur at different space points. Then, again one would like to catch and resolve these gradients by the least costly way, which is the adaptive mesh

system. The redistribution of mesh points is not like a local grid refinement nor a periodic rezoning as used in *ad hoc* ways with eulerian and lagrangian schemes. It is quite general and it can treat many problems with a great deal of flexibility. Typical examples of high multigradient problems are high-temperature blast waves, laser or ion beam ablation of a surface and as mentioned previously z-pinch plasma channels.

The motivation for this work comes from the fact that the physics and numerics of the z-pinch plasma channel formation and ion beam transport for the Light Ion Beam Fusion Reactors need to be improved to more accurately predict channel behavior. **The idea of this thesis is to create a new numerical model that will solve the z-pinch channel problem on an adaptive grid system, along with a more descriptive picture of radiation hydrodynamics (RHD) and ion beam current.** An additional practical advantage of the adaptive grid method is that we can start with an existing adaptive Navier-Stokes hydro code written by Bartel [20] for slab type of problems. Extensions and modifications to the other geometries (cylindrical, spherical) as desired for channel simulations are required. Since the plasmas used in the channel could be regarded with a negligible absolute viscosity μ, the original Navier-Stokes equations will be replaced with less complicated Euler equations that are easier to cast to curvilinear coordinates. Furthermore, the equations of radiation magnetohydrodynamics (RMHD) will have to be added to the rather simple hydrodynamics equa-

tions and the whole set of equations will be casted first to the curvilinear coordinates and finally to the adaptive system.

For a general comparison with ZPINCH, some aspects of our new adaptive radiation magnetohydrodynamics (ARMHD) computational model are given in Table 1.2. It models the plasma with **single-fluid** MHD equations and therefore does not distinguish between the electrons and ions in the plasma. The plasma is subject to a discharge current of $\sim 0.5 MA/cm^2$ which elevates its temperature to many eVs due to the ohmic heating. The radiation that escapes the plasma is determined through the radiation transfer equation with a multigroup discrete ordinate S_N method. The coupling between the plasma and radiation field is a non-linear process but is eased by using appropriate numerical schemes which first solve the radiation field and then the plasma properties. It is assumed that plasma conditions do not change significantly within a given timestep during the simulation, thus the radiation field can be calculated based on the previous timestep plasma conditions. The equations are written in the laboratory frame and then transferred to the adaptive grid frame. They are solved along with a set of grid equations that describe how the grid system evolves in time. An explicit procedure will be followed to move the grid system to prevent the implicit coupling between the physical equations and the grid system. A conservative differencing scheme based on the control volume approach is chosen to retain the conservation nature of the governing equations.

A literature review of z-pinch plasma channel work and adaptive grid investigations follows in the next chapter. Chapter 3 presents the model equations for the plasma, magnetic field and the radiation field. It also describes the adaptive grid generation and the numerical methods to solve the discretized adaptive equations on the moving grid system. Chapter 4 makes comparisons of the standard lagrangian scheme used in ZPINCH and the adaptive scheme used in the current computation. An application of our adaptive computer code ARMHD to the LIBRA Fusion Reactor design is given in Chapter 5 followed by a conclusion and future considerations.

Table 1.2: A comparison between ZPINCH and ARMHD codes.

	ZPINCH	ARMHD
PHYSICS	Single-fluid plasma	Single-fluid plasma
	One temperature plasma	One temperature plasma
	Multi-group Radiation Diffusion	Multi-group Radiative Transport
	EOS & Opacities from IONMIX code	EOS & Opacities from IONMIX code
	External Discharge Current Equation	User Defined Discharge Current
	No Beam Current	Beam Current
NUMERICS	2 nd order explicit hydro	1 st order explicit hydro
	2 nd order implicit radiation diffusion	2 nd order implicit radiation transport
	Conservative Differencing	Conservative Differencing
ADAPTION	Lagrangian	General

Chapter 2

Literature Survey

Since the present investigation undergoes the numerical simulation of a plasma physics problem, it requires review of two areas of the literature : review of the theoretical and experimental work done on the understanding of the z-discharge plasma channels and review of the adaptive mesh systems. In this chapter, these two areas will be discussed in as much detail as it requires to carry the task further.

2.1 Z-Pinch Plasma Channels

The z-pinch plasma channels play an important role in light ion beam transport. In fact, not only are they found in this context but are also found in the context of lightning and gaseous electronics [21] and certain types of plasma radiation sources [22]. Plasma channels are an example of magnetized

plasmas that have drawn attention for the past three decades.

A recently published work by Watrous [14] reviewed the concept of z-pinch plasma channels starting from the electrical discharge to today's current work. However, only the most important ideas and their references will be summarized here. The following section includes the concept of discharge initiation, equilibrium z-pinch channel, its stability, and the radial evolution of a non-equilibrium z-pinch channel.

2.1.1 Discharge Initiation

As mentioned previously in the introduction chapter, the proposal of using discharge plasma channels in ion beam propagation was first made by Yonas [3]. The channel as shown in Figure 1.1 is filled with a gas and a discharge is created along the channel axis, which is hopefully the path of the ion beams. It is necessary that the discharge be both straight and uniform. Two simple methods have been used to form straight, uniform discharges. The simplest one is to form the discharge in a narrow tube which is a wall confined discharge with no choice but to be straight. The second method is that a fine wire is stretched between electrodes and a high voltage pulse is applied to vaporize all or part of the wire that then becomes a conducting plasma. However, both methods cannot be used in a realistic reactor where several repetitions per second are needed. The most effective method of creating discharges is the suggestion of using a laser beam [3,23]. Several demon-

strations of discharge guiding with lasers have been performed [24,25,26,27] and the progress made in this field has led to even better ideas. A method that meets the required criteria (such as straight and uniform discharge but low laser energy) for reactors is laser initiation based on resonance saturation (LIBORS) [28,29] and it is basically rapidly ionizing a gas that uses relatively low energy lasers. The idea is to tune a laser to an atomic transition from ground state to some relatively long-lived state. The laser pumps up the population of the higher state at the expense of the ground state population, thus it creates a pool of energy that is tapped by free electrons through super elastic collisions. Free electrons colliding with excited atoms gain energy at the expense of the excited atoms to the point where they can cause collisional ionization. The result is a rapid, nearly complete ionization of the gas.

2.1.2 Equilibrium Z-Pinch and Its Stability

The equilibrium properties of the z-pinch plasma have been studied by many researchers. One of the earliest analyses is by Pease [30]. He has considered the plasma separated from the wall by a vacuum and based his analysis on three steady-state balance equations: the balance of energy in the plasma, the balance of forces on the plasma column and the balance of momentum gained by electrons from the applied electric field to the momentum lost by collisions with ions. He has also assumed that the plasma was transparent to the radiation. The conclusion he drew was that the plasma's energy loss due

to radiation (bremsstrahlung) emission could be balanced by energy gain due to resistive heating (Joule heating) only for a unique value of the discharge current. Falthammer [31] extended this simple analysis by using the complete set of steady state magnetohydrodynamics (MHD) equations. Unlike Pease's work, he studied gas-embedded z-pinch plasmas and he additionally included the effects of bremsstrahlung radiation and thermal conduction losses. The results showed that both temperature and density of the plasma peak on axis and fall rapidly at a common radius. The magnetic field is linear within this radius and behaves as $1/r$ outside indicating that most of the current is confined within this critical radius. Whereas Pease found that the steady state could exist only for a unique current value, Falthammer showed that any value less than one megaampere ($< 1MA$) would make it.

Several other analyses [32,33] were done and these altogether have helped to characterize the steady state z-pinch channel in which plasma temperature and density are peaked on the axis and fall rapidly at a distance. The current is mainly contained in the region of elevated temperature, the magnetic field is linear inside this region and acts as $1/r$ outside it. The relative importance of the bremsstrahlung and thermal conduction losses depend on the magnitude of the current.

Having some understanding of the equilibrium z-pinch, one would wonder how stable the equilibrium is. An unstable mode, if it exists, would grow so rapidly that a smooth, straight channel could not last long enough or

could never be created. A simple example might tell us about the type of instabilities a z-pinch channel may suffer. Because the discharge plasma is highly conducting, the magnetic field in azimuthal (θ) direction is frozen in the plasma and thus it may increase or decrease if the plasma experiences a compression or a rarefaction. A consequence of a small perturbation, the imbalance between magnetic pressure and fluid pressure, would increase bowing in the cylindrical shape of the column and the bowing would further increase the imbalance in the pressure. This positive feedback would certainly cause an instability.

Therefore, a z-pinch in steady state is unstable to perturbations. Instabilities in the plasma may be more specifically studied in a numerical way by using MHD equations to follow the evolution of a perturbation imposed on a model equilibrium state or analytical methods can be used to find growing modes of a perturbed idealized equilibrium. Kruskal and Schwarzchild [34] studied perturbations of a uniform, ideally conducting, vacuum embedded z-pinch channel. The fastest growing modes they found had a growth rate of approximately $\gamma = (\frac{2k}{r_c})^{1/2} c_s$. Tayler [35] extended their analysis by studying a more realistic equilibrium state in which a current density as $J(r) = const. * r^n$ is formed by the plasma column. A uniform current density tended to stabilize the column and $m = 0$, $m = 1$ azimuthal modes had a growth rate of the Alfven time, $\tau_A = r_c / v_A$.

Mannheimer, Lame and Boris [36] studied the instabilities of a z-pinch

containing an ideally conducting plasma in the center and surrounded by a corona of a resistive-current carrying plasma. The last layer beyond the corona was a cool and neutral gas. The maximum growth rate of unstable modes depending on the ratios of the temperatures and densities in the three regions could be lower by as much as one-hundredth of an Alfven timescale.

For the typical parameters of the z-pinch plasmas as a beam transport medium the Alfven timescale is about 200 nsec. Therefore, if we would like to place an upper bound on the time during which the optimized channels may be created a useful value for this upper bound is about 1 μsec [14].

2.1.3 Evolution of Z-Pinch Channel

As mentioned above, the timescale that characterizes the formation and evolution of the discharge is as important as the timescales involved in the growth rate of the instabilities. A snowplow model has been used by several people to estimate the timescale on which the discharge radius changes. Killeen and Lippman [37], by working with this method, indicated that a discharge channel with a radius of around a centimeter could pinch significantly.

A search for whether there may exist a dynamic equilibrium was attempted by Braginskii [33] and he found that the radius of the discharge could be held constant if the discharge current increased as $t^{1/3}$. For more slowly rising currents the channel's radius would increase while rapidly rising currents would cause the channel to pinch. Mannheimer [38] tried to answer

this question by studying the power flow into the confining magnetic field and into the plasma's internal energy. Again, he arrived at the same conclusion.

Consequently, the equilibrium of the channel depends on a delicate balance between energy input, joule heating, thermal conduction and radiation losses. This balance is essentially very much dependent on the current rise times.

2.1.4 Z-Pinch Plasma as a Beam Transport Channel

The last but most important step in the application of the z-pinch plasma channel in the context of light ion beam fusion is when an ion beam is introduced in the channel. Instabilities with an ion beam present are likely to be different from those mentioned so far. These instabilities can degrade the quality of the beam transport. In his review of z-pinch channels, Watrous [14] confirms that there are two basic instabilities with an ion beam present in the channel. These are called macroscopic and microscopic instabilities. Macroscopic ones can alter the shape and the position of the beam whereas microscopic ones can cause turbulence in the channel. Ottinger, Mosher and Goldstein [39,40,41] studied microscopic instabilities in two categories:electrostatic and electromagnetic. Electrostatic instabilities are [40] : streaming instabilities between the beam ions and the background electrons, and streaming instabilities between the background electrons and background ions. Electromagnetic instabilities are [41] : *Weibel* and *Whistler*

instabilities. The linear analysis of these modes indicated that they could be driven unstable, but the growth rates were not rapid enough to cause problems during the ion beams' propagation timescale.

Mankofsky and Sudan [42,43] used a $2\frac{1}{2}$d particle simulation code to study ion beam propagation in a z-pinch channel that was assumed in equilibrium carrying a uniformly distributed discharge current at the time of beam injection. The result was that ion beams could propagate with 80 % efficiency for a distance of one meter and that current neutralization was good for the channel electron density of one hundred times greater than the beam number density.

Many experimental investigations of the z-pinch plasma as a transport channel have been performed. Miller [44] created the discharge by an exploding wire. The wire was made of tungsten with a diameter of 2.54×10^{-3} cm and was suspended in air. A maximum of 50 kA discharge current peak was reached at about 1 μsec. The results showed a shock wave travelling radially outward and leaving a rarefaction region behind. John Olsen studied laser-guided plasma channels in ammonia and measured beam transport efficiencies [45,46]. What he found was that the transport efficiency decreased with increasing discharge current. The reason for that was explained to be the MHD instabilities occurring at high currents.

In the area of plasma channel numerical simulations in the light ion beam fusion, there have been comprehensive studies. Colombant, Goldstein and

Mosher [47] used a 1-D MHD simulation code to study the response of a deuterium channel to the passage of the ion beam. They modeled the channel with an initial step function density profile and assumed a uniformly distributed discharge current. Freeman, Baker and Cook [10] also used a 1-D MHD code to study the evolution of the discharge and current neutralization of an 8 MeV He^{+2} beam. They concentrated on producing a channel with a low MHD instability growth rate. Because the growth rate is inversely proportional to the channel radius, increasing the radius will decrease the MHD instability growth rate. What they suggested was to use a specially tailored discharge current as shown in Figure 2.1. The current consisted of two pulses with a time of $4\mu sec$ in between. The first pulse was a maximum of 5 kA at $0.5\mu sec$ causing the channel to expand. The second pulse, starting at $4\mu sec$ later reached a maximum 50 kA in $1\mu sec$ and was meant to confine the beam ions through the magnetic field it created. This method and efforts by Freeman represent a significant amount of development of an optimized channel. Most recently, Watrous, Moses and Peterson at the University of Wisconsin-Madison have spent a great deal of effort as well. In numerical simulation, they have used a 1-D lagrangian multifrequency radiation hydro code, ZPINCH [14], to find an optimized channel picture for the fusion devices TDF (Target Development Facility) and LIBRA (Light Ion Beam Fusion Reactor) in cooperation with the Sandia National Laboratory and Kernforschungszentrum- Karlsruhe (Germany). Including the MHD physics

and radiation hydrodynamics of the channel, the simulation code ZPINCH is a state of art code. However, it does not include the ion beam current in the simulation and it approximates the radiation population with a diffusion theory which is inappropriate for such small plasmas. Improvements in these two areas will be necessary for comparison with experimental work.

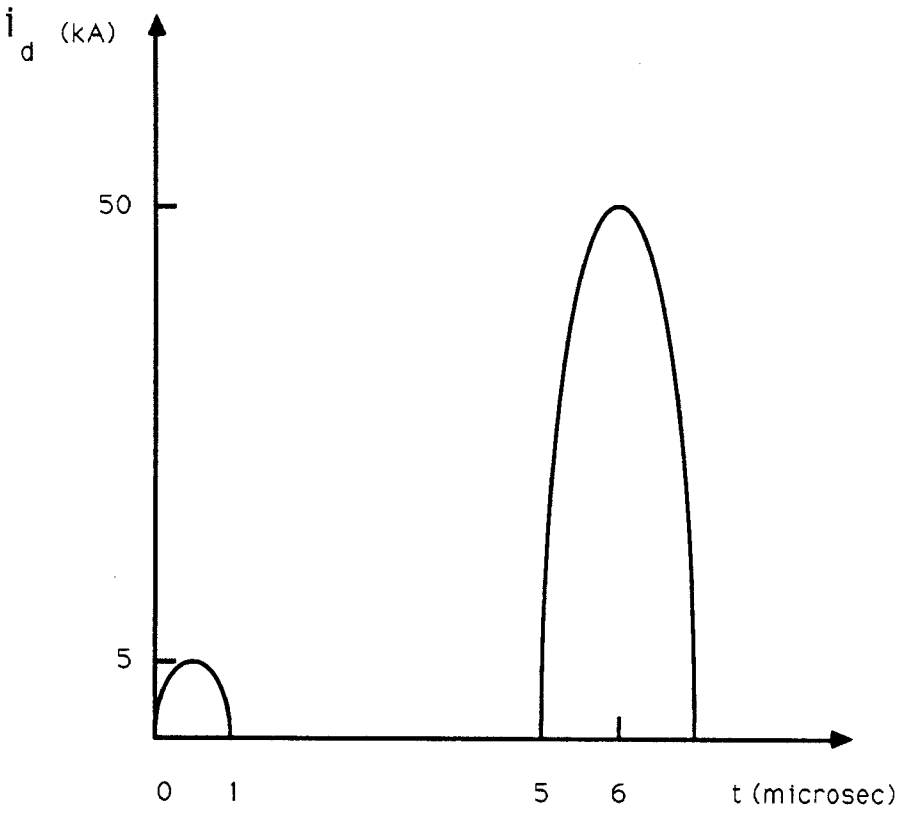

Figure 2.1: Two stage current drive by Freeman,Baker and Cook [10].

2.2 Adaptive Grid Systems

Although there might be many other studies done on the adaptive mesh systems, we will only mention the most general and and the most relevant ones to our approach. Thompson [48] and Bartel [20], in their recent publications, reviewed the current work in adaptive grid generation. Some of their ideas will be summarized here.

Adaptive grid methods fall into two categories. Despite any difference between adaptive methods, they all must provide a technique for calculating the grid distribution and the grid speed at each time step of simulation. Estimating these quantities differently puts the adaptive methods into different categories. In one of these categories, some set of rules relating the grid points in the physical and computational domain is used to establish new mesh locations at the end of each time step. The grid speed afterwards is simply estimated by using a backward difference on the new and old grid locations. The determination of the metric and the solution of PDEs in this category have been tried both implicitly and explicitly. In the second category, the schemes depend on establishing the grid speed by some rule and then the grid speed is integrated along with the PDEs to get new grid locations. A lagrangian scheme would be in this class because the the grid velocity is predetermined by using the fluid velocity and grid locations are established upon that.

The advantages and disadvantages of both categories almost compete with each other. However, it could be said that the grid metric method (class 1) is easier to apply, except that the use of a backward time difference to determine the grid speed is only first order accurate. On the other hand, the grid speed method (class 2) is harder to formulate the physical laws to determine the grid speed but it can be implemented more easily with multidimensional problems.

An important fact about differential equations which enlightens the adaptive system work is what Thompson states as:

> ... many studies on ODEs have shown that the solution error can be reduced by distributing the grid points in such a way that some positive weight function $W(x)$ satisfies the following condition

$$\Delta x_i W_i = constant. \tag{2.1}$$

This strategy is called the **Equidistribution Principle** and it can be applied also to the numerical solution of PDEs. Here; i represents the *i th* computational cell. Δx_i is the size and W_i is the average value of W for that computational cell. Note that, Δx's are going to be different each time for a time-varying W, which means the cell points will reposition themselves in such a way that the error in the solution of W is somehow reduced. Therefore, the Equidistribution principle can be used for repositioning, or so-called *mesh generation.* To see how it could be further improved for a grid metric method

(class 1), we present the following formulation.

It is often more convenient to define a new variable ξ as the successive number of mesh points, say $\xi = 1$ for the first mesh and $\xi = 2, 3..$ for the next mesh points. Then $\Delta\xi$ will be equal to 1. Now Eq.2.1 can be written as

$$x_\xi W = const. = c \tag{2.2}$$

where

$$x_\xi = \frac{\Delta x}{\Delta \xi} = \Delta x.$$

The equidistribution expression leads to the following relation

$$\sum_{i=1}^{N} \Delta x_i W_i = N \cdot c$$

and

$$\sum_{i=1}^{N_x} \Delta x_i W_i = N_x \cdot c$$

where N is the total number of mesh points and N_x is the number ($N_x = \xi(x)$) of the mesh points located at x. These relations can be used to obtain

$$\xi(x) = N_x = N \frac{\sum_{i=1}^{N_x} \Delta x_i W_i}{\sum_{i=1}^{N} \Delta x_i W_i}$$

or in the continuous form

$$\xi(x) = N \frac{\int_0^x W dx'}{\int_0^L W dx'} \tag{2.3}$$

where L is the length of the physical domain. Rearranging this equation, we obtain

$$\int_0^x W dx' = \xi(x)\left(\frac{\int_0^L W dx'}{N}\right) \tag{2.4}$$

which can be used to develop an explicit adaptive grid generation technique. The dependent variable W is a function of x and could be established from the physical variables such as *density, temperature, pressure* and *momentum.* The grid point distribution resulting from the equidistribution principle, as Bartel [20] states, is smooth and it represents the equilibrium state of a spring system. This can be seen by interpreting the following integral

$$I = \int_0^N W(\xi) x_\xi^2 d\xi$$

as representing the energy of a spring system with spring constants $W(\xi)$. With an explicit grid generation method, all that is required is to perform the integral on the right hand side of Eq.2.4 at time n and perform the left hand side integral for the new value of x at time n+1. Then all new mesh locations will be calculated and the grid speed is found from a backward time difference

$$x_\tau = \frac{x^{n+1} - x^n}{\Delta\tau}$$

where $\Delta\tau$ is the time step.

Grid metric x_ξ and velocity x_τ are two characteristic variables to be added to the set of the problem unknowns when solving the PDEs. The last thing to do before attempting such an explicit scheme is to determine the appropriate weight function $W(x)$ that indicates what physical variable (density, temperature, momentum) is adapted.

2.2.1 Weight Functions

According to the **Equidistribution Principle** the effect of the weight function is to decrease Δx when W is large and increase it when W is small. Hence, the weight function W is established from the solution variations so that Δx becomes small where a better resolution is needed in the region of high variations (high W).

Most of the studies done in the literature have taken W in terms of a single variable, such as $U(x)$. The simplest choice would be taking W as the derivative of $U(x)$ so that Δx spacing is arranged as shown in Figure 2.2. That choice of W, however, has a disadvantage of making the spacing (Δx) very large where the solution is constant ($W = \frac{\partial U}{\partial x} \Rightarrow 0$). Another choice for W is

$$W = \sqrt{(1 + U_x^2)}$$

and it requires that the *arc length* be kept constant as shown in Figure 2.3. The disadvantage with that is the point concentration in the high gradient region is decreased.

Many other choices have been made by researchers, such as by Eiseman [50,51] in the following way;

$$W = (1 + \beta^2 \cdot \mid K \mid \sqrt{1 + \alpha^2 U_x^2})$$

where β controls the concentration of points near the extrema of $U(U_x = 0)$ and α controls the points concentration near high gradients, that is where U_x

is large. However, one of the most successful choices is by Dwyer [19,52,53] by which he suggests

$$W = 1 + \alpha \mid U_x \mid + \beta \mid U_{xx} \mid$$

where again β and α have the same meaning as in the previous example. Dwyer has developed a strategy to determine α and β through user-specified fraction of points to be assigned to each function variation. That is, if R_α is defined as the fraction of grid points to be assigned to the first derivative variation, U_x, then

$$R_\alpha = \frac{\alpha \int_0^L \mid U_x \mid dx}{\int_0^L (1 + \alpha \mid U_x \mid + \beta \mid U_{xx} \mid)} dx \tag{2.5}$$

and also for the second degree of variation U_{xx}

$$R_\beta = \frac{\beta \int_0^L \mid U_{xx} \mid dx}{\int_0^L (1 + \alpha \mid U_x \mid + \beta \mid U_{xx} \mid)} dx \tag{2.6}$$

If R_α and R_β are held constant for the problem, then α and β will be determined at each time step while the solution develops.

2.2.2 Numerical Methods

No attempt has been made to review the literature on numerical methods in great detail. One reason is that there are a large number of methods to be reviewed, second we tend to mention only the most relevant ones to our approach.

The most relevant work to us is what Dwyer [20] has suggested. He states that mesh adaption allows most numerical methods to work better and that the simpler ones work best. Dwyer and Anderson [54,55,56] have used simple-first order (Donor Cell) upwind differencing and a single step of MacCormack's method [57,58,59,60] in their adaptive grid studies. The dissipative characteristics of the upwind scheme are minimized with grid adaption. The grid speed near high gradient regions (shocks) will be close to the fluid velocity and the adaptive grid scheme is then similar to a lagrangian scheme in these regions. Bartel's adaptive work also proves what Dwyer and Anderson have suggested about the upwind scheme. The artificial diffusive characteristics of first upwind differencing schemes are being addressed by second order or quadratic upwind schemes (QUD). Leonard [61] has developed such a method. In his method, the upwind derivatives are determined assuming a quadratic rather than a constant (Donor Cell) or a linear profile for the dependent variables.

The Donor Cell method is a simple (and first order accurate) algorithm and proceeds according to Figure 2.4. In Figure 2.4 q is a physical variable such as density, momentum and energy flux. The cell edge values of $q(q_{i\mp 1/2})$ are simply set to the upstream, cell averaged value as

$$q_{i+1/2} = q_i \;\; if \;\; u_{i+1/2} \geq 0 \;\; and \;\; q_{i+1/2} = q_{i+1} \;\; if \;\; u_{i+1/2} < 0,$$

and

$$q_{i-1/2} = q_{i-1} \;\; if \;\; u_{i-1/2} \geq 0 \;\; and \;\; q_{i-1/2} = q_i \;\; if \;\; u_{i-1/2} < 0.$$

This scheme is basically a *piecewise constant* grid representation and q is assumed constant over the computational cell. This is a fairly simple assumption and q has no slope at the cell center. A *piecewise linear* description called *van Leer method* [76] can be used instead for a better accuracy which assumes a slope for q at the cell center. This scheme is shown in Figure 2.5 and sets the cell edge values of q to an upstream, but a weighted value as

$$q_{i+1/2} = q_i + \frac{1}{2} dq_i \;\; if \;\; u_{i+1/2} \geq 0,$$

$$q_{i+1/2} = q_{i+1} - \frac{1}{2} dq_{i+1} \;\; if \;\; u_{i+1/2} < 0,$$

and

$$q_{i-1/2} = q_{i-1} + \frac{1}{2} dq_{i-1} \;\; if \;\; u_{i-1/2} \geq 0,$$

$$q_{i-1/2} = q_i - \frac{1}{2} dq_i \;\; if \;\; u_{i-1/2} < 0,$$

where $dq_i = \frac{c\Delta q_i \Delta q_{i-1}}{\Delta q_i + \Delta q_{i-1}} \;\; if \;\; \Delta q_i \Delta q_{i-1} > 0 \;\; and \;\; dq_i = 0 \;\; otherwise.$ Here $\Delta q_i = q_{i+1} - q_i$ and the constant c controls the order of interpolation. If c is set to zero then the scheme recovers the Donor Cell scheme and if it is chosen to be 2, the scheme becomes second order accurate.

The van Leer scheme has a higher order of accuracy when compared with the Donor Cell method, but because it involves more neighboring cell points for each step, it requires more calculations than what a Donor Cell method

does. Therefore, due to its lower cost and simplicity the Donor Cell method is used in our computational model which altogether is decribed in the next chapter.

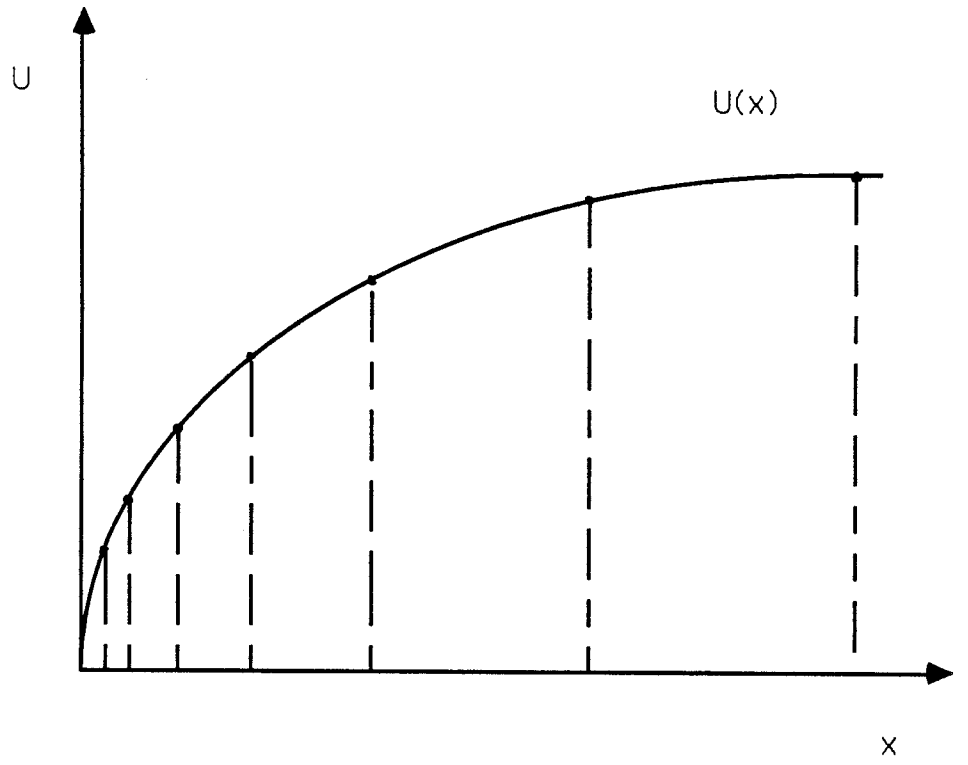

Figure 2.2: Solution gradient weighting [49].

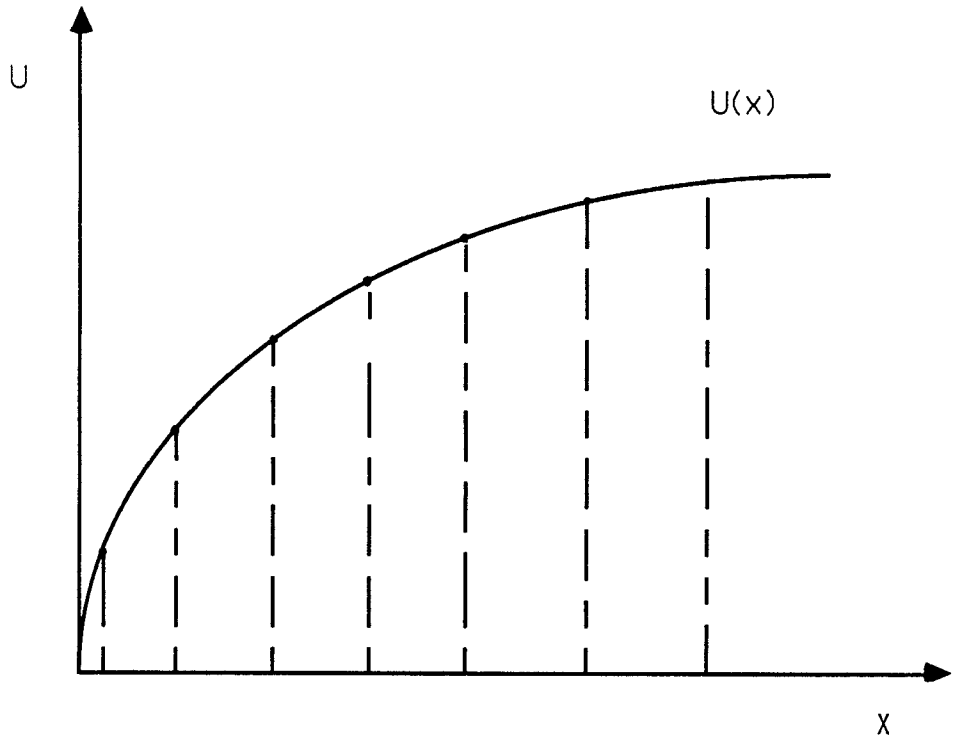

Figure 2.3: Arc length weighting [49].

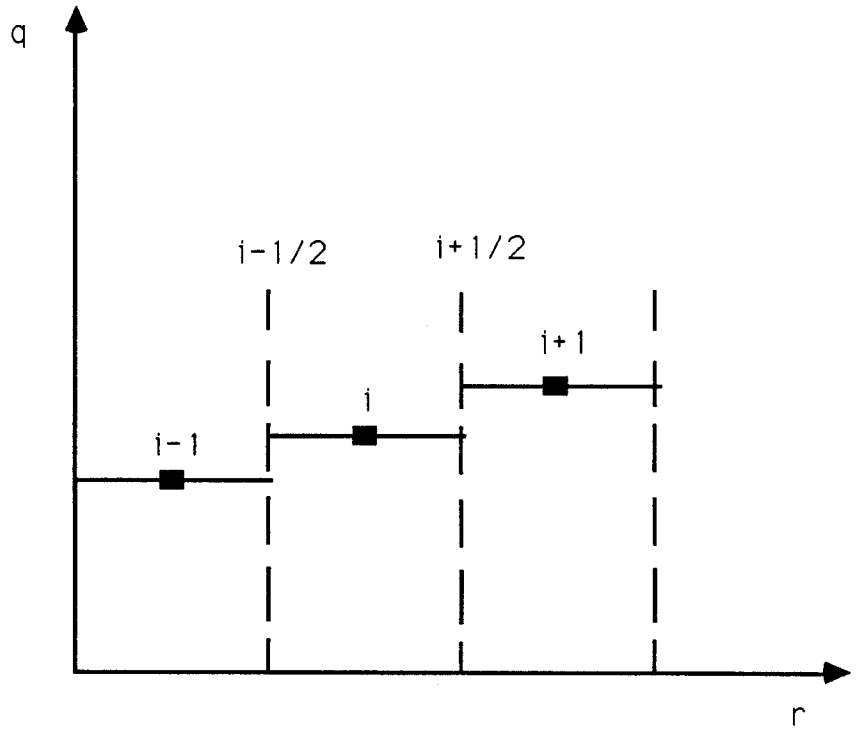

Figure 2.4: Schematic of first order Donor Cell method.

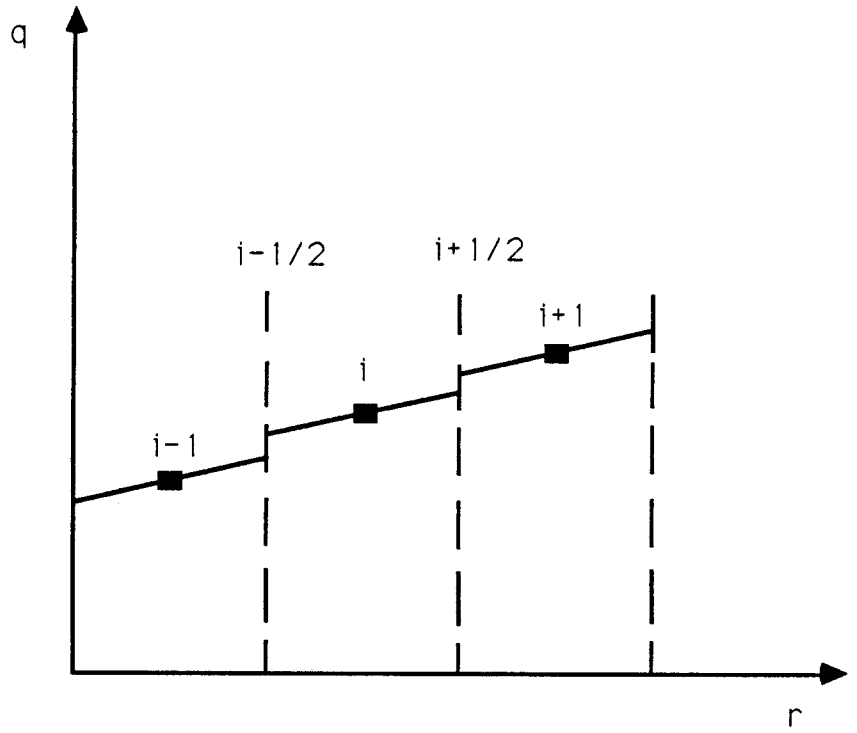

Figure 2.5: Schematic of second order van Leer method.

Chapter 3

Computational Model and Method

A numerical simulation requires four distinct parts : *1) forming the physical equations of the system (PDEs), 2) transferring the equations into the mesh system, 3) discretizing the transferred equations and 4) implementing numerical methods to solve the differenced equations.* This chapter will present these four parts and their implementation for the simulation of z-pinch plasma channels.

3.1 Model Equations

The physical problem, as mentioned in the previous chapters, is the beam transporting plasma channels or so-called *z-pinch plasma channels.* A z-pinch plasma channel, in the context of LIB fusion, can be considered as a cylindrical plasma column with a length of several meters and a radius of several centimeters [16]. Since the concern is the focusing of ion beams around the center of the plasma column, we are interested mostly in investigating the radial motion of the plasma rather than the axial and azimuthal motions. Indeed, for such a problem one can assume symmetry in axial and azimuthal directions [10]. The matter in the column is the plasma of ions and electrons with different properties (density, temperature) but further assumptions are made by taking the electron and ion velocity and temperature the same so that a **single-fluid** treatment can be used. Therefore, the plasma as a fluid obeys the standard fluid conservation laws [71] ;

$$\begin{aligned} \frac{\partial \rho}{\partial t} + \nabla \cdot (\rho \mathbf{u}) &= 0 \ \ \textbf{(continuity)} \\ \frac{\partial}{\partial t}(\rho \mathbf{u}) + \nabla \cdot (\rho \mathbf{u}\mathbf{u}) + \nabla p &= 0 \ \ \textbf{(momentum)} \\ \frac{\partial e}{\partial t} + \nabla \cdot (\mathbf{u}(p+e)) + \nabla \cdot \mathbf{q} &= 0 \ \ \textbf{(energy)} \end{aligned} \tag{3.1}$$

where ρ is mass density, $\mathbf{u}$ is fluid velocity, p is pressure, e is the total energy density per unit volume as $e = \rho(\epsilon + \frac{1}{2}u^2)$ and $\mathbf{q}$ is the heat flux as $\mathbf{q} = -\kappa \nabla T$.

In addition to these fluid equations for the plasma, one has to have another relation between the pressure, density and temperature to close the

system of equations in Eq.3.1. The required relation is the *equation of state* (EOS) and is usually entered into the calculations by tabulated forms. The equations given above are solved for ρ, $\mathbf{u}$ and e. Then one can find the specific energy, ϵ, and have a *table lookup* to evaluate the temperature that is tabulated for the various density ρ and ϵ values. The pressure is then [66] found by

$$p = (1 + \bar{Z})nkT$$

where $\bar{Z}$ is the average charge state, n is number density and T is temperature.

For the plasma in the z-pinch channel one would also like to account for the discharge current I_d, magnetic field B and coupling terms between the plasma and radiation that is emitted, absorbed or scattered by the plasma. Hence, the equations to describe the radiating-magnetized plasma in the channel should be rather a modification and an extension of Eq.3.1. Including the coupling terms of magnetic and radiation fields in the Eq.3.1 and also adding the descriptive magnetic and radiation field equations (the so-called magnetic diffusion equation and radiative transfer equation) complete the set of governing equations.

3.1.1 Magnetic Diffusion Equation

The equation governing the magnetic field **B** is obtained by combining the Maxwell's equations as follow

$$\nabla \times \mathbf{B} = \frac{4\pi}{c}\mathbf{J}_{net} \ \ (Ampere's\ law)$$

$$\nabla \times \mathbf{E}_l = -\frac{1}{c}\frac{\partial \mathbf{B}}{\partial t} \ \ (Faraday's\ law)$$

and

$$\eta \mathbf{J}_p = \mathbf{E}_p \ \ (Ohm's\ law) \tag{3.2}$$

where $\mathbf{J}_{net} = \mathbf{J}_b(ion\ beam) + \mathbf{J}_p(plasma)$ and $\mathbf{E}_p = \mathbf{E}_l + \frac{1}{c}\mathbf{u} \times \mathbf{B}$. Here $\mathbf{J}_b$ is the ion beam current density, $\mathbf{J}_p$ is the plasma conduction current density (sum of the return current density $\mathbf{J}_r$ and the discharge current density $\mathbf{J}_d$; $\mathbf{J}_p = \mathbf{J}_r + \mathbf{J}_d$). Also $\mathbf{E}_p$ and $\mathbf{E}_l$ are electric fields in the plasma and laboratory frames and η is the resistivity of the plasma.

In cylindrical coordinates in which $\mathbf{J}_{net} = J_{net}(r,t)\hat{z}$, $\mathbf{E} = E(r,t)\hat{z}$ and $\mathbf{B} = B(r,t)\hat{\theta}$, the result of combining the Maxwell equations is

$$\frac{1}{c}\frac{\partial B}{\partial t} - \frac{\partial}{\partial r}\left(\frac{\eta c}{4\pi}\frac{1}{r}\frac{\partial}{\partial r}(rB)\right) + \frac{1}{c}\frac{\partial}{\partial r}(uB) = -\frac{\partial}{\partial r}(\eta J_b) \tag{3.3}$$

This equation is called the magnetic diffusion equation and describes how the magnetic field diffuses through the plasma. Notice that the plasma has been considered in the MHD frame and therefore it is assumed non-relativistic and it involves low frequencies. Also, the displacement current $\frac{\partial \mathbf{D}}{\partial t}$ has been

neglected. This implies, of course, that we are working with conductors and not dielectrics in which case $\frac{\partial \mathbf{D}}{\partial t}$ would have to be retained.

3.1.2 Radiative Transfer Equation

The radiation present in the plasma interacts with matter through the processes of absorption, emission and scattering of photons. Photons are massless particles associated with a frequency ν, energy $E = h\nu$ and momentum $p = \frac{E}{c}$. Between collisions with matter, a photon travels in a straight line with speed c and no change in frequency ν. The population of photons at a space point $\mathbf{r}$ and at a time t furnishes further information about the radiation field, energy density, flux and momentum there. The governing equation for photon population is best represented by the *transfer equation.* It is a mathematical statement of the conservation of photons and is given in the following form [62] ;

$$(\frac{1}{c}\frac{\partial}{\partial t} + \hat{\Omega}\cdot\nabla)I(\mathbf{r},t,\hat{\Omega},\nu) = s(\mathbf{r},t,\hat{\Omega},\nu) - \sigma(\mathbf{r},t,\hat{\Omega},\nu)I(\mathbf{r},t,\hat{\Omega},\nu)$$
$$+\int_0^\infty d\nu' \int_{4\pi} d\Omega' \frac{\nu}{\nu'}\sigma_s(\nu' \rightarrow \nu, \hat{\Omega'}\cdot\hat{\Omega})I(\mathbf{r},t,\hat{\Omega'},\nu')$$

where I is specific intensity, s is thermal emissivity, σ is total cross section (absorption + outscattering), integral term is inscattering and $\hat{\Omega}$ is the solid angle.

Another way of writing the transfer equation is given by Mihalas [63] as

following

$$(\frac{1}{c}\frac{\partial}{\partial t} + \hat{\Omega}\cdot\nabla)I(\mathbf{r},t,\hat{\Omega},\nu) = \eta(\mathbf{r},t,\hat{\Omega},\nu) - \chi(\mathbf{r},t,\hat{\Omega},\nu)I(\mathbf{r},t,\hat{\Omega},\nu) \qquad (3.4)$$

where η and χ are called emissivity and extinction coefficients and are given as

$$\eta = \eta^t(thermal) + \eta^s(inscattering)$$

and

$$\chi = \kappa(true\ absorption) + \sigma_s(outscattering).$$

For application of z-pinch plasmas, scattering is just a process in which the photons' direction is changed (Thomson scattering), its frequency remains the same [63]. Therefore η^s is totally neglected and σ_s is taken as just scattering in the same energy group.

For a multigroup representation, the transfer equation can be written as

$$(\frac{1}{c}\frac{\partial}{\partial t} + \hat{\Omega}\cdot\nabla)I_g(\mathbf{r},t,\hat{\Omega}) = \bar{\eta}_g(\mathbf{r},t,\hat{\Omega})B_g - \bar{\chi}_g(\mathbf{r},t,\hat{\Omega})I_g(\mathbf{r},t,\hat{\Omega})$$

where

$$\bar{\eta}_g \equiv \frac{\int_{\nu_{g-1}}^{\nu_g} d\nu\eta(\mathbf{r},t,\hat{\Omega},\nu)}{\int_{\nu_{g-1}}^{\nu_g} d\nu B(\nu)}$$

$$\bar{\chi}_g \equiv \frac{\int_{\nu_{g-1}}^{\nu_g} d\nu\chi(\mathbf{r},t,\hat{\Omega},\nu)I(\mathbf{r},t,\hat{\Omega},\nu)}{\int_{\nu_{g-1}}^{\nu_g} d\nu I(\mathbf{r},t,\hat{\Omega},\nu)}$$

and

$$I_g \equiv \int_{\nu_{g-1}}^{\nu_g} d\nu I(\mathbf{r},t,\hat{\Omega},\nu)$$

and

$$B_g \equiv \int_{\nu_{g-1}}^{\nu_g} d\nu B(\nu) = \int_{\nu_{g-1}}^{\nu_g} (\frac{2h\nu^3}{c^2}) \frac{d\nu}{(1 - e^{-\frac{h\nu}{kT}})} \tag{3.5}$$

Here $B(\nu)$ is the Planck function.

In applications, in order for the transfer equation to be solved, these group constants should be given beforehand. Mihalas gives formulas for emissivity and opacity in the following form [64]

$$\begin{aligned}
\chi_\nu = \sum_k \sum_j \{ \sum_n \sum_{m>n} [n_{njk} - (\frac{g_{njk}}{g_{mjk}}) n_{mjk}] \alpha_{nm}^{bb}(\nu) \\
+ \sum_{n>n'} [n_{njk} - n_{njk}^* e^{-\frac{h\nu}{k_B T}}] \alpha_n^{bf}(\nu) \\
+ n_e n_{j+1,k} \alpha^{ff}(\nu)(1 - e^{-\frac{h\nu}{k_B T}}) \} + \sigma_s \\
\equiv \kappa_\nu + \sigma_{s,\nu} \quad (Opacity)
\end{aligned}$$

and

$$\begin{aligned}
\eta_\nu = (\frac{2h\nu^3}{c^2}) \sum_k \sum_j \{ \sum_n \sum_m (\frac{g_{njk}}{g_{mjk}} n_{mjk} \alpha_{nm}^{bb}(\nu) \\
+ \sum_{n>n'} n_{njk}^* e^{-\frac{h\nu}{k_B T}} \alpha_n^{bf}(\nu) \\
+ n_e n_{j+1,k} \alpha^{ff}(\nu) e^{-\frac{h\nu}{k_B T}} \}
\end{aligned} \tag{3.6}$$

where g's are statistical weights for atomic levels, n's are number densities and α's are cross sections for *bound-bound, bound-free, free-free* cases. The second term inside each of the square brackets in the opacity expression

is the contribution from stimulated (induced) emission to the absorption. Notice that these expressions involve no approximation (such as *local thermodynamic equilibrium (LTE)*) and in the high density limit (i.e LTE) they justify the well-known *Kirchoff-Planck* relation $\eta_\nu = \kappa_\nu B_\nu$. Furthermore, these formulas are given for a fluid (rest) frame and should be modified if lab-frame formulas are needed. This modification is due to the Doppler Shift $\mid \Delta\nu \mid = \nu\frac{u}{c}$ in the frequencies. Nevertheless this shift is negligible for non-relativistic radiation hydrodynamics such as in the z-pinch plasma channels where the plasma (fluid) velocity u is much smaller than c and therefore these formulas can be used in lab-frame channel calculations.

The group constants $\bar{\eta}_g$ and $\bar{\chi}_g$ in Eq.3.5, in fact, could be named as *Planck* and *Rosseland* group opacities, as found in the literature, if the specific intensity $I(\mathbf{r}, \hat{\Omega}, \nu)$ profile in the integrals is approximated by the Planck function $B(\nu)$ or its derivative with respect to temperature. Even though this is assuming an LTE profile for $I(\mathbf{r}, \hat{\Omega}, \nu)$, the degree of approximation decreases when one uses many frequency groups.

For the plasmas used in the z-pinch plasma channels for LIB fusion, a computer code by Peterson and Moses [65] calculates the Planck and Rosseland group opacities for about 20 frequency groups. However because it assumes an LTE approximation ($\eta_\nu = \kappa_\nu B_\nu$) and we try not to fall into this limit, we could use a more recent opacity calculation code by MacFarlane [66], expressing the group constants with the following formulas

$$\bar{\eta}_g = \frac{\int_{\nu_{g-1}}^{\nu_g} d\nu \eta_\nu}{\int_{\nu_{g-1}}^{\nu_g} d\nu}$$

and

$$\bar{\chi}_g = \frac{\int_{\nu_{g-1}}^{\nu_g} d\nu}{\int_{\nu_{g-1}}^{\nu_g} d\nu \frac{1}{\kappa_\nu + \sigma_{s,\nu}}} \tag{3.7}$$

where $\sigma_{s,\nu}$ is due to Thomson electron scattering and plasma waves.

These group constants are dependent on the plasma properties (plasma density and temperature) and therefore they couple the plasma and radiation equations. One would have to recalculate these constants for each time step of simulation. For such a non-linear problem a better way of providing the group constants $\bar{\eta}_g$ and $\bar{\chi}_g$ would be trying to use the specific intensity I itself in the integrals as shown in Eq.3.5. If an implicit scheme is used, then this may require the value I^{n+1} (at time $n+1$) in the integrand. Therefore, an iterative procedure would be followed, which will start with an initial value of group constants to solve the transfer equation and substitute back I for recalculation of $\bar{\eta}_g$ and $\bar{\chi}_g$. The initial value for group constants could be those given by Eq.3.7. On the other hand, with an explicit scheme, constants (integrals over I) could be evaluated more easily by using the value I^n , which is known in advance.

After solving for the specific intensity $I(\mathbf{r}, t, \hat{\Omega}, \nu)$, one could evaluate the radiation energy density e_R, flux $\mathbf{F}$ and pressure tensor $\vec{\mathbf{P}}$ by taking the

moments;

$$e_R(\mathbf{r},t) = \frac{1}{c}\sum_{g=1}^{G}\int_{4\pi} d\Omega I_g(\mathbf{r},t,\hat{\Omega})$$

$$\mathbf{F}(\mathbf{r},t) = \sum_{g=1}^{G}\int_{4\pi} d\Omega\hat{\Omega} I_g(\mathbf{r},t,\hat{\Omega})$$

$$\vec{\mathbf{P}}(\mathbf{r},t) = \frac{1}{c}\sum_{g=1}^{G}\int_{4\pi} d\Omega\hat{\Omega}\hat{\Omega} I_g(\mathbf{r},t,\hat{\Omega}) \tag{3.8}$$

Another way of calculating e_R, $\mathbf{F}$ and $\vec{\mathbf{P}}$ rather than carrying the transfer equation solution further by Eq.3.8 is to take the moments of Eq.3.4. This results in a *zeroth moment*

$$\frac{\partial e_R}{\partial t} + \nabla\cdot\mathbf{F} = \int_0^\infty d\nu \int_{4\pi} d\Omega[\eta(\mathbf{r},t,\hat{\Omega},\nu) - \chi(\mathbf{r},t,\hat{\Omega},\nu)I(\mathbf{r},t,\hat{\Omega},\nu)]$$

and a *first moment*

$$\frac{1}{c^2}\frac{\partial \mathbf{F}}{\partial t} + \nabla\cdot\vec{\mathbf{P}} = \frac{1}{c}\int_0^\infty d\nu \int_{4\pi} d\Omega\hat{\Omega}[\eta(\mathbf{r},t,\hat{\Omega},\nu) - \chi(\mathbf{r},t,\hat{\Omega},\nu)I(\mathbf{r},t,\hat{\Omega},\nu)]. \tag{3.9}$$

Notice that these are integro-differential equations and $I(\mathbf{r},t,\hat{\Omega},\nu)$ in the integral terms should be solved to get the complete solution for e_R, $\mathbf{F}$ and $\vec{\mathbf{P}}$. Mihalas, in his book [63], presents a method of solving these moments equations.

3.1.3 Complete Set of Equations

The coupling terms between the magnetic field, radiation field and the plasma are what have been left out so far and they are needed to complete the set

of equations. The fluid equations coupled to the radiative transfer and MHD equations become [67,62]

$$\frac{\partial \rho}{\partial t} + \nabla \cdot (\rho \mathbf{u}) = 0$$

$$\frac{\partial}{\partial t}(\rho \mathbf{u} + \frac{1}{c^2}\mathbf{F}) + \nabla p + \nabla \cdot (\rho \mathbf{u}\mathbf{u} + \vec{\mathbf{P}}) = \frac{\mathbf{J}_p \times \mathbf{B}}{c}$$

$$\frac{\partial}{\partial t}(e_p + e_R) + \nabla \cdot (\mathbf{q} + (e_p + p)\mathbf{u} + \mathbf{F}) = \mathbf{J}_p \cdot \mathbf{E}_l + S_{col.} \qquad (3.10)$$

where e_R, $\mathbf{F}$ and $\vec{\mathbf{P}}$ are given by Eq.3.8 in terms of radiation specific intensity $I(\mathbf{r}, t, \hat{\Omega}, \nu)$. $\mathbf{J_p} \cdot \mathbf{E}_l$ is equal to $\mathbf{E}\prime \cdot \mathbf{J}\prime$, the rate of Joulean dissipation, plus $\mathbf{u} \cdot (\frac{\mathbf{J}_p \times \mathbf{B}}{c})$, the rate at which the force $\frac{\mathbf{J}_p \times \mathbf{B}}{c}$ does work [67]. Also, $S_{col.}$ is the collisional heating between beam ions and background electrons.

Notice that the problem is highly non-linear and time-dependent, therefore one may want to reduce the dimensionality of the equations to avoid the complex situations. Since we only would like to investigate the radial motion of the plasma, the equations are rather simplified as

$$\frac{\partial \rho}{\partial t} + \frac{1}{r}\frac{\partial}{\partial r}(r\rho u) = 0$$

$$\frac{\partial}{\partial t}(\rho u + \frac{1}{c^2}F) + \frac{\partial p}{\partial r} + \frac{1}{r}\frac{\partial}{\partial r}(r\rho u^2 + P) = \frac{1}{c}J_b B - \frac{1}{r^2}\frac{\partial}{\partial r}\frac{r^2 B^2}{8\pi}$$

$$\frac{\partial}{\partial t}(e_p + e_R) + \frac{1}{r}\frac{\partial}{\partial r}(r(e_p + p)u) + \frac{1}{r}\frac{\partial}{\partial r}(r(q + F)) = JE + S_{col} \qquad (3.11)$$

where only the r component of vectors are present.

In addition to these, we can rewrite the magnetic and radiation field equations in the radial direction (r);

$$\frac{1}{c}\frac{\partial B}{\partial t} - \frac{\partial}{\partial r}(\frac{\eta c}{4\pi}\frac{1}{r}\frac{\partial}{\partial r}(rB)) + \frac{1}{c}\frac{\partial}{\partial r}(uB) = -\frac{\partial}{\partial r}(\eta J_b) \qquad (Eq.3.3)$$

and

$$\frac{1}{c}\frac{\partial}{\partial t}I_g(r,t,\hat{\Omega}) + \frac{\mu}{r}\frac{\partial}{\partial r}(rI_g(r,t,\hat{\Omega})) - \frac{1}{r}\frac{\partial}{\partial \omega}(\zeta I_g(r,t,\hat{\Omega})) = \bar{\eta}_g B_g - \bar{\chi}_g I_g(r,t,\hat{\Omega}) \tag{3.12}$$

where we have replaced the streaming term [70] in the radiative transfer equation by

$$\hat{\Omega}\cdot\nabla I_g = \frac{\mu}{r}\frac{\partial}{\partial r}(rI_g) - \frac{1}{r}\frac{\partial}{\partial \omega}(\zeta I_g). \tag{3.13}$$

Here ; μ, ω and ζ are angular variables as shown in Figure 3.1. Cylindrical coordinates are complicated by the fact that even in one spatial dimension two angular variables ζ and ω, are needed to describe the angular dependency of specific intensity I. As shown in Figure 3.1, ω is the angle between $\hat{r}$ and $\hat{\Omega}$ and μ and ζ are given as

$$\begin{aligned}\mu &= (1-\varsigma^2)^{\frac{1}{2}}\cos\omega \\ \zeta &= (1-\varsigma^2)^{\frac{1}{2}}\sin\omega.\end{aligned} \tag{3.14}$$

Conclusively, the problem of a radiating-magnetized plasma seems to be non-linear and time-dependent. A numerical solution is required and the chosen method should solve the whole set of equations simultaneously. The equations (Eq.3.11 and 3.12) are in the lab frame now and must be transferred to the *adaptive system* before any attempt of discretization. The following section will describe the adaptive mesh system and present the transformation for the whole set of equations.

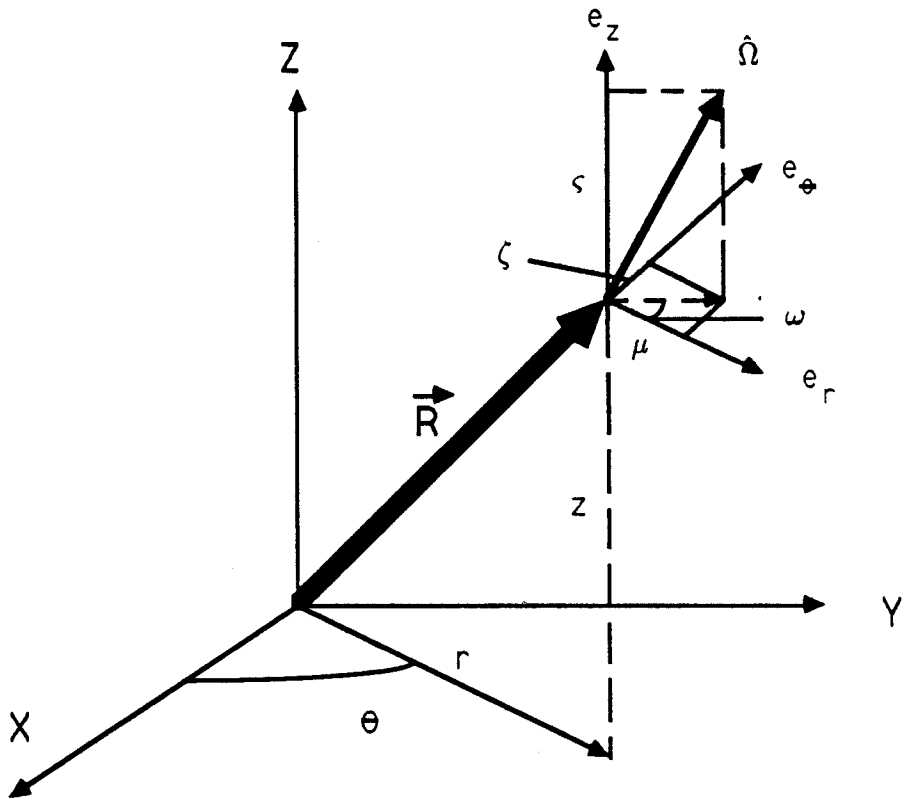

Figure 3.1: Cylindrical space-angle coordinate system

3.2 Adaptive Mesh System

The governing equations in the previous section were written on a laboratory frame and if they were discretized the way they are, then they would be evaluated on a fixed mesh system which is called *eulerian.* However, as an alternative one can work on *lagrangian* or more generally *adaptive* systems. Eulerian and lagrangian schemes are indeed special cases of adaptive schemes. When mesh points are fixed in space it is eulerian, when they move with the fluid speed then it is lagrangian. Therefore in an adaptive scheme, mesh points move arbitrarily. However, we should keep track of mesh points and their motion when the governing solution is sought. For the purpose of the current work, the mesh points motion will be following specified gradients of the solution to provide greater resolution where the solution varies the fastest.

In order to transfer the governing equations (Eq. 3.11 and 3.12) from (r,t) to an adaptive system (ξ,τ), we can use a variable transformation as follows

$$\tau = t$$

$$\xi = \xi(r,t)$$

and thus

$$\frac{\partial}{\partial \tau} = \frac{\partial}{\partial r}\frac{\partial r}{\partial \tau} + \frac{\partial}{\partial t}\frac{\partial t}{\partial \tau},$$
$$\frac{\partial}{\partial \xi} = \frac{\partial}{\partial r}\frac{\partial r}{\partial \xi} + \frac{\partial}{\partial t}\frac{\partial t}{\partial \xi}.$$

We choose $\frac{\partial t}{\partial \tau} = 1$ and thus $\frac{\partial t}{\partial \xi} = 0$. That leaves us with

$$\frac{\partial}{\partial t} = \frac{\partial}{\partial \tau} - r_\tau \frac{\partial}{\partial r},$$

$$\frac{\partial}{\partial r} = \frac{1}{r_\xi} \frac{\partial}{\partial \xi}$$

or in another representation ;

$$[\,]_t = [\,]_\tau - r_\tau [\,]_r$$

$$[\,]_r = \frac{1}{r_\xi} [\,]_\xi. \tag{3.15}$$

Here, r_ξ and r_τ are the mesh metric (jacobian) and speed that will appear with the unknowns in the transferred equations. In order to solve the set of transferred equations, which are given in section 3.2.2, we have to estimate these mesh quantities somehow in advance. Therefore, a *mesh generation technique* will be followed to find the point distribution for each time step. This technique will be discussed in the next section.

3.2.1 Adaptive Mesh Generation

The physical equations of the system include the mesh metric x_ξ and speed x_τ when they are transferred to the adaptive frame. This is obtained in section 3.2.2. In order for these equations to be solved we have to estimate the grid metric and grid speed. The information required about these quantities could be sought for the time *n+1* as well as for the time *n*. However, before any attempt to solve physical equations at time *n+1*, we let the mesh points

move from time n to $n+1$ depending on the values and *gradients* of some chosen physical variables at time n. This procedure of determining the mesh distribution at time $n+1$ in terms of information given at the time n is an *explicit* procedure. Recall that Eq.2.4 in the previous chapter was the explicit equation for determining the mesh distribution with the given *weight* function W. We rewrite it here for convenience as

$$\int_0^x W dx' = \xi(x)(\frac{\int_0^L W dx'}{N}) \qquad (Eq.2.4)$$

We call this procedure "explicit" because all the quantities on the right hand side are given at time n and the weight function W on the left hand side is also defined at time n with the exception of the integral's upper limit x being given at time $n+1$. Here; $\xi(x)$ is simply a function whose value is chosen to be equal to the mesh number. The second term on the right hand side represents the average $W\Delta x$ for each mesh cell.

After x^{n+1} is calculated, the mesh edge velocity could be found by differencing the old and new values of x with respect to time. The formula for this, x_τ, will be given later in another section. The mesh metric x_ξ is simply the difference in the space locations during the time step from t_n to t_{n+1}.

Therefore, knowing x_ξ and x_τ beforehand, the physical equations can be evaluated without any difficulty. However, one has to determine what the weight function should be before any attempt. Many forms of weight function can be postulated. The one that we have chosen for this research is

the following [20]

$$W = 1 + \alpha_a \mid A_x \mid + \beta_a \mid A_{xx} \mid + \alpha_b \mid B_x \mid + \beta_b \mid B_{xx} \mid \tag{3.16}$$

where A and B are some normalized physical quantity such as *velocity, pressure, mass, density, momentum density and temperature.* Also A_x, A_{xx}, B_x, and B_{xx} are the first and second derivatives of A and B with respect to the spatial coordinate x. The α's and β's are determined by the formulas in Eq.2.5 and 2.6 provided R's are given. Recall that R is the fraction of mesh points that the user would like to reserve for chosen gradients of A or B. Notice that Eq.3.16 enables one to construct W out of two variables, A and B, which means one can *adapt* more than one function. That obviously enhances the power of solving *multigradient* problems accurately.

3.2.2 Equations on Adaptive Mesh System

We will transfer our equations from the physical space (r, t) to the computational space (ξ, τ) by applying Eq.3.15 to Eq.3.11 and 3.12.

Continuity Equation :

$$\frac{\partial \rho}{\partial t} + \frac{1}{r}\frac{\partial}{\partial r}(r\rho u) = 0.$$

Multiply this equation by r and apply the transformation

$$r\frac{\partial \rho}{\partial t} + \frac{\partial}{\partial r}(r\rho u) = 0$$

or $r[\rho]_t + [r\rho u]_r = 0$, and subsequently

$$r([\rho]_\tau - r_\tau[\rho]_r) + \frac{1}{r_\xi}[r\rho u]_\xi = 0.$$

Now, take out the terms in the bracket and apply Eq.3.15 on r derivative

$$r[\rho]_\tau - r\frac{r_\tau}{r_\xi}[\rho]_\xi + \frac{1}{r_\xi}[r\rho u]_\xi = 0.$$

Multiplied by r_ξ ; it becomes $rr_\xi[\rho]_\tau - rr_\tau[\rho]_\xi + [r\rho u]_\xi = 0$. Here;

$$rr_\xi[\rho]_\tau = [rr_\xi\rho]_\tau - \rho[rr_\xi]_\tau$$

and

$$rr_\tau[\rho]_\xi = [rr_\tau\rho]_\xi - \rho[rr_\tau]_\xi. \tag{3.17}$$

We claim that $r_{\xi\tau} = r_{\tau\xi}$ and therefore

$$[rr_\xi]_\tau = [rr_\tau]_\xi. \tag{3.18}$$

This identity is important to remember when discretizing the equations. Because numerically that equality should be satisfied for a particular computational cell in order for conservation laws still to hold.

Now, the first two terms in the continuity equation above can be simplified upon relation in Eq.3.17 as ;

$$rr_\xi[\rho]_\tau - rr_\tau[\rho]_\xi = [rr_\xi\rho]_\tau - [rr_\tau\rho]_\xi.$$

Finally, we arrive at

$$[rr_\xi\rho]_\tau + [r\rho(u - r_\tau)]_\xi = 0. \tag{3.19}$$

Momentum Equation :

$$\frac{\partial}{\partial t}(\rho u + \frac{1}{c^2}F) + \frac{\partial p}{\partial r} + \frac{1}{r}\frac{\partial}{\partial r}(r\rho u^2 + rP) = \frac{1}{c}J_b B - \frac{1}{r^2}\frac{\partial}{\partial r}(\frac{r^2B^2}{8\pi}) \text{ or}$$

$$r[\rho u + \frac{1}{c^2}F]_\tau + r[p]_r + [r\rho u^2 + rP]_r = \frac{r}{c}J_b B - \frac{1}{r}[\frac{r^2B^2}{8\pi}]_r.$$

The same discussion for the continuity equation holds here, therefore we find

$$[rr_\xi(\rho u + \frac{1}{c^2}F)]_\tau + [r\rho u(u - r_\tau)]_\xi - [rr_\tau\frac{F}{c^2}]_\xi$$

$$+ r[p]_\xi + [P]_\xi - \frac{rr_\xi}{c}J_b B + \frac{1}{r}[\frac{r^2B^2}{8\pi}]_\xi = 0. \tag{3.20}$$

Energy Equation :

$$\frac{\partial}{\partial t}(e_p + e_R) + \frac{1}{r}\frac{\partial}{\partial r}(r(e_p + p)u) + \frac{1}{r}\frac{\partial}{\partial r}(r(q + F)) = JE + S_{col.} \text{ or}$$

$$r[e_p + e_R]_t + [r(e_p + p)u]_r + [r(q + F)]_r = rJE + rS_{col.}.$$

Applying the transformation, we find

$$[rr_\xi(e_p + e_R)]_\tau + [re_p(u - r_\tau)]_\xi - [rr_\tau e_R]_\xi$$

$$+ [rpu]_\xi + [r(q + F)]_\xi = rr_\xi(JE + S_{col.}). \tag{3.21}$$

Magnetic Diffusion Equation :

$$\frac{1}{c}\frac{\partial B}{\partial t} - \frac{\partial}{\partial r}(\frac{\eta c}{4\pi}\frac{1}{r}\frac{\partial}{\partial r}(rB)) + \frac{1}{c}\frac{\partial}{\partial r}(uB) + \frac{\partial}{\partial r}(\eta J_b) = 0.$$

After the transformation to the adaptive system, we have

$$\frac{1}{c}[B]_\tau - \frac{r_\xi r_\tau}{c}[B]_\xi - \frac{1}{r}[\frac{\eta c}{4\pi}\frac{1}{rr_\xi}[rB]_\xi]_\xi + \frac{1}{c}\frac{1}{r_\xi}[uB]_\xi + \frac{1}{r_\xi}[\eta J_b]_\xi = 0 \text{ or}$$

$$\frac{1}{c}(r_\xi[B]_\tau - r_\tau[B]_\xi) - [\frac{\eta c}{4\pi}\frac{1}{rr_\xi}[rB]_\xi]_\xi + \frac{1}{c}[uB]_\xi + [\eta J_b]_\xi = 0.$$

The terms in the bracket can be combined as

$$r_\xi[B]_\tau - r_\tau[B]_\xi = [r_\xi B]_\tau - [r_\tau B]_\xi - B[r_\xi]_\tau + B[r_\tau]_\xi$$

$$= [r_\xi B]_\tau - [r_\tau B]_\xi;\ \textit{because}\ r_{\xi\tau} = r_{\tau\xi}.$$

Therefore, we obtain

$$\frac{1}{c}[r_\xi B]_\tau + \frac{1}{c}[B(u - r_\tau)]_\xi - [\frac{\eta c}{4\pi}\frac{1}{rr_\xi}[rB]_\xi]_\xi + [\eta J_b]_\xi = 0. \qquad (3.22)$$

Radiation Transfer Equation :

$$\frac{1}{c}\frac{\partial}{\partial t}I_g + \frac{\mu}{r}\frac{\partial}{\partial r}(rI_g) - \frac{1}{r}\frac{\partial}{\partial \omega}(\zeta I_g) = \bar{\eta}_g B_g - \bar{\chi}_g I_g$$

where I_g represents $I_g(\mathbf{r}, t, \hat{\Omega})$ and B_g represents group Planck function.

The transformation from (r, t) to (ξ,τ) will give the following

$$\frac{1}{c}[rr_\xi I_g]_\tau - \frac{1}{c}[rr_\tau I_g]_\xi + \mu[rI_g]_\xi - r_\xi[\zeta I_g]_\omega - rr_\xi(\bar{\eta}_g B_g - \bar{\chi}_g I_g) = 0. \quad (3.23)$$

General form of Fluid Equations

For the sake of other possible applications that may stem from the current work, we will cast the ordinary fluid equations in Eq.3.1 into three coordinate systems :

Continuity

$$[x_\xi x^\delta \rho]_\tau + [x^\delta \rho(u - x_\tau)]_\xi = 0\ ,$$

Momentum

$$[x_\xi x^\delta \rho u]_\tau + [x^\delta \rho u(u - x_\tau)]_\xi + x^\delta [p]_\xi = 0 \ ,$$

Energy

$$[x_\xi x^\delta e]_\tau + [x^\delta e(u - x_\tau)]_\xi + [x^\delta (pu + q)]_\xi = 0 \tag{3.24}$$

where $\delta = 0, 1, 2$ for *plane, cylindrical and spherical* coordinates.

It is important to recognize that for curvilinear geometries the identity

$$[x^\delta x_\xi]_\tau = [x^\delta x_\tau]_\xi$$

must be preserved in the difference equations. That is, when differenced equations are solved on the discretized coordinates, care should be taken to provide this identity relation which also introduces a formula to calculate the grid speed while the grid points move from x^n to x^{n+1}. This formula will be given in the next section.

3.3 Methods to Solve Discretized Equations

The transferred equations on the adaptive frame and the ones on the lab frame are equivalent when $r_\tau = 0$. Both sets of equations include some undifferentiated terms and are not in strongly conservative form. Therefore they should be given care when discretized.

There are two paths to discretize the given equations: the differential approach and the control volume approach. In the differential approach, the

equations are considered to be PDEs and it follows a pure mathematical tack, and the physical significance of the variables can be lost. In the control volume approach, the conservation nature of the equations is preserved and for the adaptive mesh the control volume approach is the only viable approach if conservation of the physical quantities is to be achieved [20]. The reason is that the mesh dilates and translates each time step, thus the relative fluid and mesh velocities at the cell edges and at the center are different. Care should be given to distinguish the cell edge and center velocities, which is done in the control volume approach.

Most control volume schemes define the location of *density, pressure, and energy* at the center of the mesh while defining the location of the velocities at the mesh edge as shown in Figure 3.2. The procedure followed here to discretize the equations of continuity, momentum and energy is based on Bartel's adaptive scheme [20] for the ordinary fluid equations in the cartesian coordinates. The general form of fluid equations on other geometries were given in Eq.3.24 and they will be discussed here again.

Under the control volume approach, the *identity* equation

$$[x^{\delta} x_{\xi}]_{\tau} = [x^{\delta} x_{\tau}]_{\xi}$$

would be discretized as follows

$$\frac{(x^{\delta} x_{\xi})_i^{n+1} - (x^{\delta} x_{\xi})_i^n}{\Delta\tau} = (x^{\delta} x_{\tau})_{i+\frac{1}{2}}^n - (x^{\delta} x_{\tau})_{i-\frac{1}{2}}^n$$

where indices i and $i \mp \frac{1}{2}$ represent the i *th* cell's center and edge values. ξ

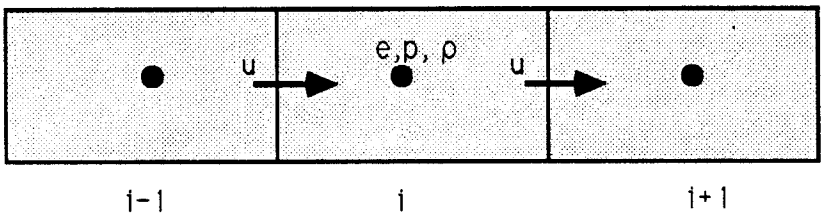

a) Cell edge oriented

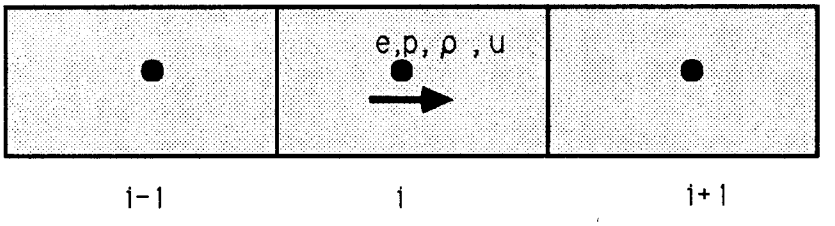

b) Cell center oriented

Figure 3.2: Control Volume approach.

is chosen to be the successive number of mesh points as explained in section 2.2. Therefore $\Delta\xi$ is equal to 1. In order for this differencing equation to conserve the involved quantities, the cell edge velocities should be given as follows

$$(x_\tau)^n_{i\mp\frac{1}{2}} = \frac{(x^\delta)^{n+1}_i x^{n+1}_{i\mp\frac{1}{2}} - x^n_{i\mp\frac{1}{2}}(x^\delta)^n_i}{(x^\delta)^n_{i\mp\frac{1}{2}}\Delta\tau} \tag{3.25}$$

Before discretizing the fluid equations in Eq.3.24, or in Eq.3.19 through 3.24, we should make a note that these equations may not be able to detect the possible *shocks* in the fluid properly, therefore we should present a scheme that handles the shocks automatically, wherever and whenever they arise. The mechanism to overcome these difficulties is to introduce into the difference equations an *artificial dissipative (viscosity)* process that gives the correct jump but smears the jump (shock) over a few mesh points. The particular method to use here is *von Neumann-Richtmyer* artificial viscosity method [68] that replaces the fluid pressure by

$$p \Rightarrow p + Q$$

where $Q = \rho(c\Delta x)^2 \mid \frac{\Delta u}{\Delta x} \mid$. Here c is a constant and u is the fluid velocity. As c is increased, the stable CFL number is reduced for a fixed mesh. The CFL (Courant-Friedrichs-Lewy) number is the ratio of the fluid velocity to the characteristic mesh velocity, $\frac{\Delta x}{\Delta t}$.

3.3.1 Discretized Fluid Equations

Continuity Equation :

$$[r^{\delta} r_{\xi} \rho]_{\tau} + [r^{\delta} \rho (u - r_{\tau})]_{\xi} = 0 \ .$$

An explicit control volume scheme for that would give the following

$$\frac{(r^{\delta} r_{\xi} \rho)_i^{n+1} - (r^{\delta} r_{\xi} \rho)_i^n}{\Delta \tau} + \frac{(r^{\delta} \rho (u - r_{\tau}))_{i+\frac{1}{2}}^n - (r^{\delta} \rho (u - r_{\tau}))_{i-\frac{1}{2}}^n}{\Delta \xi} = 0.$$

Because ξ is under our control we choose it to be the number of mesh points, say $\xi = 1$ for the first mesh and 2,3,...N for the rest. From this $\Delta\xi$ becomes unity ($\Delta x_i = 1$). In order to evaluate the cell edge ($i \mp \frac{1}{2}$) values of physical variables we apply a first-order *upwind* (donor cell) scheme [69]. This scheme simply equates the edge value with one of the neighboring cell center values depending upon the sign of the edge velocity $u_{i \mp \frac{1}{2}}$. That is,

$$\rho_{i+1/2} = \rho_i \ \ if \ u_{i+1/2} \geq 0 \ \ \ and \ \ \ \rho_{i+1/2} = \rho_{i+1} \ \ \ if \ u_{i+1/2} < 0$$

and

$$\rho_{i-1/2} = \rho_{i-1} \ \ if \ u_{i-1/2} \geq 0 \ \ \ and \ \ \ \rho_{i-1/2} = \rho_i \ \ \ if \ u_{i-1/2} < 0.$$

The differencing formula to find ρ_i^{n+1} is then

$$\rho_i^{n+1} = \frac{1}{(r^{\delta} r_{\xi})_i^{n+1}} \{(r^{\delta} r_{\xi} \rho)_i^n - \Delta\tau \{(r^{\delta} \rho (u - r_{\tau}))_{i+1/2}^n - (r^{\delta} \rho (u - r_{\tau}))_{i-1/2}^n\}\}. \tag{3.26}$$

Notice that the mesh distribution $(r^{\delta}, r_{\xi}, r_{\tau})$ on the right hand side at time n and $n+1$ is known before the partial differential equation is solved for ρ_i^{n+1}. The method of determining the mesh distribution was discussed earlier in section 3.2.1.

Momentum equation :

The same discussion for the continuity equation applies for the momentum equation except that the discretization on the pressure term should not be done by the upwind scheme, but rather be discretized [69] as

$$[p]_{\xi} = \frac{p_{i+1} - p_{i-1}}{\Delta\xi_i + \Delta\xi_{i-1}} = \frac{p_{i+1} - p_{i-1}}{2}$$

The differenced momentum equation for the radiating-magnetized plasma is then

$$\frac{1}{\Delta\tau}\{(rr_{\xi}(\rho u + \frac{F}{c^2}))_i^{n+1} - (rr_{\xi}(\rho u + \frac{F}{c^2}))_i^n\}$$

$$+\{(r\rho u(u - r_{\tau}))_{i+1/2}^n - (r\rho u(u - r_{\tau}))_{i-1/2}^n\}$$

$$-\{(rr_{\tau}\frac{F}{c^2})_{i+1/2}^n - (rr_{\tau}\frac{F}{c^2})_{i-1/2}^n\} + r_i(\{\frac{p_{i+1}^n - p_{i-1}^n}{2}\} + \{\frac{P_{i+1}^n - P_{i-1}^n}{2}\})$$

$$-\frac{(rr_{\xi})_i^n}{c}(J_b B)_i^n + \frac{1}{8\pi r_i^n}\{(r^2B^2)_{i+1/2}^n - (r^2B^2)_{i-1/2}^n\} = 0\,. \qquad (3.27)$$

Again, the upwind scheme is used to evaluate the cell edge values. As a last step u_i^{n+1} is found provided that all values at time n and F at time $n+1$ are known. Ideally, the plasma equations and the auxiliary radiation field equation are to be solved simultaneously but because of the explicit scheme being used here, one can solve the radiation field for time $n+1$ upon

plasma properties at time n and then further solve the plasma equations. The magnetic field B in the fluid equation appears to be at time n, therefore B^n is known in advance.

Energy Equation :

Recall that the energy equation for the radiating-magnetized plasma was

$$[rr_\xi(e_p + e_R)]_\tau + [re_p(u - r_\tau)]_\xi - [rr_\tau e_R]_\xi$$

$$+[rpu]_\xi + [r(q + F)]_\xi - rr_\xi[JE + S_{col.}] = 0.$$

The differenced form will be

$$\frac{1}{\Delta\tau}\{(rr_\xi(e_p + e_R))_i^{n+1} - (rr_\xi(e_p + e_R))_i^n\}$$

$$+\{(re_p(u - r_\tau))_{i+1/2}^n - (re_p(u - r_\tau))_{i-1/2}^n\}$$

$$-\{(rr_\tau e_R)_{i+1/2}^n - (rr_\tau e_R)_{i-1/2}^n\} + \{(rpu)_{i+1/2}^n - (rpu)_{i-1/2}^n\}$$

$$+ \{(r(q + F))_{i+1/2}^n - (r(q + F)_{i-1/2}^n\} - (rr_\xi)_i^n(JE + S_{col.})_i^n = 0\ . \quad (3.28)$$

This equation is solved for $(e_p)_i^{n+1}$ in terms of the values given partially at time n and at time $n + 1(r_\xi, r_\tau, e_R)$.

Magnetic Diffusion Equation :

For a discharge current in the axial direction ($\hat{z}$) and thus a magnetic field in the azimuthal direction ($\hat{\theta}$), the adaptive magnetic field equation we found was

$$\frac{1}{c}[r_\xi B]_\tau + \frac{1}{c}[B(u - r_\tau)]_\xi - [\frac{\eta c}{4\pi}\frac{1}{rr_\xi}[rB]_\xi]_\xi + [\eta J_b]_\xi = 0.$$

Because the timescale for magnetic field *diffusion* is very short compared to other events in the plasma and because we know about the values of B at the innermost ($r = 0$) and outermost ($r = r_{max}$) boundaries for time $n + 1$, the diffusion equation above is solved rather differently from density, momentum and energy equations. The assumption is to use an implicit scheme provided that we know everything in the equation (except B) at the time $n + 1$. That is, in fact, possible by deferring the solution of B after density, momentum and energy are solved at time $n + 1$. Therefore, in the differenced form, it becomes

$$\frac{1}{c\Delta\tau}\{(r_\xi B)_i^{n+1} - (r_\xi B)_i^n\} + \frac{1}{c}\{(B(u - r_\tau))_{i+1/2}^{n+1} - (B(u - r_\tau))_{i-1/2}^{n+1}\} -$$

$$\{(\frac{\eta c}{4\pi}\frac{1}{r r_\xi}[rB]_\xi)_{i+1/2}^{n+1} - (\frac{\eta c}{4\pi}\frac{1}{r r_\xi}[rB]_\xi)_{i-1/2}^{n+1}\} + \{(\eta J_b)_{i+1/2}^{n+1} - (\eta J_b)_{i-1/2}^{n+1}\} = 0$$

where

$$B_{i\mp1/2} = \frac{B_i \Delta r_{i\mp1} + B_{i\mp1}\Delta r_i}{\Delta r_i + \Delta r_{i\mp1}}$$

and $([rB])_{i+1/2} = (rB)_{i+1} - (rB)_i$ and $([rB])_{i-1/2} = (rB)_i - (rB)_{i-1}$.

Reorganizing the terms, we get

$$B_{i-1}^{n+1}\{-\frac{1}{c}\frac{\Delta r_i^{n+1}}{\Delta r_i^{n+1} + \Delta r_{i-1}^{n+1}}(u - r_\tau)_{i-1/2}^{n+1} - (\frac{\eta c}{4\pi})_{i-1/2}^{n+1}\frac{r_{i-1}^{n+1}}{r_i^{n+1} - r_{i-1}^{n+1}}\}$$

$$+B_i^{n+1}\{\frac{1}{c}\frac{\Delta r_{i+1}^{n+1}}{\Delta r_i^{n+1} + \Delta r_{i+1}^{n+1}}(u - r_\tau)_{i+1/2}^{n+1} + (\frac{\eta c}{4\pi})_{i+1/2}^{n+1}\frac{r_i^{n+1}}{r_{i+1}^{n+1} - r_i^{n+1}}$$

$$-\frac{1}{c}\frac{\Delta r_{i-1}^{n+1}}{\Delta r_i^{n+1} + \Delta r_{i-1}^{n+1}}(u - r_\tau)_{i-1/2}^{n+1} + (\frac{\eta c}{4\pi})_{i-1/2}^{n+1}\frac{r_i^{n+1}}{r_i^{n+1} - r_{i-1}^{n+1}} + \frac{1}{c\Delta\tau}(r_\xi)_i^{n+1}\}$$

$$+B_{i+1}^{n+1}\{\frac{1}{c}\frac{\Delta r_i^{n+1}}{\Delta r_i^{n+1}+\Delta r_{i+1}^{n+1}}(u-r_\tau)_{i+1/2}^{n+1}-(\frac{\eta c}{4\pi})_{i+1/2}^{n+1}\frac{r_{i+1}^{n+1}}{r_{i+1}^{n+1}-r_i^{n+1}}\}$$

$$=\frac{1}{c\Delta\tau}(r_\xi B)_i^n. \tag{3.29}$$

or more concisely

$$a_i\ B_{i-1}^{n+1}+c_i\ B_i^{n+1}+d_i\ B_{i+1}^{n+1}=s_i^n \tag{3.30}$$

where $i=2,..m-1$.

Eq. 3.30 is a tridiagonal system with

$$B_1^{n+1}=0\ \ and\ \ B_m^{n+1}=\frac{2I_d}{c\,r_{max}}. \tag{3.31}$$

Here I_d is the discharge current and r_{max} is the channel radius.

The solution found by the so-called Thomas algorithm [73] is

$$B_i^{n+1}=e_{i+1}B_{i+1}^{n+1}+f_{i+1}\quad i=1,2,..,m-1.$$

Here $e_{i+1}=-\frac{d_i}{a_ie_i+c_i}$ and $f_{i+1}=\frac{(s_i-a_if_i)}{a_ie_i+c_i}$ where $i=2,3,..,m$. The values of e_2 and f_2 are found from the boundary condition of B in Eq.3.31. These conditions are consistent if $e_2=f_2=0$.

Current Density and Electric Field :

We know that

$$\mathbf{J}=\frac{c}{4\pi}\nabla\times\mathbf{B};\ \ J_z=\frac{c}{4\pi}\frac{1}{r}\frac{\partial}{\partial r}(rB). \tag{3.32}$$

This is the expression to find J_z in terms of $B(r,t)$. The magnetic field has been calculated at the cell centers, but the current density J will be

calculated at the cell edges as

$$J^n_{i+1/2} = \frac{c}{4\pi}\frac{1}{r^n_{i+1/2}}\frac{(rB)^n_{i+1} - (rB)^n_i}{r^n_{i+1} - r^n_i}$$

$$J^n_{i-1/2} = \frac{c}{4\pi}\frac{1}{r^n_{i-1/2}}\frac{(rB)^n_i - (rB)^n_{i-1}}{r^n_i - r^n_{i-1}}. \tag{3.33}$$

Now, we can also calculate the electric fields in the fluid and lab frame:

$$E_f = \eta J \quad and \quad (E_f)^n_{i\mp 1/2} = (\eta J)^n_{i\mp 1/2}, \tag{3.34}$$

and

$$(E_l)^n_{i\mp 1/2} = (E_f)^n_{i\mp 1/2} - \frac{1}{c}(uB)^n_{i\mp 1/2}. \tag{3.35}$$

Then, the heat term $(EJ)^n_i$ in Eq.3.28 will be given as

$$(EJ)^n_i = \frac{1}{2}\{(E_l J)^n_{i+1/2} + (E_l J)^n_{i-1/2}\}. \tag{3.36}$$

Radiation Transfer Equation :

We have previously derived the multigroup radiation transfer equation and transferred it into the adaptive mesh system as shown below

$$\frac{1}{c}[rr_\xi I_g]_\tau - \frac{1}{c}[rr_\tau I_g]_\xi + \mu[rI_g]_\xi - r_\xi[\zeta I_g]_\omega - rr_\xi(\bar{\eta}_g B_g - \bar{\chi}_g I_g) = 0.$$

The numerical solution of this equation is more complicated than that of the continuity, momentum, energy and magnetic field because of the degree of discretization it requires. Even though it describes the radiation transport in only the radial direction, by assuming symmetry in azimuthal and axial directions, it includes surprisingly two angular variables ζ and μ besides the

radial component r. Therefore more care must be taken in indexing the discrete directions so that the angular differencing formulas can be applied in a consistent manner.

In order to solve Eq.3.23, which is given above, we need to discretize the angular variables as well as the spatial variable r. The method chosen for angular discretization is called the *Discrete Ordinate Method* or briefly S_N method and is a common practice for neutronics problems. Here, N is the level of discretization.

Discretization of Radiation Transfer Equation

Recall from Figure 3.1 that the direction of photons are represented by the solid angle direction $\hat{\Omega}$. The trace of this unit vector on the z direction is ς and on the radial direction is μ. The ζ and μ are the angular variables that appear in the differential equation and are given in terms of ς and ω as in Eq.3.14. The relation between these angular variables can also be seen in Figure 3.1. To facilitate the angular discretization, we associate two indices with each direction: $\hat{\Omega} \rightarrow \hat{\Omega}_{pq}$. The first index indicates the value ς_p with $\varsigma_1 < \varsigma_2 < \varsigma_3 < \cdots < \varsigma_N$. The second index increases with the value of μ associated with ς_p. Hence for fixed ς_p, $\mu_{p1} < \mu_{p2} \cdots < \mu_{pN_p}$ where N_p varies between 1 and N.

We choose a level-symmetric quadrature set [70] for discrete ς and μ values where the directions are enumerated pairs of $\pm\mu_i$, $\pm\varsigma_j$ for $i = 1, ...N/2$. Although full rotational symmetry is not required it is important to place

the quadrature points on levels of constant ζ_j about the z axis, because only with such an arrangement is it possible to handle the derivative numerically with respect to ω in Eq.3.23 without the complication of differing values of ζ_j entering into the expression.

The numbering scheme for ς_p and μ_{pq} is illustrated schematically in Figure 3.3, where the ordinate points are projected on the μ,ς plane.

Because we assume symmetry in θ and z directions (infinite cylinder), the angular specific intensity $I(r, \Omega_{pq})$ must obey *mirror* reflection with respect to the plane perpendicular to the z axis. Thus we have

$$I_g(r, \mu, \varsigma) = I_g(r, \mu, -\varsigma).$$

Therefore we need to solve only for the angular distribution in two octants $\mu < 0, \varsigma > 0$ and $\mu > 0, \varsigma > 0$. The total radiation intensity in terms of the chosen quadrature set is given as

$$I_g(r, t) = \frac{1}{4} \sum_{pq} w_{pq} I_{g;pq}(r, t). \tag{3.37}$$

where w_{pq} is a weight number, not the angular variable ω. The derivative term with respect of ω can be written in terms of angular differencing coefficients α [70] as

$$-r_\xi[\zeta I_g]_\omega = \frac{r_\xi}{w_{pq}}(\alpha^p_{q+1/2} I_{g;p,q+1/2} - \alpha^p_{q-1/2} I_{g;p,q-1/2}).$$

Substituting this into Eq.3.23, we get

$$\frac{1}{c}[r r_\xi I_{g;pq}]_\tau - \frac{1}{c}[r r_\tau I_{g;pq}]_\xi + \mu_{pq}[r I_{g;pq}]_\xi$$

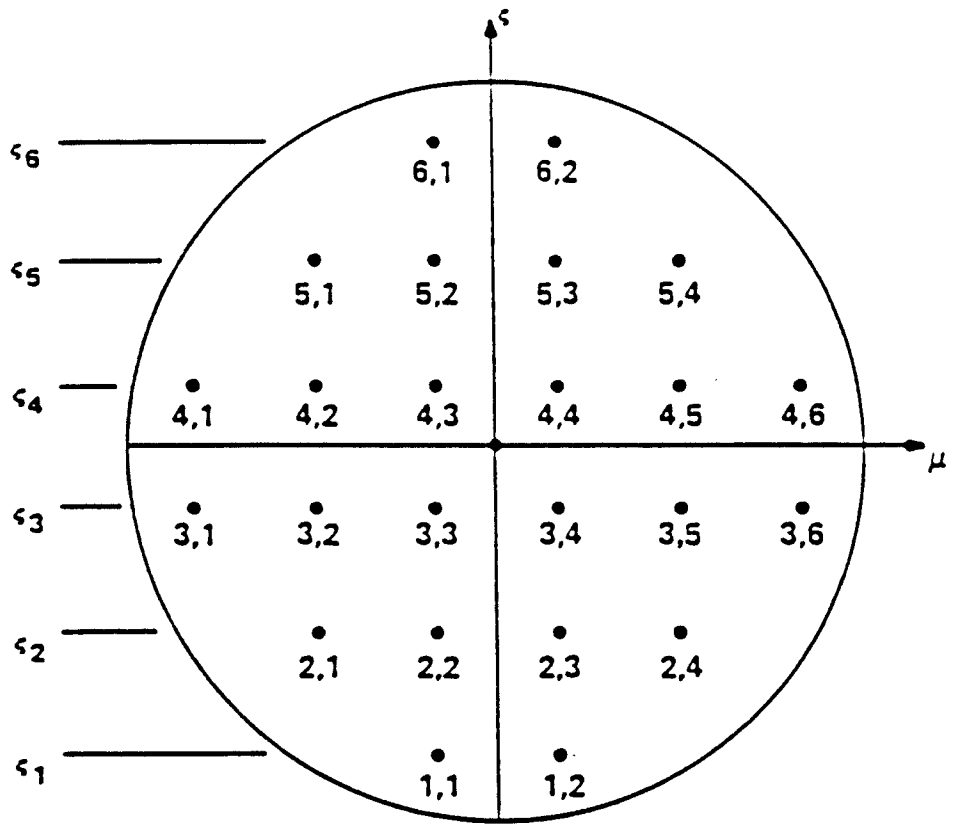

Figure 3.3: Projection of an S_6 quadrature set on the μ,ς plane using p,q numbering in cylindrical coordinates [70] .

$$+\frac{r_\xi}{w_{pq}}(\alpha^p_{q+1/2}I_{g;p,q+1/2}-\alpha^p_{q-1/2}I_{g;p,q-1/2})-rr_\xi(\bar{\eta}_g B_g-\bar{\chi}_g I_{g;pq})=0. \tag{3.38}$$

To solve this differenced equation, one has to know the α's. The criteria for determining these angular coefficients is based on the fact that the streaming operator $(\hat{\Omega}\cdot\nabla I)$ must vanish when the I is both uniform and isotropic as it would be in a uniform infinite medium ;

$$\mu_{pq}[rI_g]_\xi+\frac{r_\xi}{w_{pq}}(\alpha^p_{q+1/2}I_g-\alpha^p_{q-1/2}I_g)=0, \qquad or$$

$$(\mu_{pq}+\frac{1}{w_{pq}}(\alpha^p_{q+1/2}-\alpha^p_{q-1/2}))r_\xi I_g=0.$$

Then,

$$\mu_{pq}+\frac{1}{w_{pq}}(\alpha^p_{q+1/2}-\alpha^p_{q-1/2})=0. \tag{3.39}$$

We rewrite that as

$$\alpha^p_{q+1/2}=\alpha^p_{q-1/2}-\mu_{pq}w_{pq} \tag{3.40}$$

where $\quad p=1,2,...N \quad and \quad q=1,2,...N_p.$

Similarly, to assume that the photon conservation holds in the discrete ordinate (S_N) method we use the quadrature formula to integrate Eq.3.38 over angle. We obtain the *zeroth* moment of the transfer equation

$$[rr_\xi e_{g;R}]_\tau-[rr_\tau e_{g;R}]_\xi+[rF_g]_\xi-(\bar{\eta}_g Q_{g;1}-\bar{\chi}_g I_g)rr_\xi=0 \tag{3.41}$$

with

$$I_g\equiv\frac{1}{4}\sum_{pq}w_{pq}I_{g;pq} \quad ,$$

$$e_{g;R} \equiv \frac{1}{4c}\sum_{pq} w_{pq} I_{g;pq} \quad ,$$

$$F_g \equiv \frac{1}{4}\sum_{pq} w_{pq}\mu_{pq} I_{g;pq} \quad and$$

$$Q_{g;1} \equiv \frac{1}{4}\sum_{pq} w_{pq} B_g \quad ,$$

if and only if

$$\sum_{p=1}^{N}\sum_{q=1}^{Np}(\alpha^p_{q+1/2} I_{g;p,q+1/2} - \alpha^p_{q-1/2} I_{g;p,q-1/2}) = 0. \qquad (3.42)$$

This condition along with the previous condition on α, Eq.3.40, can be met for arbitrary I only if

$$\alpha^p_{1/2} = 0 \qquad p = 1, 2, ...N.$$

Now multiply Eq.3.38 by $\frac{\mu_{pq}}{c}$ and integrate again over the angle to get the *first moment* equation ;

$$\frac{1}{c^2}([r r_\xi F_g]_\tau - [r r_\tau F_g]_\xi) + [r P_g]_\xi - \frac{r r_\xi}{c}(\bar{\eta}_g Q_{g;2} + \bar{\chi}_g F_g) = 0 \qquad (3.43)$$

where now

$$P_g \equiv \frac{1}{4c}\sum_{pq} w_{pq}\mu_{pq}\mu_{pq} I_{g;pq},$$

$$Q_{g;2} \equiv \frac{1}{4}\sum_{pq} w_{pq}\mu_{pq} B_g.$$

Having determined the values $\alpha^p_{q+1/2}$, we must relate the $I_{g;p,q+1/2}$ values to the center I_{pq} values. We define an *angular diamond difference* approximation such as

$$I_{g;pq} = \frac{1}{2}(I_{g;p,q+1/2} + I_{g;p,q-1/2}) \quad ; p = 1, 2, ..N \quad and \quad q = 1, 2, ..N_p. \qquad (3.44)$$

Solving this for $I_{g;p,q+1/2}$ and substituting into Eq.3.38 to eliminate $I_{g;p,q+1/2}$ we get the following

$$\frac{1}{c}[rr_\xi I_{g;pq}]_\tau - \frac{1}{c}[rr_\tau I_{g;pq}]_\xi + \mu_{pq}[rI_{g;pq}]_\xi + \frac{2r_\xi}{w_{pq}}\alpha^p_{q+1/2} I_{g;pq}$$

$$- \frac{r_\xi}{w_{pq}}(\alpha^p_{q+1/2} + \alpha^p_{q-1/2}) I_{g;p,q-1/2} - rr_\xi(\bar{\eta}_g B_g - \bar{\chi}_g I_{g;pq}) = 0. \qquad (3.45)$$

Now once $I_{g;p,1/2}$ is known, Eq.3.44 and 3.45 can be solved for increasing q. A technique to evaluate $I_{g;p,1/2}$ is the step differencing approximation, $I_{g;p,1/2} = I_{g;p,1}$.

Spatial discretization of Eq.3.45 will be followed by the same discussion made for the density, momentum, energy and magnetic field equations. A control volume approach will be used and a first order diamond differencing method will be tried to evaluate the cell edge values of variables.

Now, if we apply an implicit scheme to discretize Eq.3.45 in time and follow the control volume approach, we get the following ;

$$\frac{1}{c}\{\frac{(rr_\xi I_{g;pq})^{n+1}_i - (rr_\xi I_{g;pq})^n_i}{\Delta\tau}\} - \frac{1}{c}\{(rr_\tau I_{g;pq})^{n+1}_{i+1/2} - (rr_\tau I_{g;pq})^{n+1}_{i-1/2}\}$$

$$+\mu_{pq}\{(rI_{g;pq})^{n+1}_{i+1/2} - (rI_{g;pq})^{n+1}_{i-1/2}\} + \frac{2\alpha^p_{q+1/2}}{w_{pq}}(r_\xi I_{g;pq})^{n+1}_i$$

$$- \frac{(\alpha^p_{q+1/2} + \alpha^p_{q-1/2})}{w_{pq}}(r_\xi I_{g;p,q-1/2})^{n+1}_i - (\, rr_\xi(\bar{\eta}_g B_g - \bar{\chi}_g I_{g;pq})\,)^{n+1}_i = 0. \qquad (3.46)$$

To go one step further, take the spatial diamond approximation

$$I_{pq,i} = \frac{1}{2}(I_{pq,i+1/2} + I_{pq,i-1/2}) \qquad (3.47)$$

Then for $\varsigma_p > 0$ and $\mu_{pq} < 0$ we take

$$I_{pq,i-1/2} = 2I_{pq,i} - I_{pq,i+1/2}$$

and Eq.3.46 becomes

$$I^{n+1}_{g;pq,i} = \{\frac{1}{c\Delta\tau}(rr_\xi I_{g;pq})^n_i + \frac{(r_\xi)^{n+1}_i}{w_{pq}}(\alpha^p_{q+1/2} + \alpha^p_{q-1/2})I_{g;p,q-1/2,i}$$

$$+I_{g;pq,i+1/2}\ \{\frac{1}{c}((rr_\tau)_{i+1/2} + (rr_\tau)_{i-1/2}) - \mu_{pq}(r_{i+1/2} + r_{i-1/2})\}$$

$$+(rr_\xi)^{n+1}_i \bar{\eta}_g B_g\}\cdot\{\frac{(rr_\xi)^{n+1}_i}{c\Delta\tau} + \frac{2(r_\xi)^{n+1}_i}{w_{pq}}\alpha^p_{q+1/2}$$

$$+\bar{\chi}_g(rr_\xi)^{n+1}_i + \frac{2(rr_\tau)^{n+1}_{i-1/2}}{c} - 2\mu_{pq}r^{n+1}_{i-1/2}\}^{-1}. \qquad (3.48)$$

Similarly for $\varsigma_p > 0$ and $\mu_{pq} > 0$ we have

$$I_{pq,i+1/2} = 2I_{pq,i} - I_{pq,i-1/2}$$

and hence $I_{pq,i+1/2}$ can be eliminated from Eq.3.46 to yield

$$I^{n+1}_{g;pq,i} = \{\frac{rr_\xi}{c\Delta\tau} + \frac{2r_\xi}{w_{pq}}\alpha^p_{q+1/2} + \bar{\chi}_g rr_\xi - \frac{2(rr_\tau)_{i+1/2}}{c} + 2\mu_{pq}r_{i+1/2}\}^{-1}\cdot$$

$$\{\frac{1}{c\Delta\tau}(rr_\xi I_{g;pq})^n_i - I_{g;pq,i-1/2}\ \{\frac{1}{c}(rr_\tau)_{i+1/2} + (rr_\tau)_{i-1/2} + \mu_{pq}(r_{i+1/2} + r_{i-1/2}\}$$

$$+ rr_\xi\bar{\eta}_g B_g + \frac{r_\xi}{w_{pq}}(\alpha^p_{q+1/2} + \alpha^p_{q-1/2})I_{g;p,q-1/2,i}\ \}, \qquad (3.49)$$

where indices $n+1$ and i are omitted. Equations 3.47 through 3.49 along with the angular difference relationship

$$I_{p,q+1/2,i} = 2I_{pq,i} - I_{p,q-1/2,i} \qquad (3.50)$$

constitute the necessary equations for sweeping the space-angle mesh. Note again one must first use either a starting direction equation or the step condition

$$I_{p,1/2,i} = I_{p,1,i}$$

to begin the sequence. Then we must solve for the negative μ_{pq} first. If we assume a vacuum boundary condition at the outside of the cylinder, then we have

$$I_{imax+1/2}(-\mu_{pq}) = 0.$$

We then start at the outer boundary and march inward for decreasing values of i. Once the solution for negative μ_{pq} is found the boundary condition at the center of the cylinder can be applied. If there is a reflective boundary (symmetry around the axis) then the I values for positive μ_{pq} can be set by the negative μ_{pq} direction I values which have been calculated by inward marching.Then we solve for positive μ_{pq} and increasing i.

Because $\bar{\chi}_g$ includes the integrals of I at time n+1 one would like to apply an iteration scheme for better solution by putting back the calculated solution of I in the group constants, $\bar{\chi}_g$, and solve again for I until it satisfies the convergency criteria.

3.4 Sample Problems

The adaptive Navier-Stokes hydro code written for slab geometry by Bartel was modified and extended to all geometries by 1) deriving the required expression for the mesh adaption (x_ξ and x_τ) to satisfy the differenced equations, 2) putting the fluid equations into a general form. Secondly, all governing equations including the continuity, momentum, energy, magnetic field and radiation field equations were put on the adaptive mesh for application of z-pinch channels.

Among the equations included in the model, all except magnetic diffusion and radiation transfer equations were solved by explicit schemes and also an explicit procedure was followed to generate the mesh distribution. The Equation of State tables were found by MIXERG and IONMIX computer codes which were mentioned previously. Time step control was done by setting the CFL number to a constant value. Since an explicit scheme was used, this number, CFL, has a maximum of unity. The compressible flow CFL number is typically defined [69] for a fixed mesh system and it is

$$CFL = (\mid u \mid + a)\frac{\Delta t}{\Delta x}$$

where a is the local sound speed. For an adaptive scheme we can define [20] CFL number as follows

$$CFL = (\mid u_{cell} \mid + a)\frac{\Delta t}{\Delta x}$$

where $u_{cell} = \frac{1}{2}(u_r + u_l)$; u_r and u_l are the right and left edge velocities.

A list of the major steps that the code follows to update the equations on an adaptive mesh from time t_n to t_{n+1} is given below:

- Given R_α and R_β, the fraction of the mesh points to be used for the first and second degree variation of the chosen adaptive function, calculate α and β through Eq.2.5 and 2.6.
- Calculate the weight function W using updated values (time n) of the chosen adaptive function.
- Compute new mesh points, x_ξ and mesh speeds, x_τ by Eq.2.4 and 3.25.
- Solve the governing equations for time $n + 1$.
- Set up the new time step.
- Repeat steps.

3.4.1 Shock Tube

A common test problem for a hydro code is the *shock tube* problem by which the code is examined against severe discontinuities. Hence, the following section will present how the code treats such a problem. The problem is studied in only one spatial dimension but in all geometries (slab, cylinder and sphere.) The physical domain is divided into two regions of different

pressures. The inner region has higher pressure and thus higher density. At $t = 0^+$ the system is released and a shock is formed propagating outward. Application of this problem has already been done by Bartel for Navier-Stokes fluids in cartesian coordinates. Here, we will deal instead with eularian fluids, but in all geometries.

In a shock problem like this there are three distinct regions that must be caught; the shock wave, the contact discontinuity and the rarefaction wave. Figure 3.4 shows the initial pressure distribution for the problem. A ratio of 3 was used to set the pressures in two regions. The gas is assumed to be initially isothermal. The initial density profile is also shown in Figure 3.5. These figures show the pressure and density profiles (for a slab) at other times too. Here a donor cell (first upwind) method with 100 mesh points has been used.

Using an adaptive system saves us many mesh points. A MacCormack method with 1000 mesh points and a Leonard's QUD method with 500 mesh points and a donor cell (upwind) method with 500 mesh points on a fixed mesh scheme were tried previously by Bartel and the results are shown in Figures 3.6 through 3.8. These results are not good compared to the adaptive results. Note that the donor cell on a fixed mesh system is the simplest and the least accurate one. However, Figure 3.5 proves that even a first-order donor cell method on an adaptive scheme is able to detect the three regions of the problem mentioned before. A fewer number of mesh points have been

used and the *momentum density* has been adapted. The reason that the momentum density was chosen as the weight function is that its derivatives capture not only the shock front and rarefaction but also the discontinuity region. A value of $CFL = 1$ was used for this run.

The same shock problem on other geometries would be expected to behave the same qualitatively. An important difference between the curvilinear geometries and the slab geometry is that in slab geometry the mass of a computational cell is not proportional to the distance to the origin of the problem whereas in cylindrical and spherical geometries the mass is proportional to the distance r and r^2. That difference, therefore, should show up in the simulations of cylindrical and spherical cases. Figures 3.9 through 3.10 show the density profiles for these cases with 200 mesh points and a CFL number of 0.1. The adaption function was again chosen as momentum density with $R_\alpha = 0.35$ and $R_\beta = 0.15$.

As noticeable in the figures, the mass in the shock behind decreases whereas it increases in front. In the slab case, it would be flat for both regions. The curvature-like behavior of mass in the sphere looks the same as in the cylinder except that the degree of curvature is higher as r^2 versus r. The fluid motion can be viewed in all three cases by looking at the velocity profiles given in Figures 3.11-13. There one can see the uniform profile of the slab case and the nonuniform profile of the cylinder and sphere cases due to the r dependency of the mass and therefore that of the fluid motion.

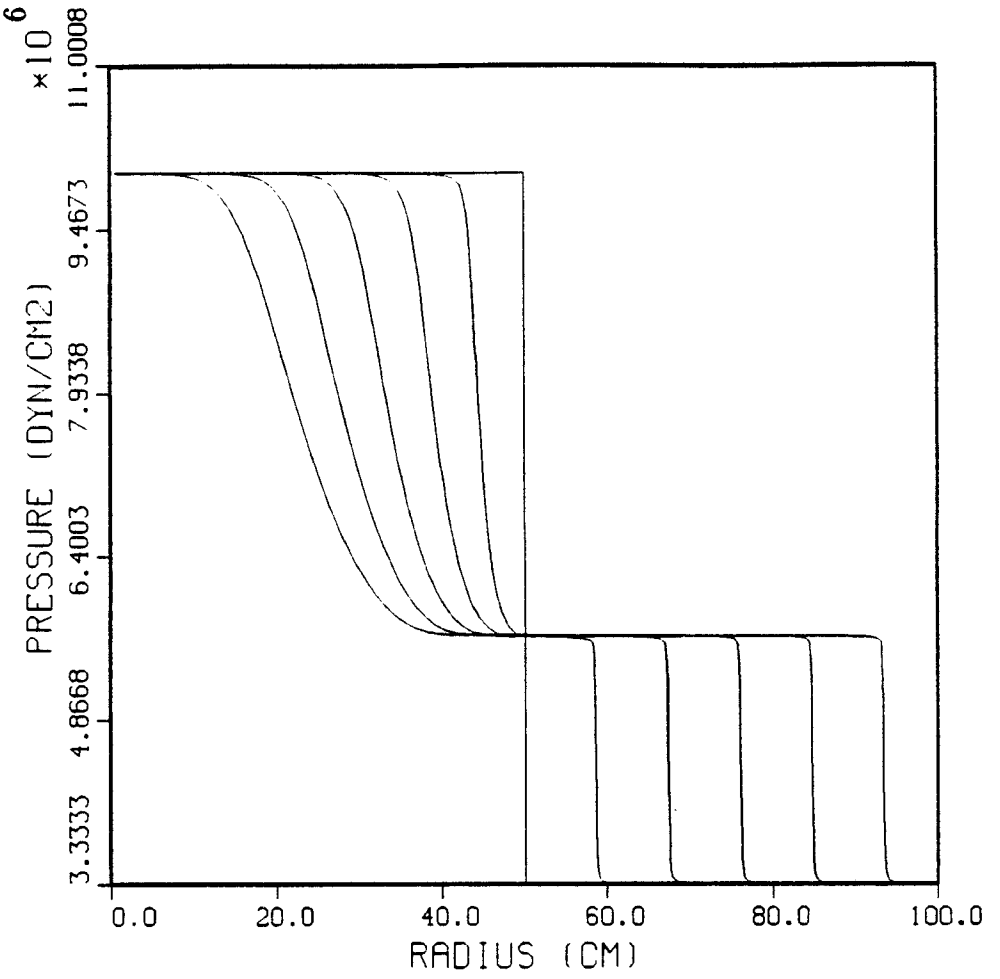

Figure 3.4: Pressure profiles at times 0.0, 0.2, 0.4, 0.6, 0.8, 1.0 milliseconds; slab.

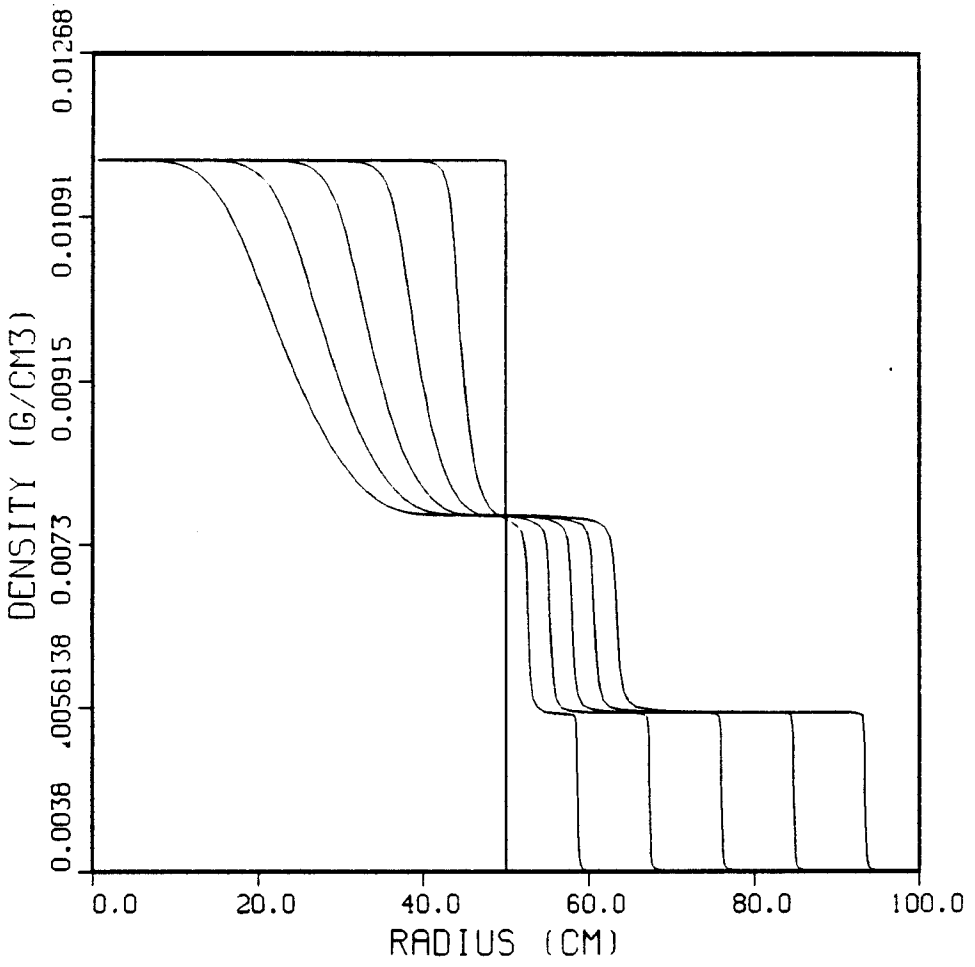

Figure 3.5: Mass density profiles at times 0.0, 0.2, 0.4, 0.6, 0.8, 1.0 milliseconds; slab.

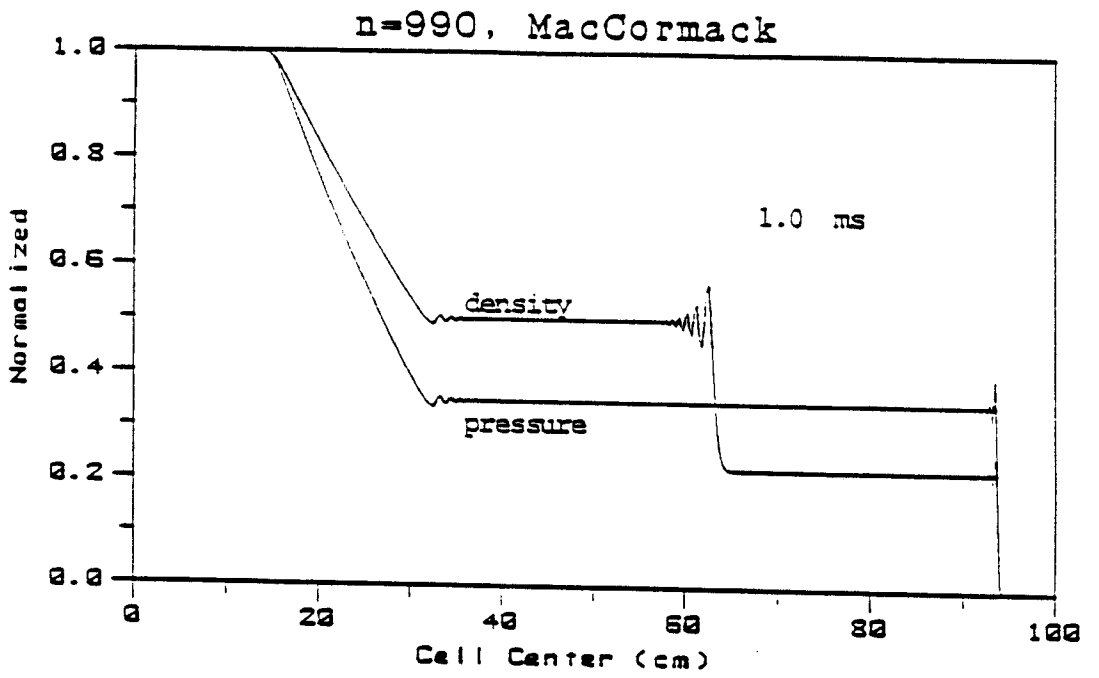

Figure 3.6: Density and pressure distributions for 990 point MacCormack method [20].

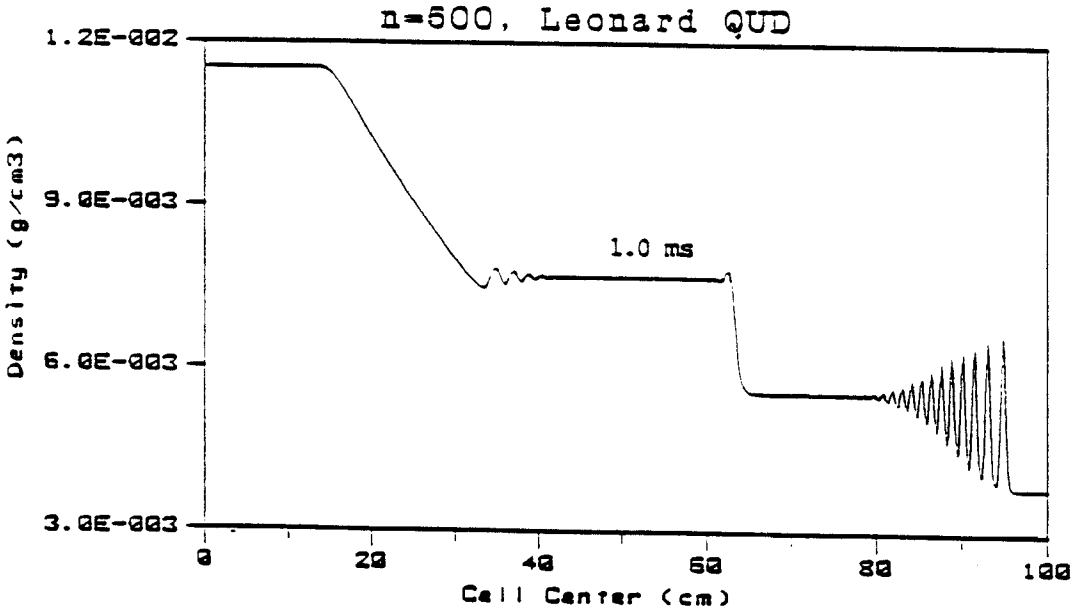

Figure 3.7: Density distribution for 500 point Leonard method [20] .

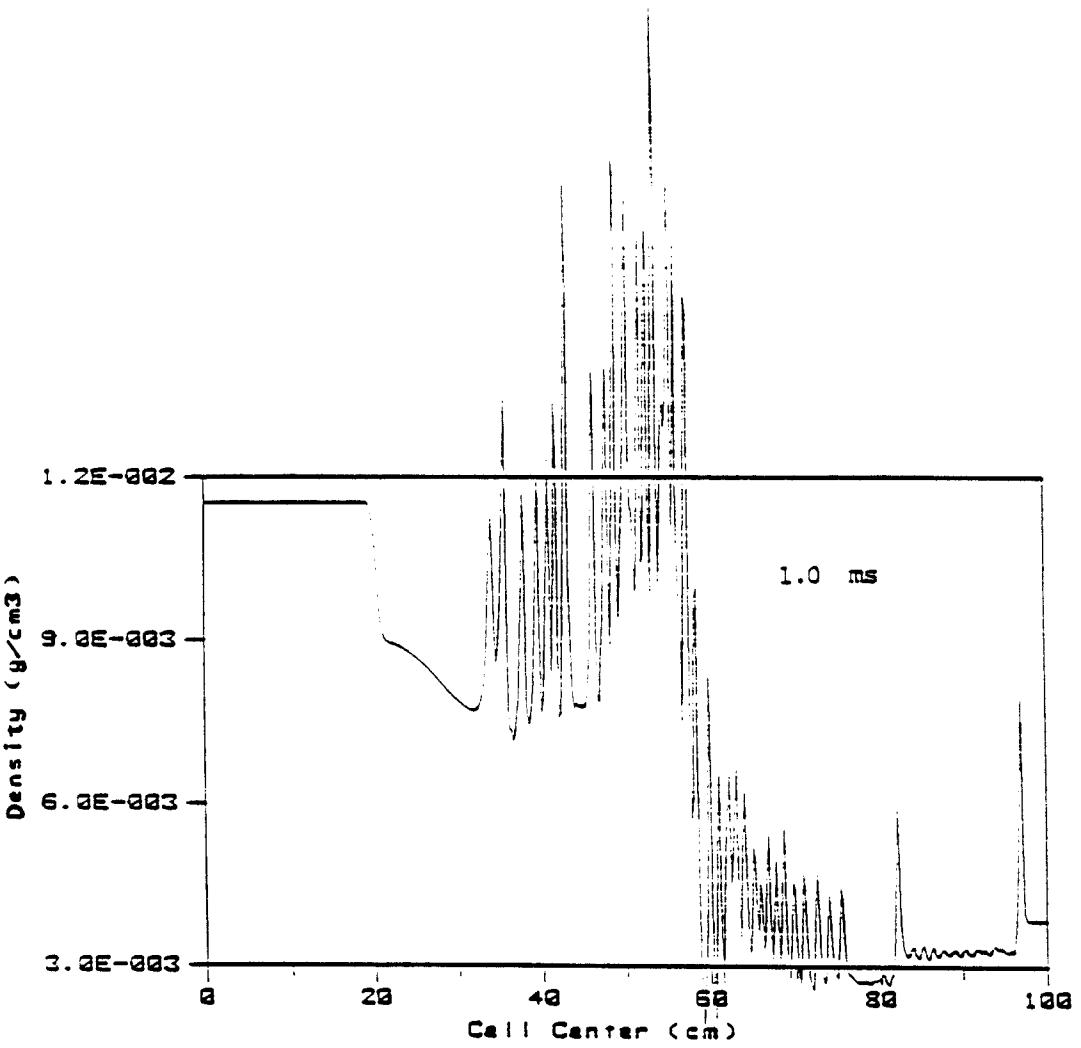

Figure 3.8: Density distribution for First Upwind (Donor Cell) method with 500 points –no adaption [20].

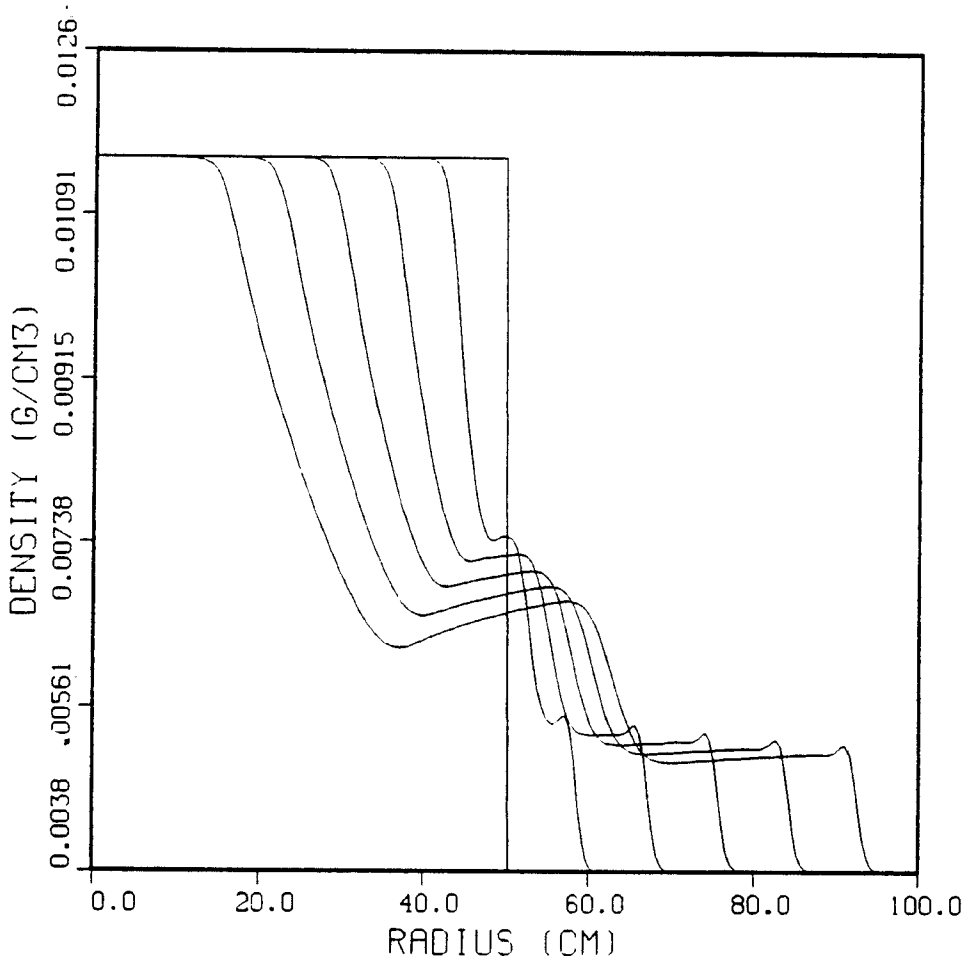

Figure 3.9: Mass density profiles at times 0.0, 0.2, 0.4, 0.6, 0.8, 1.0 milliseconds for cylindrical shock tube problem.

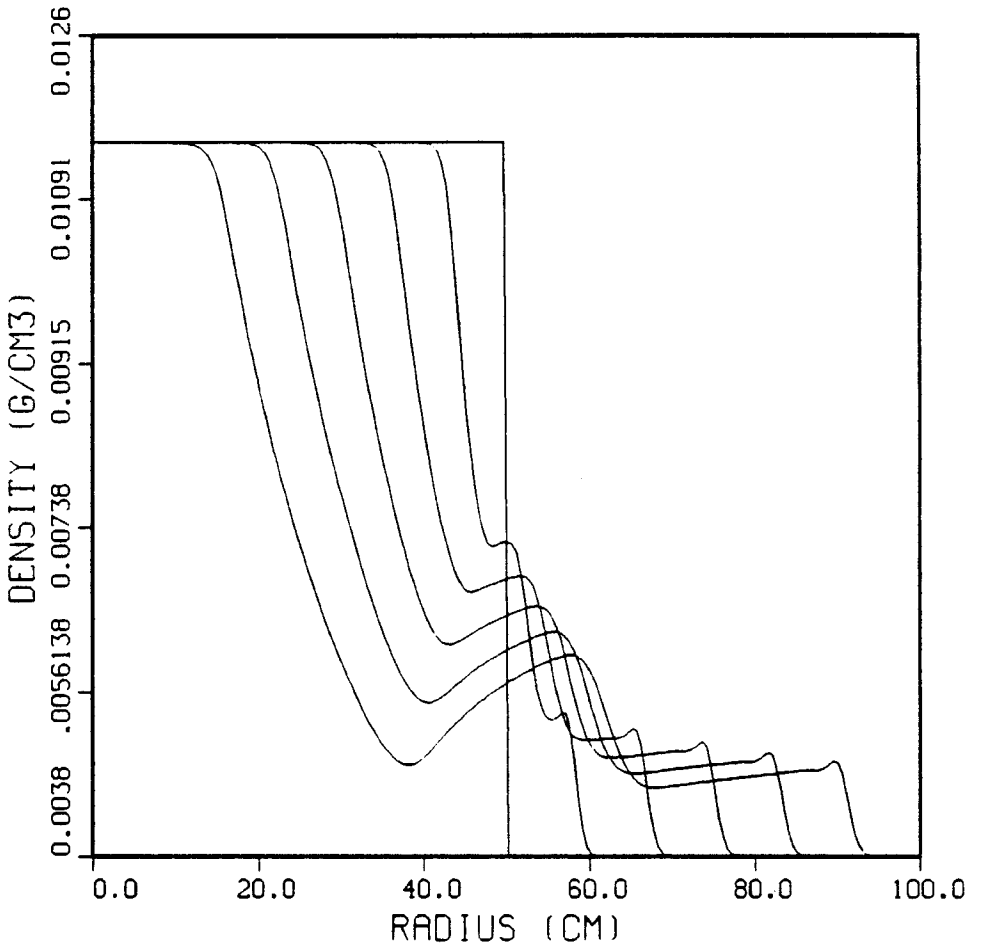

Figure 3.10: Mass density profiles at times 0.0, 0.2, 0.4, 0.6, 0.8, 1.0 milliseconds for spherical shock tube problem

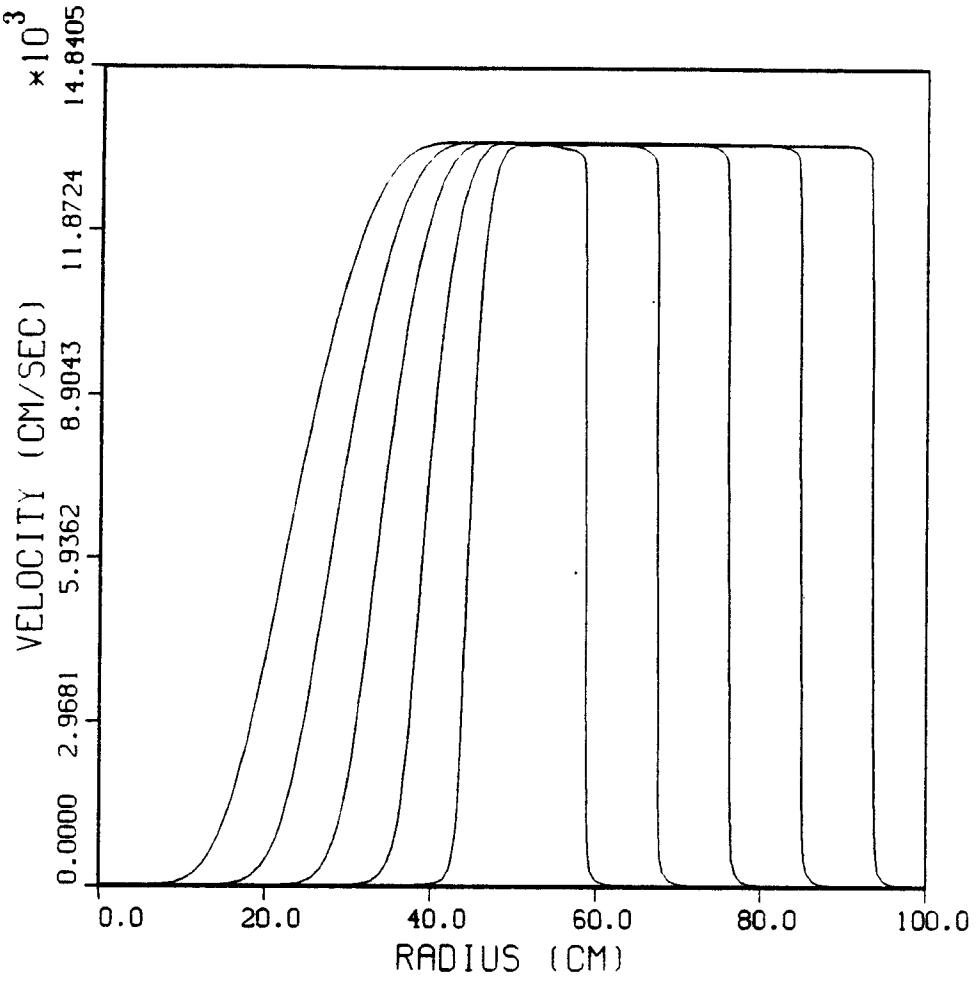

Figure 3.11: Velocity profiles at times 0.0, 0.2, 0.4, 0.6, 0.8, 1.0 milliseconds for slab shock tube problem.

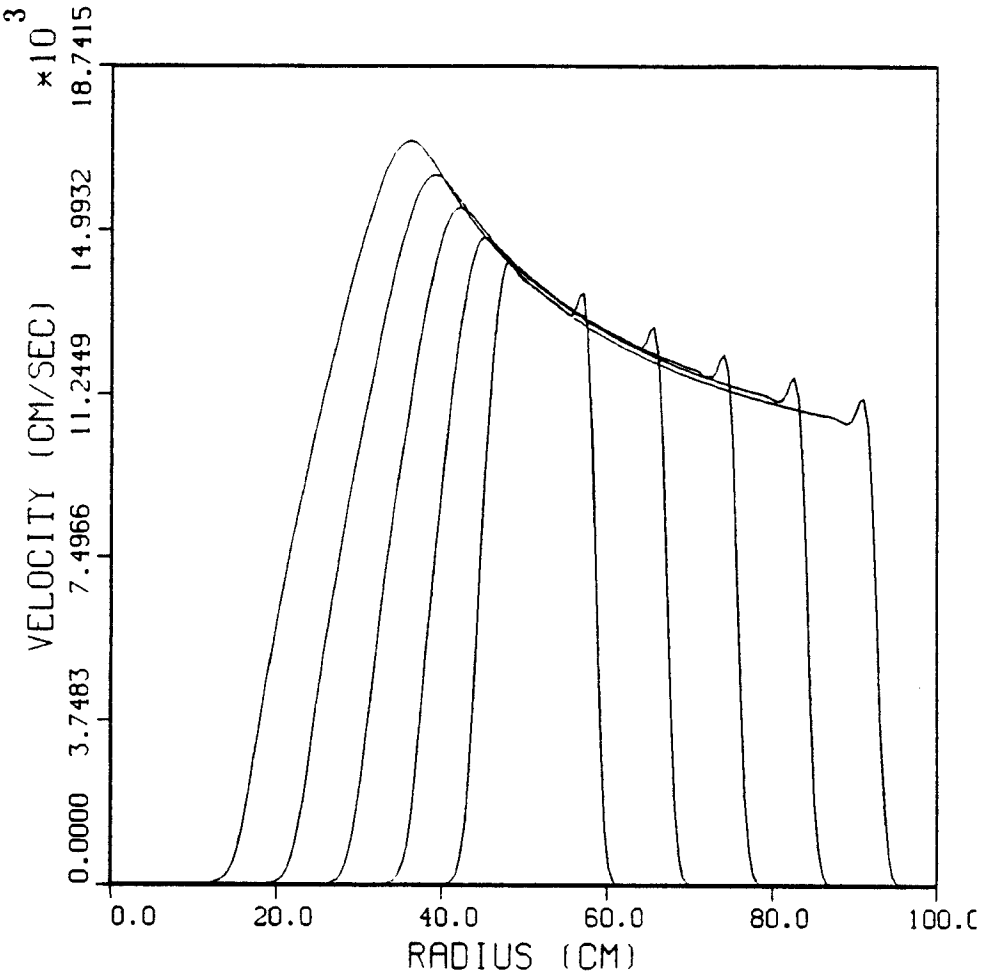

Figure 3.12: Velocity profiles at times 0.0, 0.2, 0.4, 0.6, 0.8, 1.0 milliseconds for cylindrical shock tube.

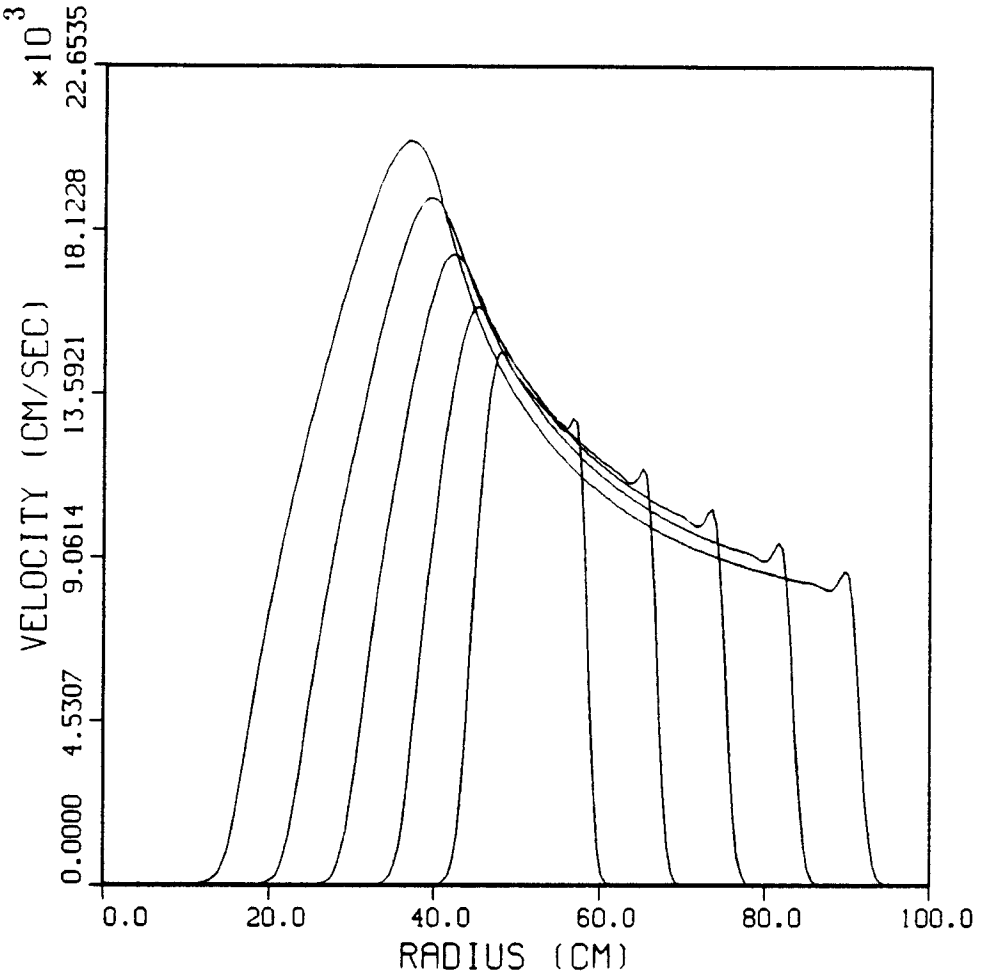

Figure 3.13: Velocity profiles at times 0.0, 0.2, 0.4, 0.6, 0.8, 1.0 milliseconds for spherical shock tube.

3.4.2 Dynamics of Plasma Channels

The dynamics of plasma channels seems to involve a blast wave expansion of the plasma. Thus, it is important to see how the ARMHD code predicts the contact discontinuities resulting from that in the plasma. We will start with a simple channel application here and defer the complete case to Chapter 5. A simplification of a z-pinch plasma channel is a cylindrical plasma with neither a magnetic field nor a radiation field. That means the discharge current is zero and the interaction of the plasma with the radiation is neglected. In addition to this simplification, ion beam injection can also be excluded. The initial conditions of the channel are created with the laser initiation that is aimed to create a conducting path along the axis of the channel. The laser heats the gas and creates a plasma of ions and electrons. The initial temperature profile due to laser heating could be taken as Gaussian with a peak value of 0.8 eV [16]. The number density of the plasma is taken uniform throughout the channel and its value is about $3.5 \times 10^{18} cm^{-3}$. The light ion beams considered for light ion fusion have power levels of tens of terrawatts and particle energies of tens of MeV. For these parameters, typical beam number densities are approximately 10^{15}-$10^{16} cm^{-3}$. To have current neutralization and to avoid rapid growth of instabilities, the channel number density must be approximately $10^{17} - 10^{18} cm^{-3}$ [14]. And this is the density range considered in our investigations.

The pulse of the laser is in the order of nanoseconds. The timescale for

the deposition of the laser energy in the channel is much shorter than the timescale of energy diffusion radially outward. Under these circumstances and due to the temperature in Figure 3.14, a blast wave may be formed that propagates radially outward. The blast wave is characterized by a sharp density peak, Figure 3.15, that moves outward into the undisturbed ambient gas at speeds somewhat greater than the upstream sound speed. The channel expansion in the form of a blast wave will even exist in the case of a discharge current but it may relatively slow down for the high current values. The timescale for magnetic diffusion is small compared to the expansion of the channel therefore the *joule heating* deposition timescale is short compared to the energy diffusion. That nature will help to expand the channel further but may do the opposite when the magnetic field is high enough to *pinch* the channel.

The adaption function here is chosen to be the *temperature* and the *momentum density* because of their expected high gradients. For both functions R_α and R_β have been chosen to be 0.3 and 0.1 respectively. Figures 3.14 through 3.15 show the temperature and density profiles for an *argon* plasma with no discharge current. The number of mesh points and the CFL number for these calculations are set respectively to 50 and 0.1. As expected earlier, these results show a blast wave moving radially outward. A **conservation check** was done during the simulations for mass and energy and it proved that the numerical method is conservative at about 98 % for the mass and

95 % for the energy.

The expression for the thermal conductivity of the plasma, κ, that is used in the simulations here is a theoretical expression developed for electrons' interaction with stationary ions [75]. This expression of κ is

$$\kappa = 20(\frac{2}{\pi})^{3/2}\frac{T^{5/2}}{m_e^{1/2}e^4}(Z+4)\ ln\Lambda$$

where m_e is the electron mass and $ln\Lambda$ is the Coulomb logarithm.

Ideally, the discharge current value and its rise time depend on what values are used for the *capacitor bank, resistor and self inductor* in the discharge circuit. Therefore there should exist a set of circuit equations to solve for the discharge current while the solution of other physical variables are sought. Practically, one may try to avoid these sophistications for the moment and use a user-defined current profile that is likely to occur in the channel. Such a profile is shown in Figure 3.16. This is not what Freeman suggested as the best profile for channel optimization, but rather is a simpler one.

Now, we would like to see how the channel's behavior changes versus an increase in the value of the current peak. Simulations in Figures 3.17 through 3.22 have been taken for the peak values of 10 kA, 50 kA and 90 kA with the same adaptive parameters (mesh number, CFL number and R_α and R_β) as those used in the previous case. The magnetic field profiles in these figures show that it diffuses into the channel in a short time (about nanoseconds). The resistivity of the plasma is a strong function of the temperature and its

dependency is shown in Figure 3.20. The relation that led to this kind of dependency is an emprical formula [11] given as

$$\eta = 5.79 \times 10^{-15} e^{\frac{0.4482}{kT(eV)-0.40}} \ (sec) \quad if \quad kT > 0.42\ eV,$$

$$\eta = 5.79 \times 10^{-15} e^{\frac{0.4482}{0.42-0.40}} \ (sec) \quad if \quad kT \leq 0.42\ eV.$$

However, a more realistic formula can be used such as the one given in Dresvin [74] that counts for both the effects of Coulomb collisions and electron-atom collisions ;

$$\eta = \eta_W \ (weakly\ ionized) + \eta_F \ (fully\ ionized)$$

where $\eta_F = 5.799 \times 10^{-15} Z(T)\ ln\ \Lambda \ \ T^{-3/2}$ and

$$\eta_W = \frac{m_e^{-1/2}}{e^2} \frac{\sigma_{ea}(T)}{\alpha(T)} T^{1/2}.$$

Here, σ_{ea} is the electron-atom collision cross section, Z is the ionic charge state, and α is the degree of ionization of the plasma. When α falls below 0.001 η_W is dominant and when it is greater than 0.1 η_F is dominant. The plasma is hot near the center and is surrounded by a cool region therefore the center plasma is more conductive. This leads the discharge current to flow mostly in the center of the plasma. The magnetic field profile would look like that of a conducting wire where magnetic field is linear in the conducting region and drops off as $1/r$ beyond that. The current density profile in the hot region is, then expected to be uniform (flat) according the relation between

the magnetic field B and current density J as in Eq.3.32. Figures 3.21 and 3.22 show typical profiles for B and J. It confirms the fact that J is almost uniform inside a radius, r_c, and drops off to a negligible value after that.

The effect of current rise time should be the same because of the same rise time for each case, but the amount of the joule heating, in each case, added to the energy of the plasma is different and that causes different effects on the channel. For the 10 kA case, the amount of joule heating is small and the magnetic field created by the discharge is not high enough to pinch the channel. The joule heating therefore helps the plasma expand more than the case when there is no current. When the current value reaches 90 kA, however, the blast wave starts fading and the plasma tends to slow down and move toward the center. This mechanism can be seen in the velocity profile. The eventual effect is the pinching of the channel. The pinching spoils the flat profile of density inside the peak radius and increases the density in the center. That by itself is not good in terms of the response that the beam ions will get from the plasma. On the other hand, the magnetic field may be required to be high to confine the beam ions. These are altogether competing effects and should be thought about when designing an optimized channel.

The results for three different discharge current cases are qualitatively consistent with our previous knowledge of the channels but still need to be checked in terms of conservation laws. A conservation check on the mass showed to be about 98 %. Because the total energy will not be conserved

but rather increased due to the joule heating, no attempt was made to say something about the energy mechanism here before any attempt to check whether or not the **magnetic flux** and the **current** are conserved in the calculations. If they are, that would insure the value of joule heating which is eventually added to the energy of the plasma.

Conservation of Magnetic Flux and Current:

The magnetic flux conservation check provides an indication of how accurately the magnetic diffusion is being solved. To get an expression for a numerical check on magnetic flux we will integrate Eq.3.3 over space and time. That is,

$$\int_0^{rmax} dr' \int_0^t dt' \frac{1}{c}\frac{\partial B}{\partial t} = \int_0^{rmax} dr' \int_0^t dt' \frac{\partial}{\partial r}\{\frac{\eta c}{4\pi}\frac{1}{r}\frac{\partial}{\partial r}(rB) - \frac{1}{c}uB - \eta J_b\}.$$

This indeed is **Faraday's Law** and becomes

$$\frac{1}{c}[\phi(t) - \phi(0)] = \int_0^t [E_l(r_{max}, t) - E_l(0, t)] \tag{3.51}$$

where $\phi = \int_0^{rmax} dr' B(r', t)$, $E_l = E_f - \frac{1}{c}uB$. In finite difference form,

$$\frac{1}{c}(\phi^{n+1} - \phi^0) = \varepsilon^{n+1}$$

where $\varepsilon^{n+1} = \varepsilon^n + \Delta t^n (E_{imax}^{n+1} - E_{i=1}^{n+1})$.

The current conservation check is a comparison between the discharge current I_d and the current calculated by integrating the net current density J_{net}. In other words, the current conservation check compares the discharge

current I_d^n, as obtained either from the current equation solver or the user-specified current, and the following one that is calculated through the current density J_i^n as

$$I_d^n = 2\pi \int_0^{rmax} J_{net} r \, dr \cong 2\pi \sum_{i=1}^{imax} J_i^n r_i^n \Delta r_i^n. \tag{3.52}$$

These conservation checks were applied to the three cases mentioned earlier. The conservation degree is nearly 100 %, which indicates that the magnetic diffusion equation has been solved correctly.

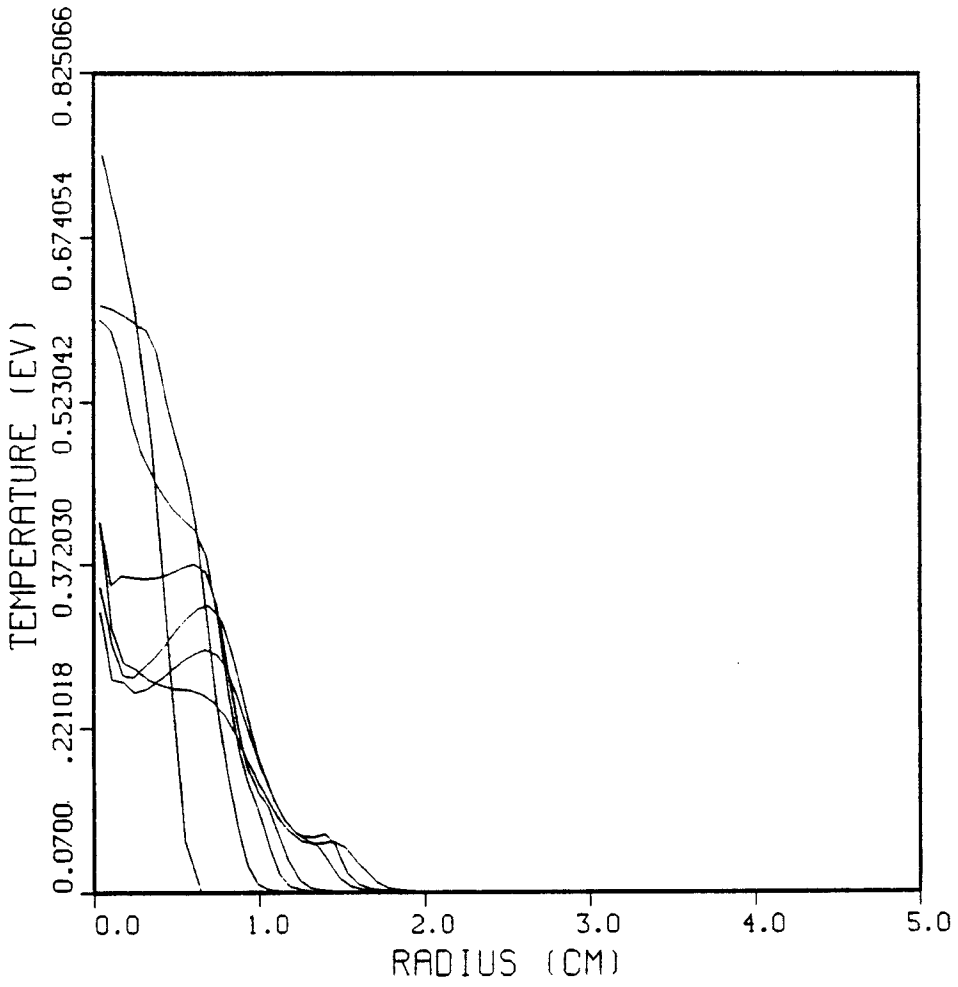

Figure 3.14: Plasma temperature profiles at times 0.0, 2.0, 4.0, 6.0, 8.0, 10.0, 12.0 microseconds in the channel with no discharge current.

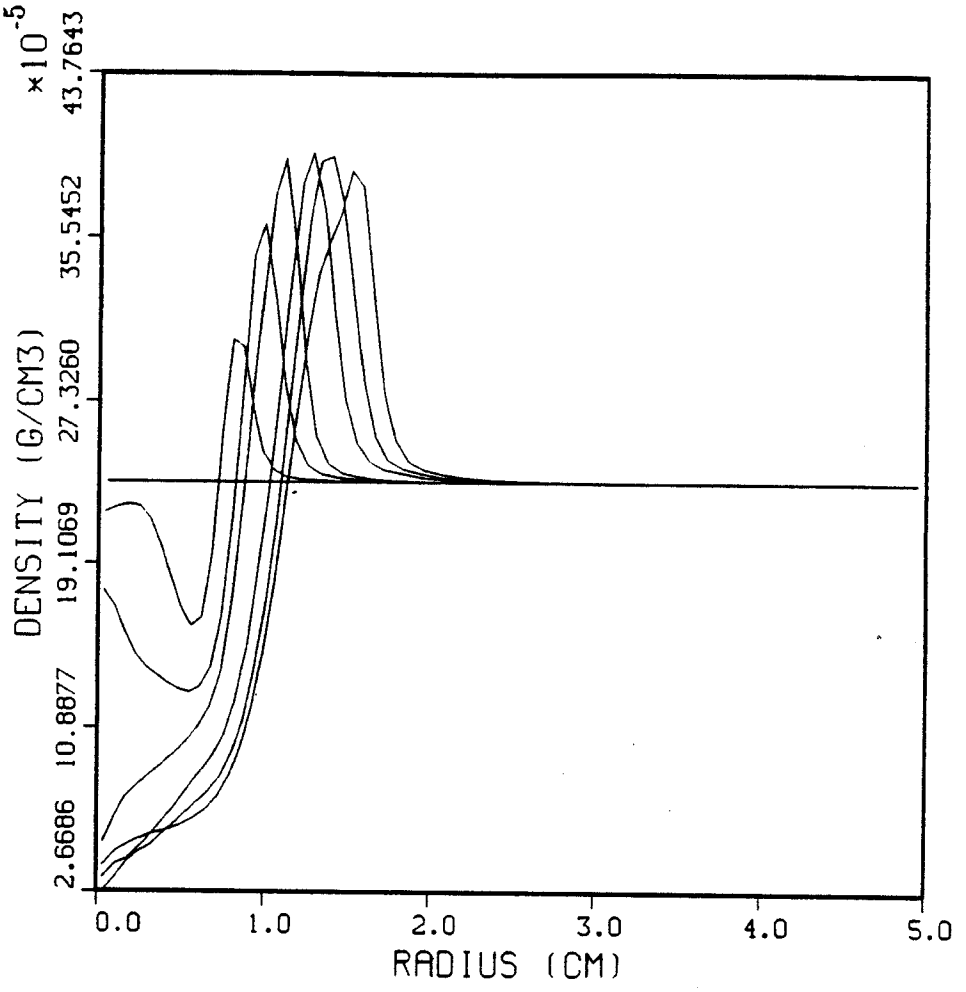

Figure 3.15: Plasma density profiles at times 0.0, 2.0, 4.0, 6.0, 8.0, 10.0, 12.0 microseconds in the channel with no discharge current.

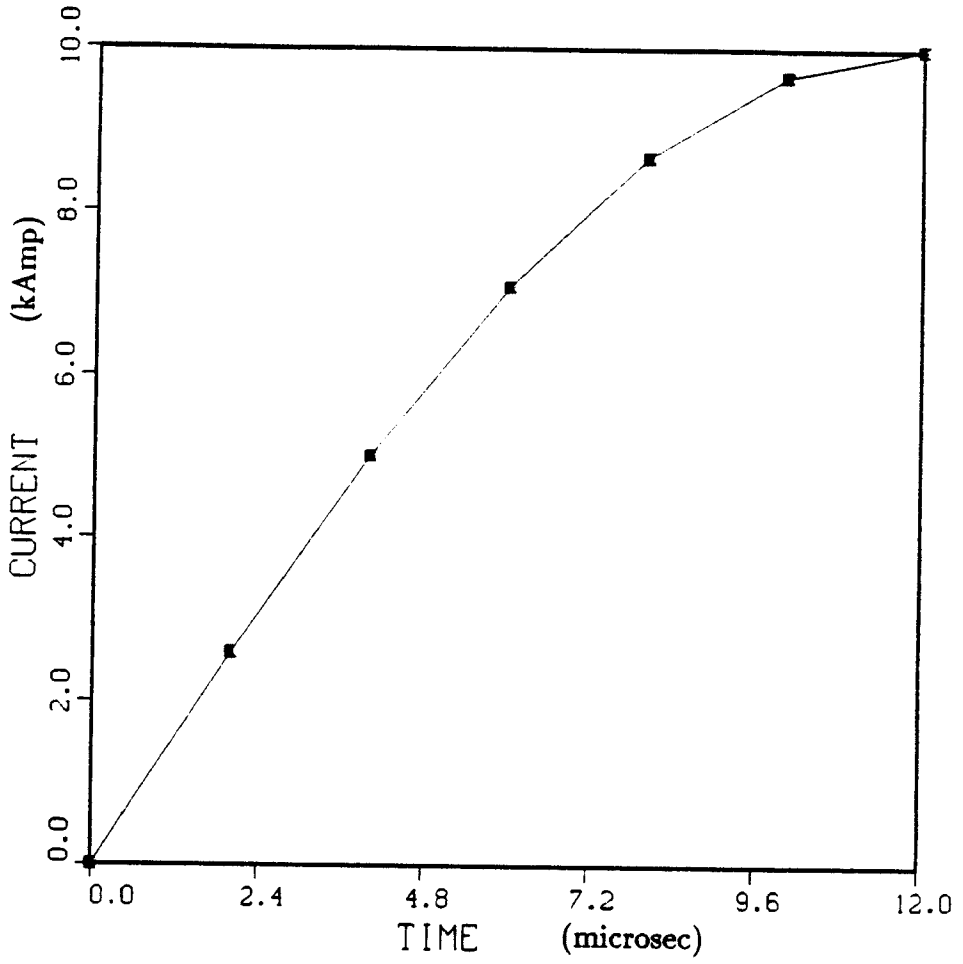

Figure 3.16: Discharge current profile used in the simulations.

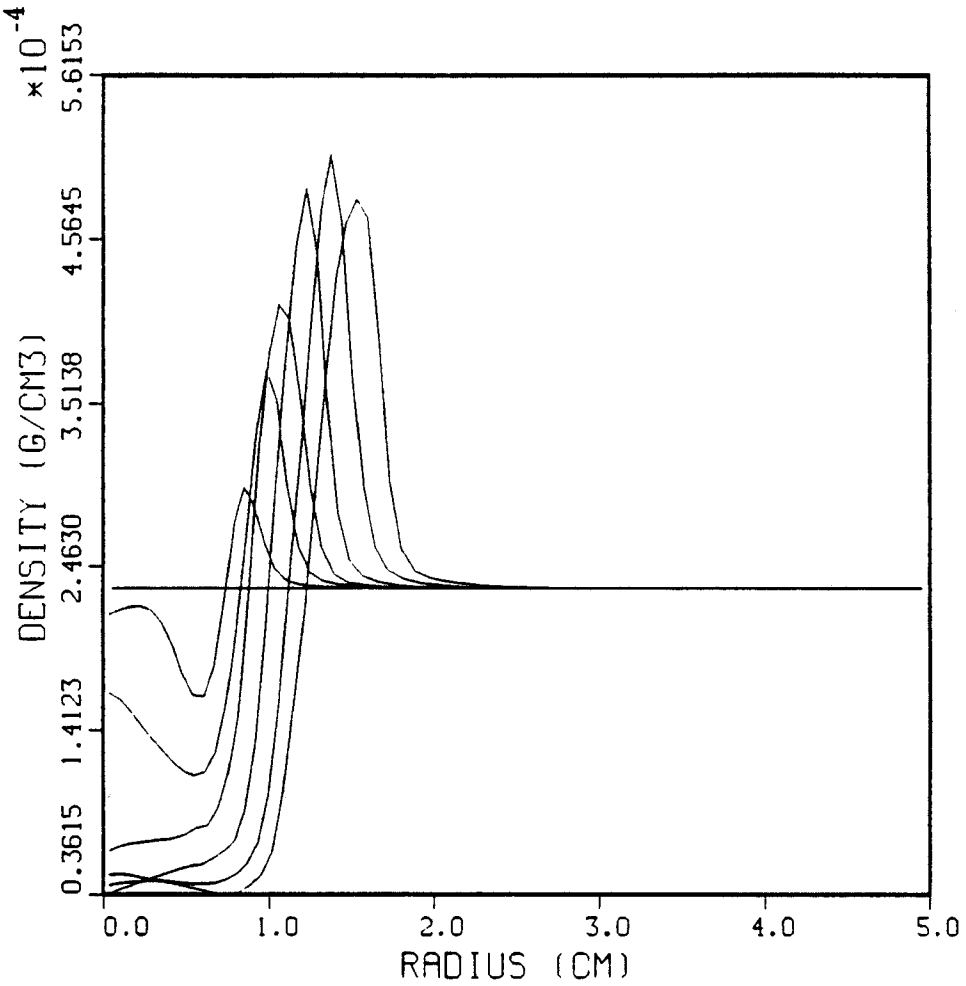

Figure 3.17: Plasma mass density profiles at times 0.0, 2.0, 4.0, 6.0, 8.0, 10.0, 12.0 microseconds for $I_{d,max} = 10$ kA.

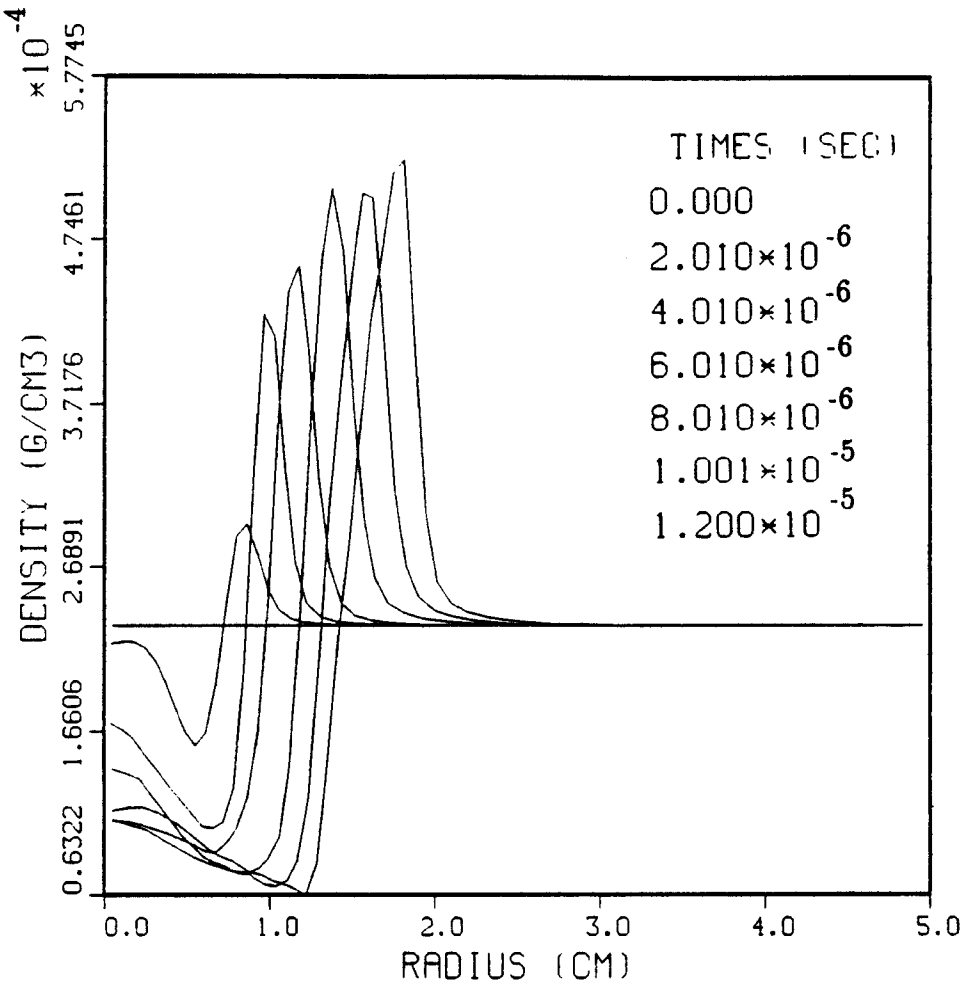

Figure 3.18: Plasma mass density profiles at times 0.0, 2.0, 4.0, 6.0, 8.0, 10.0, 12.0 microseconds for $I_{d,max} = 50$ kA.

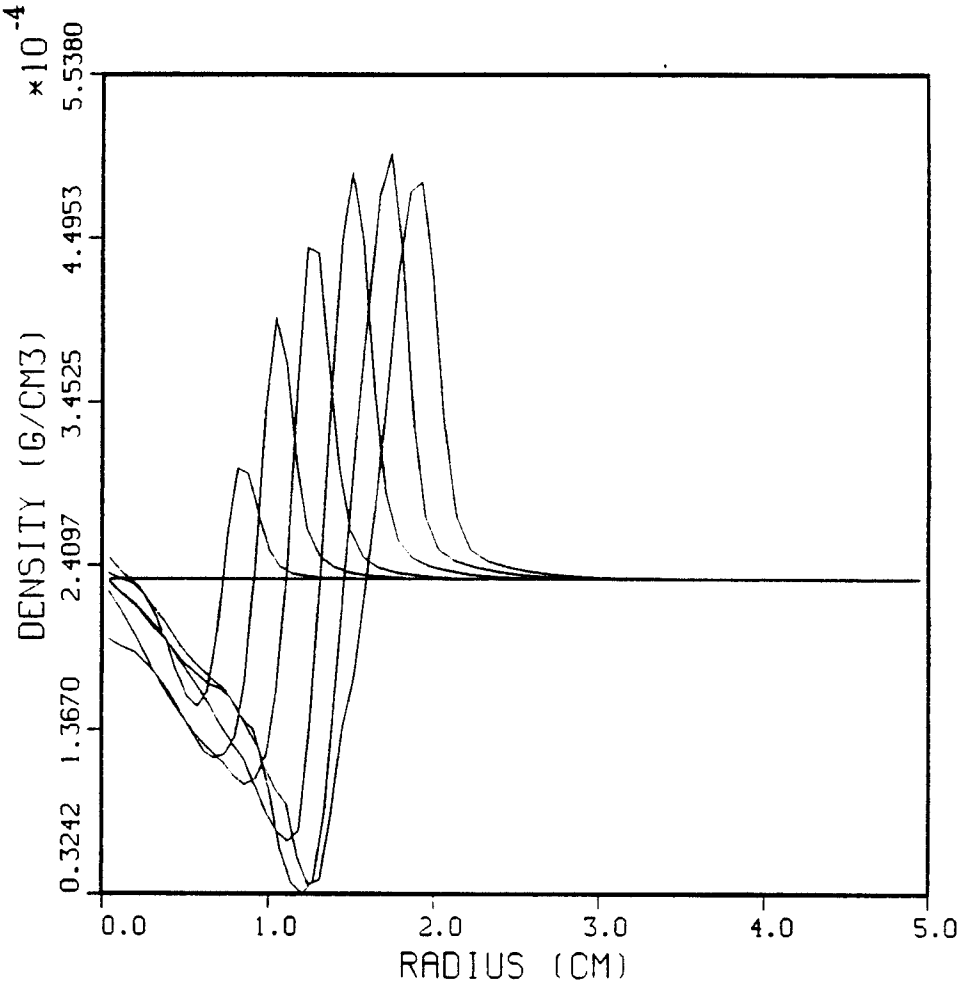

Figure 3.19: Plasma mass density profiles at times 0.0, 2.0, 4.0, 6.0, 8.0, 10.0, 12.0 microseconds for $I_{d,max} = 90$ kA.

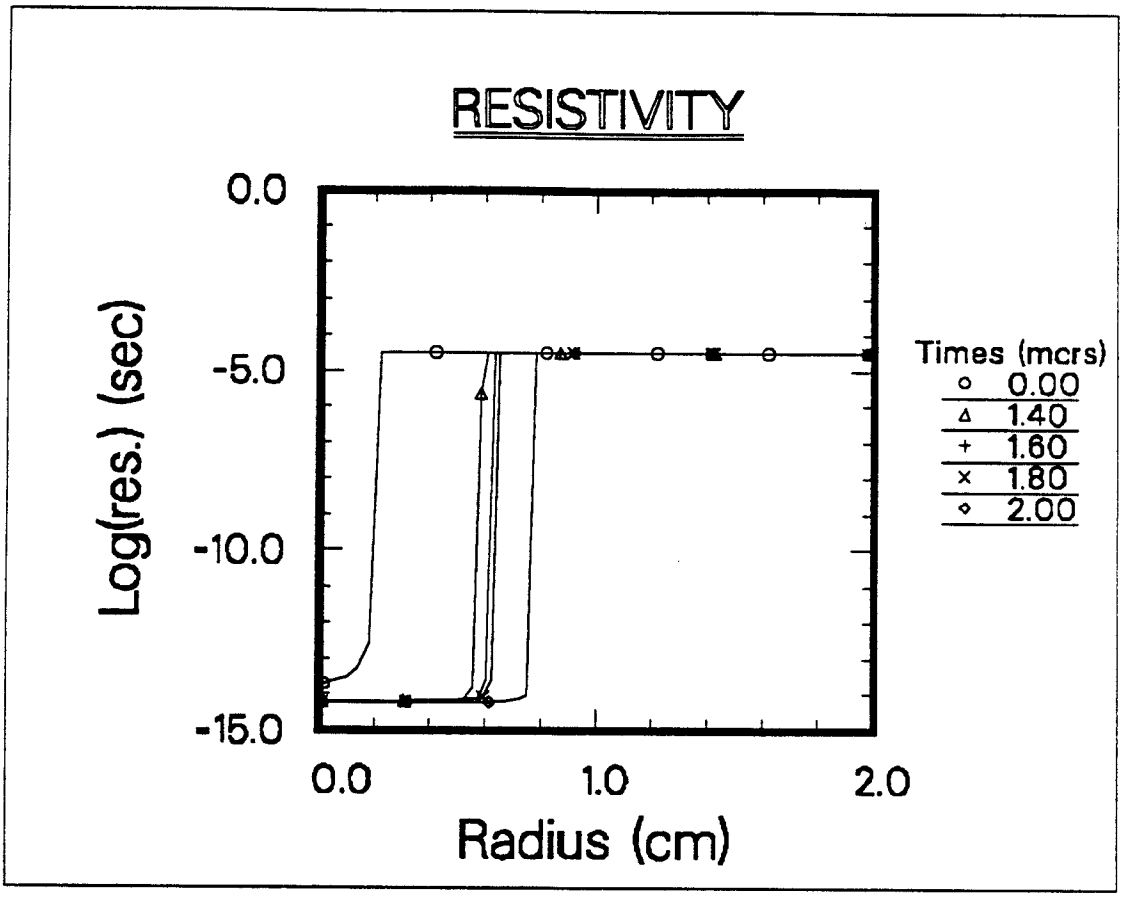

Figure 3.20: Typical temperature dependency of resistivity of plasma used in calculations.

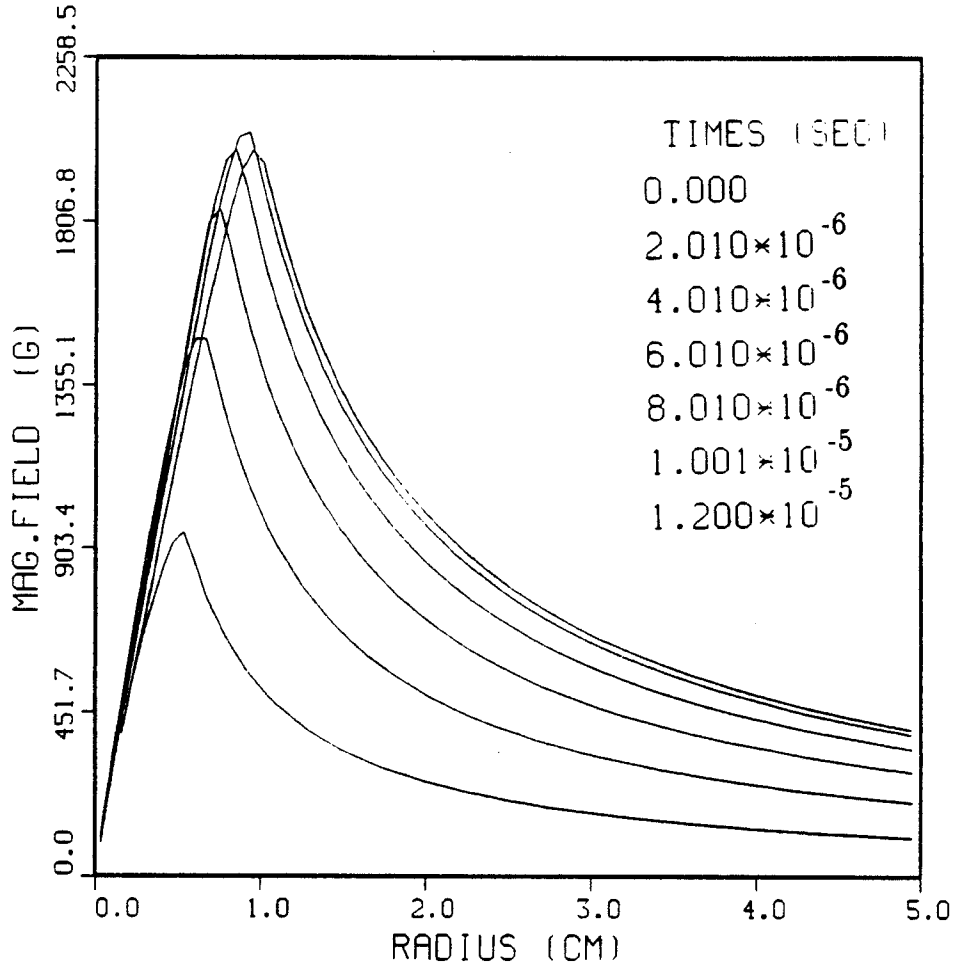

Figure 3.21: Magnetic field for $I_{d,max} = 10$ kA.

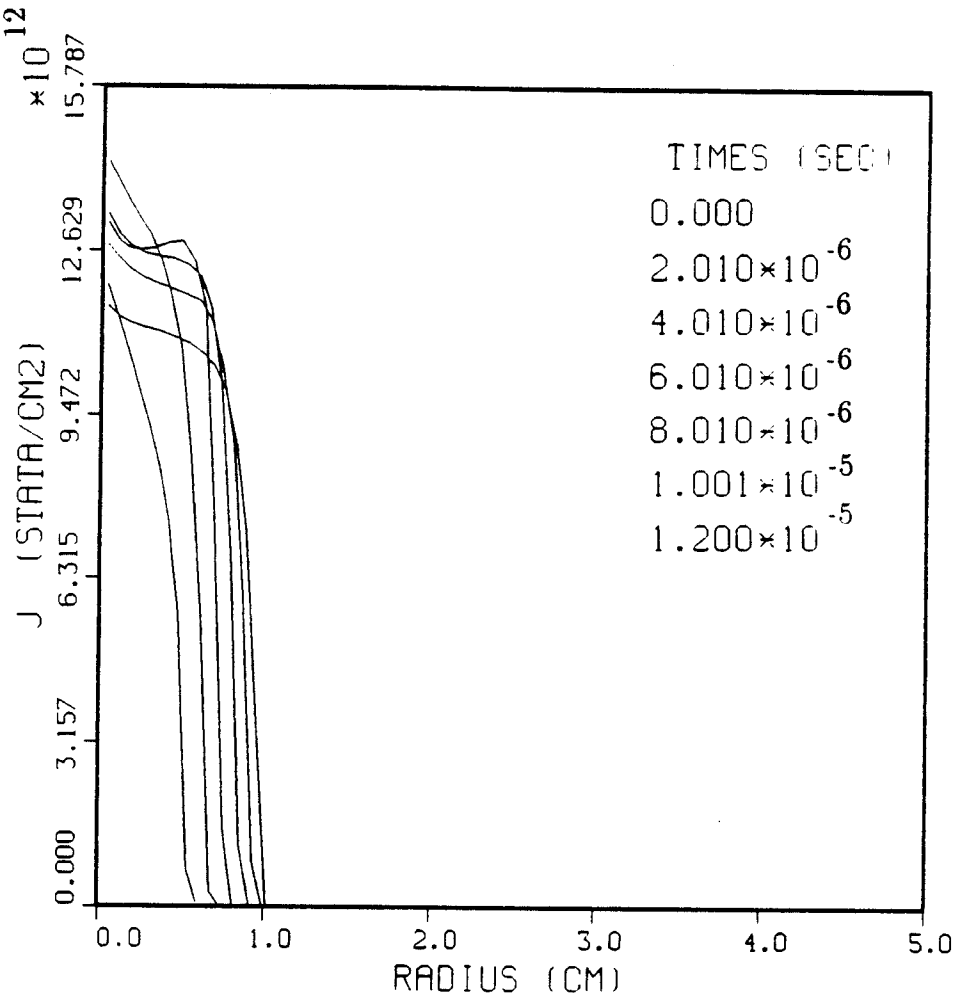

Figure 3.22: Current density for $I_{d,max} = 10$ kA.

Chapter 4

Adaptive Method versus Lagrangian Method

The adaptive mesh systems are not historically the original systems that were used with finite difference methods. Either *eulerian* or *lagrangian* coordinate systems were used. An eulerian (inertial or laboratory) one is that in which the grid points remain fixed and a lagrangian one is that in which the grid points move with the local velocity of the fluid. In lagrangian systems, each computational cell can be considered as having a constant mass throughout the simulation.

These two systems, indeed, can be viewed as special cases of the general set of adaptive systems. In order to see this, consider the following simple

wave equation;

$$\frac{\partial U}{\partial t} + c\frac{\partial U}{\partial x} = 0,$$

or

$$[U]_t + c[U]_x = 0 \tag{4.1}$$

where $U(x,t)$ is an unknown dependent variable, $[U]_{x,t}$ represents partial derivatives. The constant c is just the wave speed in the laboratory frame. Now if we transform x and t to a computational domain (ξ, τ) as

$$\tau = t$$

$$\xi = \xi(x,t) \tag{4.2}$$

then the wave equation becomes

$$[U]_\tau + (\frac{c - x_\tau}{x_\xi})[U]_\xi = 0. \tag{4.3}$$

Here;

$$x_\xi = \frac{dx}{d\xi} \quad (grid\ \ metric - jacobian),$$

and

$$x_\tau = \frac{dx}{d\tau} \quad (grid\ \ velocity).$$

Now, we can examine Eq.4.3 to see whether we can reproduce the *eulerian* and *lagrangian* special cases from it. If the grid speed, x_τ, is zero then the result is simply an eulerian mesh. If the grid speed is equal to the wave speed $x_\tau = c$, then the result is a lagrangian mesh. It is obvious that eulerian and

lagrangian mesh systems are only special cases of the adaptive grid system. Some local grid refinement or periodic rezoning (*ad hoc* methods) can be used with eulerian or lagrangian systems to solve complicated problems, but adaptive grid systems provide a systematic approach to determining the best time dependent mesh distribution for a problem.

For problems like plasma channels where gradients in different physical quantities must be resolved, we want to test whether the adaptive grid method is better than the standard lagrangian approach. The following section presents such a comparison for the plasma channels in the context of the LIBRA reactor study.

4.1 Lagrangian Method

The fluid equations, Eq.3.1, that we have seen before are in *eulerian* form, which means they view the flow from a fixed laboratory frame. A conventional way to convert these equations into the *lagrangian* form is to replace the time derivative $(\partial/\partial t)$ with the fluid-frame time derivative -convective derivative- (D/Dt) :

$$\frac{D}{Dt} = \frac{\partial}{\partial t} + \mathbf{u} \cdot \nabla$$

Therefore, the lagrangian derivative $\frac{D\rho}{Dt}$ is the time rate of change of ρ in an element of the fluid moving with the fluid. The replacement of the *eulerian* time derivative with the *lagrangian* derivative in Eq.3.1 results in the

following :

$$\frac{D\rho}{Dt} + \rho(\nabla \cdot \mathbf{u}) = 0$$

$$\rho\frac{Du}{Dt} + \nabla p = 0. \tag{4.4}$$

Note that the conversion of Eq.3.1 into the adaptive system, as is done in Chapter 3, is a more general formulation than the lagrangian one. One could derive the lagrangian equations Eq.4.4 as a special case from our adaptive formulas by simply replacing the grid velocity r_τ with the fluid velocity u in equations Eq.3.15, 3.19 and 3.20. The lagrangian derivative (D/Dt) would correspond to $(\partial/\partial\tau)$ as

$$\frac{D}{Dt} = [\,]_\tau + u[\,]_r.$$

The continuity and momentum equations would be

$$[rr_\xi\rho]_\tau = 0,$$

$$[rr_\xi\rho u]_\tau + r[\rho]_\xi = 0. \tag{4.5}$$

Furthermore, in the conventional lagrangian formulation the spatial derivative is replaced by the *mass* since it simplifies the equations. Each fluid element has constant mass with a zero flux of mass at the boundaries. This, infact, means one equation (continuity) is eliminated from the system.

Alternatively, one can again do these kinds of simplifications when deriving the lagrangian equations from more general adaptive ones. The idea of replacing the spatial variable r with *mass* in the conventional way can be

seen to be equivalent to taking the adaptive variable ξ equal to *mass* as

$$\xi = \xi(r) = m.$$

Since the mass of a cell (Δm) with a volume $r\Delta r$ is

$$\Delta m = \rho r \Delta r,$$

we find

$$r_m = \frac{dr}{dm} = \rho r$$

which is in fact r_ξ in our case because ξ is equivalent to m.

In brief, we see that the *lagrangian* formulation can be derived from the more general *adaptive* formulation simply by choosing the adaptive variables (τ, ξ) as the lagrangian time and mass and restricting the grid velocity (r_τ) to the fluid velocity (u). Thus taking $r_\tau = u$ and $r_\xi = \rho r$, Eq.4.5 are written as

$$[\ constant\ ]_\tau = 0 \ \ (continuity)$$

$$[u]_\tau + r[p]_m = 0 \ \ (momentum). \tag{4.6}$$

The most relevant lagrangian hydrodynamics computer code to us, as mentioned before, is the ZPINCH code. It uses the formulation that was described above. In addition to the basic *fluid-like* equations for the plasma, it also solves for the *magnetic* and *radiation* fields. The magnetic field is calculated from the *magnetic diffusion* equation and tne radiation field is calculated from the *radiation diffusion* equation.

ZPINCH is currently used in the design of LIBRA and LMF at UW-Madison. It simulates the formation of plasma channels up to the time the ion beam is injected. Through the simulations one can find an optimized set of channel parameters (such as peak magnetic field, channel radius, discharge current and so on) that is appropriate for the overall design.

The channel, as described before, is preionized with a 2 J laser to provide a straight conducting path for the discharge current and the ion beam. The latest simulations [1] were done for nitrogen and helium gases at a mass density of $2.37 \times 10^{-5} \frac{g}{cm^3}$. Channel formation for a discharge current history of the type shown in Figure 4.1 was studied where a large main pulse follows a smaller prepulse. A preionizing laser with a Gaussian radial intensity profile was assumed. The double pulsed current history was first proposed several years ago [10]. The results for nitrogen gas show that, even for the optimum current history and laser profile, radiation transport prevents the formation of nitrogen channels acceptable for the LIBRA reactor design. The required azimuthal magnetic field to confine 30 MeV Li^{+3} ions at 0.5 cm radius is 27 kG, while the best simulation result with nitrogen is 18 kG if radiant heat transfer is considered.

The radiation diffusion model used in ZPINCH predicts a radial expanding temperature front which causes a geometric degradation of the magnetic field by expanding the current profile over a larger area. The question of whether this is what really happens depends upon the validity of the diffu-

Table 4.1: Parameters for LIBRA Channels [1].

Number of beam channels	$16 + 2$
Number of return current channels	$16 + 2$
Channel length	6.6 m
Channel radius	0.5 cm
Beam ion	30 MeV Li^{+3}
Confining azimuthal magnetic field	27 kG
Average channel mass density	$< 5 \times 10^{-6} g/cm^3$
Target chamber gas	$3.55 \times 10^{18} cm^{-3}$ helium
Time delay between discharge current pulses	1 microsecond
Laser beam diameter	4 mm

sion model and the opacities of the hot plasma.

The results that arose from the nitrogen simulations led to the choice of a low atomic number gas (helium) that should radiate less and therefore allow the formation of more acceptable channels. Results for the helium gas predicted a magnetic field of 27 kG at about 0.5 cm radius, indicating the feasibility of a channel to focus 30 MeV lithium ions onto a light ion beam driven target for LIBRA.

The point design for LIBRA channels has parameters outlined in Table 4.1. Studies following ZPINCH results indicate that this design is successful due to the fact that helium gas does not radiate strongly when it is fully ionized. The proposed discharge current is shown in Figure 4.1. This profile leads to the magnetic field profiles of Figure 4.2. At a time around 1.7 μsec, the code predicts a magnetic field of 27 kG at 0.5 cm. The mass density profiles in Figure 4.3 show *pinching* near the center of the channel.

A plot of mesh point position versus the time, Figure 4.4, shows us how grid points change position during the simulation. In the lagrangian scheme, because each cell has a constant mass, the cell boundaries elongate or shrink (to keep the mass constant) in case of a decrease and increase in the mass density ρ. So for equal mass zoning, the mesh points are more concentrated in the regions where ρ is higher; grossly equivalent to adapting the mass density ρ in the adaptive method. This plot shows the hydromotion of the plasma indicating where the plasma is moving in the form of a cylindrical shock. It also shows the pinching that we noticed in the density profiles. As the discharge current approaches its maximum value, the center of the discharge begins to pinch, while the edge of the discharge continues expanding as an outward moving cylindrical shock. The peak magnetic field and the edge of the discharge current remain inside the shock front, thus they are subject to less resolution than the mass density peak.

The fact that the magnetic field and also temperature (Figure 4.5) gradi-

ents stay behind the mass density peak, where most of the mesh points are located, is an unwanted situation that raises questions about the degree of accuracy and resolution in them. We need more accurate results because the efficiency of beam transport depends on the temperature, magnetic field and the channel radius. The temperature determines the growth rates of filamentation and two-stream instabilities [77] and it also determines the magnitude of the electric field associated with the beam-induced return current through the electrical resistivity. The instabilities can degrade the quality of beam transport and the induced electric field can deccelarate the beam ions. The density, on the other hand, determines the degree of current neutralization and collisional energy losses. The radius of the discharge and discharge current determine the strength of the channel's magnetic field which governs how much beam power can be trapped in the channel.

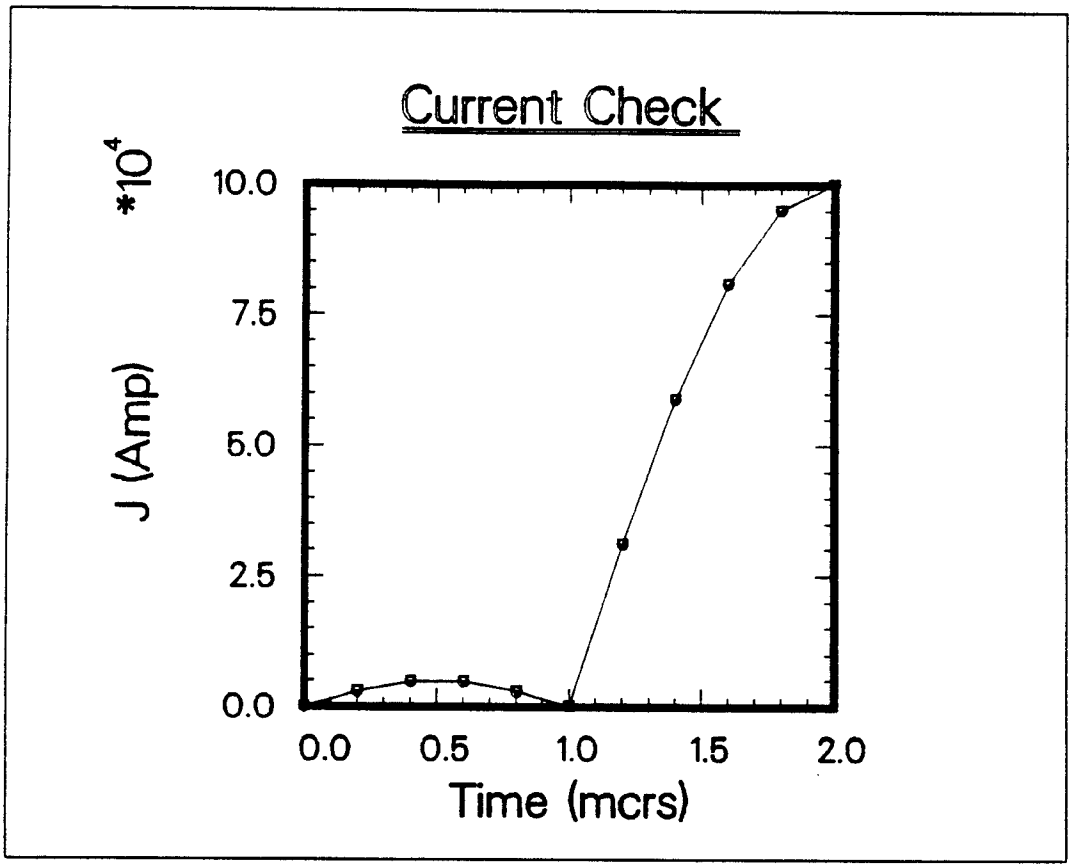

Figure 4.1: Double pulse discharge current history for the formation of plasma channels for LIBRA [1].

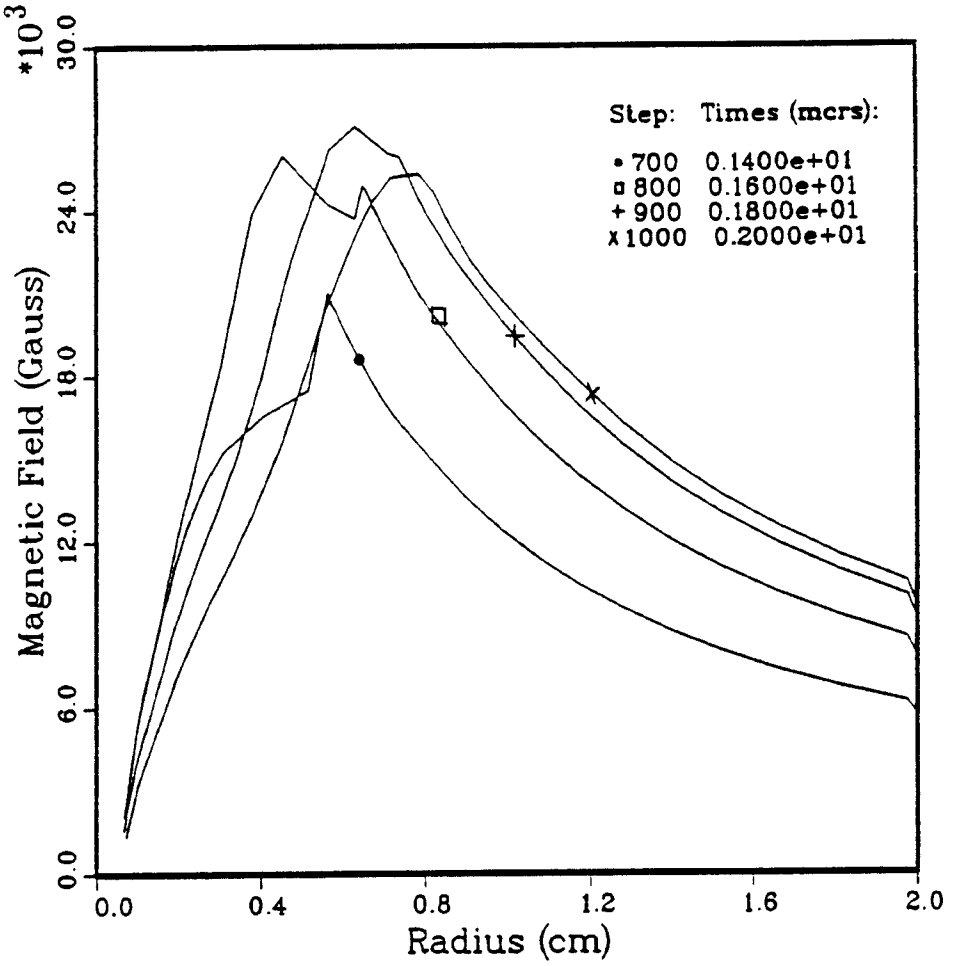

Figure 4.2: Magnetic field profiles during formation of LIBRA channels [1].

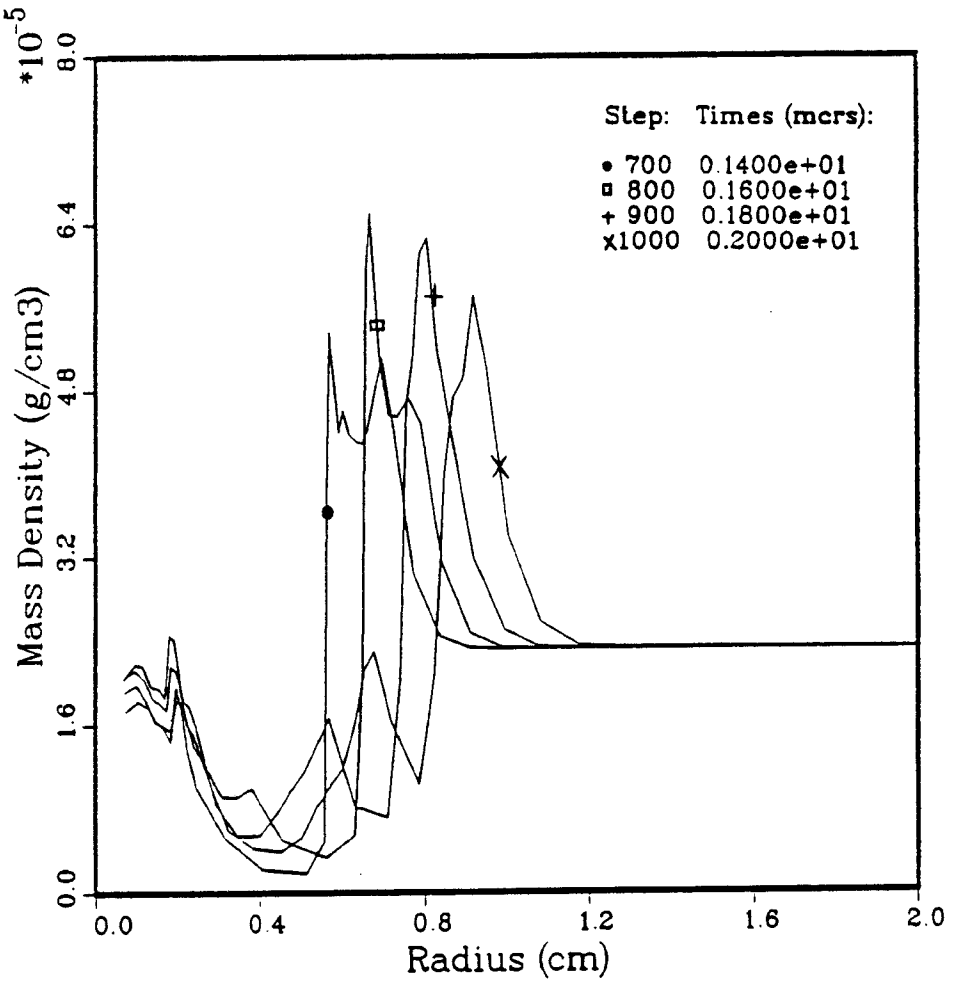

Figure 4.3: Plasma mass density profiles during formation of LIBRA channels [1].

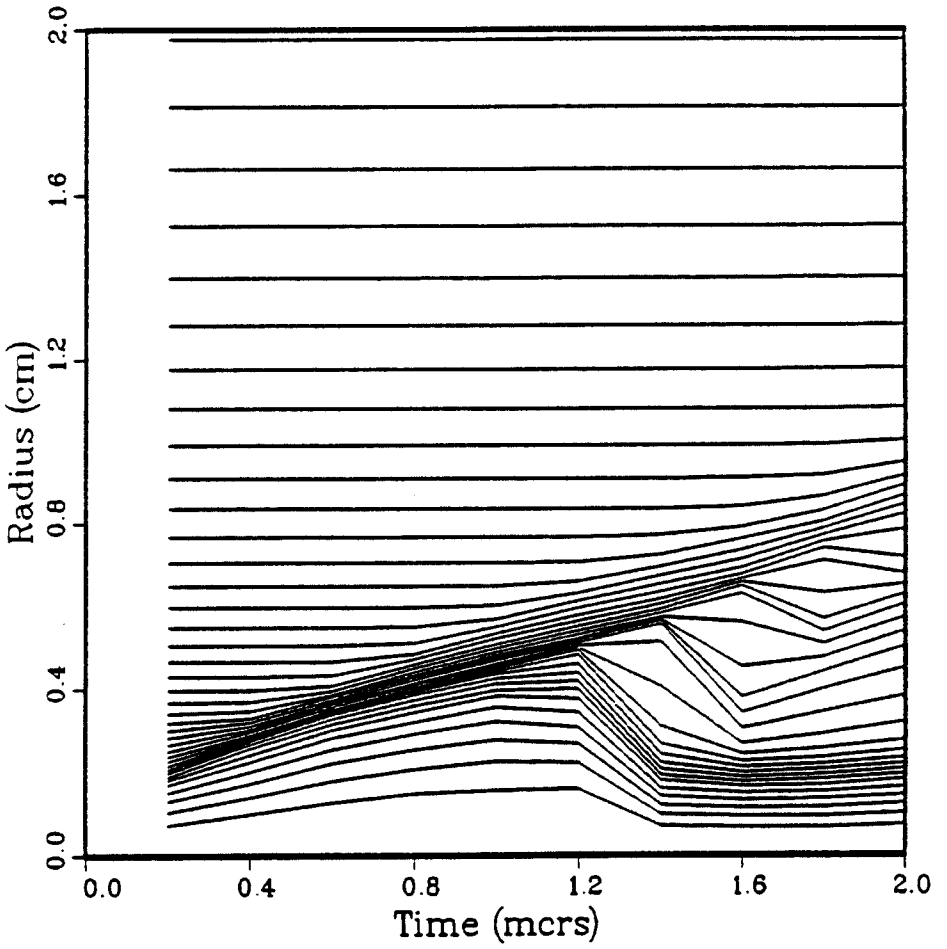

Figure 4.4: Hydromotion during formation of LIBRA channels [1]

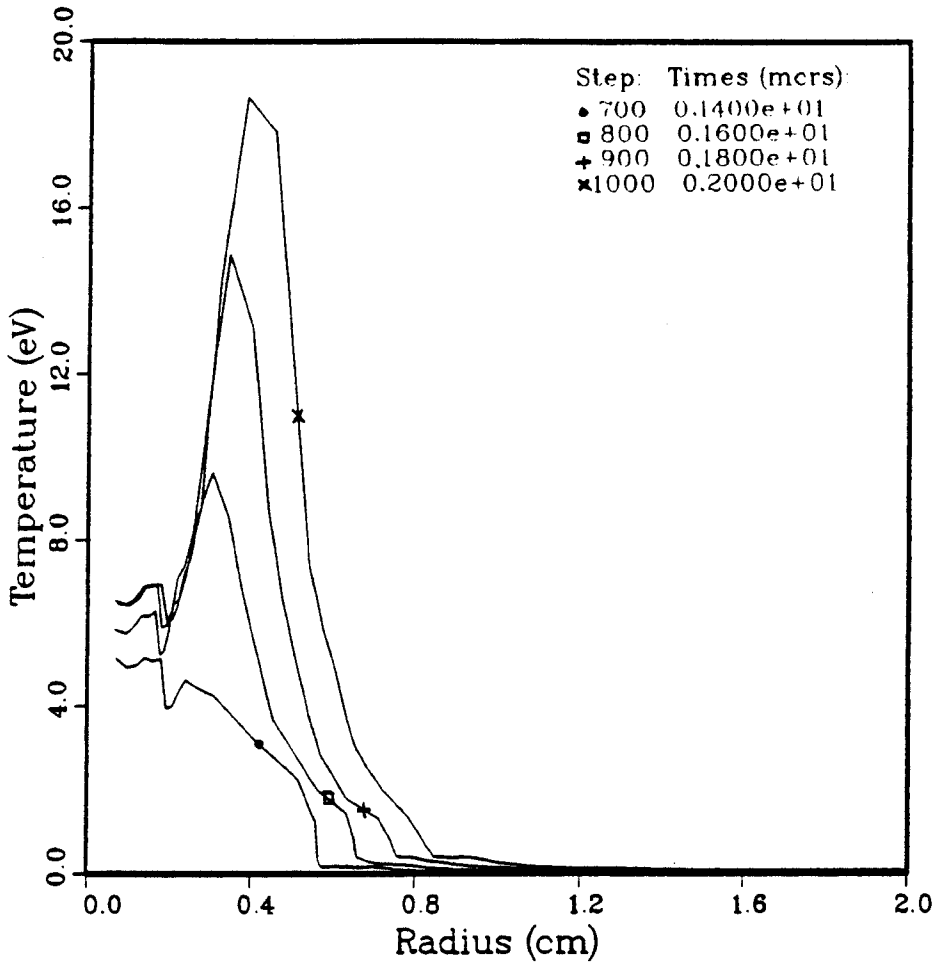

Figure 4.5: Plasma temperature profiles during formation of LIBRA channels [1].

4.2 Adaptive Method

The governing equations for the z-pinch plasma simulation were developed and put into the adaptive form in Chapter 3 and they will be restated here for convenience:

Continuity Equation :

$$[rr_\xi \rho]_\tau + [r\rho(u - r_\tau)]_\xi = 0. \tag{4.7}$$

Momentum Equation :

$$[rr_\xi(\rho u + \frac{1}{c^2}F)]_\tau + [r\rho u(u - r_\tau)]_\xi - [rr_\tau \frac{F}{c^2}]_\xi$$

$$+ r[p]_\xi + [P]_\xi - \frac{rr_\xi}{c} J_b B + \frac{1}{r}[\frac{r^2 B^2}{8\pi}]_\xi = 0. \tag{4.8}$$

Energy Equation :

$$[rr_\xi(e_p + e_R)]_\tau + [re_p(u - r_\tau)]_\xi - [rr_\tau e_R]_\xi$$

$$+ [rpu]_\xi + [r(q + F)]_\xi = rr_\xi(JE + S_{col.}). \tag{4.9}$$

Magnetic Diffusion Equation :

$$\frac{1}{c}[r_\xi B]_\tau + \frac{1}{c}[B(u - r_\tau)]_\xi - [\frac{\eta c}{4\pi}\frac{1}{rr_\xi}[rB]_\xi]_\xi + [\eta J_b]_\xi = 0. \tag{4.10}$$

Radiation Transfer Equation :

$$\frac{1}{c}[rr_\xi I_g]_\tau - \frac{1}{c}[rr_\tau I_g]_\xi + \mu[rI_g]_\xi - r_\xi[\zeta I_g]_\omega - rr_\xi(\bar{\eta}_g B_g - \bar{\chi}_g I_g) = 0. \tag{4.11}$$

Among these equations, continuity, momentum and energy are solved with an explicit scheme whereas the magnetic diffusion and radiation transfer are solved with an implicit scheme. The timestep, Δt, for the simulations is calculated as

$$\Delta t = min(\Delta t_{CFL}, \Delta t_{jh}, \Delta t_{bc}, \Delta t_{re}, \Delta t_{ra})$$

where the CFL condition follows as

$$CFL = (\mid u \mid + a)\frac{\Delta t_{CFL}}{\Delta x} \leq 1$$

and $\Delta t_{jh}, \Delta t_{bc}, \Delta t_{re}, \Delta t_{ra}$ are calculated from a constraint on the allowed change in plasma energy (e_p) due to joule heating, beam-collisional energy, radiation emission and absorption for a given time step. That is, we assume

$$\Delta t_i \;\; \Delta \dot{e}_{p,i} = 0.1 e_p.$$

where i represents the components above.

The differencing formulation done in earlier chapters describe the solution at a mesh point in terms of the solutions at neighbooring points. Hence, in order for the solutions to be stable and error-free (as much as possible), we do not want any information to move more than one cell at a time step. This is a stability condition for the explicitly solved continuity, momentum and energy equations. For most of the simulations Δt is on the order of nanoseconds and this is small compared to the timescale of hydromotion but large compared to the magnetic diffusion and radiation transfer timescales. An attempt to work

with smaller time steps would certainly make the simulations more costly and lengthy. Therefore we have chosen to solve magnetic and radiation equations with an implicit scheme that does not have any time constraint.

The heart-beating feature of the adaptive method, as we know by now, is its ability to move the grid points wherever and however we want. The procedure followed here is an explicit method which means the grid points are explicitly (somehow independently) moved and located to the new positions for the new time step before any physical equation is solved. The criteria upon which to construct the new mesh distribution could be anything we wish, but because we want to relate it to the high gradients of some desired function, we would have to use those functions to do so. Even though the mesh generation equation Eq.2.4 is solved explicitly, that does not restrict the physical equations to be solved explicitly too. An implicitly solved equation would couple itself to the mesh metric, x_ξ, and the mesh velocity, x_τ, at the time step $n+1$ but because they are calculated in advance it makes no trouble to use an implicit as well as an explicit scheme with the explicitly generated adaptive mesh scheme.

Using an explicit mesh generation procedure in fact has a distinct advantage over an implicit approach (which couples the physical equations and the mesh generation tightly). Because the mesh distribution is done on any strategy, one could take into consideration the *smoothness* of the distribution if desired. The scheme used in our code does take advantage of this and the

smoothing is rather done on the weight function, W, which indeed results in a smooth mesh distribution. Also there are other conditions to impose on the grid movement. The size of the cells in the grid should change gradually and rapid changes are to be avoided because they usually reduce accuracy in the approximation of the derivatives and thus of the solutions. Secondly, there has to be a limit on the minimum mesh spacing so that the stable time step does not get smaller than what one could really afford. The procedure in the present model does not limit the mesh spacing to an exact value, but rather limits it approximately to a user-given value.

The weight function W used in the simulations has the form

$$W = 1 + \alpha_a \mid A_x \mid + \beta_a \mid A_{xx} \mid + \alpha_b \mid B_x \mid + \beta_b \mid B_{xx} \mid \qquad (4.12)$$

where A and B are some normalized function for adaption such as *velocity, pressure, mass density, momentum density and temperature.* Also A_x, A_{xx}, B_x, and B_{xx} are the first and second derivatives of A and B with respect to the spatial coordinate x. The α's and β's are determined by the formulas in Eq.2.5 and 2.6 provided R's are given. Here, one is really free to choose A and B as any function. The adaption of the chosen function will mean that the mesh distribution at each time step is so constructed that the error in the solution of the chosen function is reduced by some degree.

For the z-pinch plasma simulations, there are some functions of particular interest. These are *electrical resistivity, temperature* and *momentum.* Elec-

trical resistivity is of interest because of the sharp gradient between the hot and cool plasma regions. A typical resistivity profile is shown in Figure 3.20. The jump in the resistivity is where actually the channel radius and the peak magnetic field are. The plasma goes from a highly conductive region to a highly resistive region in a distance of several mesh points. It is important to have as many mesh points as possible at this critical radius to help the error go down in the magnetic field peak value. Secondly, temperature is of special interest due to the expected temperature gradients at the inner radii resulting from shock heating. Because the lagrangian code ZPINCH seems not to put many mesh points where the temperature peak lies, it is also of interest to adapt temperature in our simulations. Finally, momentum is a good adaption function to follow the hydro motion. It can capture the shock front, rarefaction fans and the contact discontinuites in the plasma. In most cases, choosing only one function is not satisfactory (as in the lagrangian case). Therefore, we have run simulations for *multiple adaption* to feature the best out of the code.

The problem described in the previous section is tested here with different adaptions to show how important the adaption might be. Results are given in Figures 4.6 through 4.22 for the cases shown in Table 4.2. The number of mesh points and the listed times are kept the same as those for ZPINCH results to make reasonable comparisons. Here, it is most important to look at the magnetic field profiles, Figures 4.6-10, for various adaptions. Table

Table 4.2: Weight functions and their relative coefficients for adaption.

ADAPTION FUNCTION	R_α	R_β
Temperature	0.3	0.1
Resistivity	0.3	0.1
Momentum	0.3	0.1
Temperature and Momentum	0.3 0.3	0.1 0.1
Resistivity and Momentum	0.3 0.3	0.1 0.1

Table 4.3: Results at 1.8 μs vs. adaption function.

Adaption Function	Peak B-field (kG)	Channel radius (cm)
Temperature	35.0	0.5
Resistivity	33.0	0.57
Momentum	33.0	0.5
Temperature&Momentum	35.7	0.5
Resistivity&Momentum	33.5	0.45

4.3 lists the magnetic field peak values and the channel radii at time 1.8μs for various adaption functions. The peak value and the channel radius for that peak value are different for each case. The differences range from 5 % to 10 % in magnetic field peak and from 5% to 15 % in the channel radius. This is quite a difference to show how important the grid distribution can be, inspite of the same numerical method (first order upwind differencing) used for the calculations.

Which one of the adaptions do we trust? There is only one right answer and in these complex problems we probably do not know which is right. We can test by introducing more and less mesh points, changing the time step and the adaption of the scheme and look at variations in the result. If it is the hydro motion, probably momentum adaption would be helpful, if it is the magnetic properties then resistivity and temperature would be more appropriate. Nevertheless, the hydro and magnetic properties of the plasma are coupled and the better treatment of one would do good for the other too. Thus one may like to adapt both properties at the same time. Not to our surprise, the developed code here is designed to adapt more than one property.

A nice presentation of how the grid points move during the simulation time is shown in Figures 4.18 through 4.22. Starting with a uniform distribution, the mesh points reposition themselves to concentrate on the desired locations. Comparing the distributions for temperature, resistivity and mo-

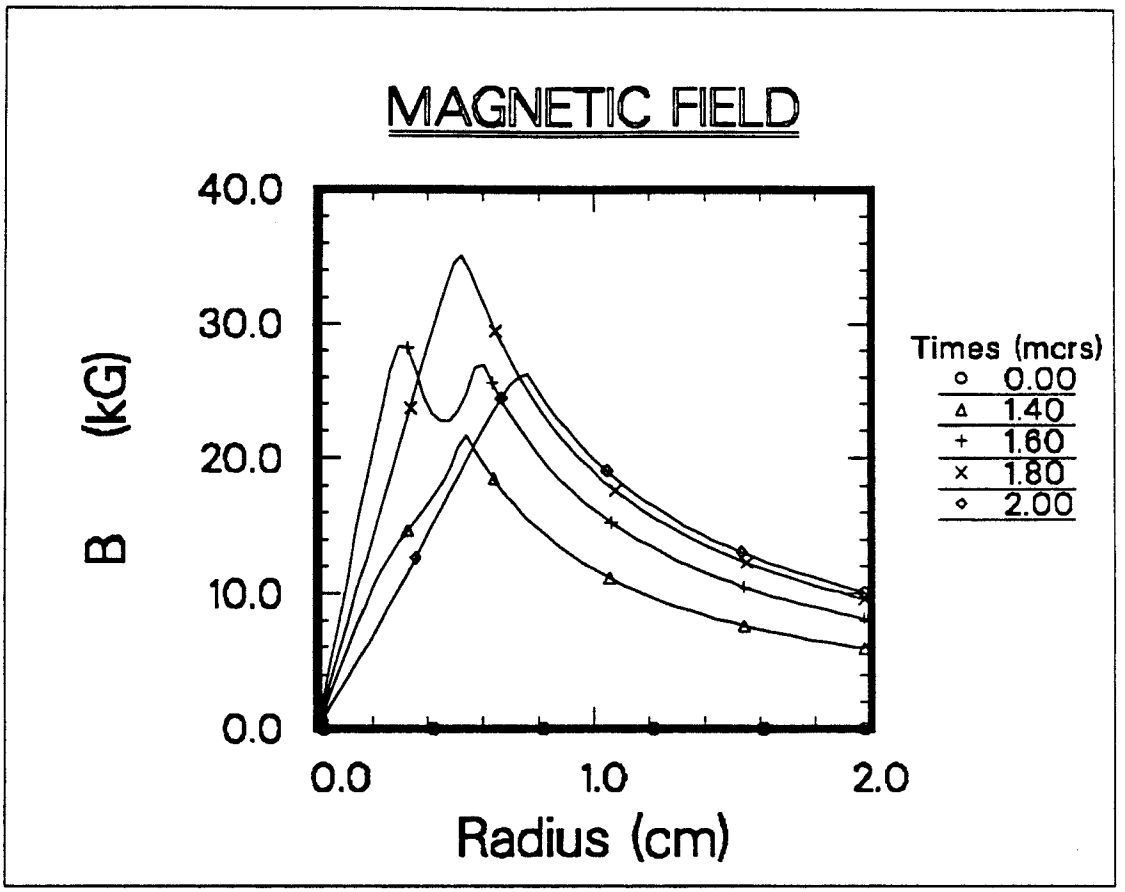

Figure 4.6: Magnetic Field profiles with temperature adaption.

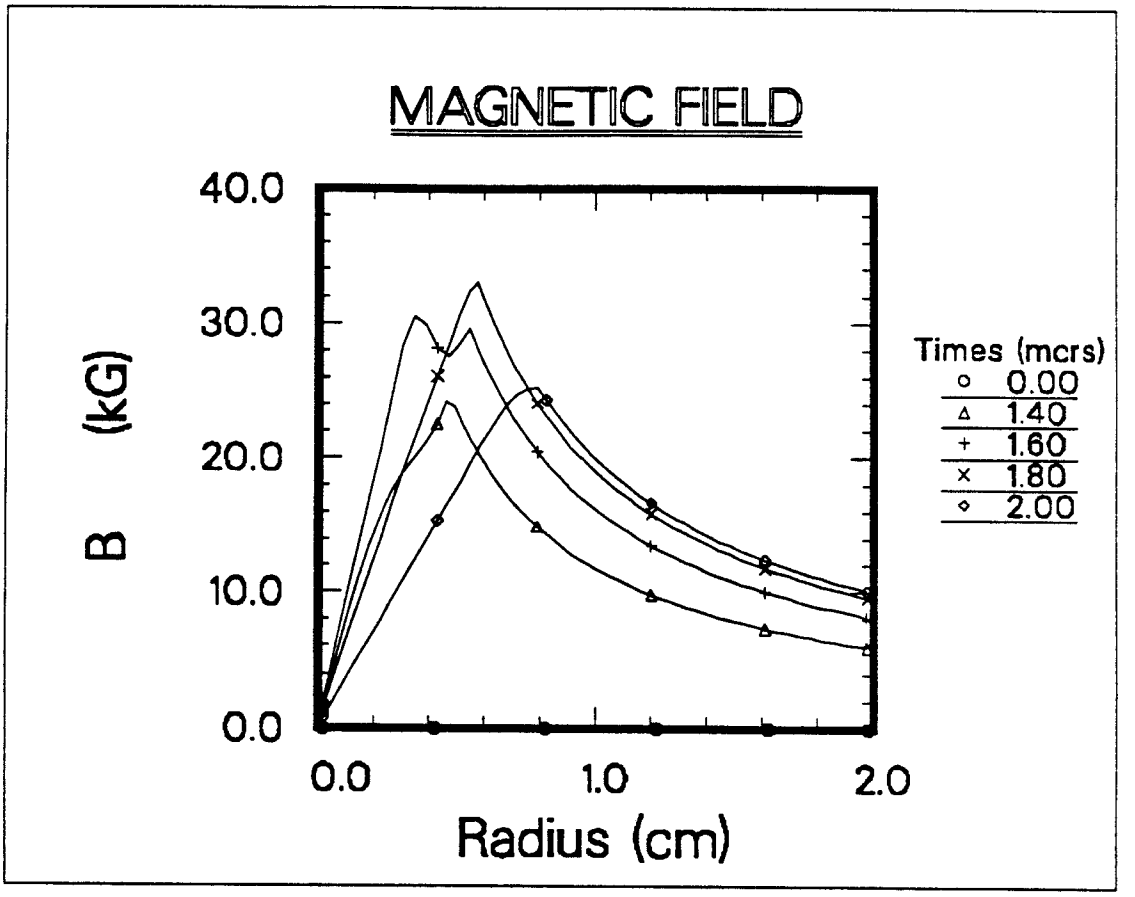

Figure 4.7: Magnetic Field profiles with resistivity adaption.

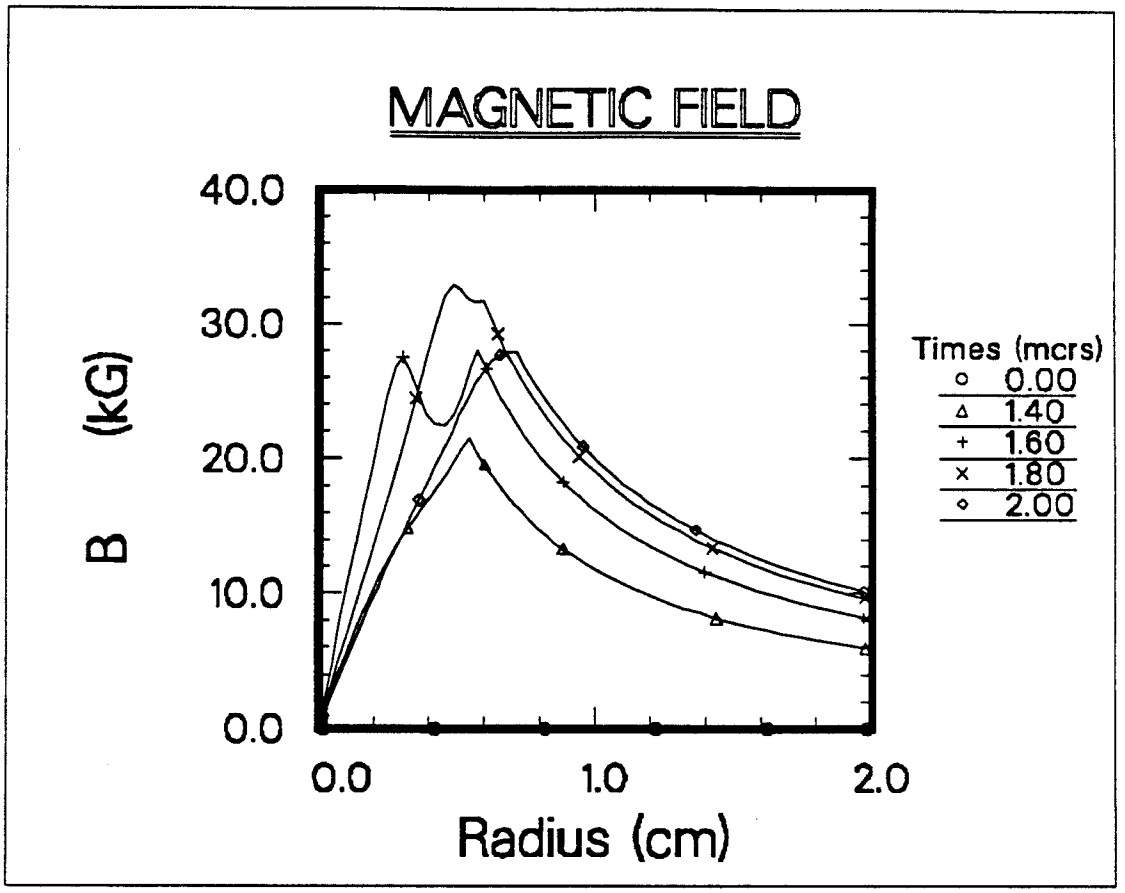

Figure 4.8: Magnetic Field profiles with momentum adaption.

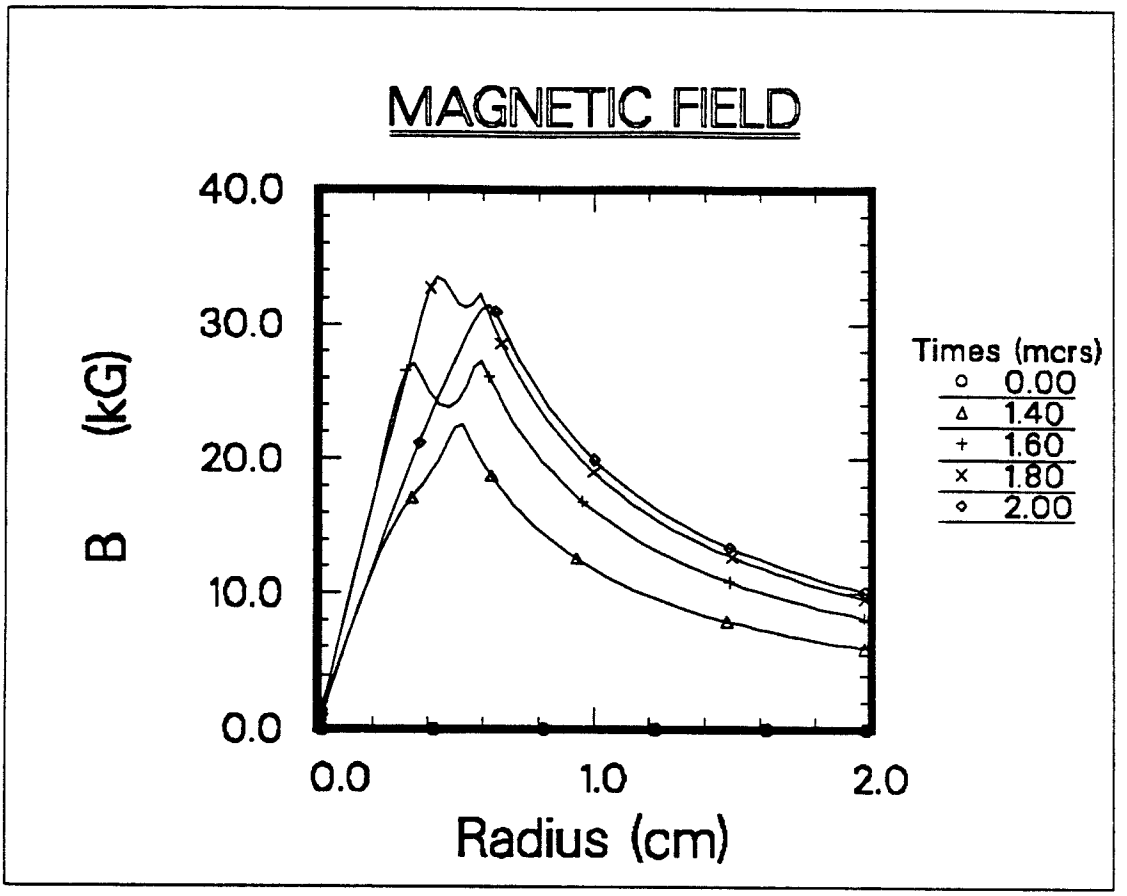

Figure 4.9: Magnetic Field profiles with resistivity-momentum adaption.

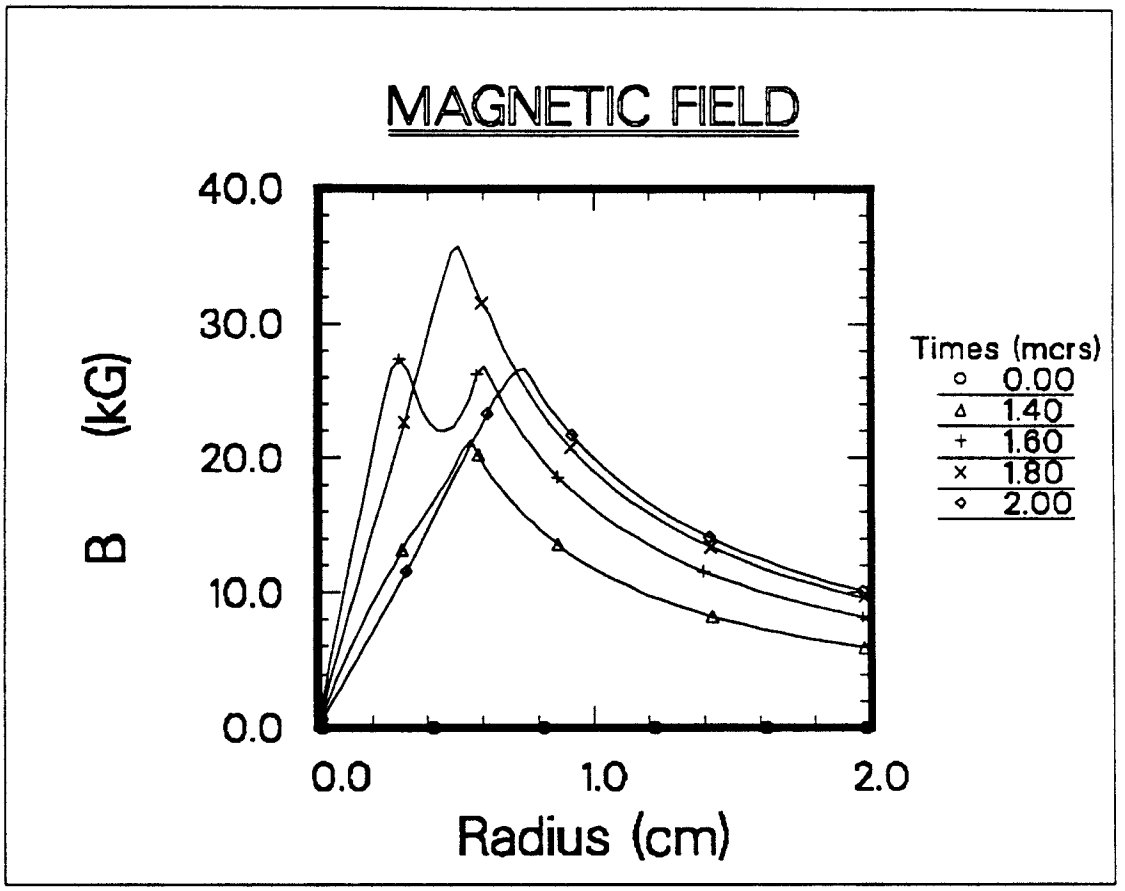

Figure 4.10: Magnetic Field profiles with temperature-momentum adaption.

mentum adaptions, we can see adapting only resistivity would not do a terrific job other than putting a few more points around the channel radius. Most of the events are happening inside the channel and we ought to consider that. Momentum adaption drags the concentration point along with the expanding plasma, thus leaving a rarefaction region with less points behind. The temperature adaption on the other hand, spreads the points from the center up to a moving edge with more or less the same intensity. Yet a combination of the temperature and momentum produces a mesh distribution with the smallest uniform mesh spacing (0.027 cm) throughout the channel, raising the chance for a better resolution in the magnetic field peak as well as in other quantities.

Almost all mass density profiles in Figures 4.11 through 4.15 show a strong pinching effect on the plasma. The magnetic field created by the discharge current is high enough to pinch the plasma. The pinching seems to be severe and the high density at the center may cause a significant energy loss for beam ions. For this reason, the density inside the channel is desired to be uniform and low compared to the outer density (a factor of four on the average). Therefore, the results raise some degree of concern in that regard.

The discharge current, Figure 4.16, in the channel flows through the hot plasma and shows a flat profile with a sharp drop at the channel's outer surface. This is similar to a coaxial cable with a uniform current density and

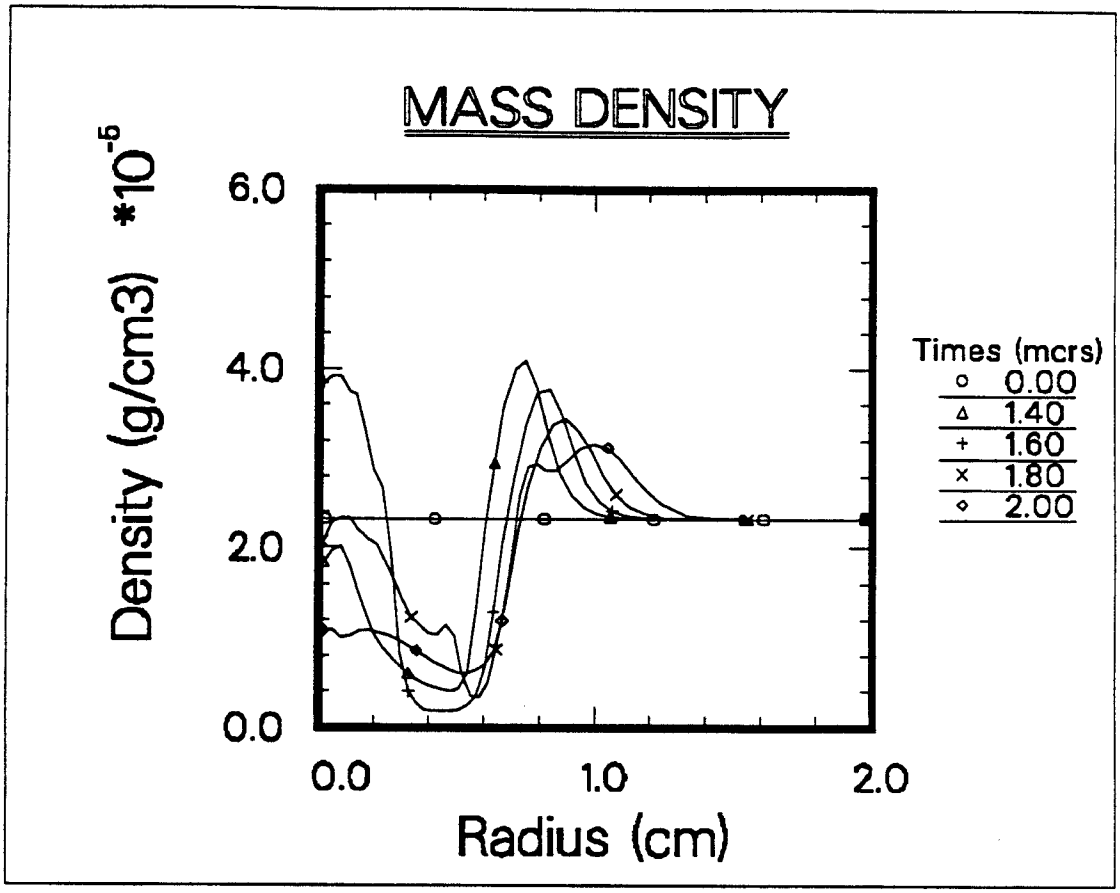

Figure 4.11: Mass Density profiles with temperature adaption.

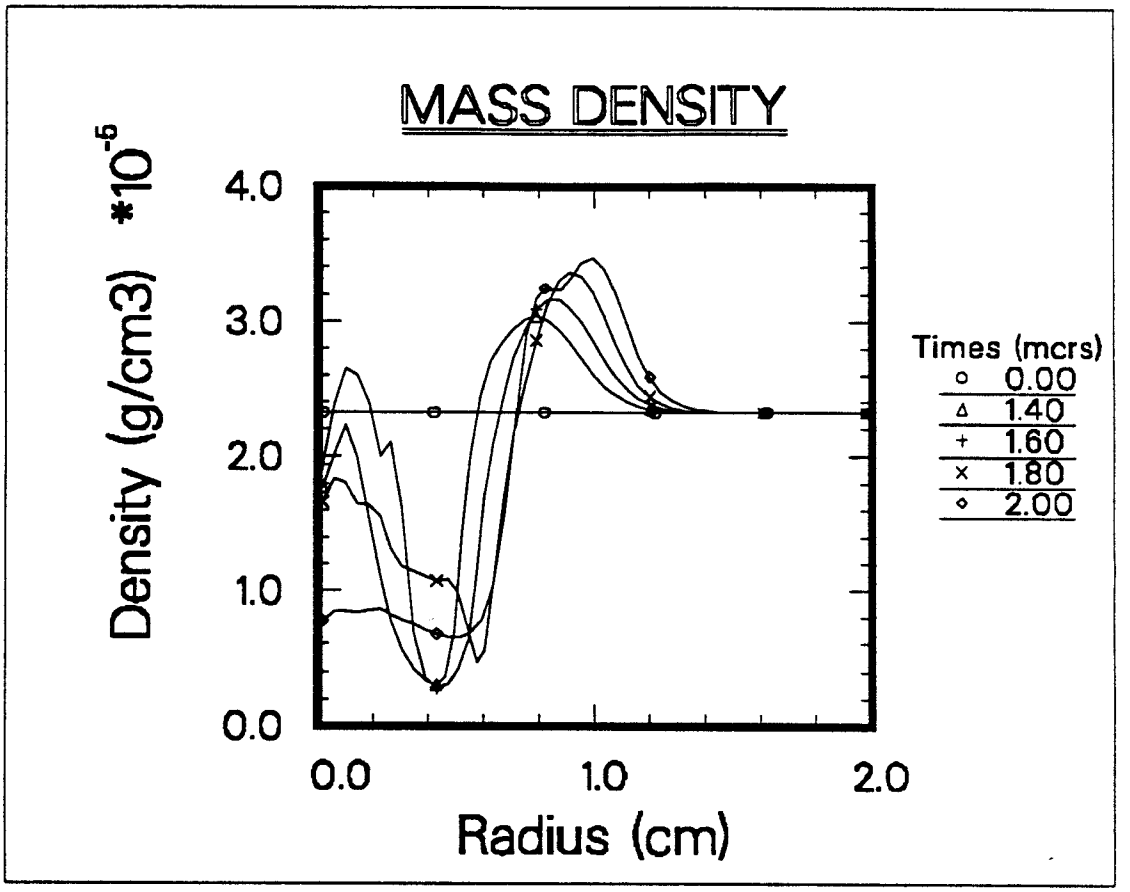

Figure 4.12: Mass Density profiles with resistivity adaption.

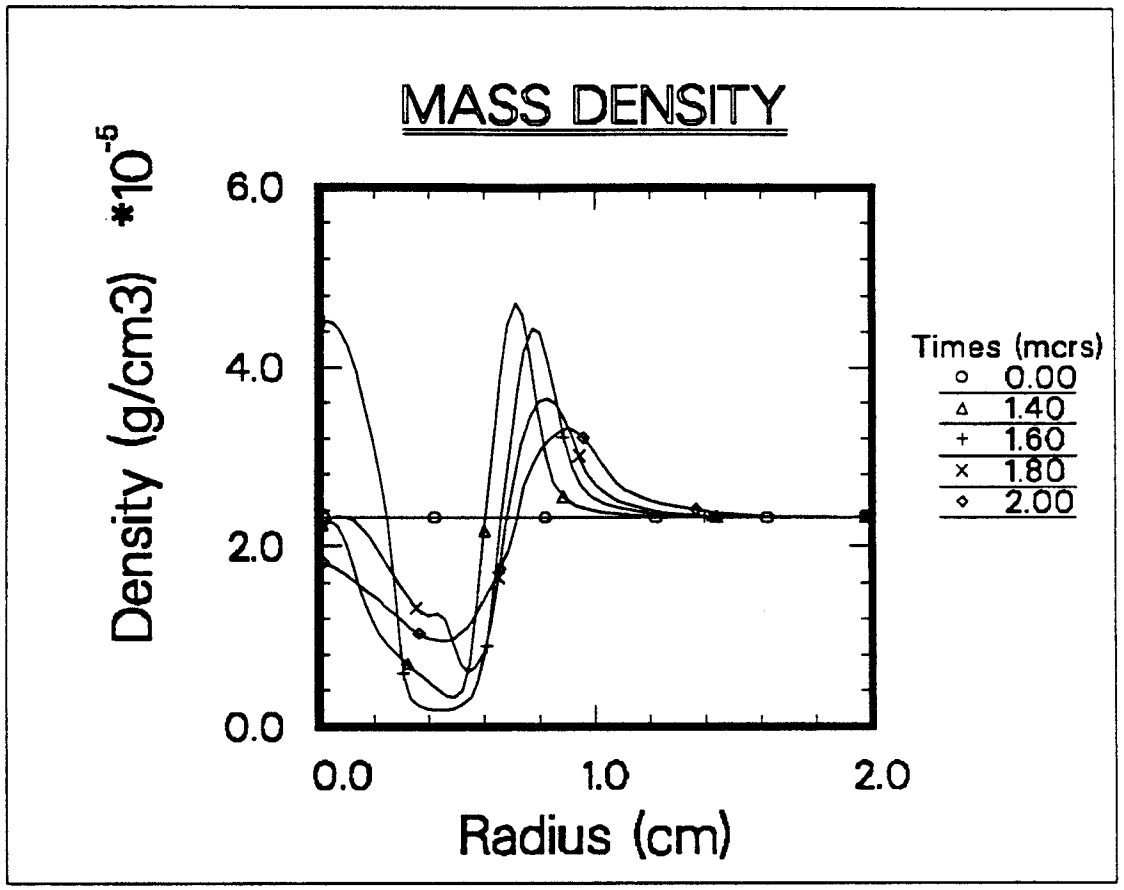

Figure 4.13: Mass Density profiles with momentum adaption.

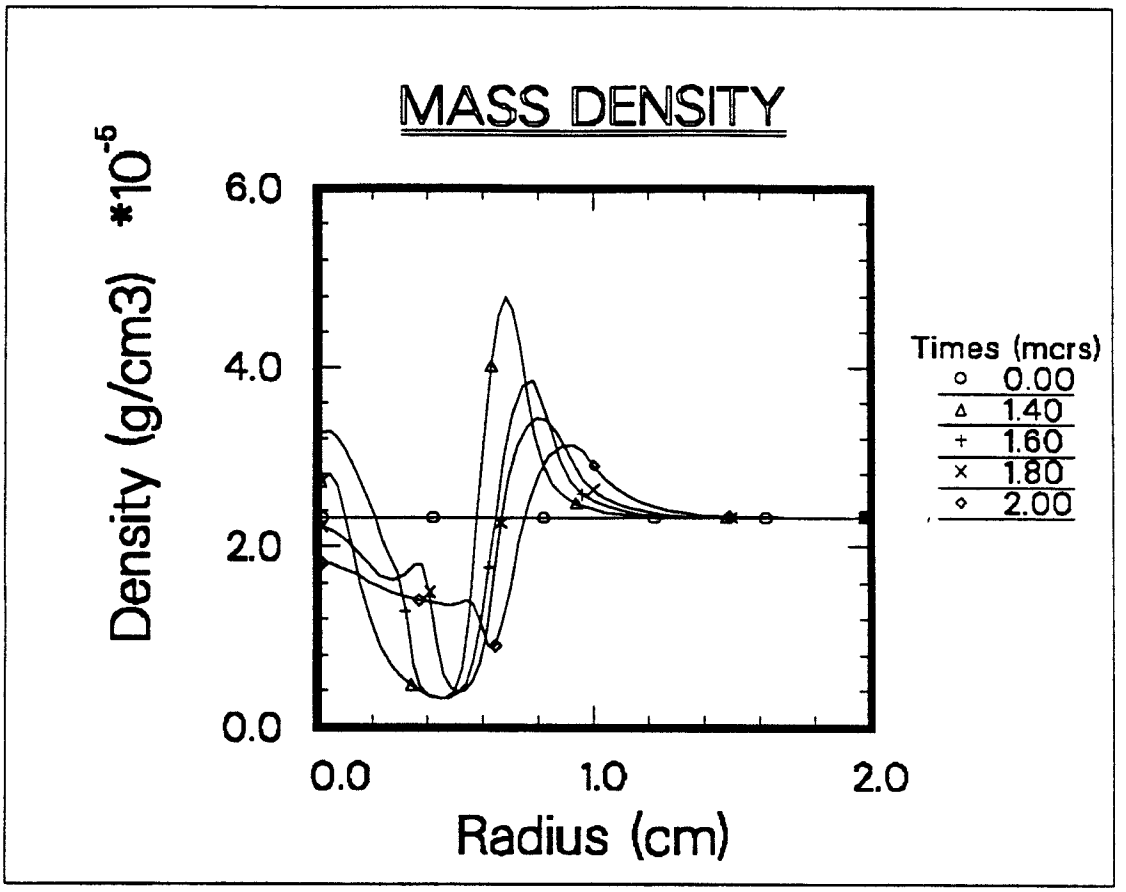

Figure 4.14: Mass Density profiles with resistivity-momentum adaption.

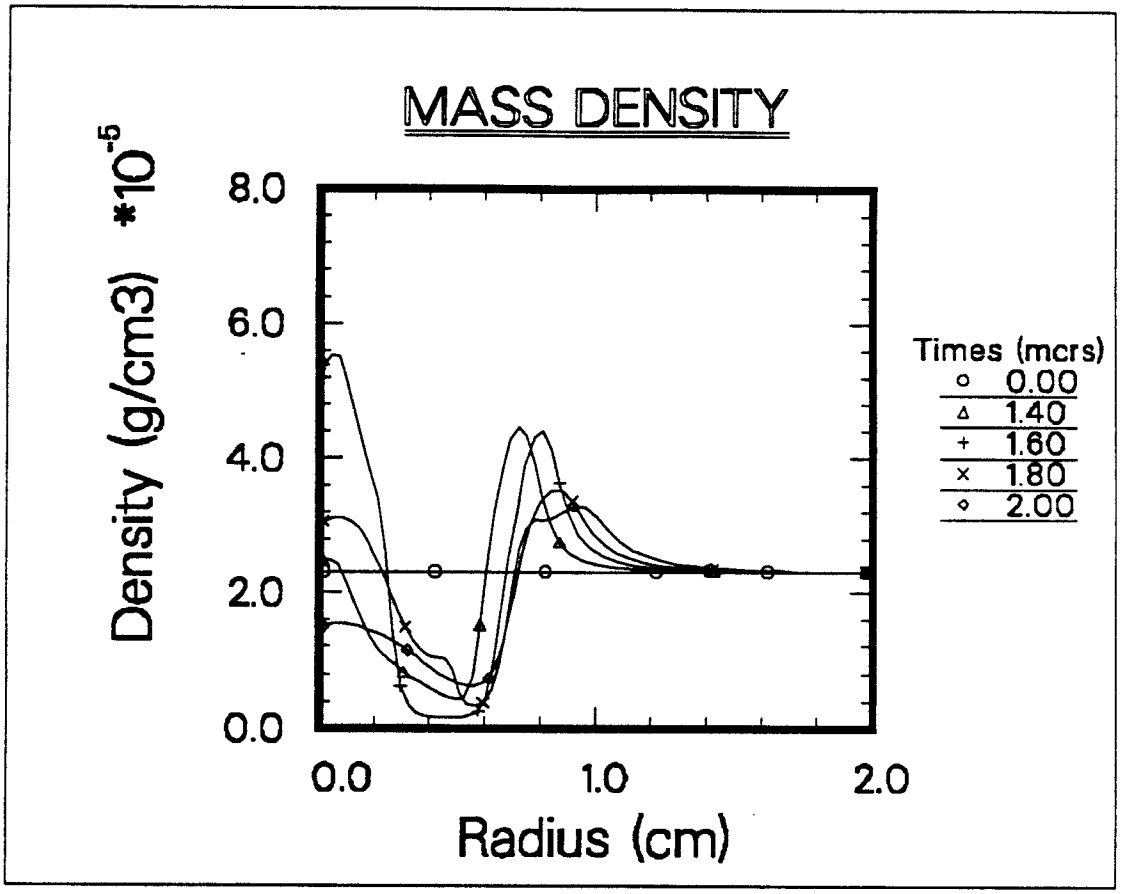

Figure 4.15: Mass Density profiles with temperature-momentum adaption.

a linearly increasing magnetic field (Figures 4.6-10). At some time steps, however, the current density losses its uniform profile and lets a drop occur inside the channel. This could be understood by looking at the magnetic diffusion equation that governs the behavior of the magnetic field and thus of the current density.

$$\frac{1}{c}\frac{\partial B}{\partial t} - \frac{\partial}{\partial r}(\frac{\eta c}{4\pi}\frac{1}{r}\frac{\partial}{\partial r}(rB)) + \frac{1}{c}\frac{\partial}{\partial r}(uB) = 0 \tag{4.13}$$

The second term which involves the resistivity ($10^{-15} sec$) is negligible and the behavior of the magnetic field is given by the convective term. The magnetic flux through any loop moving with fluid velocity u is constant in time and from that we say the B lines are frozen into the fluid and are carried along with it. If the plasma experiences a compression or a rarefaction, the magnetic field intensity similarly is increased or decreased. Indeed, the pinching that pushes the plasma toward the center causes both compression and rarefaction which can be seen in Figure 4.17. Thus, the bumps in the magnetic profiles and the resultant drop in current density is due to the fact that the plasma column experiences a magnetic pinching in the center.

The radiation field in the channel is as high as $10^{13} erg/(cm^2.sec)$ at the center and drops gradually to its half value at the channel radius. This indicates that most of the radiation leaves the channel as soon as it is emitted confirming the fact that the mean free path of the photons is comparable with the channel dimensions and many photons escape the channel before they

make a collision. The effect of this energy loss through the radiation may or may not play a significant role in the formation of an optimized channel which is deferred to an oncoming discussion.

An outcome of the simulations shown so far would point out that we should adapt two functions for better results. Choosing the momentum as the standard one, one might like to add either the temperature or the resistivity next. Due to the fact that a *temperature-momentum* adaption keeps the point concentration high all over the inner region of the channel, we have decided to do the rest of the simulations with that adaption. The simulation results for this case are given in Figures 4.10, 4.15 and 4.22. These results again are only for channel formation and do not include the injection of the ion beam. However, in the next chapter, when we seek an optimized channel for LIBRA designs we will include the beam in the channel and see how much energy indeed can be transported to the target.

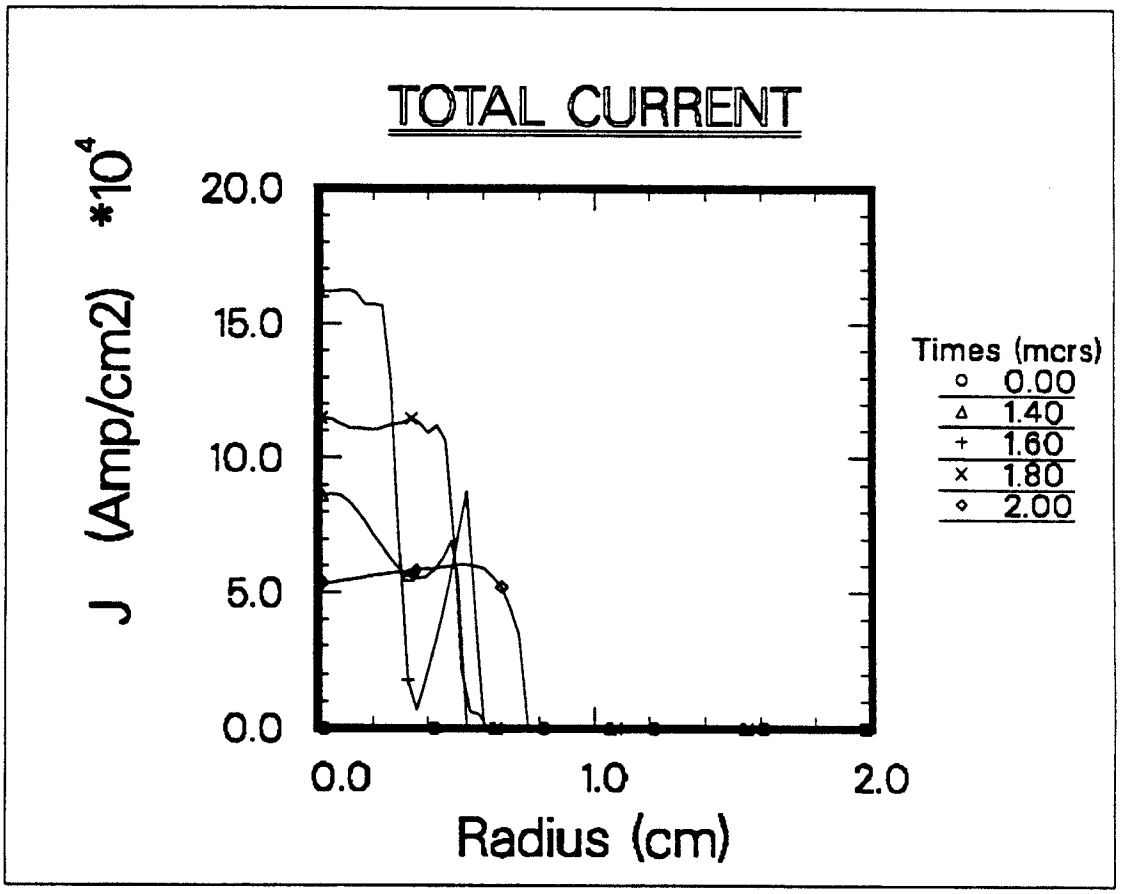

Figure 4.16: Current Density profiles with temperature adaption.

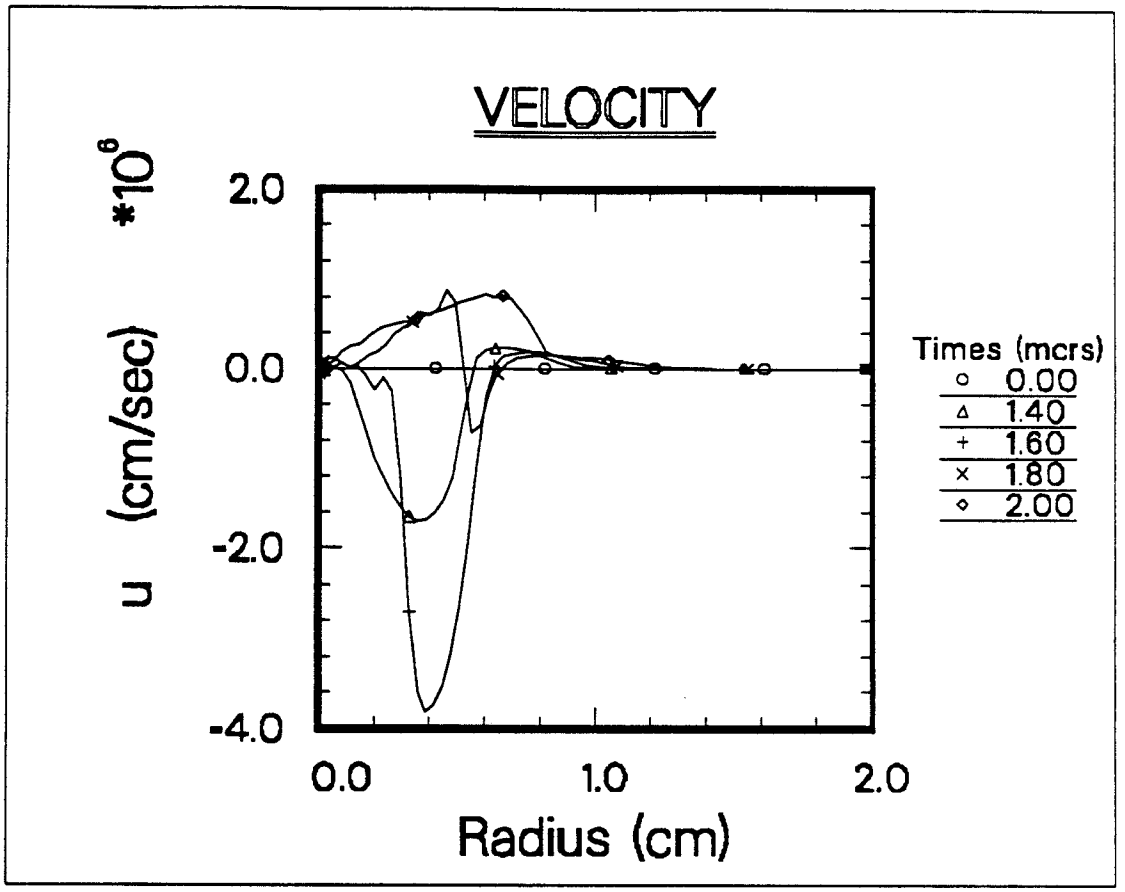

Figure 4.17: Plasma velocity profiles with temperature adaption.

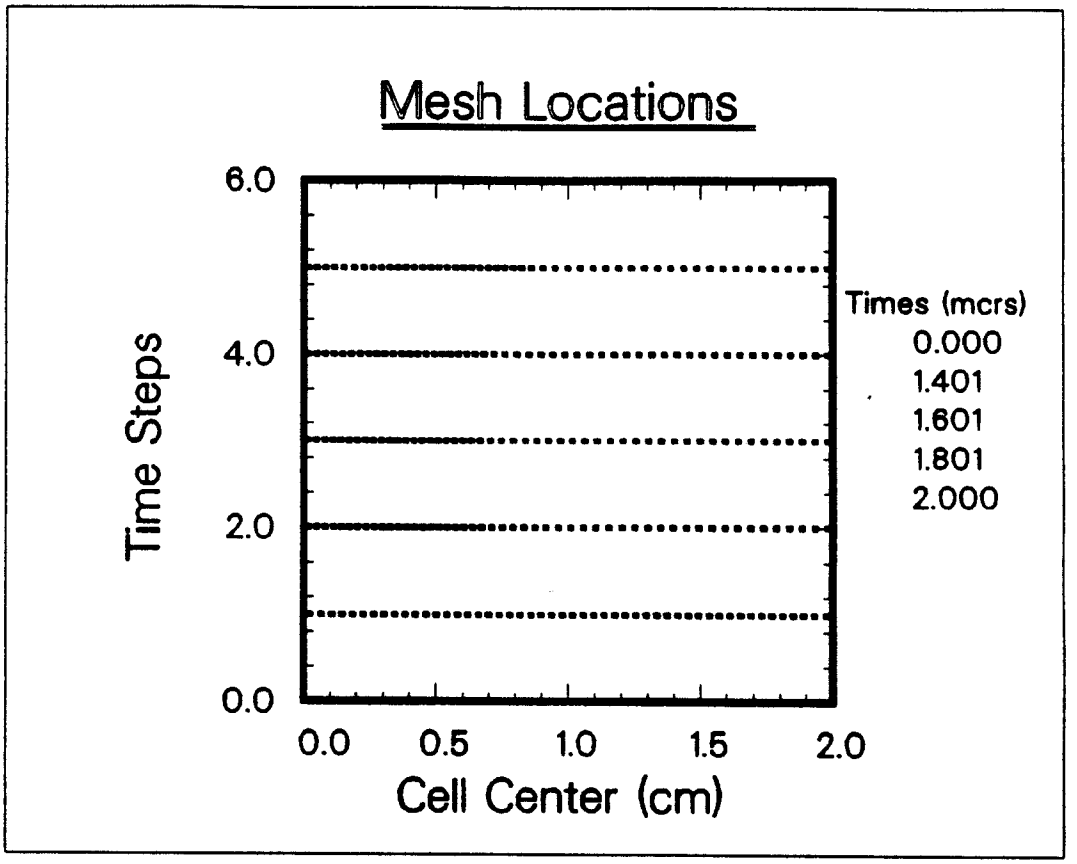

Figure 4.18: Mesh Locations with temperature adaption.

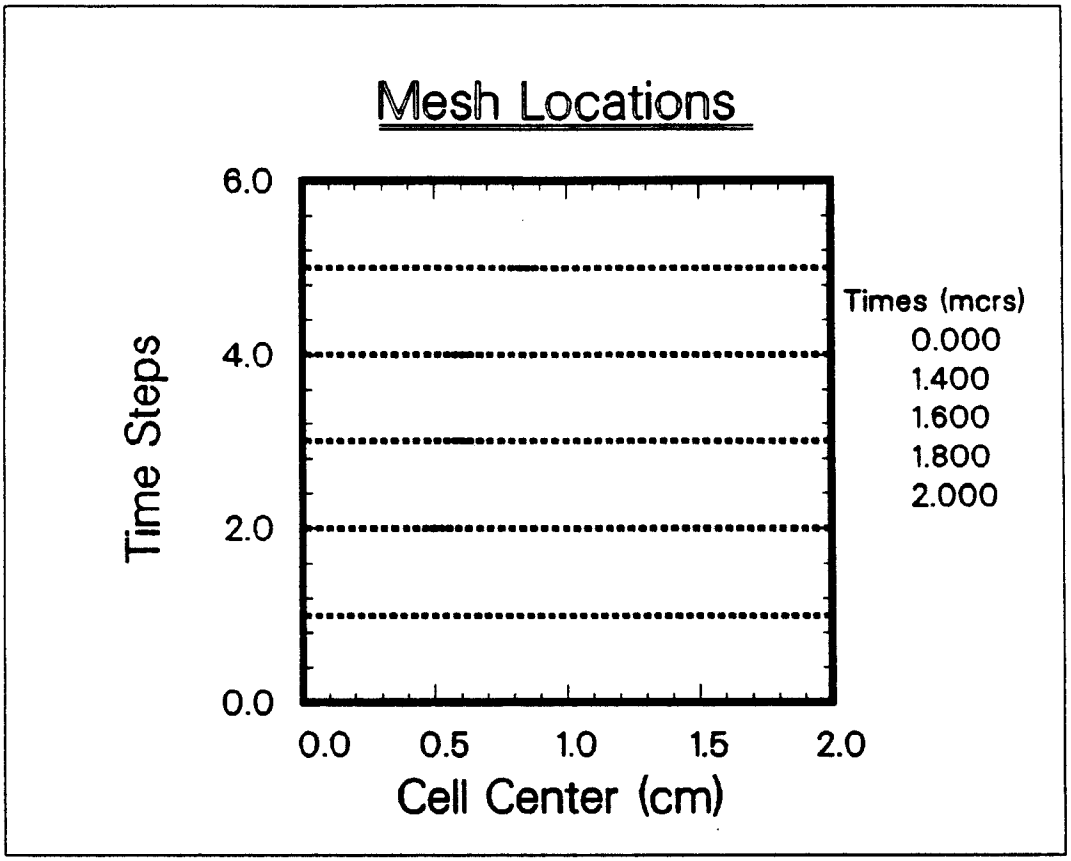

Figure 4.19: Mesh Locations with resistivity adaption.

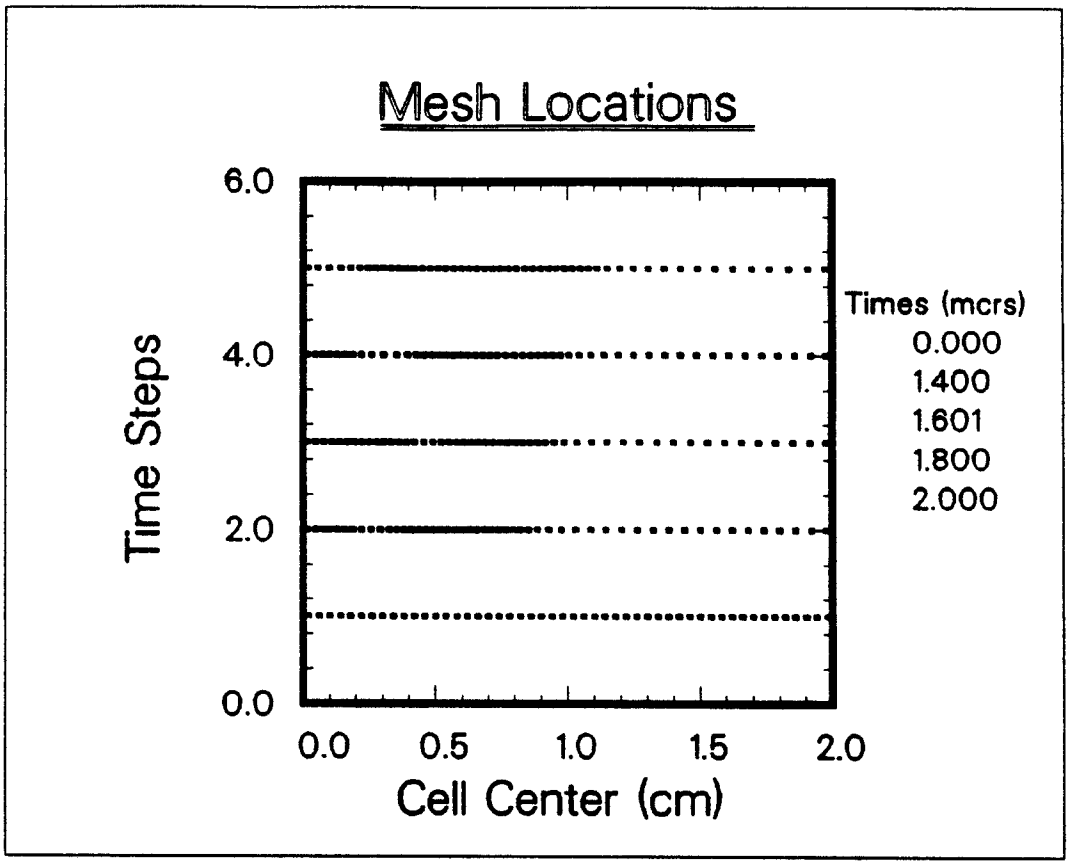

Figure 4.20: Mesh Locations with momentum adaption.

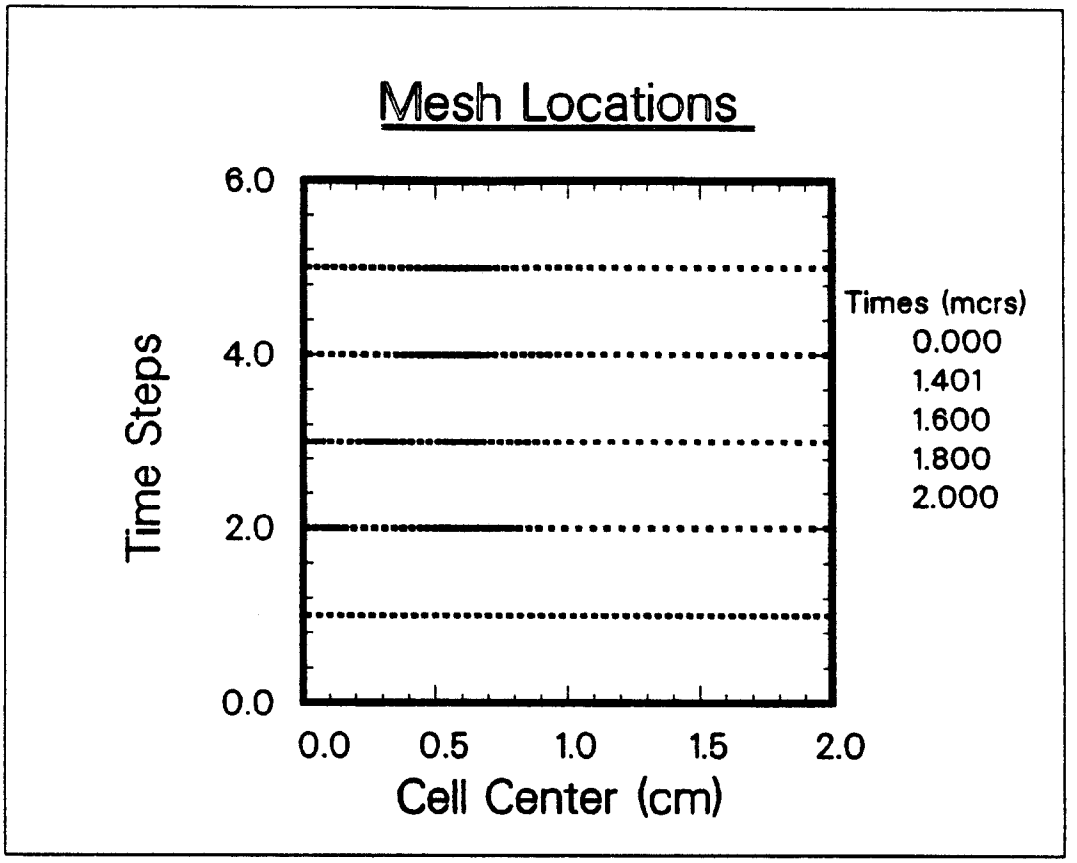

Figure 4.21: Mesh Locations with resistivity-momentum adaption.

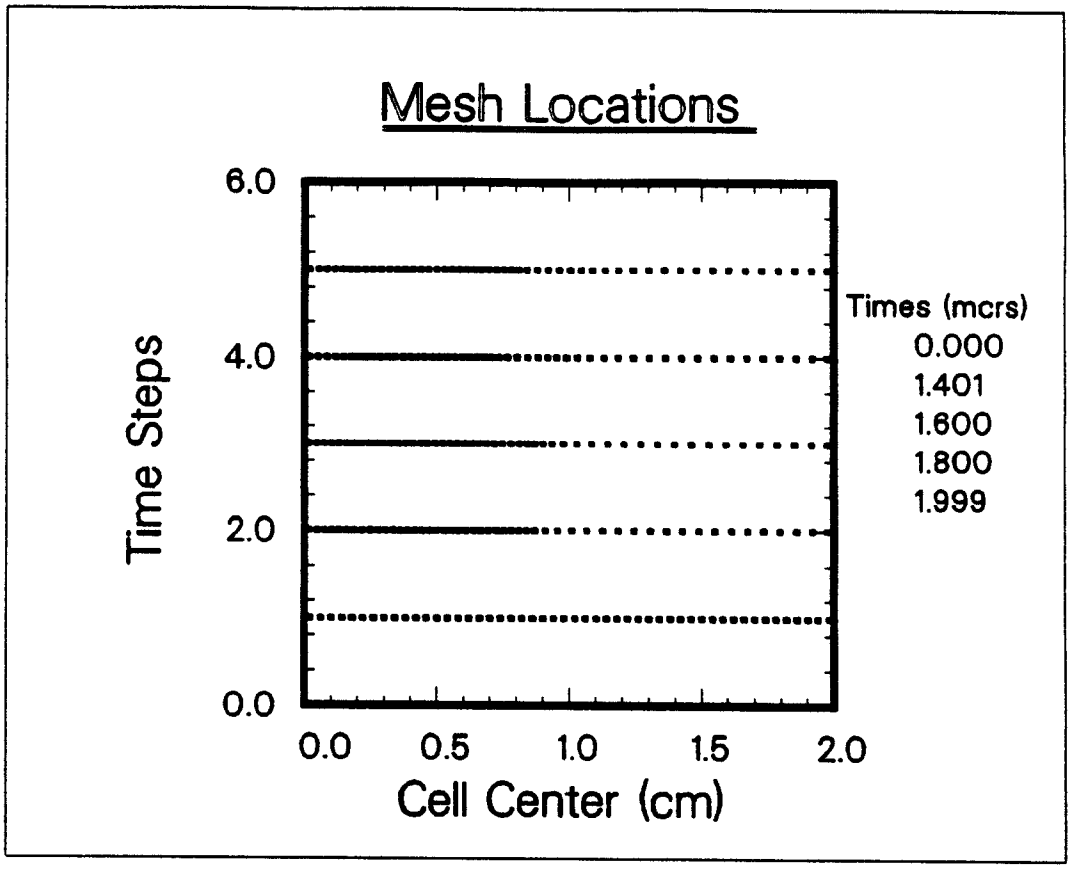

Figure 4.22: Mesh Locations with temperature-momentum adaption.

4.3 Remarks on Comparison

As stated in the previous sections, the lagrangian code ZPINCH and the adaptive code we have written for radiating magnetized plasmas were run for a channel formation problem in the LIBRA design. Using the power of the adaptive code, we have tried different adaption functions and noticed the importance of the adaption in such calculations. Viewing the lagrangian scheme as a special case of the adaptive scheme just as each one of three cases of adaptive runs (temperature, resistivity and momentum), we should judge on the difference in the methods not the codes as a whole. The clear distinction between the ZPINCH and the adaptive code is mostly the adaption, the radiation model and ion beam injection. When we add the ion beam in the channel though, we can no longer make any assessment on the differences between the two approaches. For that reason the test problem mentioned in this chapter considers no beam in the channel and therefore we shall only examine the adaption and the radiation models in both. The supplementary data (EOS and Opacity tables) was taken from the same computer code, IONMIX [66], but the form of opacities used in ZPINCH and ARMHD is not the same. We have used the emission and absorption group constants in Eq.3.7, whereas ZPINCH uses so-called Planck and Rossland opacities. The physical models and the method to produce the data from IONMIX, however, is the same.

Table 4.4: A comparison between ZPINCH and ARMHD at 1.8 μs for helium channels.

Code	Peak B-field (kG)	Δ x (cm) around B_{peak}	Channel radius (cm)
ZPINCH	27.5	0.04	0.65
ARMHD	35.7	0.027	0.5

The comparison of magnetic field profiles in Figures 4.2 and 4.6-10 yield a significant difference in the range of 30-35 %. Table 4.4 also makes a comparison at time 1.8 μs. The difference is important here because the mass density profiles in Figure 4.3 and Figures 4.11-15 show a severe pinching with the adaptive code compared to a harmless pinching shown by ZPINCH. Pinching is not good because it destroys the stability of the channel and causes more energy loss of beam ions. As far as adaption goes, the adaptive code that we use put a lot more points where the magnetic field gradient lies. Table 4.4 gives the minimum mesh spacing around the magnetic peak and it is two times lower for ARMHD with the same number of mesh points (50) as used in ZPINCH. The deficiency of a lagrangian scheme for such a multigradient problem, in other words the limited power of only being able to follow the mass gradient, is obvious here. In addition to adaption, part of the difference may be caused by the distinction between the radiation mod-

els. ZPINCH, as mentioned before, uses a radiation diffusion approximation which assumes that a photon makes many collisions before leaving the channel. This assumption is noted shaky by Watrous [14] in his ZPINCH work. The diffusion approximation assumes that the radiation intensity is nearly isotropic and this would not be true near a source of radiation where infact the intensity is highly anisotropic. Because the mean free path of photons for most of the channel gases (argon, nitrogen and hydrogen) is comparable with the channel radius, the degree of anisotropy should be high all over the channel. One consequence of the diffusion approximation is as Watrous calls [14] a *radiatively driven expansion* (RDE) of the channel. Photons emitted in the hot plasma may very well be absorbed in the cool plasma if one assumes diffusion. The absorption in the cool region causes the channel to expand and the expansion degrades the magnetic field bringing the peak to lower values which infact could partially count for some of the magnetic field degradation in the ZPINCH results shown here. The channel radius is larger by 30 % than that of our results indicating that the difference in radiation models may have some degree of influence on the results.

In order to cancel the differences due to the radiation models we suggest to make a comparison for a channel with the radiation artifically removed. A simulation in that nature has been actually done before with ZPINCH for the nitrogen gas with a preionizing laser of 1 mm half-width to see the effect of the radition field [1]. The magnetic field profiles for a nitrogen channel with

Table 4.5: A comparison for nitrogen channels by ZPINCH and ARMHD at time $1.8\mu s$.

Code	Peak B-field (kG)	Δx	Channel radius (cm)
ZPINCH	24.5	0.028	0.83
ARMHD	32.5	0.018	0.5

the same mass density and discharge current as helium are shown in Figure 4.23 and 4.24 by ZPINCH and ARMHD respectively. Also a comparison in the B-field peak values, Δx -mesh spacing around the peak value, and channel radius at time $1.8\mu s$ is given in Table 4.5. An illustration of the mesh distribution resulting from the ARMHD simulations for nitrogen is given in Figures 4.25 and 4.26. It is obvious that the distribution is high in the channel and low outside the channel, which is what we need. On the other hand, the mesh distribution by ZPINCH, Figure 4.27, shows a high concentration far from the magnetic field peak, either in front of it for an expanding channel or behind it for a pinched channel. Although the numerical method used with ZPINCH has a higher order of accuracy (second order) compared to what is used with ARMHD (first order), the finer mesh spacing with ARMHD gives better credit to our results indicating that we possess more accurate results. Also the conservation checks for energy, mass, magnetic flux and discharge current are highly satisfactory ($97 - 99\%$) implying the performance of its

conservative model equations and scheme. The typical energy conservation with ZPINCH is about $90 - 94\%$.

An important outcome of the adaptive scheme, along with the new physics embodied in the computational model, is that the required magnetic field of 27 kG can be obtained for helium channels with less discharge current. Thus, the channel can be formed with a 30-40 % less discharge voltage, possibly reducing the breakdown between the discharge and the reactor chamber. Another outcome is that the reasons to change the channel gas from argon to nitrogen and to helium may have to be reconsidered in the future channel designs because of the fact that argon and nitrogen showed high magnetic fields here as opposed to the low values obtained earlier with ZPINCH. The difference due to the grid scheme proved to be significant as in the case of the nitrogen channel but further investigations on the differences due to radiation models should be studied too. The next chapter will in fact present such a case.

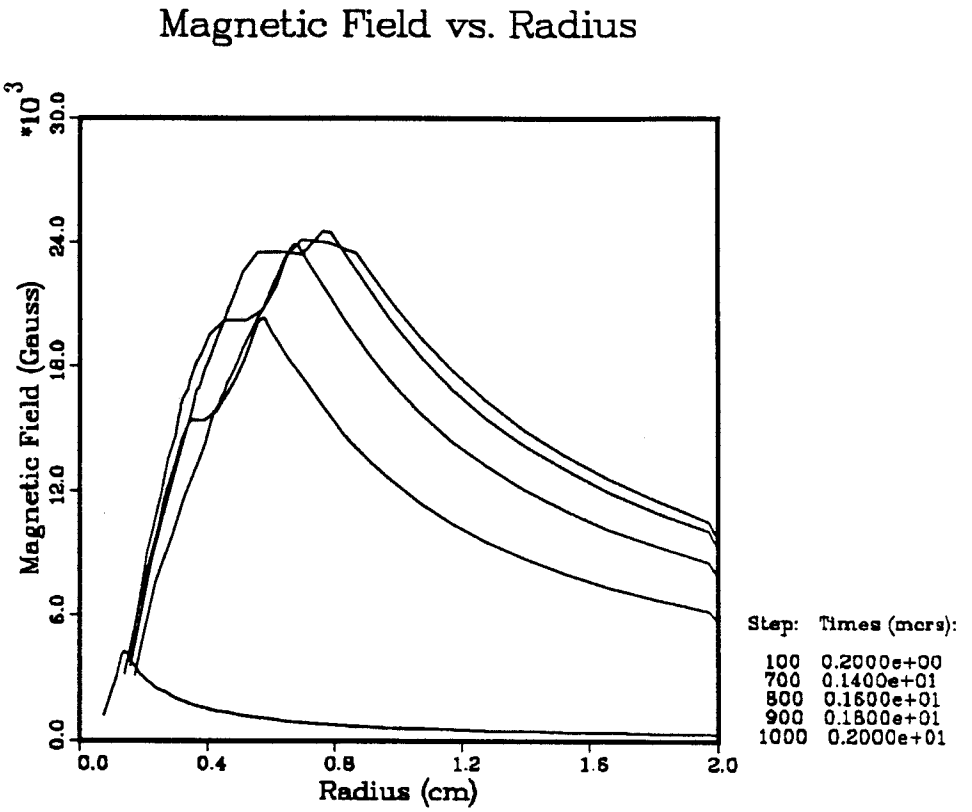

Figure 4.23: Magnetic Field profiles for nitrogen channel by ZPINCH.

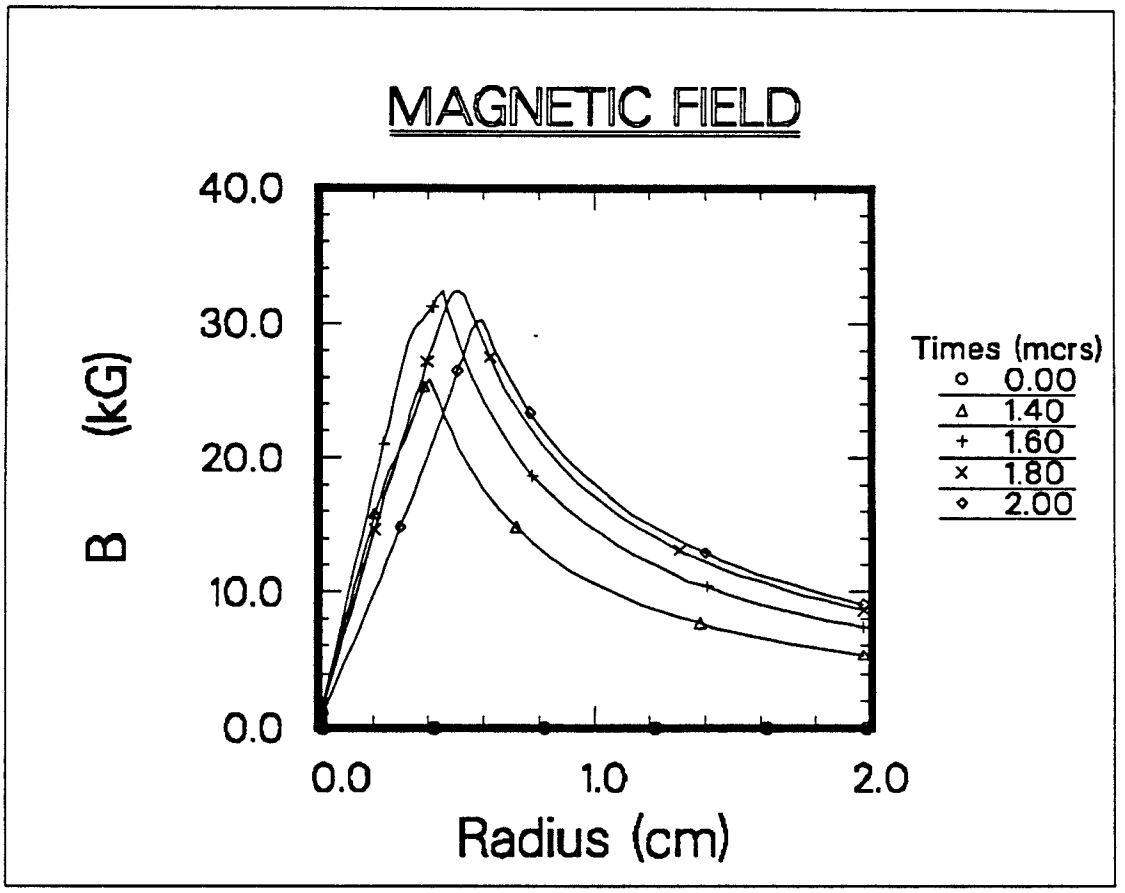

Figure 4.24: Magnetic Field profiles for nitrogen channel by ARMHD.

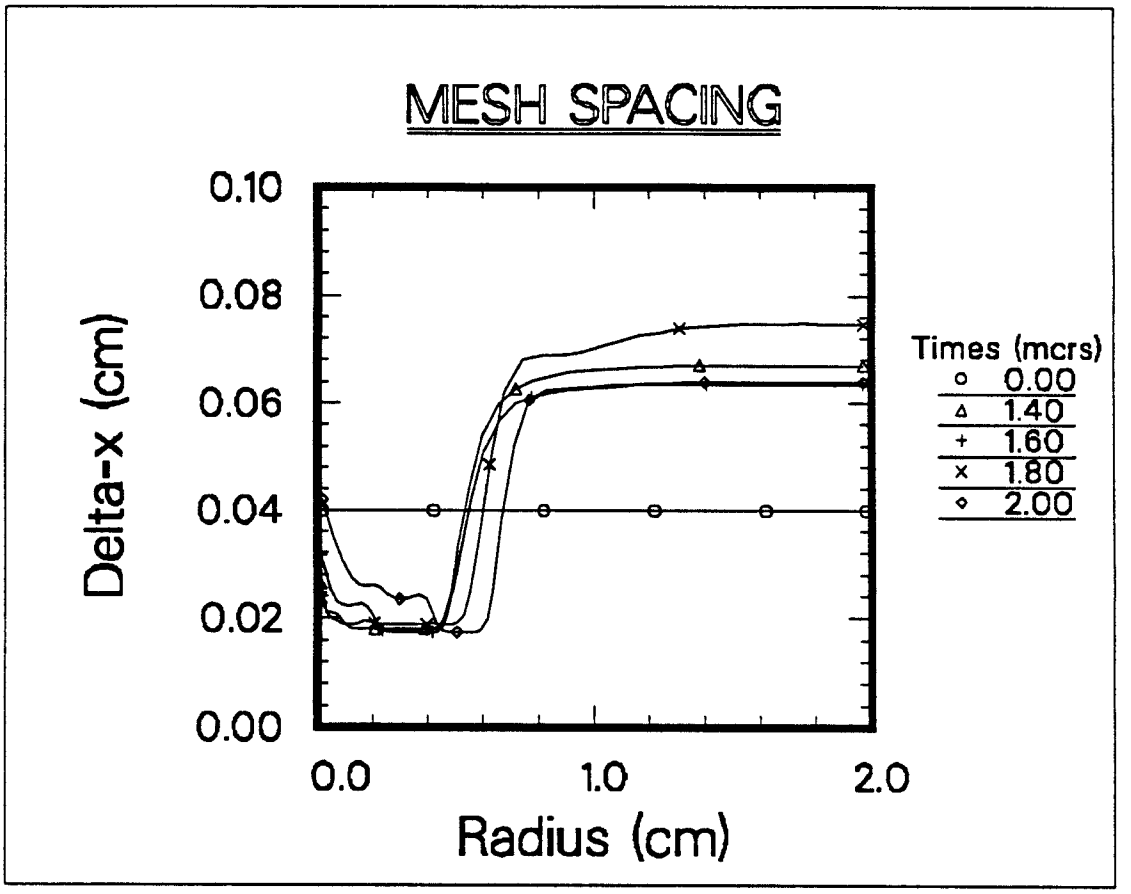

Figure 4.25: Mesh spacing for nitrogen channel by ARMHD.

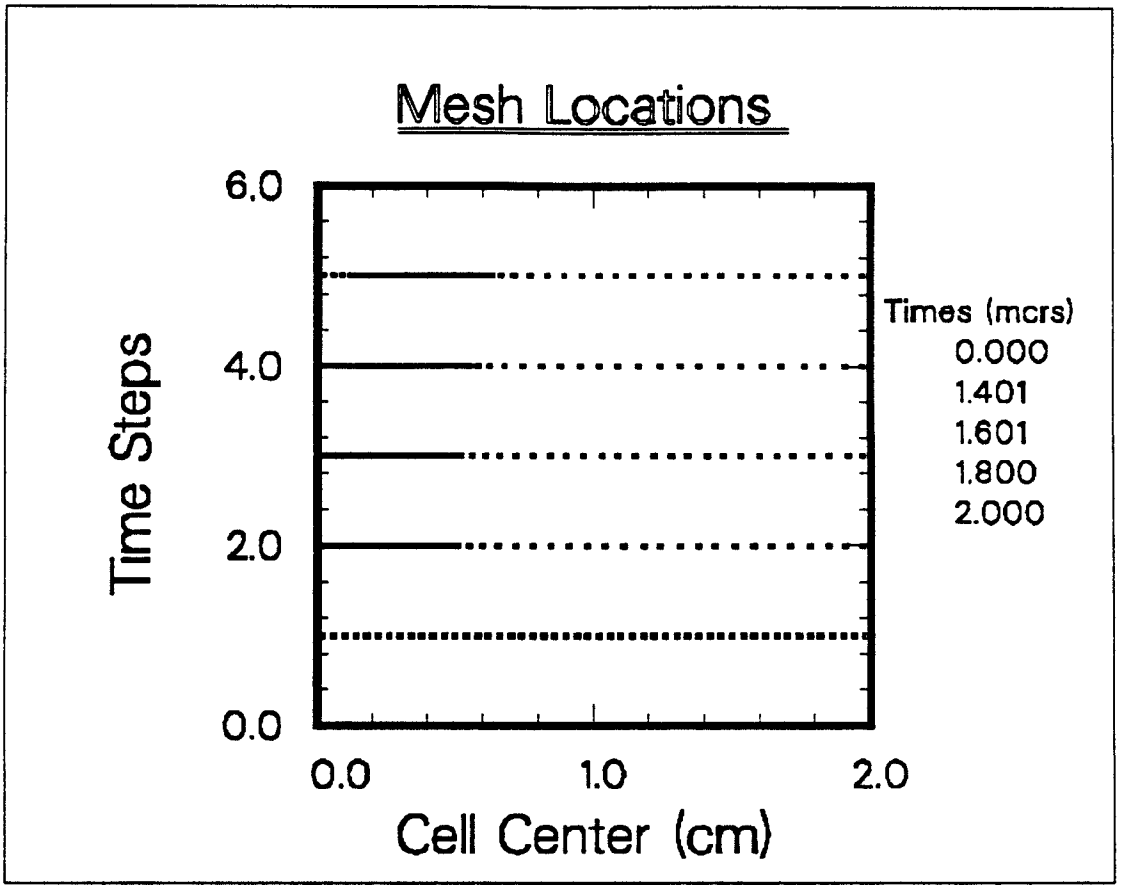

Figure 4.26: Mesh locations for nitrogen channel by ARMHD.

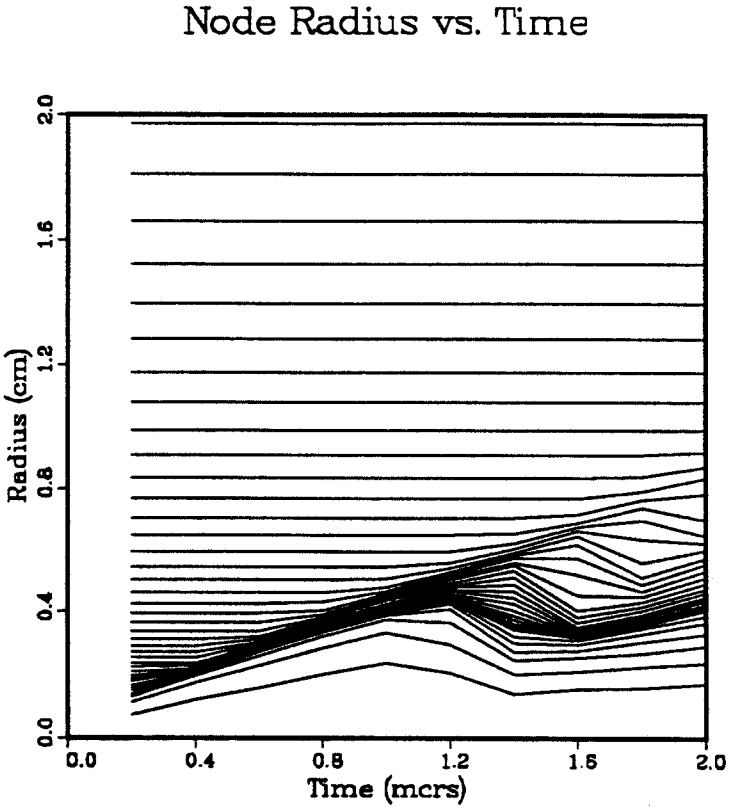

Figure 4.27: Mesh spacing for nitrogen channel by ZPINCH.

Chapter 5

Applications to LIBRA

The plasma channels for LIBRA must be consistent with both beam propagation parameters and the reactor chamber and diode design as specified in Table 1.1. Earlier studies of different cavity gases (argon, nitrogen, helium) indicated that the lower Z helium was most suitable for plasma channel formation.

Magnetohydrodynamic simulations using the multigroup diffusion approximation for radiative transfer indicated that the radiation had a great effect on the channel dynamics. Watrous noted that radiation diffusion from the hot channel center to the surrounding cold gas led to a premature expansion of the channel plasma with the required peak magnetic fields being unattainable. Watrous [14] observed this expansion in the channel for argon and nitrogen gases. This led Peterson to later conclude that helium was

the preferred cavity gas because it radiated so much less than the higher Z gases [78]. In this section we reexamine this issue and present what our radiation model predicts about the channel dynamics. The model is applied to argon and helium which are considered to be at opposite extremes of radiative properties. Both gases are considered to have the same mass density ($2.37 \times 10^{-5} g/cm^3$) and a series of simulations is done to learn the differences in hydrodynamics, magnetohydrodynamics and radiation hydrodynamics of these two gases. To present the differences we will start with simple hydrodynamics, then move to magnetohydrodynamics and finally to radiation magnetohydrodynamics.

The idea of starting from the simplest situation and moving up to the rather realistic and thus complex case is to identify the various events affecting the channel dynamics. This will basically give us an understanding of how to control the competing effects in the system to come up with an **optimized channel.** A picture of what simulations and assumptions are done along the way for an understanding of the magnetic and radiative effects on channel creation for LIBRA is given here in Table 5.1. The adaption functions are chosen as *temperature* and *momentum* and the relative weight coefficients R_α and R_β are 0.3 and 0.1 respectively. Those simulations and their outcome will be presented in the following sections.

Table 5.1: A list of MHD and RMHD simulations for LIBRA channels.

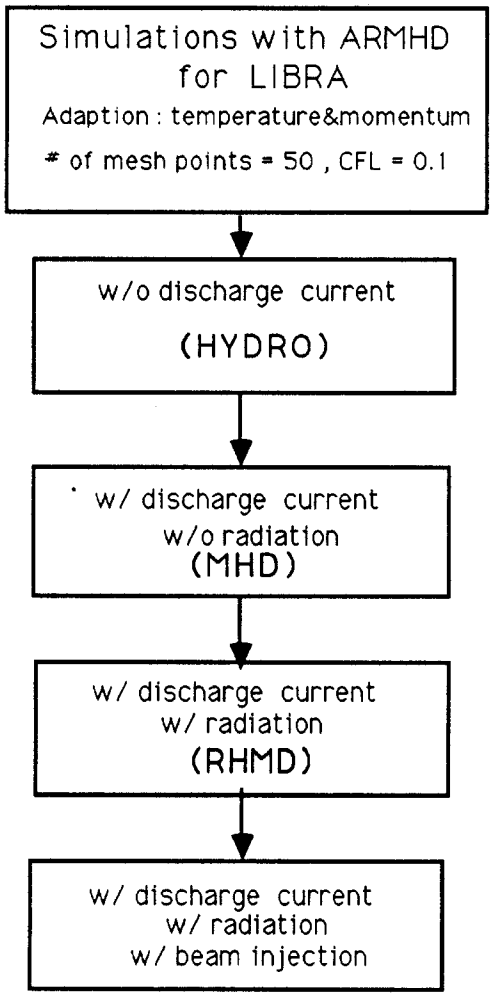

Table 5.2: A hydrodynamic comparison of argon and helium at 1.8μs.

Gas type	Channel radius (cm)	Channel front velocity (cm/sec)	Temperature at center (eV)
Argon	0.5	5.6×10^4	0.63
Helium	0.8	1.5×10^5	0.4

5.1 MHD Simulations of Plasma Channels

Argon's atomic weight ($40g/mol$) is ten times higher than that of helium ($4g/mol$). Therefore, working with the same mass density to preserve consistency we let the number densities be $3.5 \times 10^{17} cm^{-3}$ for argon and $3.5 \times 10^{18} cm^{-3}$ for helium. The simulations specified in the first two steps in Table 5.1 are done here for argon and helium. A comparison of pure hydrodynamic properties resulting from the first set of simulations is given in Table 5.2. Also Figures 5.1 and 5.2 show the mass density profiles at various times to better illustrate the hydro motion.

Due to the difference in number densities, helium has a higher initial pressure and this ends up making helium channels expand faster. Whether this difference is going to be effective in the RMHD picture is yet to be seen.

When the discharge current is applied to the plasma, it heats up the channel through ohmic heating. The ohmic heating forces the channel to

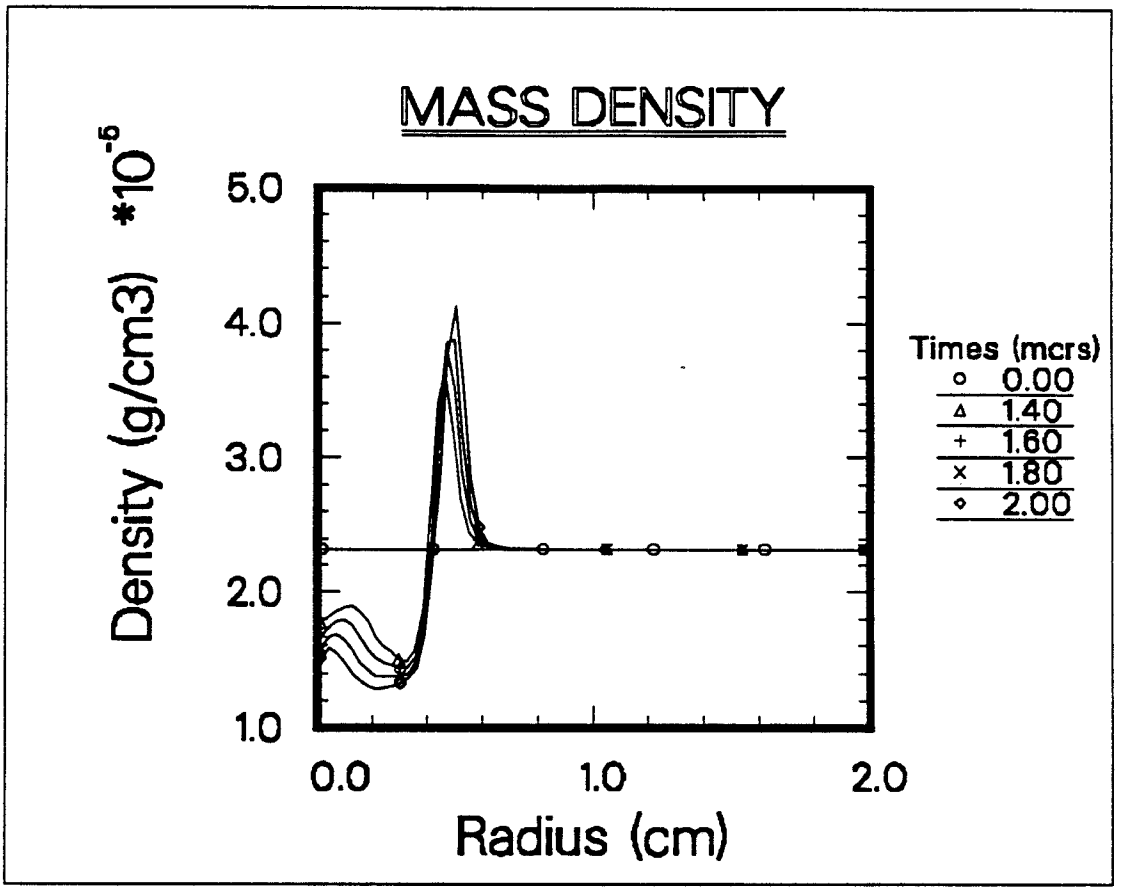

Figure 5.1: Mass density profiles for argon channel with no discharge current.

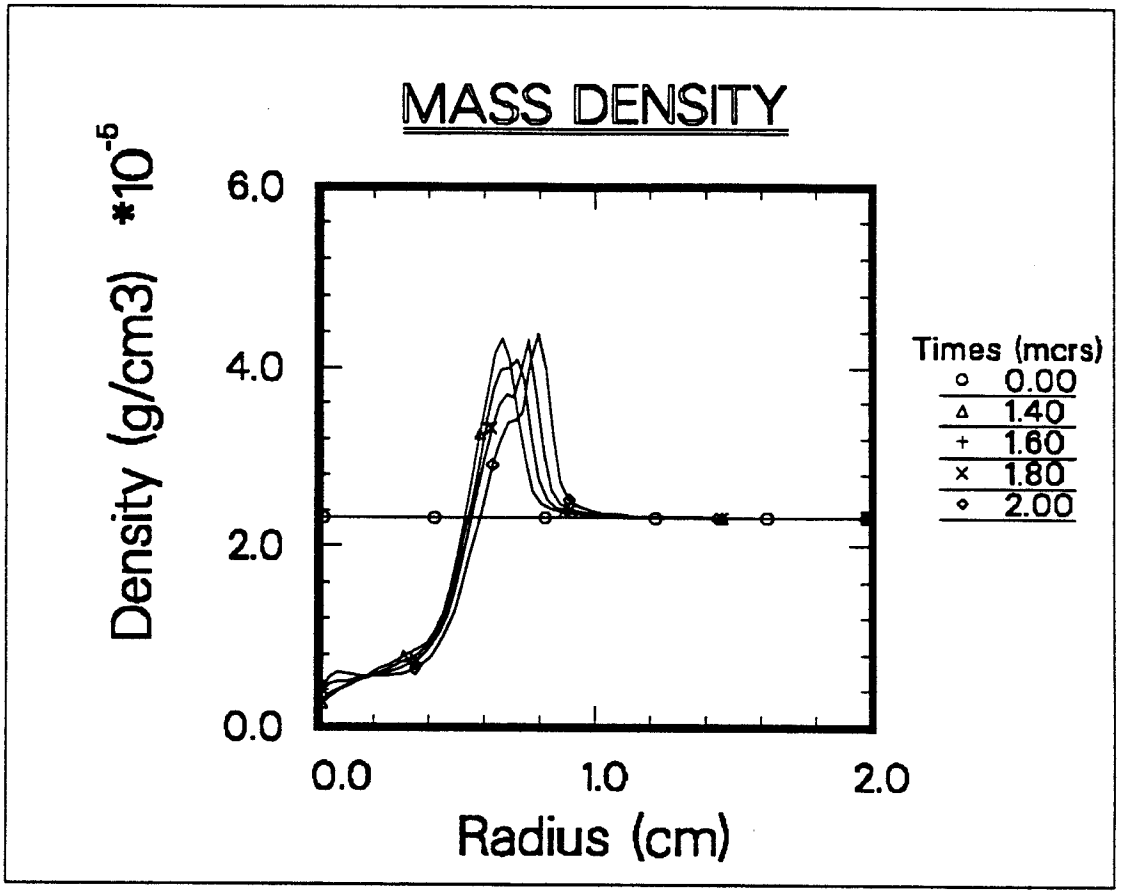

Figure 5.2: Mass density profiles for helium channel with no discharge current.

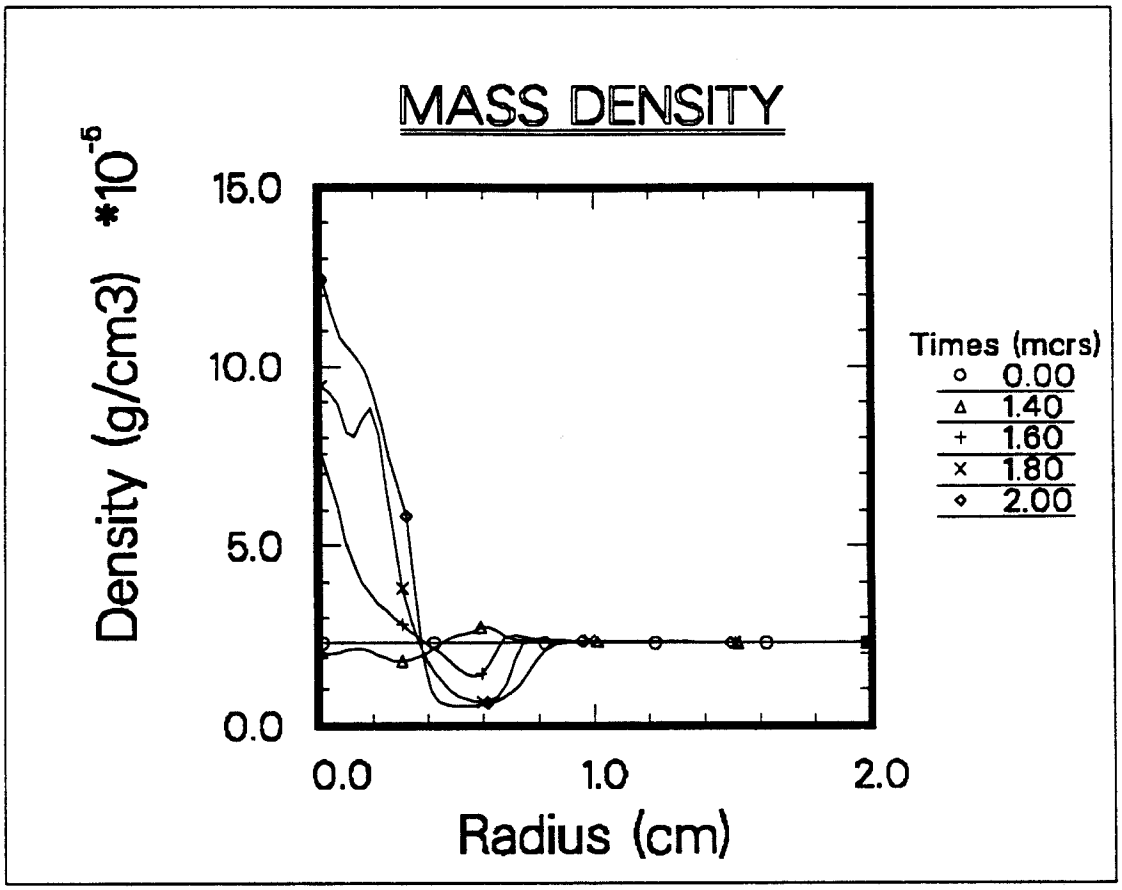

Figure 5.3: Mass density profile for magnetized argon channel.

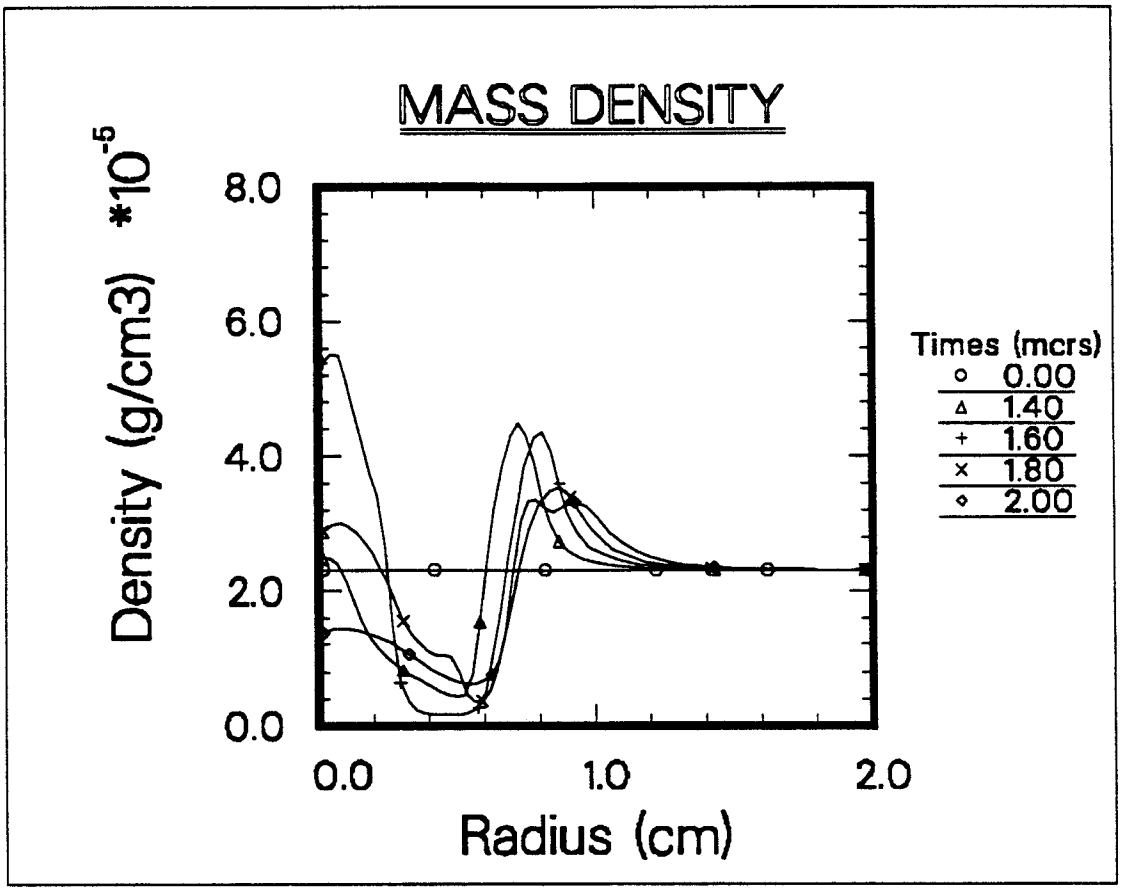

Figure 5.4: Mass density profile for magnetized helium channel.

expand. The balance between the gas pressure gradient and the magnetic force is what directs the expansion or pinching. When the discharge current rise time is short, the ohmic heating rate is high. If the time at which the plasma turns this ohmic heating into expansion is long, because the magnetic field is already diffused in to its full scale it will cause pinching. For a discharge current shown in Figure 4.1 both argon and helium feel the pinching as seen in Figures 5.3 and 5.4. However, for the discharge current in Figure 3.16 which has a longer rise time, the argon gas feels no pinching at all.

The main goal of comparing the gas types for channel formation here is to investigate their responses to the radiation field. The results mentioned above are provided to make clear how argon and helium act with the artificial removal of radiation. The outcome is presented with Table 5.3. The argon gas is slower in response to the magnetic force, and thus is subject to pinching for most of the time as seen in Figure 5.3. The rarefaction behind the pinching point causes the area of current flow to become wider. From the table and mass density profiles we also notice that the channel radius grows faster in the presence of the magnetic field compared to the rate at which it expands without it. Therefore the argon channel with a discharge current in it has a greater radius when compared to the helium channel, despite the fact the situation was the reverse for the pure hydrodynamic case. Because the magnetic field at the channel radius goes as $(2I_d/cr)$, its value is

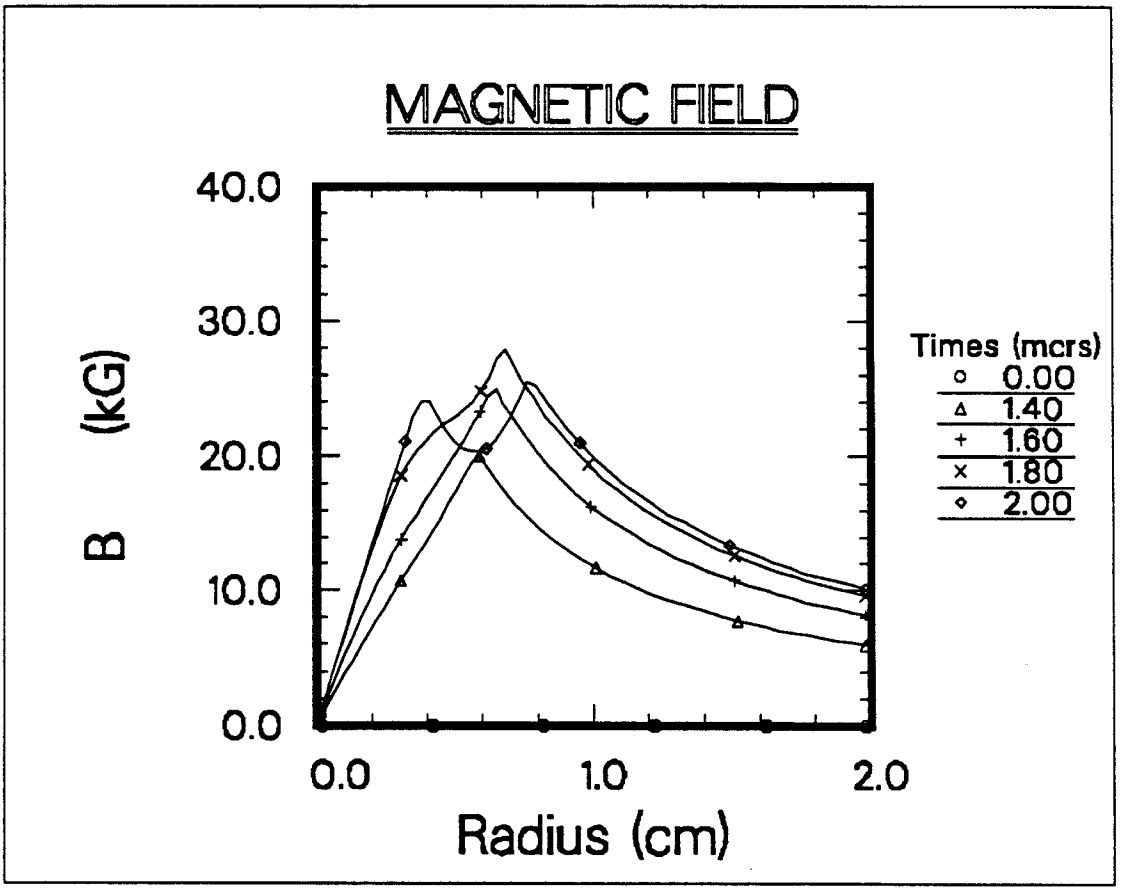

Figure 5.5: Magnetic field profile for argon channel.

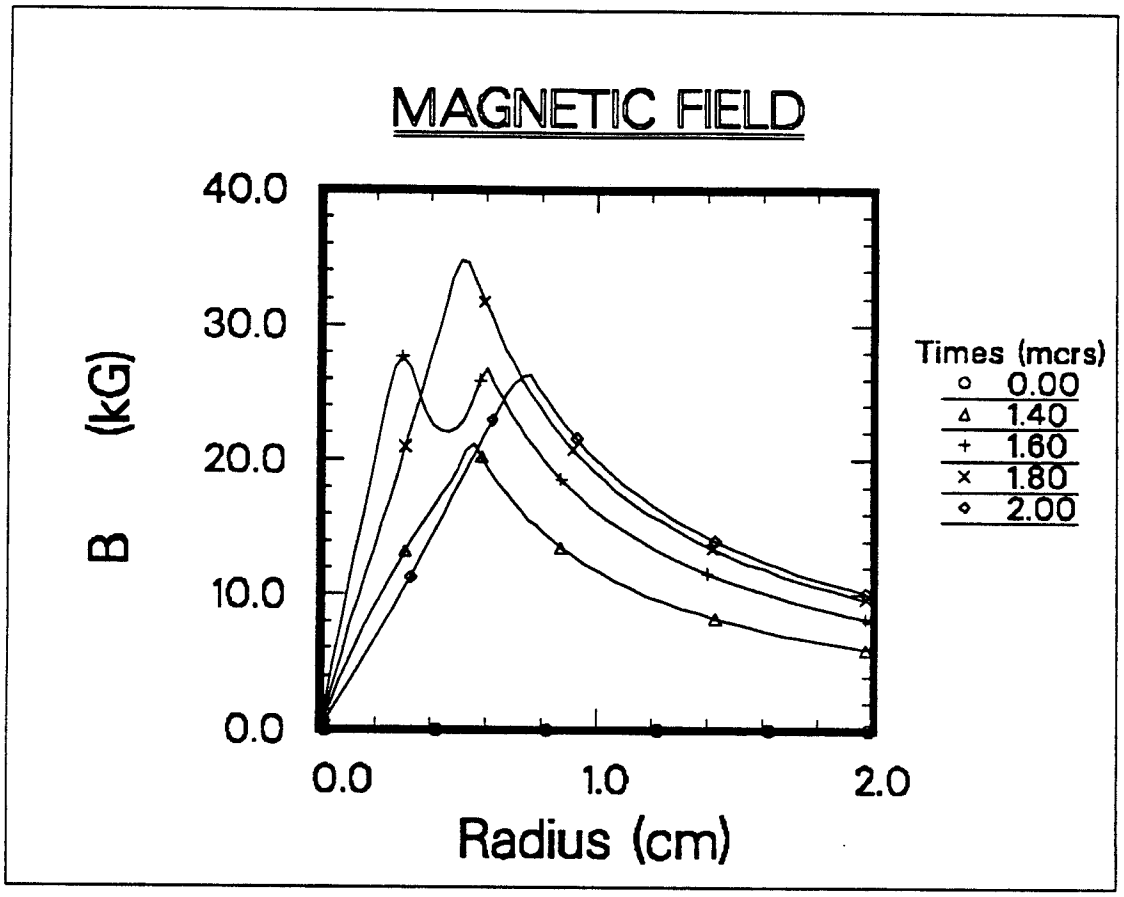

Figure 5.6: Magnetic field profile for helium channel.

Table 5.3: Argon and helium channels at time 1.8μs with and without discharge current.

Gas type	Discharge current	Channel radius (cm)	Peak B-Field (kG)
Argon	No	0.5	0.0
	Yes	0.7	28.0
Helium	No	0.8	0.0
	Yes	0.5	35.0

lower for larger distances. At time 1.8 microseconds, right before the beam injection, it rises up to 28 kG at $r_c = 0.7cm$ for argon, whereas it is 35 kG at $r_c = 0.5cm$ for helium. A detailed illustration of the magnetic field at various times is given in Figure 5.5-6. This clearly makes helium the better choice for channel designs.

5.2 RMHD Simulations of Plasma Channels

As opposed to the classical diffusion approximation of the radiation field, we have chosen to work with the photon transport equation Eq.3.12. A discrete ordinate S_N method is used to numerically solve this equation. The angular dependence is exact to an extent defined by the number of angles N in the

method: the more angles used, the better the results. For linear angular dependency this equation turns to a diffusion equation.

In fact, the basic assumption underlying the diffusion, or Eddington, description of radiation transfer is that the specific intensity $I(\mathbf{r}, \nu, \mathbf{\Omega}, t)$ can be represented by the first two terms in a spherical harmonic expansion. That is, it is assumed that

$$I(\mathbf{r}, \nu, \mathbf{\Omega}, t) = \frac{1}{4\pi} I_0(\mathbf{r}, \nu, t) + \frac{3}{4\pi} \mathbf{\Omega} \cdot \mathbf{I}_1(\mathbf{r}, \nu, t) \tag{5.1}$$

where I_0 and $\mathbf{I}_1$ are found by integrating Eq.5.1 over angle

$$I_0 = \int_{4\pi} d\mathbf{\Omega} I(\mathbf{r}, \nu, \mathbf{\Omega}, t) = c e_R$$

$$\mathbf{I}_1 = \int_{4\pi} d\mathbf{\Omega} \mathbf{\Omega} I(\mathbf{r}, \nu, \mathbf{\Omega}, t) = \mathbf{F}$$

Using the assumed form of I, the divergence of the pressure tensor, Eq.3.8, may be found as

$$\nabla \cdot \vec{\mathbf{P}} = \frac{1}{3} \nabla e_R.$$

The first moment equation, Eq.3.9, then becomes

$$\frac{1}{c^2} \frac{\partial \mathbf{F}}{\partial t} + \frac{1}{3} \nabla e_R = \frac{1}{c} \int_0^\infty d\nu \int_{4\pi} d\mathbf{\Omega} \mathbf{\Omega} [\eta(\mathbf{r}, t, \mathbf{\Omega}, \nu) - \chi(\mathbf{r}, t, \mathbf{\Omega}, \nu) I(\mathbf{r}, t, \mathbf{\Omega}, \nu)]. \tag{5.2}$$

It is further assumed that a high collisional rate sets the properties of the matter in such a way as to establish a local thermodynamic equilibrium (LTE) by which the emission can be written as $\eta(\nu) = \eta_e(\nu) I(\nu, T)$ where

$\eta_e(\nu) = \kappa(\nu)(1 - e^{-h\nu/kT})$ with κ being the absorption coefficient. The moment equation becomes

$$\frac{1}{c^2}\frac{\partial \mathbf{F}}{\partial t} + \frac{1}{3}\nabla e_R = \frac{1}{c}(\eta_e - \chi)\mathbf{F}.$$

and therefore

$$\mathbf{F} = -\frac{c}{3(\eta_e - \chi)}\nabla e_R + \frac{1}{(\eta_e - \chi)}\frac{\partial \mathbf{F}}{\partial t}.$$

Ignoring the second term on the right, we get Fick's law

$$\mathbf{F} = -\frac{c}{3(\eta_e - \chi)}\nabla e_R = -D\nabla e_R \tag{5.3}$$

where D is the diffusion coefficient.

Using this relation in the zeroth moment equation, Eq.3.9, we find

$$\frac{\partial e_R}{\partial t} - \nabla \cdot D\nabla e_R = (\eta_e - \chi_e)e_R. \tag{5.4}$$

This is a diffusion equation and a common place approximation to what is known as the energy equation, Eq.3.9,

$$\frac{\partial e_R}{\partial t} + \nabla \cdot \mathbf{F} = \eta - c\chi e_R \tag{5.5}$$

as used in ARMHD. Note that Eq.5.5 above is not explicitly solved in ARMHD. The radiation energy density e_R is calculated from specific intensity $I(\nu, \Omega)$ by using Eq.3.8.

Numerical solutions always bring along some error due to discretization. The solution of the model equations (PDEs) here involves **discretization**

of 1) continuum functions (finite differencing), 2) direction angles (ordinate discretizing), and 3) opacities (group averaging). The error involved in discretization is numeric as opposed to the error with non-numeric approximations such as the diffusion approximation. The best possible answer is usually achieved if one uses as many number as possible for angles, mesh points and opacity groups. There is a limit to this set by either the cost or the capacity of the computer machinery. At the stage of our code development so far we have generally used six angles, fifty mesh points and twenty opacity groups. An average run time for that on a CRAY X-MP/48 is about five minutes. Runs with larger numbers (especially in mesh points and group numbers) are tried but only if needed.

Regarding RHD, the concern is rather about how accurately the emission and extinction are modelled in the equations. A typical emission and extinction profile for argon gas is shown in Figures 5.7-8. Note that lines (peaks) are too narrow to allow a good group averaging over the whole spectrum. Probably one needs more than twenty groups! One way of getting away with this is to divide the radiation transport problem into two parts. That is, the lines are taken out of the spectrum to allow a reasonable group averaging on the continuum part. The group averaged opacities are then used with the radiation transport equation to solve for the continuum intensity. The lines, on the other hand are handled with so-called *line transport* methods and this is added to the continuum part to come up with a total result for

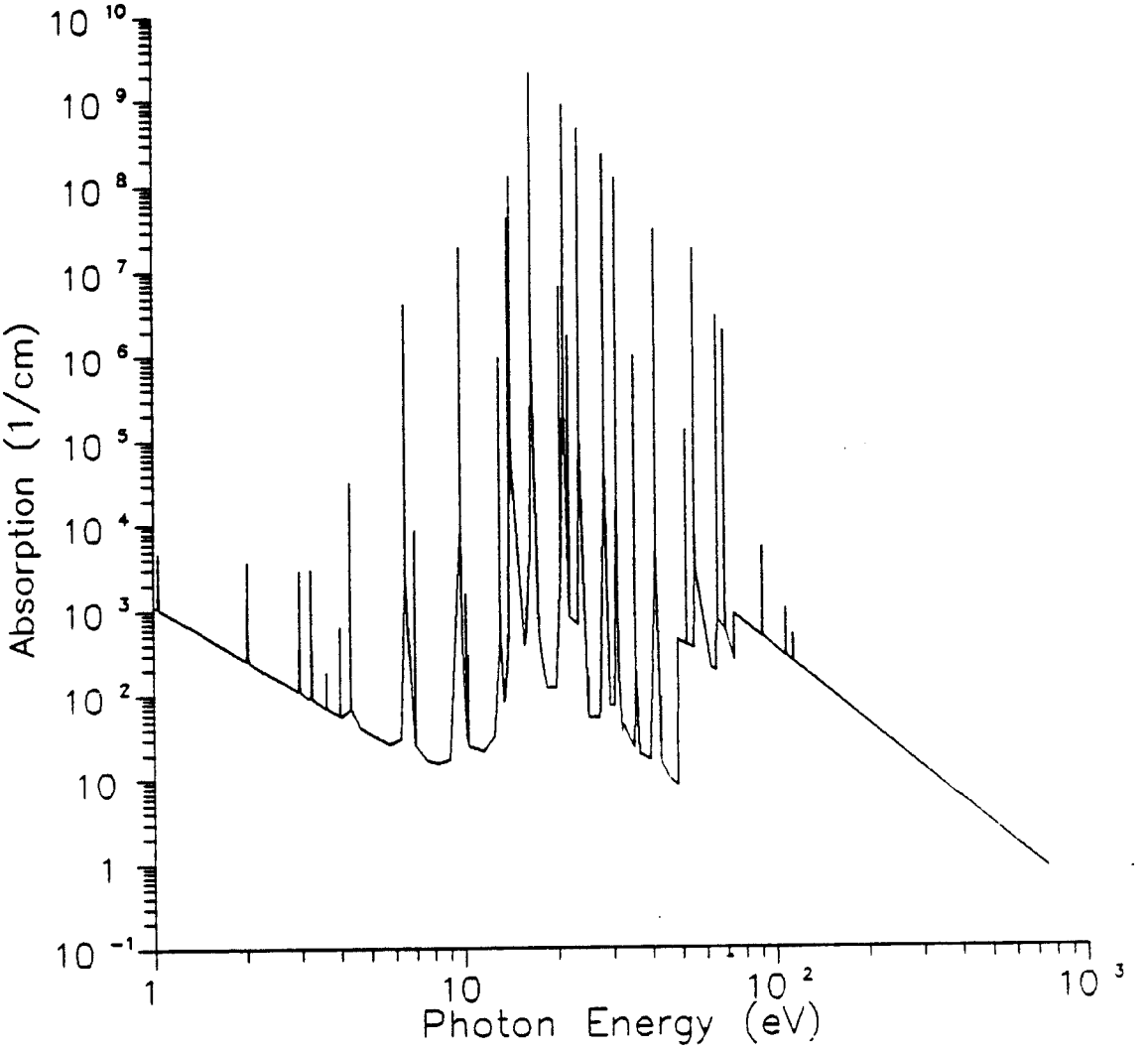

Figure 5.7: Absorption coefficient vs. photon energy for a plasma of 90 % Ar and 10 % Li. Temperature is 5 eV and density is $3 \times 10^{17} cm^{-3}$ [66].

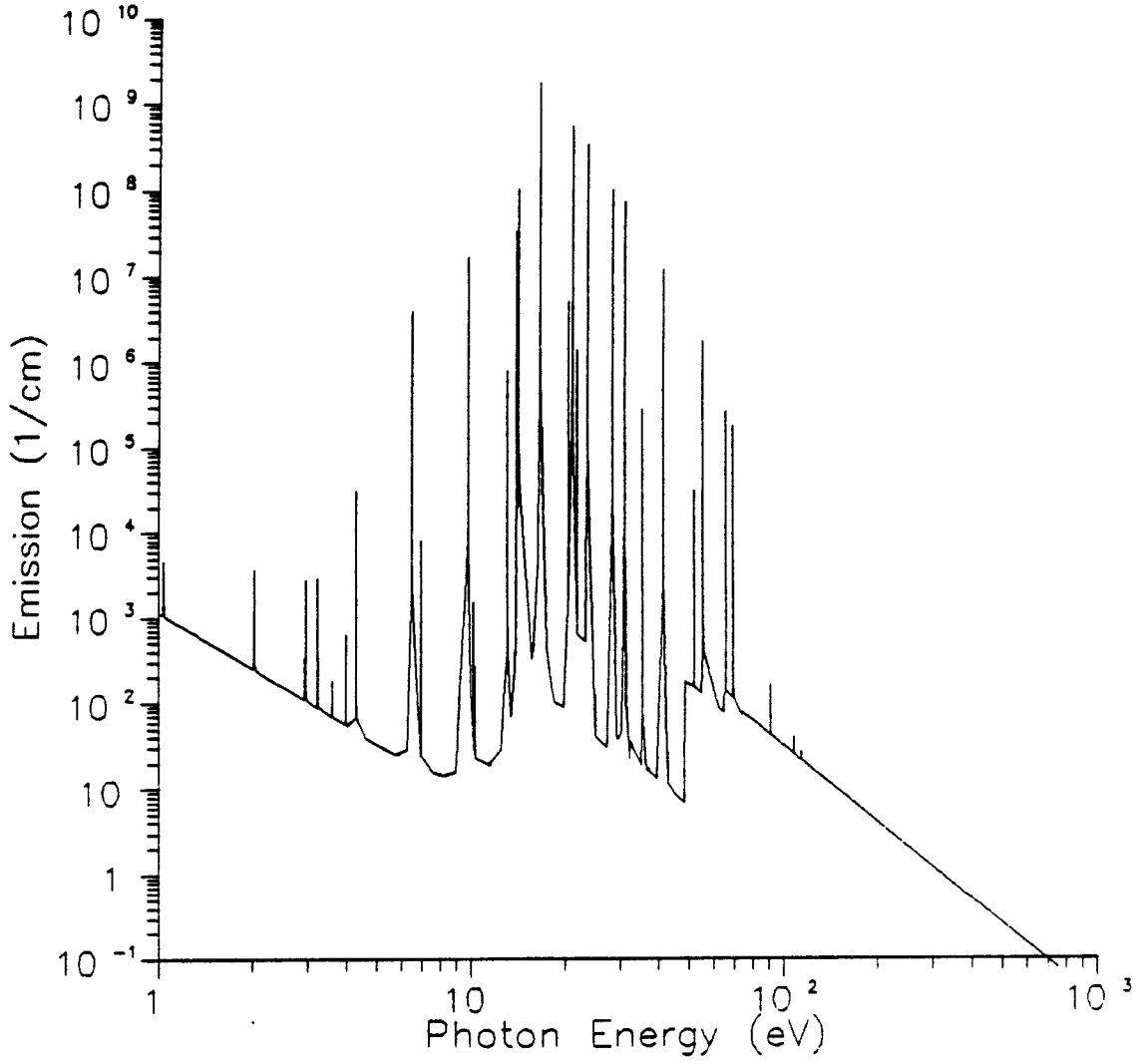

Figure 5.8: Emission coefficient vs. photon energy for a plasma of 90 % Ar and 10 % Li. Temperature is 5 eV and density is $3 \times 10^{17} cm^{-3}$ [66].

the radiation field.

Any line transport method will require an extensive studying and is beyond what we have developed here. In fact, there is an ongoing effort now by MacFarlane [79] in that area to be combined with what we have developed for the continuum part. Therefore the primary goal here is to treat the continuum radiation transport as well as possible and leave the lines out for a better approach *if not satisfied with the group averaging that considers the lines as well.*

As mentioned before, argon and helium are studied for posssible differences in their RHD nature. The channel simulation described in the previous section is repeated here with the radiation field included. The opacities are initially handled with 20 groups over the continuum spectrum (lines excluded). Figures 5.9 through 5.14 illustrate the results for argon and helium. Note that the radiation emitted at the center of the plasma leaves the channel without being significantly absorbed. In other words, both argon and helium seem to be *transparent* to the radiation and thus the radiation has no effects on the channel dynamics. That would also mean the plasma is optically thin and the radiation is highly anisotropic, violating the validity of the diffusion approximation in the region.

Whether this is the right answer, indicating that RHD is not important for z-pinch plasma channels, can not be said before investigating further. Knowing that we have excluded the lines in the opacity calculations, we

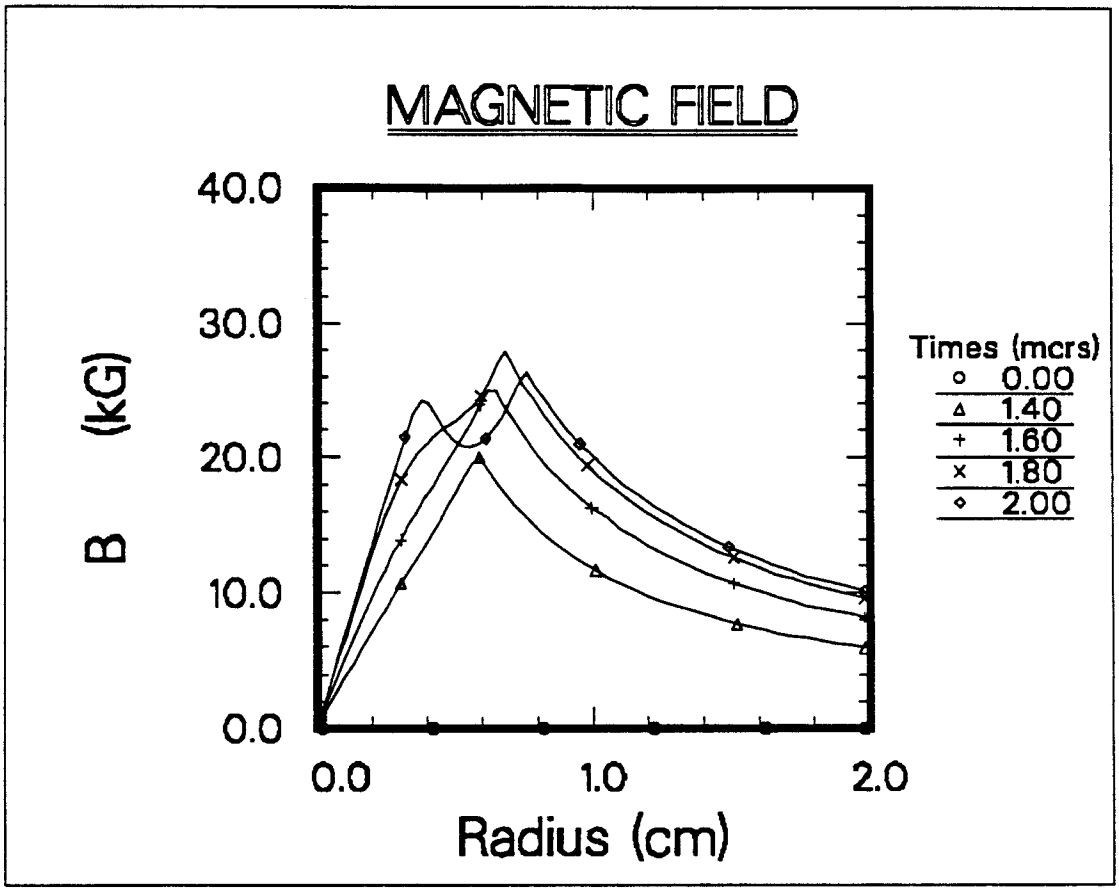

Figure 5.9: Magnetic field profiles for argon channel with 20 group continuum opacity calculations.

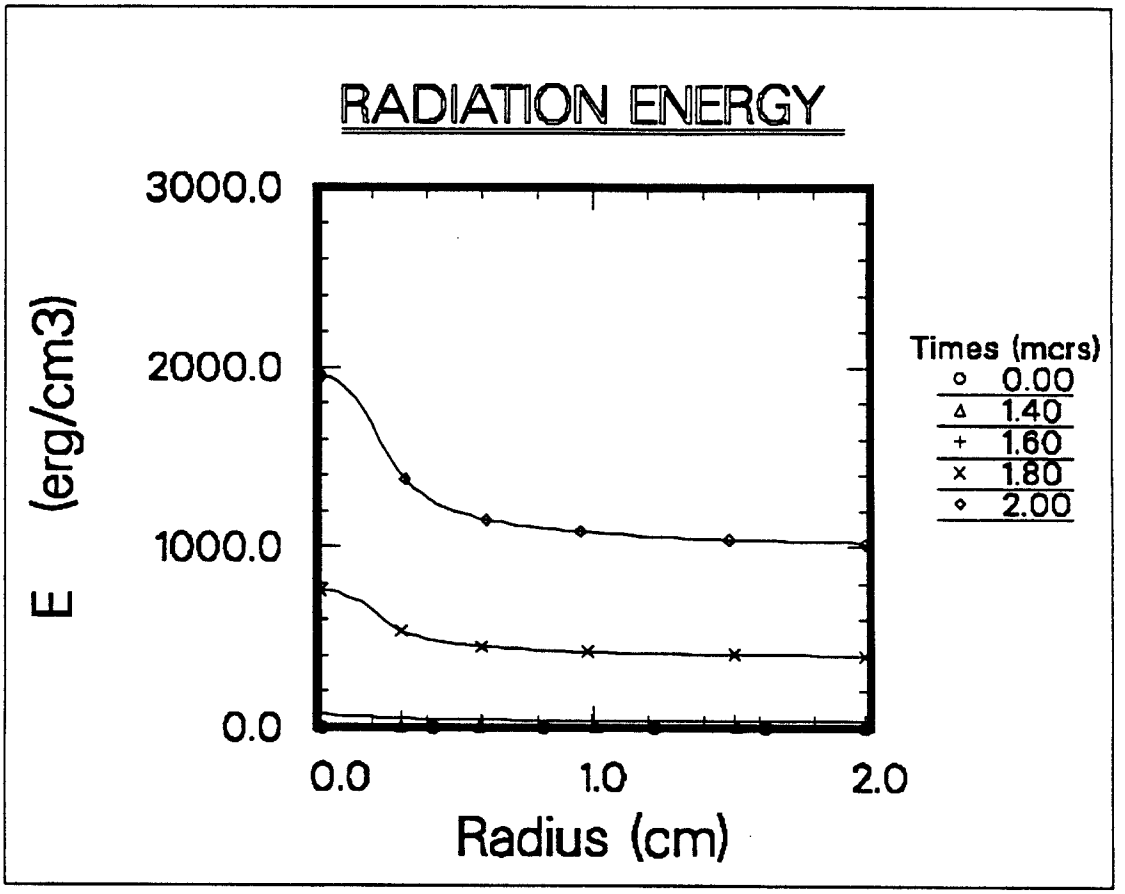

Figure 5.10: Radiation energy profiles for argon channel with 20 group continuum opacity calculations.

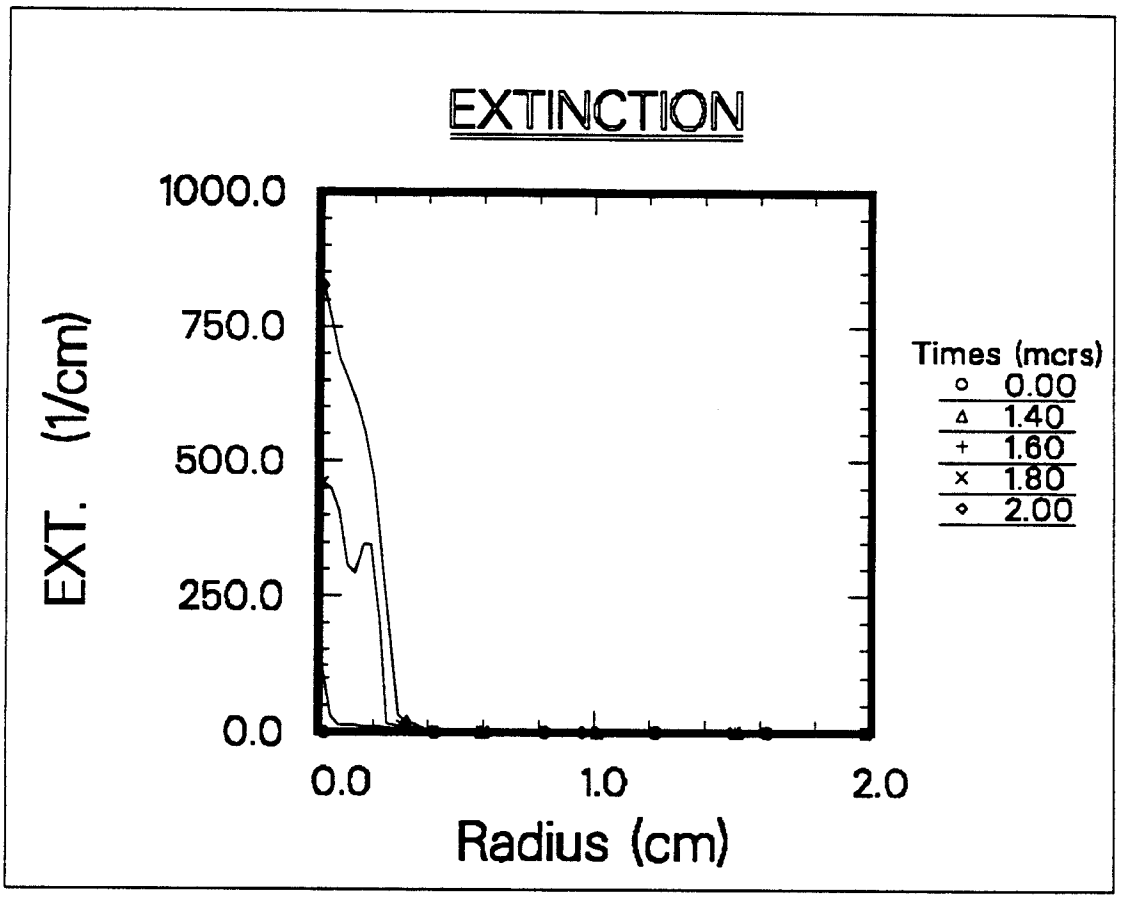

Figure 5.11: Extinction (absorption) for argon channel with 20 group continuum opacity calculations.

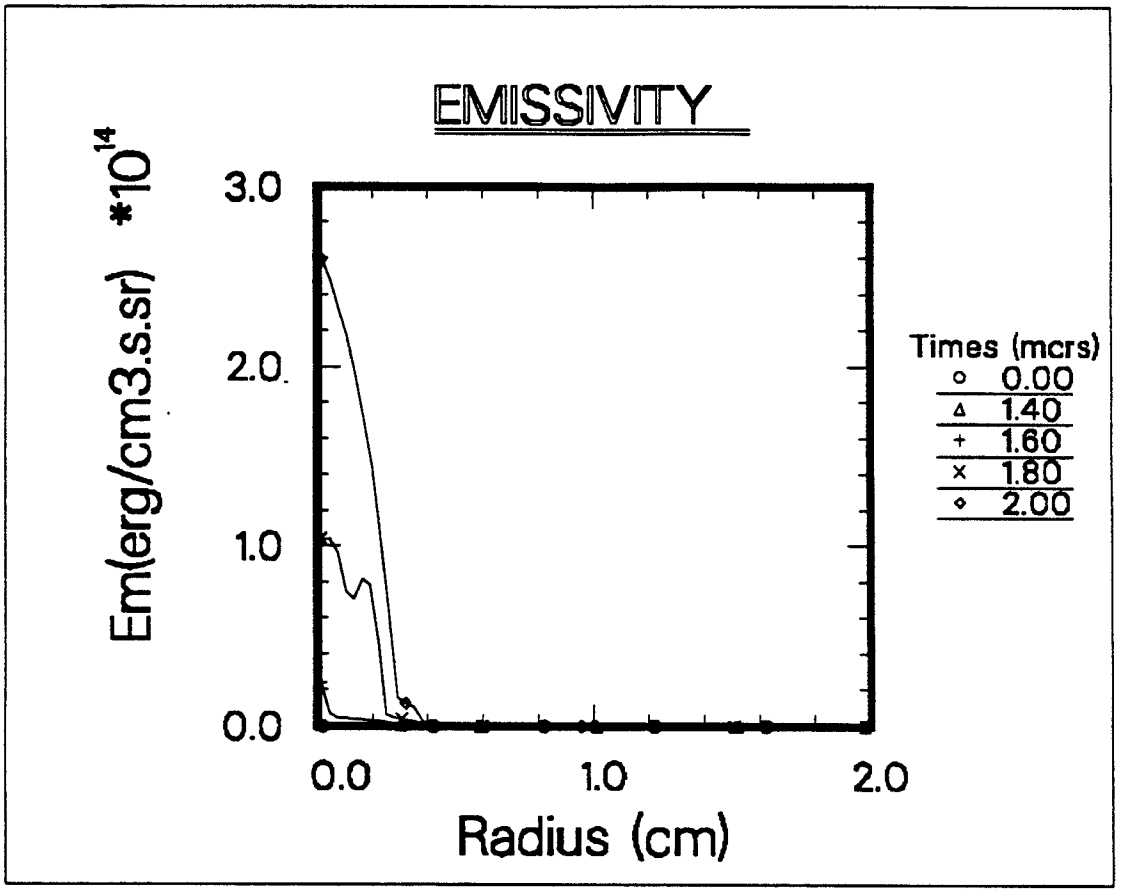

Figure 5.12: Emissivity profiles for argon channel with 20 group continuum opacity calculations.

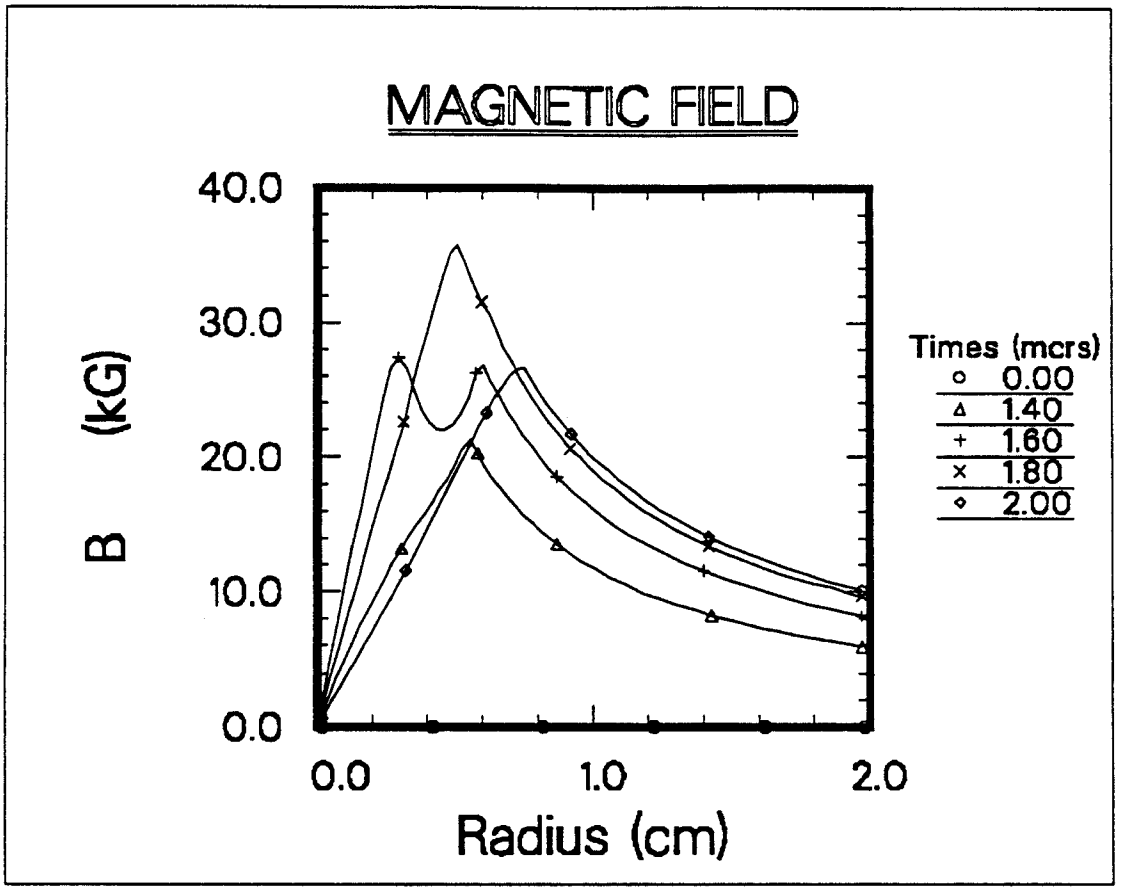

Figure 5.13: Magnetic field profiles for helium channel with 20 group continuum opacity calculations.

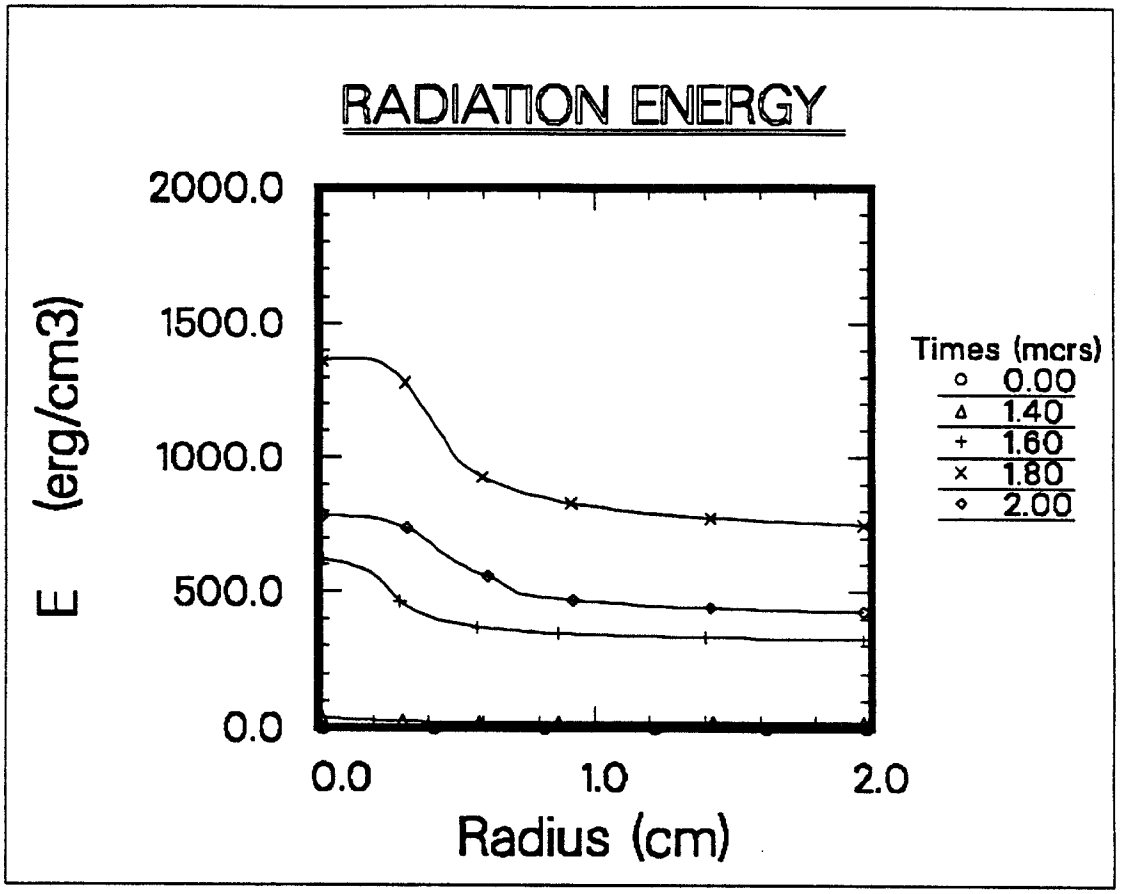

Figure 5.14: Radiation energy profiles for helium channel with 20 group continuum opacity calculations.

should get back to that point and run the same case with the lines included. Figures 5.15 through 5.20 illustrate the results again for 20 groups. Both emission and extinction (absorption) profiles show higher values this time just simply because of the line inclusion. They are highly temperature dependent. The radiation field is much higher at the center again due to high line emission and it drops rather sharply at the channel edge. The main reason for that drop is the high absorption caused by the temperature drop.

The degree to which the reabsorption at the channel edge plays an important role varies for helium and argon. It causes a far more significant heating for argon that responds in turn with a further expansion in the channel. That, of course, leads to a degradation in the peak magnetic field. Helium radiates about ten times less than argon and thus has fewer lines to make a difference between a calculation with and without lines.

The inclusion of lines resulted in a high degree of absorption and therefore introduced a diffusion-like phenomena of radiation transfer which should not be taken without suspicion. The same problem should be indeed run for more opacity groups, particularly with argon gas. Figures 5.21 through 5.22 illustrate the results for 80 groups. By introducing more groups we canceled to a degree the overestimation of lines as was for the 20-group case. The indication with 80-group results is that there seems to be a shift toward the continuum results. That trend could be taken seriously to see the borderline between ignoring and not ignoring the lines. A possible effort, at least for

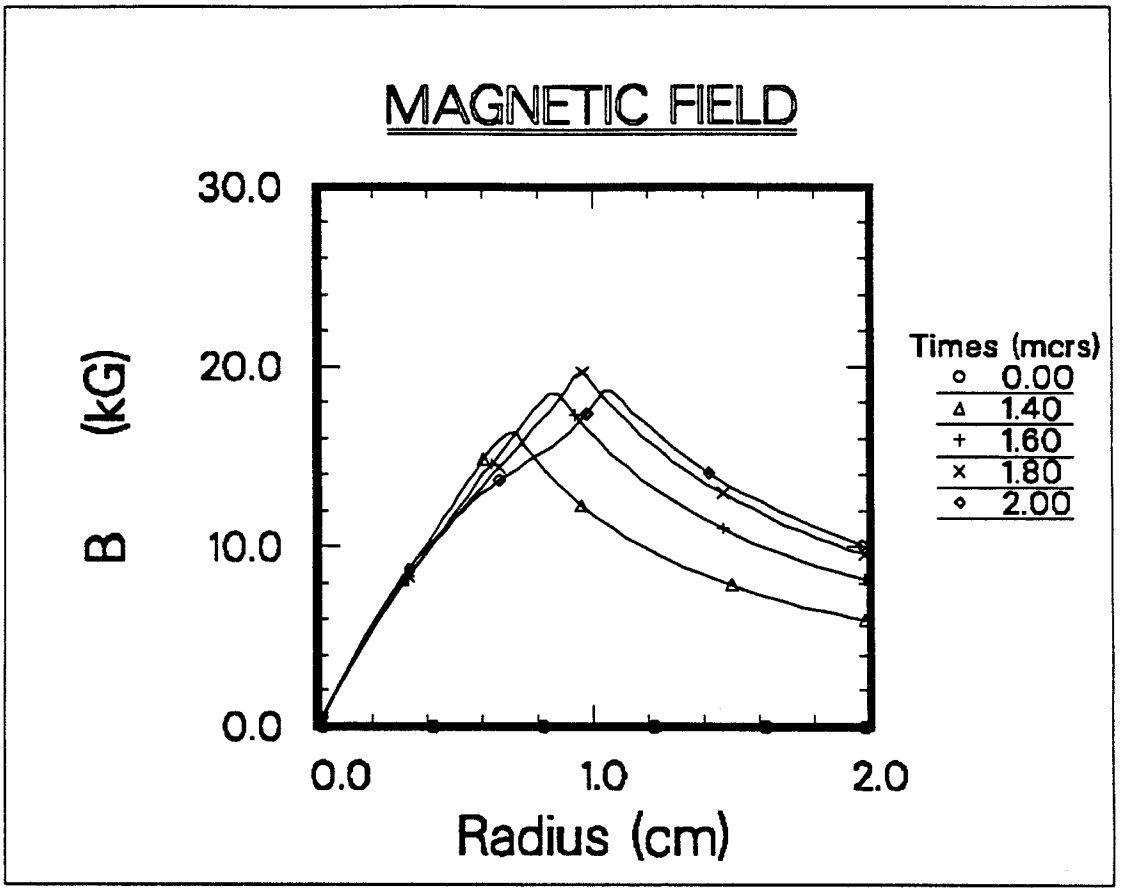

Figure 5.15: Magnetic field profiles for argon channel with 20 group continuum+lines opacity calculations.

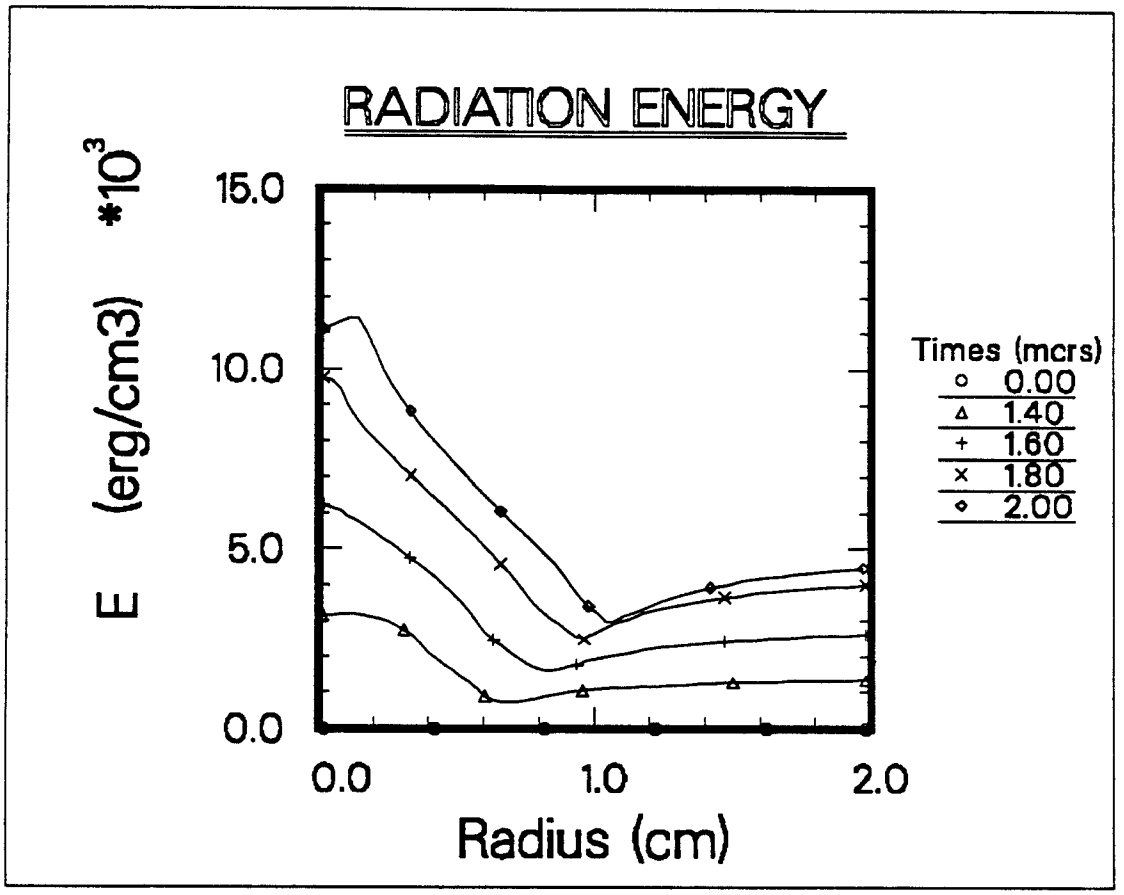

Figure 5.16: Radiation energy profiles for argon channel with 20 group continuum+lines opacity calculations.

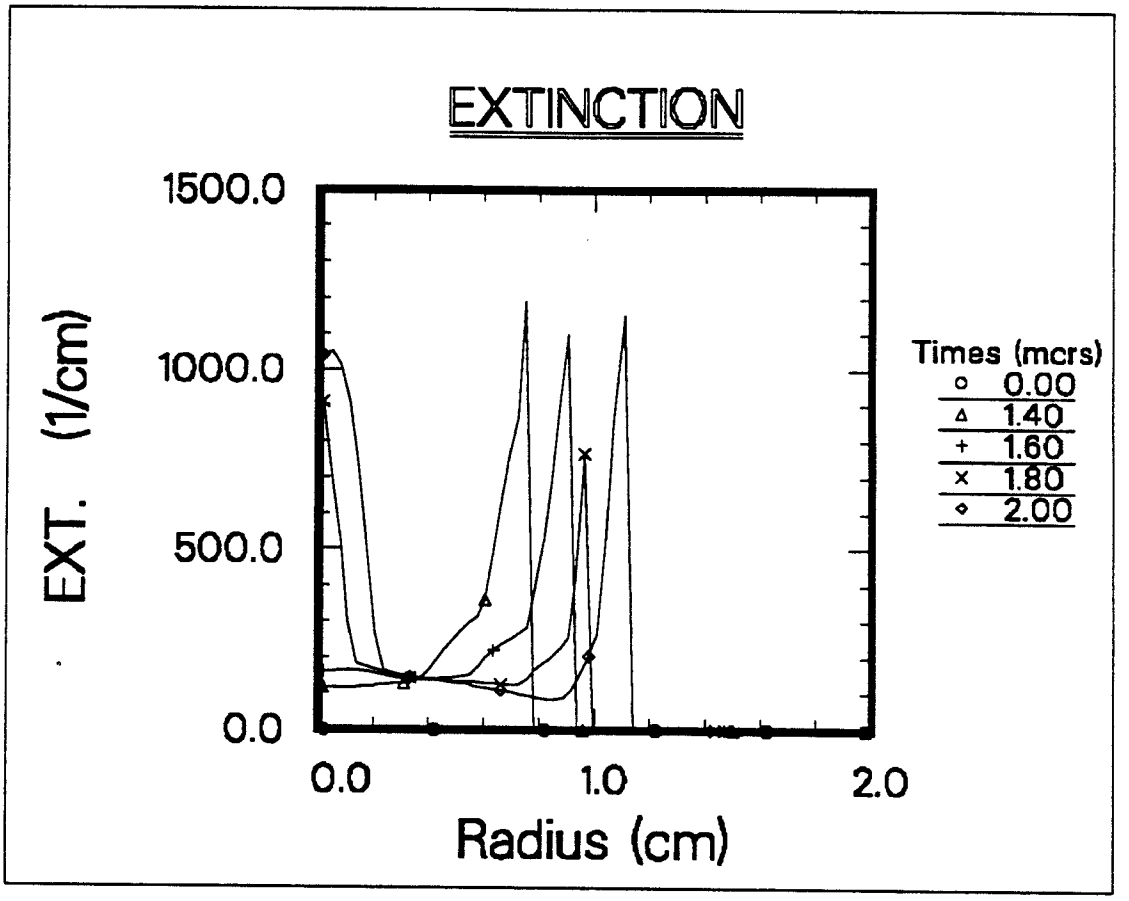

Figure 5.17: Extinction (absorption) for argon channel with 20 group continuum+lines opacity calculations.

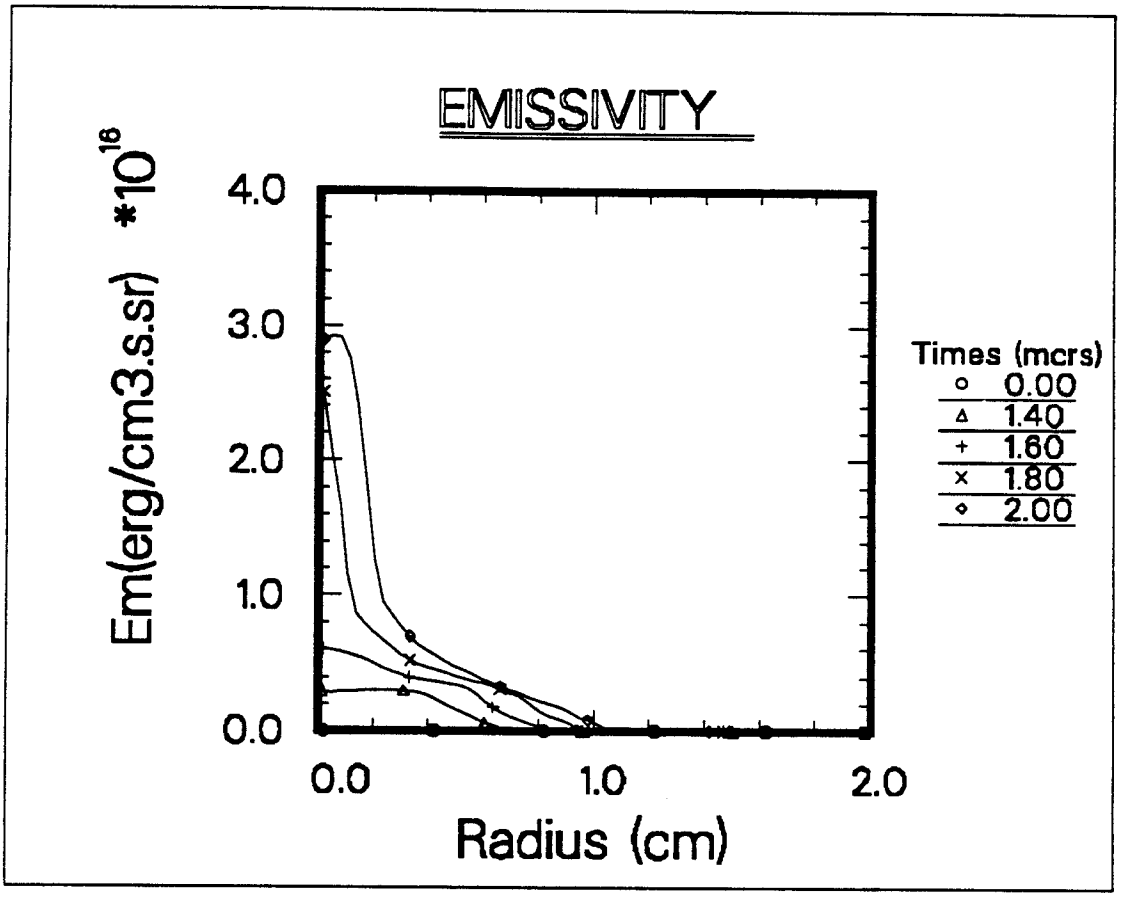

Figure 5.18: Emissivity profiles for argon channel with 20 group continuum+lines opacity calculations.

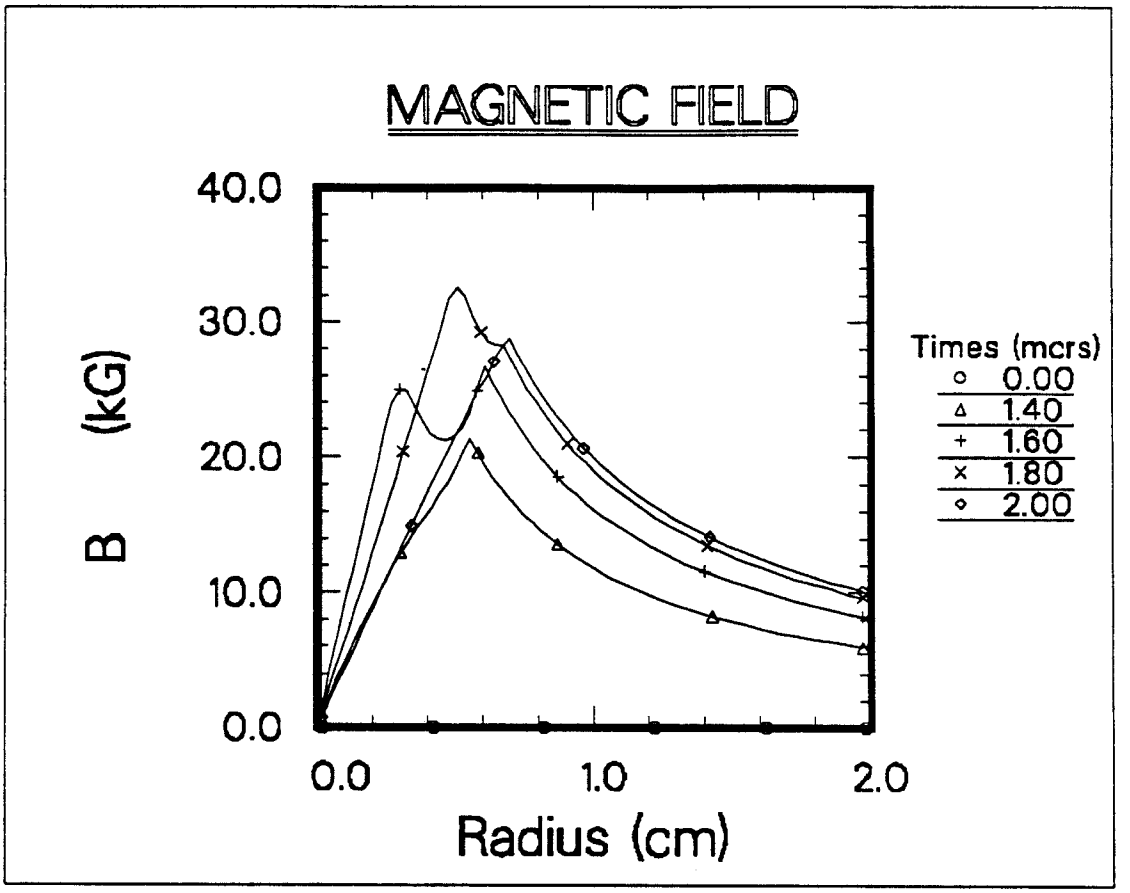

Figure 5.19: Magnetic field profiles for helium channel with 20 group continuum+lines opacity calculations.

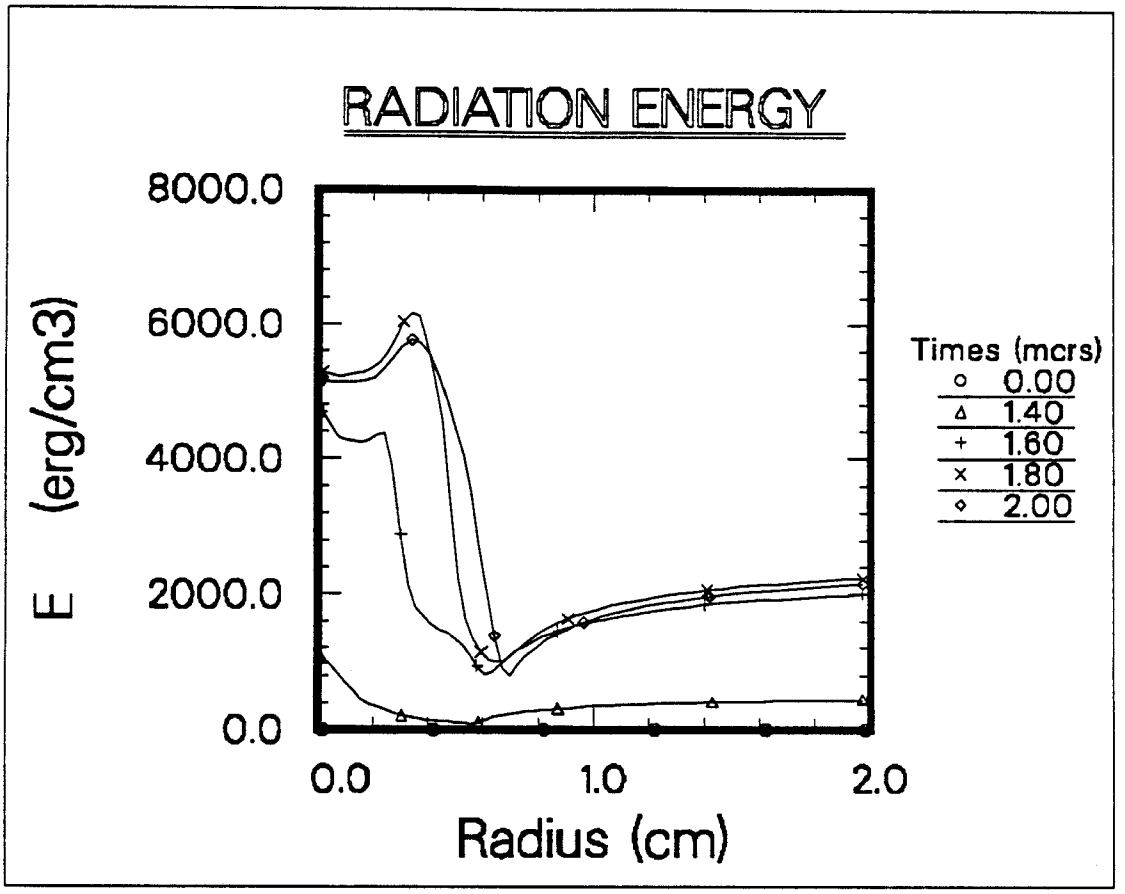

Figure 5.20: Radiation energy profiles for helium channel with 20 group continuum+lines opacity calculations.

Table 5.4: Simulation results vs the number of opacity groups (argon).

Case	# of opacity groups	Peak B-Field value (kG)	Channel radius (cm)	Temperature at center (eV)
continuum				
0	20	26.5	0.75	9.0
1	80	26.5	0.75	9.0
cont.+ lines				
2	160	22.6	0.84	7.0
3	80	21.3	0.94	6.4
4	20	18.5	1.08	4.8

the time being, is shown in Figures 5.23 through 5.25 for which the number of opacity groups is 160.

The increase in the number of opacity groups is making a difference in the results. This is especially true when lines are accounted for and it should be tested for the continuum case too. Therefore the continuum run has been repeated for 80 groups too. Table 5.4 compares the channel radius and its magnetic field at a time of 1.8 microseconds for 20, 80 and 160 group opacity based cases. The expansion in channel radius is attributed to the reabsorption at the channel edge of radiation emitted from the inner region. Case 4 as mentioned before presents a diffusion-like transport of the radiation

which is obviously far from the real answer. The radiation field drops fast in the channel up to the channel edge as shown in Figure 5.20. A rather different profile is observed with case 2 which is similar to case 1 indicating that the correct description of the phenomena occuring in the channel is not a diffusion but rather an anisotropic transport event.

The exact answer to these simulations as far as RHD is concerned may require many more groups and therefore will not be further searched simply because argon is not a main concern for the moment and also the self-consistent line transport study is underway now by colleagues. This will eventually provide a benchmark calculation to determine the viability of including lines in the multigroup formalism. Simulations with more groups is possible but will require far more computer time (hours) than is reasonable to spend on this problem.

5.3 Beam Propagation and Energy Losses

5.3.1 Current Neutralization

A transport channel is required to current neutralize the beam so that the beam is protected from a number of damaging instabilities, in particular the filamentation instability [42]. In other words, the beam's own magnetic field should be neutralized so that it does not cause pinching to itself. The idea of creating the transport channel with an ionized medium (plasma) is basically

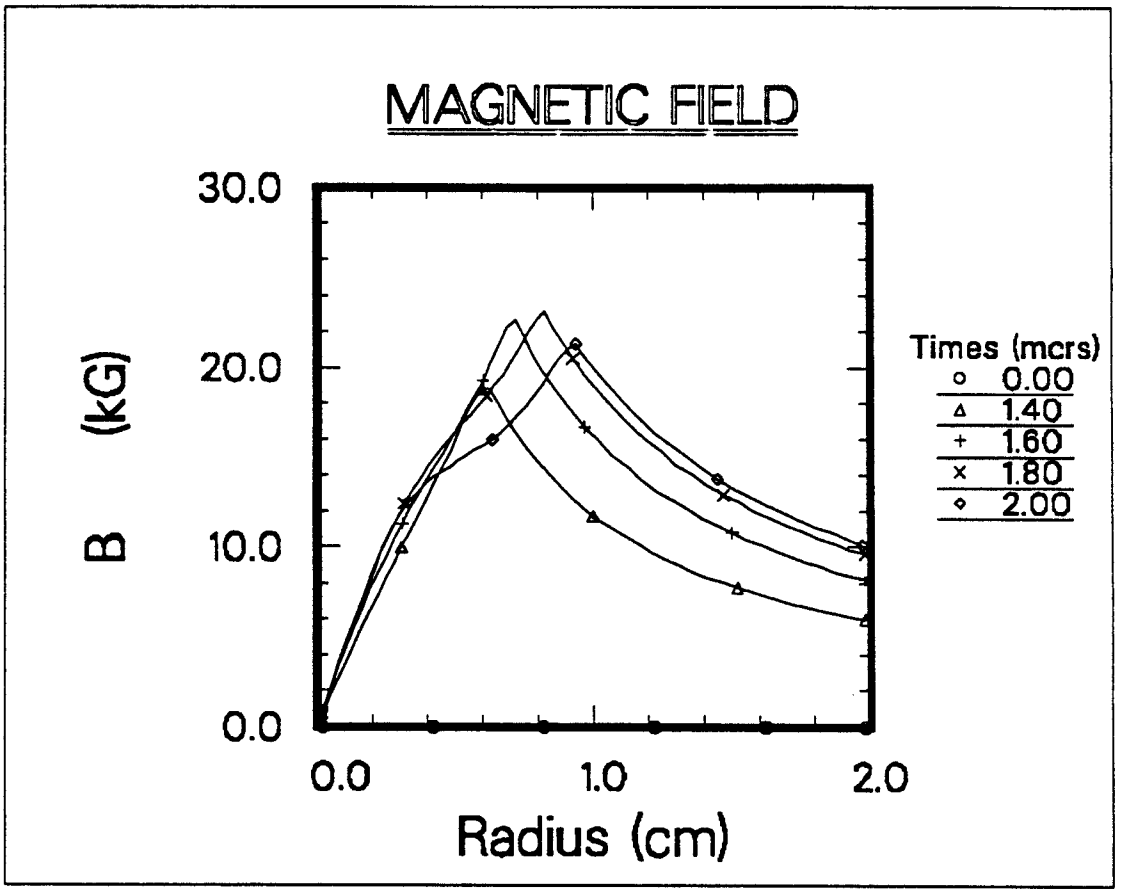

Figure 5.21: Magnetic field profiles for argon channel with 80 group continuum+lines opacity calculations.

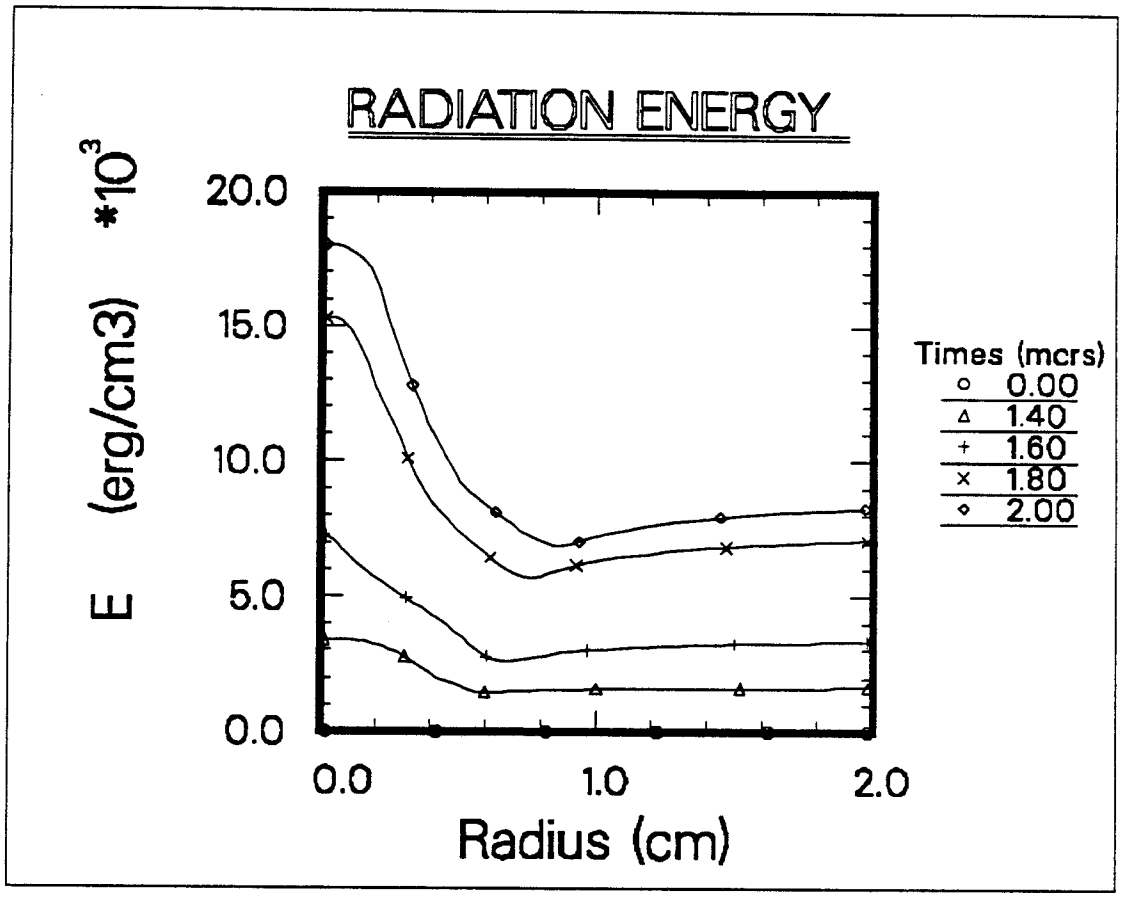

Figure 5.22: Radiation energy profiles for argon channel with 80 group continuum+lines opacity calculations.

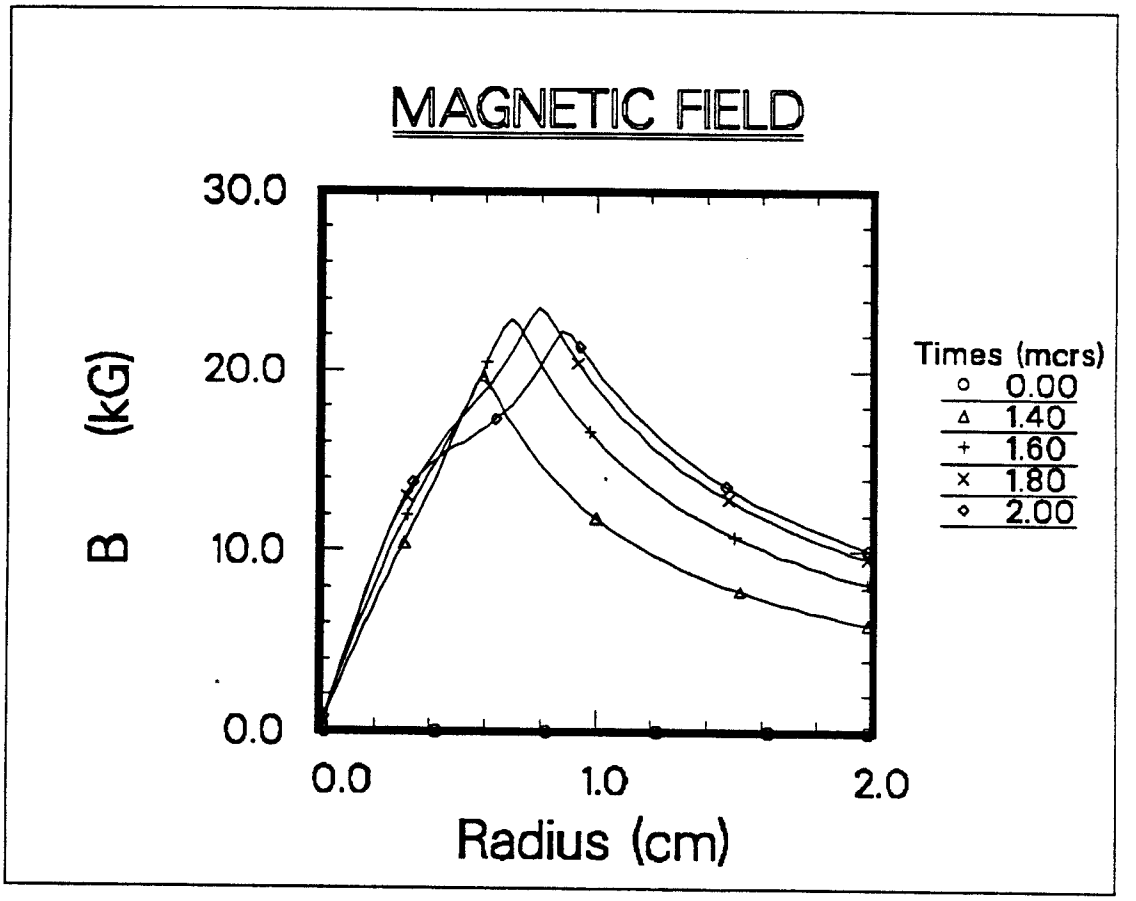

Figure 5.23: Magnetic field profiles for argon channel with 160 group continuum+lines opacity calculations.

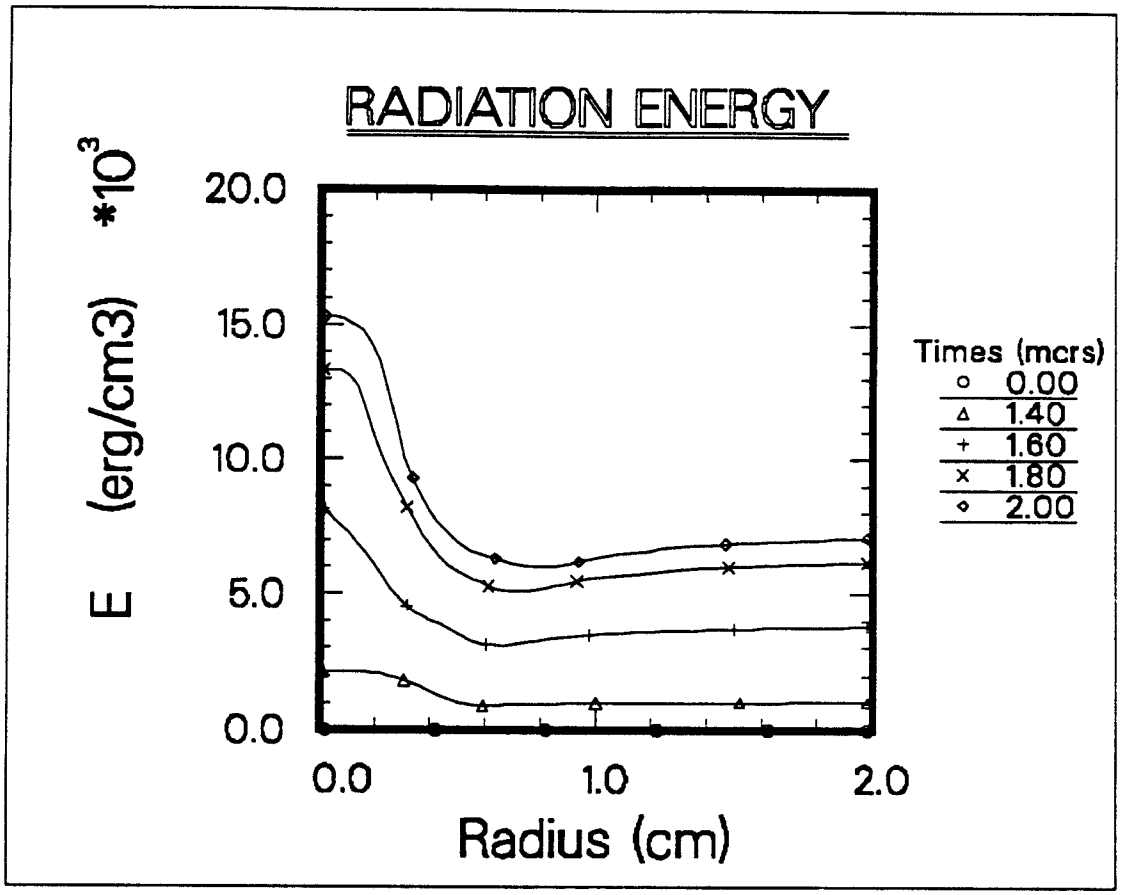

Figure 5.24: Radiation energy profiles for argon channel with 160 group continuum+lines opacity calculations.

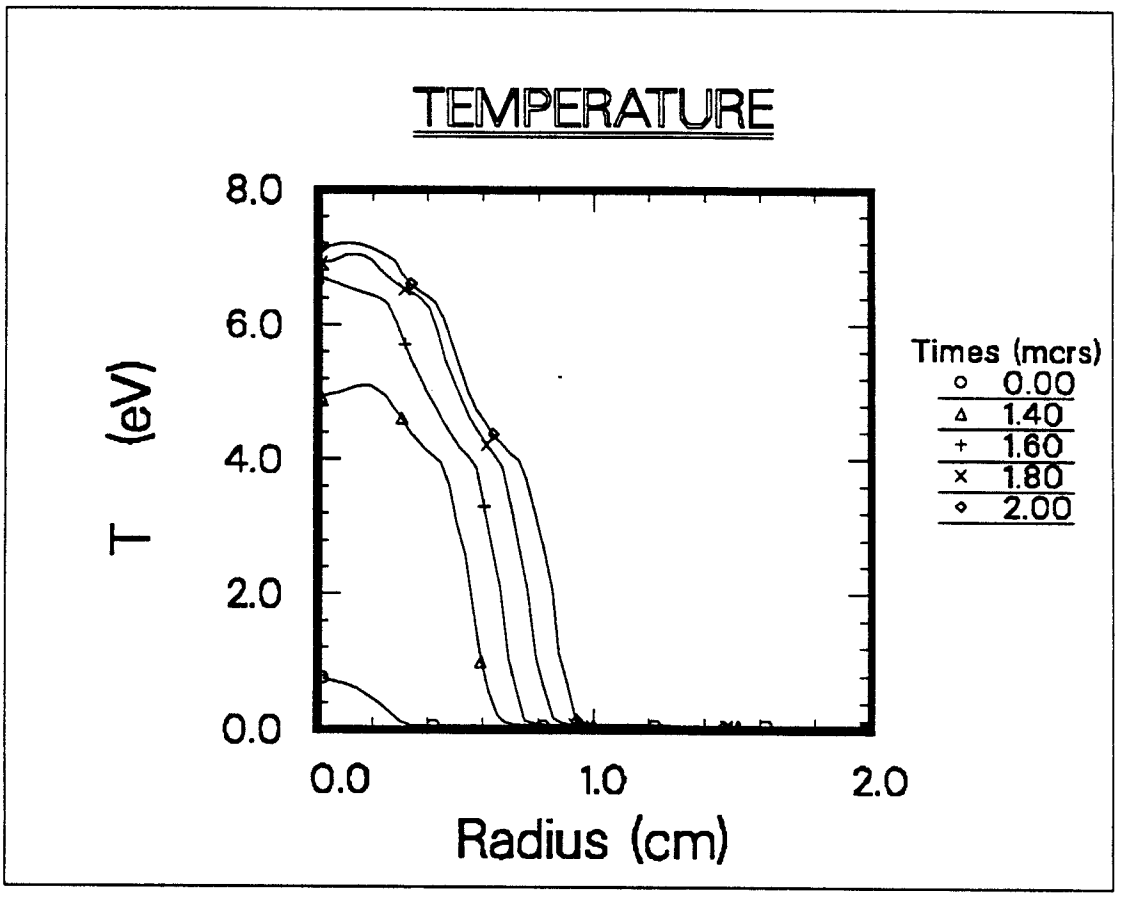

Figure 5.25: Temperature profiles for argon channel with 160 group continuum+lines opacity calculations.

to provide such a neutralization. Whether neutralization occurs depends on a number of plasma and beam parameters such as *magnetic skin depth of plasma* (λ) and *beam radius* (a). An analytical approach by Lovelace and Sudan [80] which basically uses the generalized ohm's law along with Faraday's and Ampere's laws concludes with a criteria of $\lambda_E/a \ll 1$ for current neutralization. Here $\lambda_E = c/\omega_p$ is the electromagnetic skin depth. The injection of the beam into a plasma is accompanied by a *return current* that grows up to the beam current value,that is $\mathbf{J_r} \approx -\mathbf{J_b}$, if this criteria is met. Another way of checking if the neutralization occurs is to test the magnetic diffusion equation given earlier as Eq.3.3. Notice that the term on the right, $\frac{\partial}{\partial r}(\eta J_b)$, enters the equation as a source term for the magnetic field. It is apparent that this term would be negligible for a highly conducting media with small η and thus λ. Due to the dependency of η on the temperature, this requires high temperatures (at least several eVs) in the plasma channel prior to the beam injection. The plasma in the channel starts with a low temperature around 0.8 eV and is heated later through the discharge current. For slow rising currents, as in Figure 3.16 the argon gas is not heated enough, therefore a beam injection of $3.2kA/cm^2$ Li^{+3} ions at 1 microsecond causes a jump in the magnetic flux and field as seen in Figures 5.26-27. The plasma current in Figure 5.28 consists of the return current and the discharge current as $\mathbf{J_p} = \mathbf{J_r} + \mathbf{J_d}$. It follows from this that $\mathbf{J_r}$ is about 2.6 kA/cm^2 and cannot cancel the 50% jump in the magnetic flux and

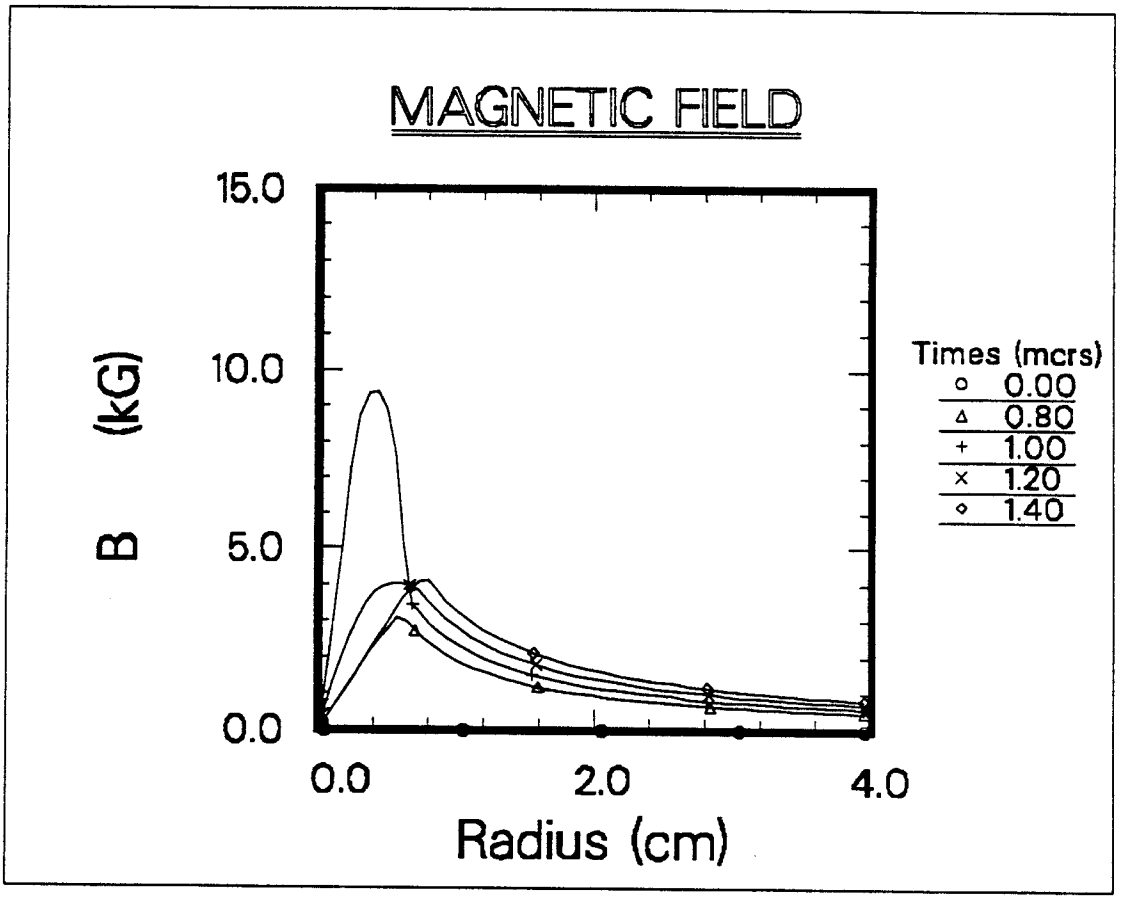

Figure 5.26: Magnetic field profiles for argon channel subject to the discharge current in Figure 3.16.

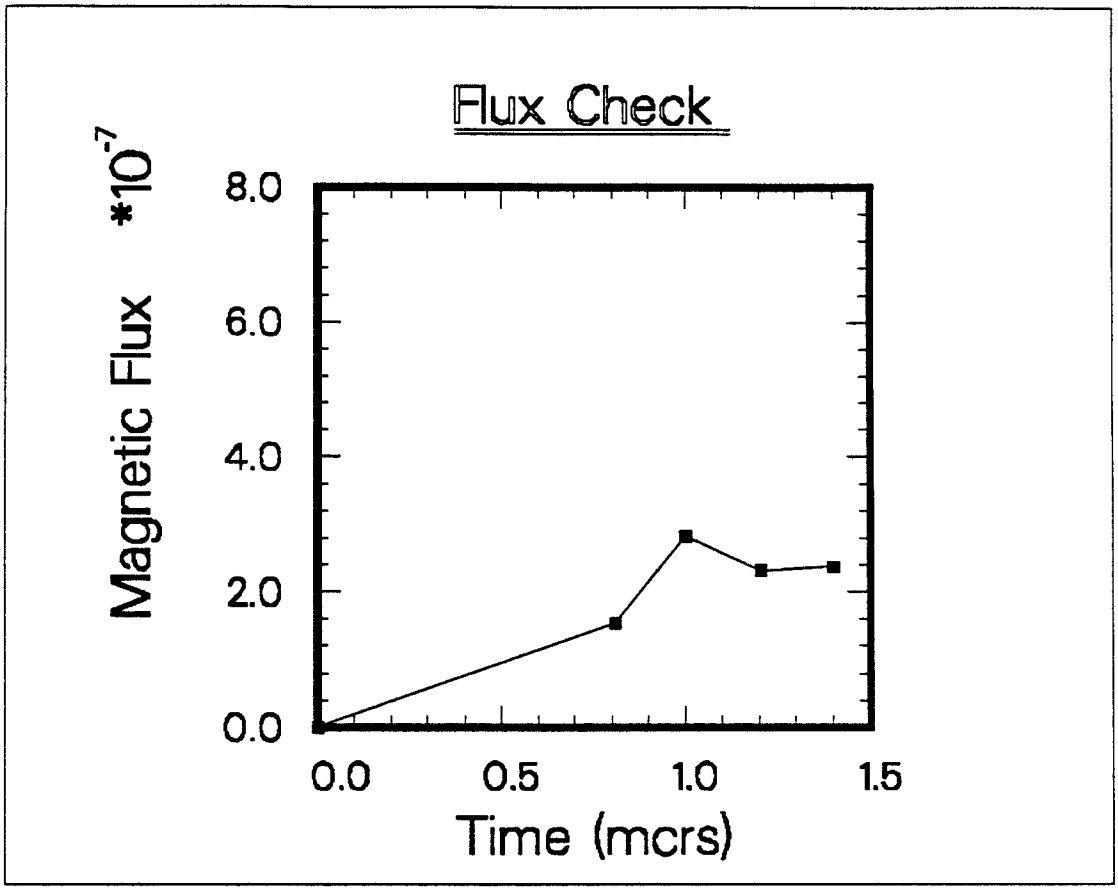

Figure 5.27: Magnetic flux profiles for argon channel subject to the discharge current in Figure 3.16.

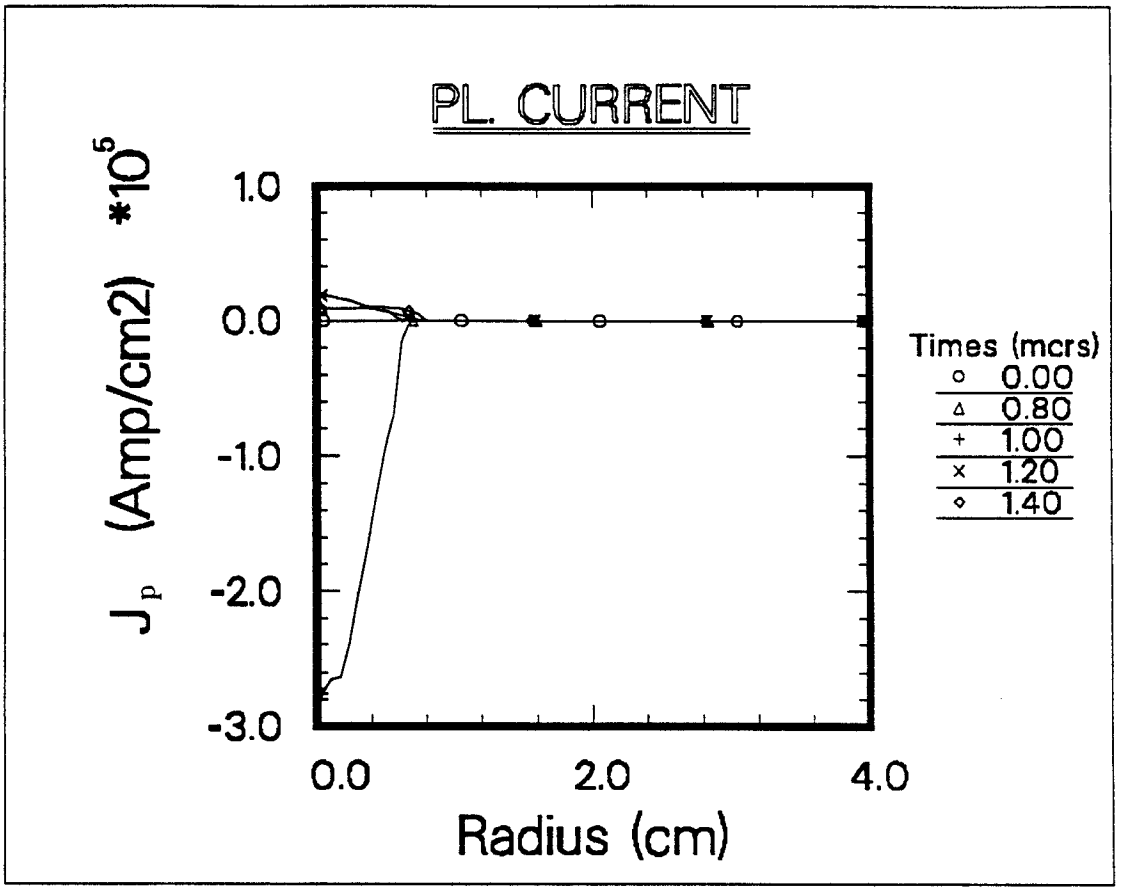

Figure 5.28: Plasma current density profiles for argon channel subject to the discharge current in Figure 3.16.

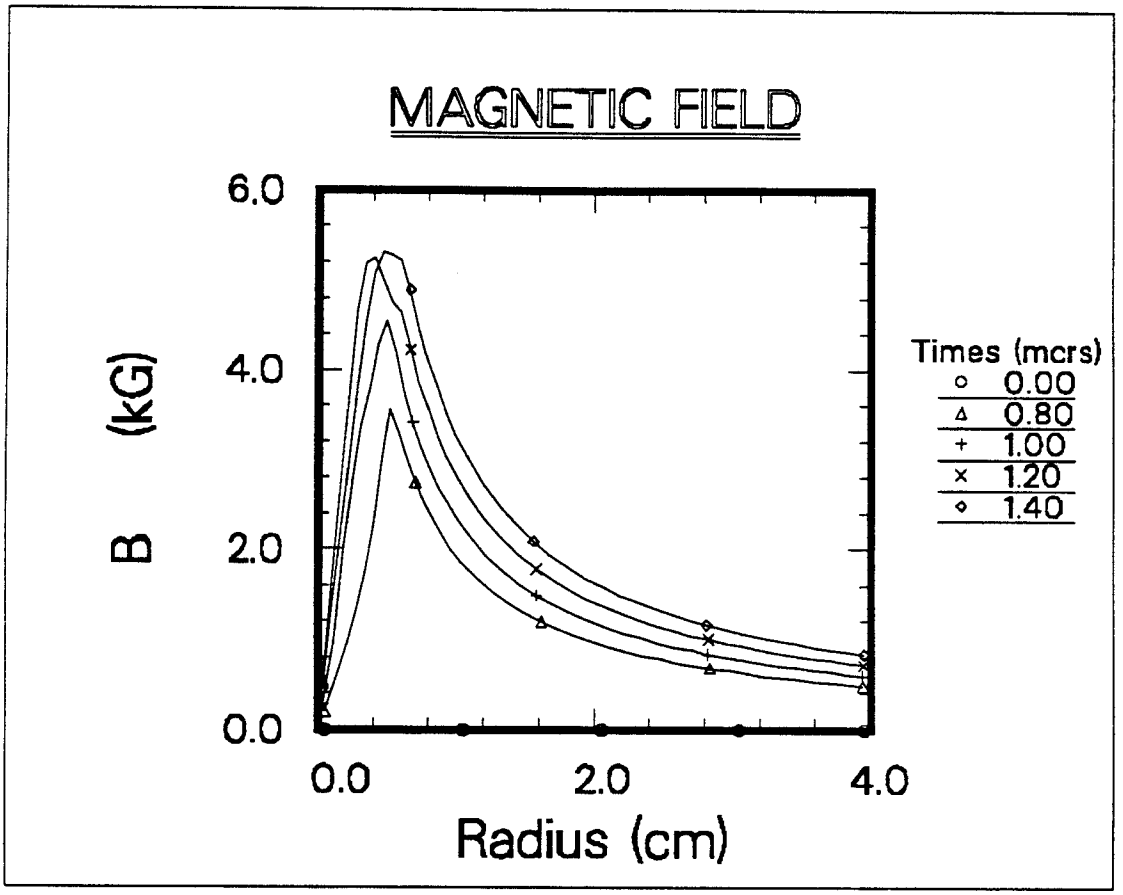

Figure 5.29: Magnetic field profiles for argon channel with $\eta/10$ resistivity. Discharge current in channel is given by Figure 3.16.

field. However, artificially lowering the resistivity ($\eta \rightarrow \eta/10$) decreases the distance into which the beam magnetic field penetrates. The return current increases to 3.0 kA/cm^2 allowing no magnetic flux through the channel due to the beam. The magnetic field shows no signs of increase either, as seen in Figure 5.29.

Fortunately, for LIBRA designs, the plasma is hot enough (5-10eV) to allow low resistivity ($10^{-15} sec$) before the beam is shot. Thus, there seems to be no problems with current neutralization as will be shown in the next section.

5.3.2 Radiation Loss

In section 5.1 we presented channel formation simulations for both argon and helium plasmas. Current LIBRA designs assume helium gas in the channel and require a beam of 30 MeV Li^{+3} ions to carry a power of tens of TWs. The duration of the ion beam is 40 nanoseconds with increasing voltage. This is called *ramping* and is used to allow *beam bunching* in the channel so that a pulse of less duration and thus of higher power is created at the target.

The typical energy and power flow in the LIBRA beam propagation system is shown in Figure 5.30. A model by Colombant, *et al* [47] can be used here to represent the transported beam as described in this figure:

$$J_b = J_{b0}(t) \qquad ; r \leq y r_{ch}$$

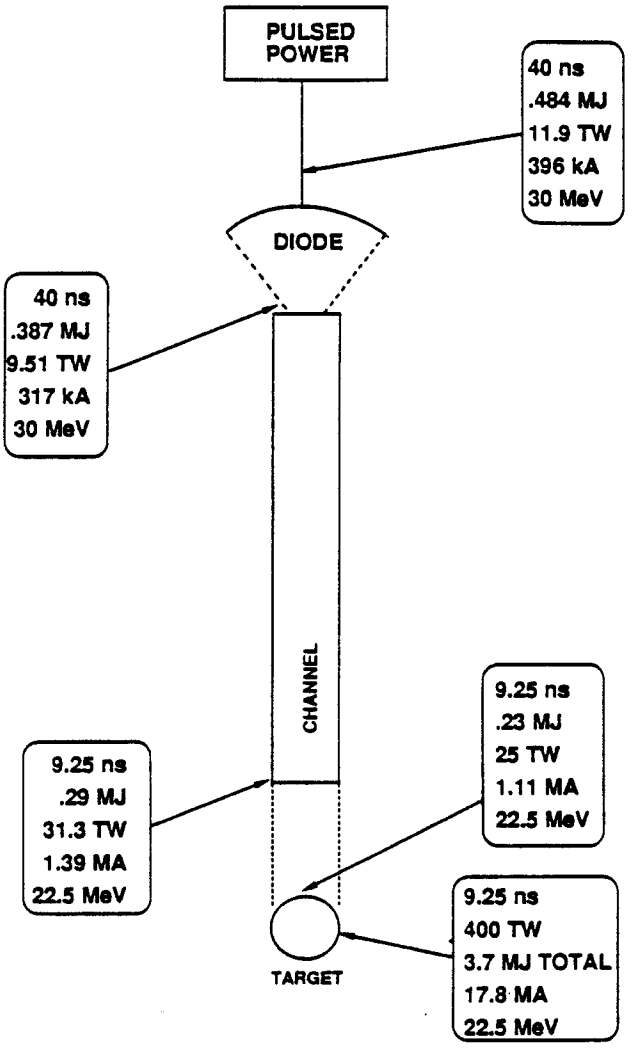

Figure 5.30: Energy and power flow in LIBRA design [1].

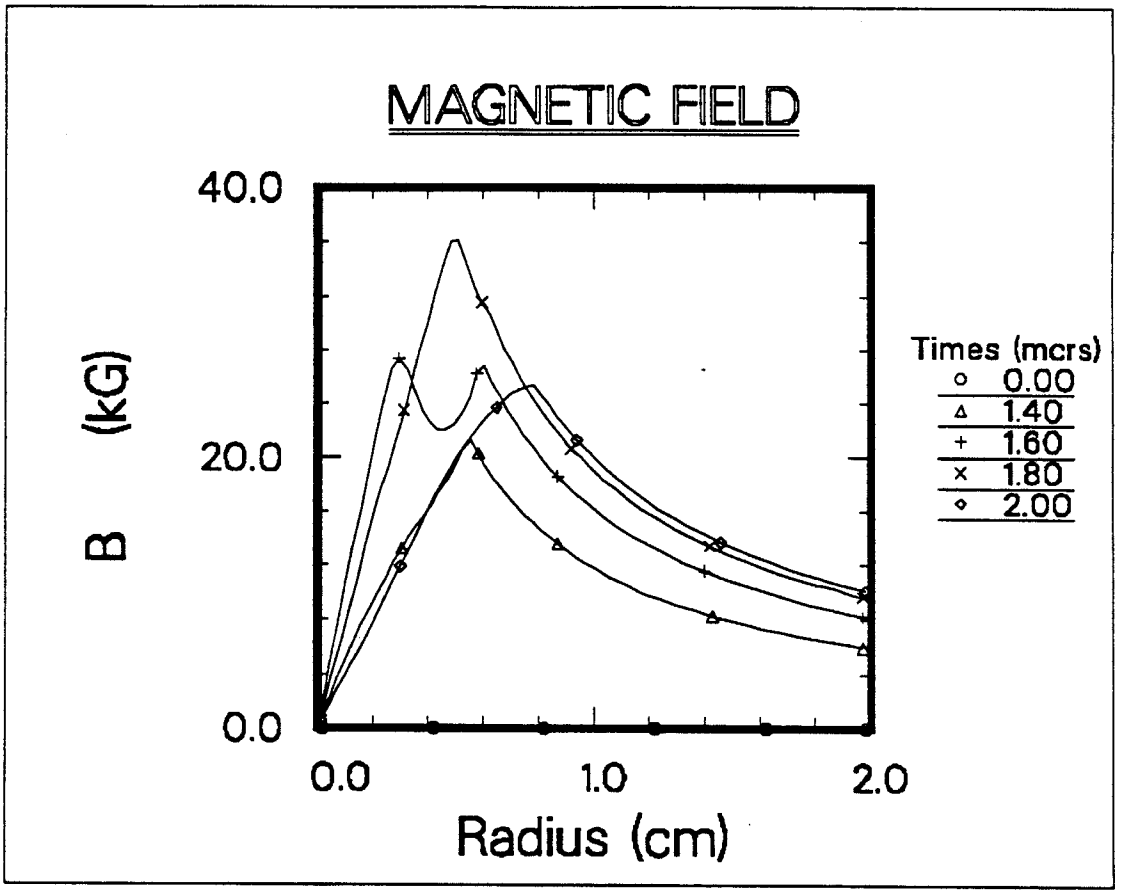

Figure 5.31: Magnetic field profiles for helium channel subject to the discharge current in Figure 4.1 and a beam injection at 1.8 μs.

$$J_b = J_{b0}(1 - \frac{r}{r_{ch}})/(1-y); \qquad yr_{ch} < r < r_{ch} \ \ and \ \ 0.1 \leq y \leq 0.35.$$

and for beam duration τ, $J_{b0} = J_{bm}(1 + \frac{t}{\tau})/2$. Ion energy ϵ_b increases in time like J_{b0}, reaching ϵ_{bm} at $t = \tau$. This energy ramp permits beam power multiplication by axial bunching during transport.

The time to shoot the beam into the channel is chosen to be 1.8 microseconds. The channel radius is 0.5 cm and the magnetic field is 36 kG at this moment (Figure 5.31). Even though this magnetic value is higher than the required value (27 kG), we will use it and delay the issue of a better optimized channel to a later discussion. Profiles for beam, plasma and net current densities J_b, J_p, J_{net} are shown in Figures 5.32-34. The beam current density peaks at 0.56 MA/cm^2. The plasma current density, at the time of beam injection, reverses the sign and reaches $0.44MA/cm^2$ in the opposite direction. The discharge current is small compared to the return current and therefore $\mathbf{J}_p \approx \mathbf{J}_r$. The return current is then $\mathbf{J}_r \approx -\mathbf{J}_b$, although its amplitude should have been closer to J_b for a full neutralization. Nevertheless, the temperature in the channel center is 7.5 eV and therefore the resistivity is low enough ($10^{-15} sec$) to keep the beam current from causing an increase in the magnetic flux and field.

The ion beam deposits energy in the plasma in three ways : joule heating by return current, work done by inductive electric fields and collisional heating through beam ion collisions with background plasma. The results indicate that the joule heating elevates the plasma temperature by 50%,

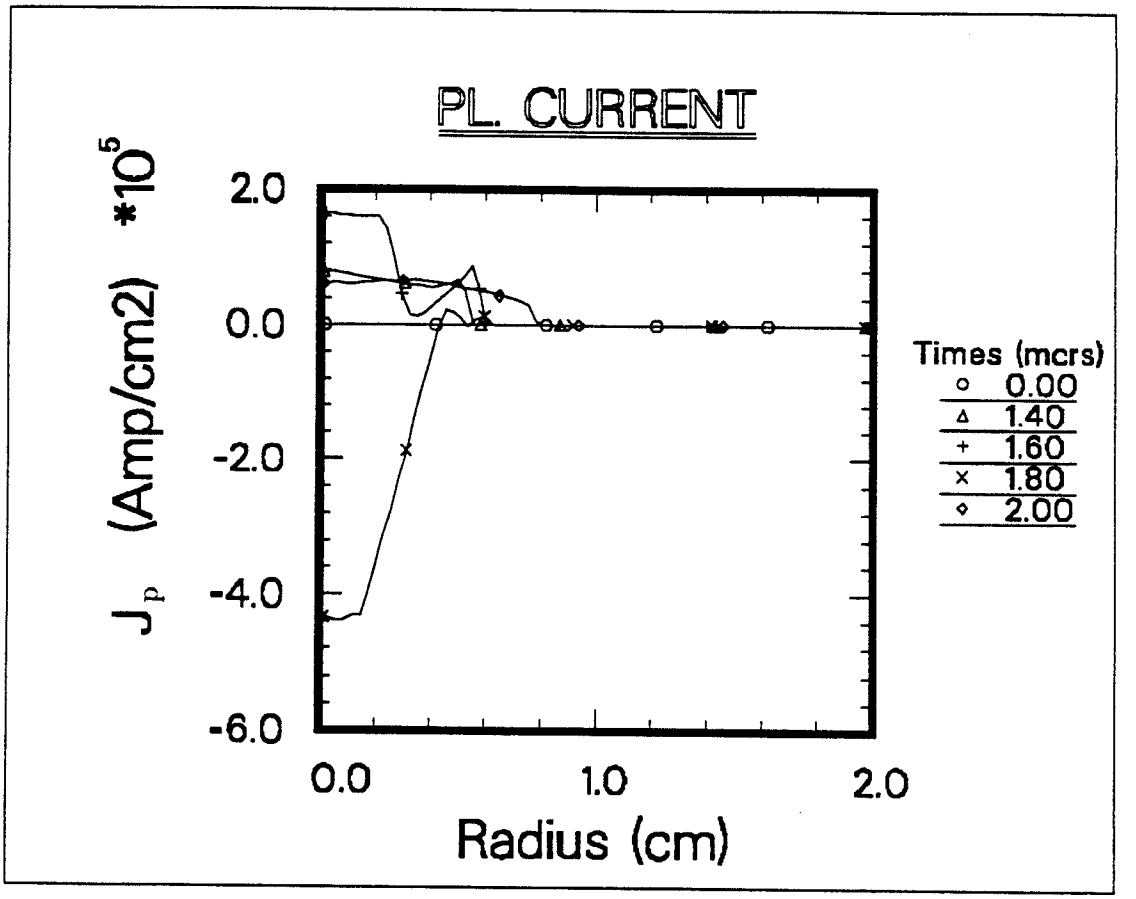

Figure 5.32: Plasma current density profiles for helium channel subject to the discharge current in Figure 4.1 and beam injection at 1.8 μs.

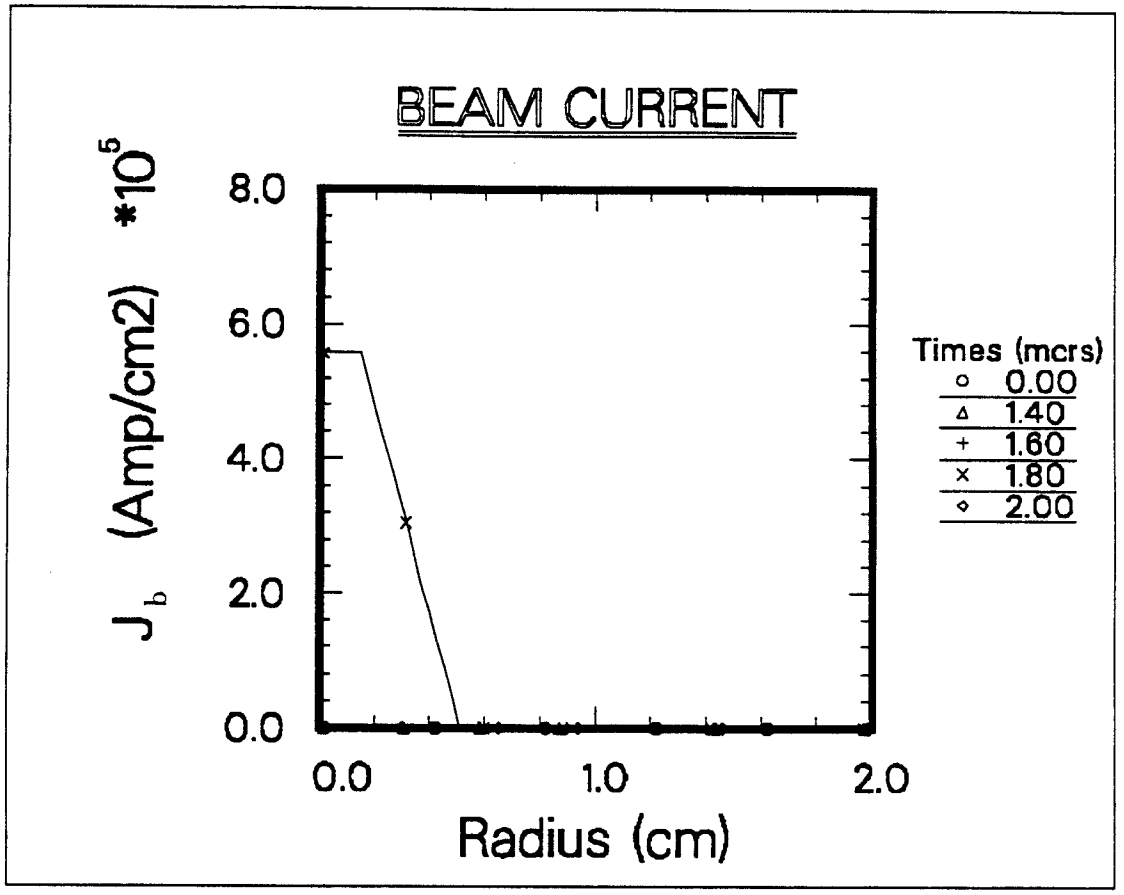

Figure 5.33: Beam current density profiles for helium channel.

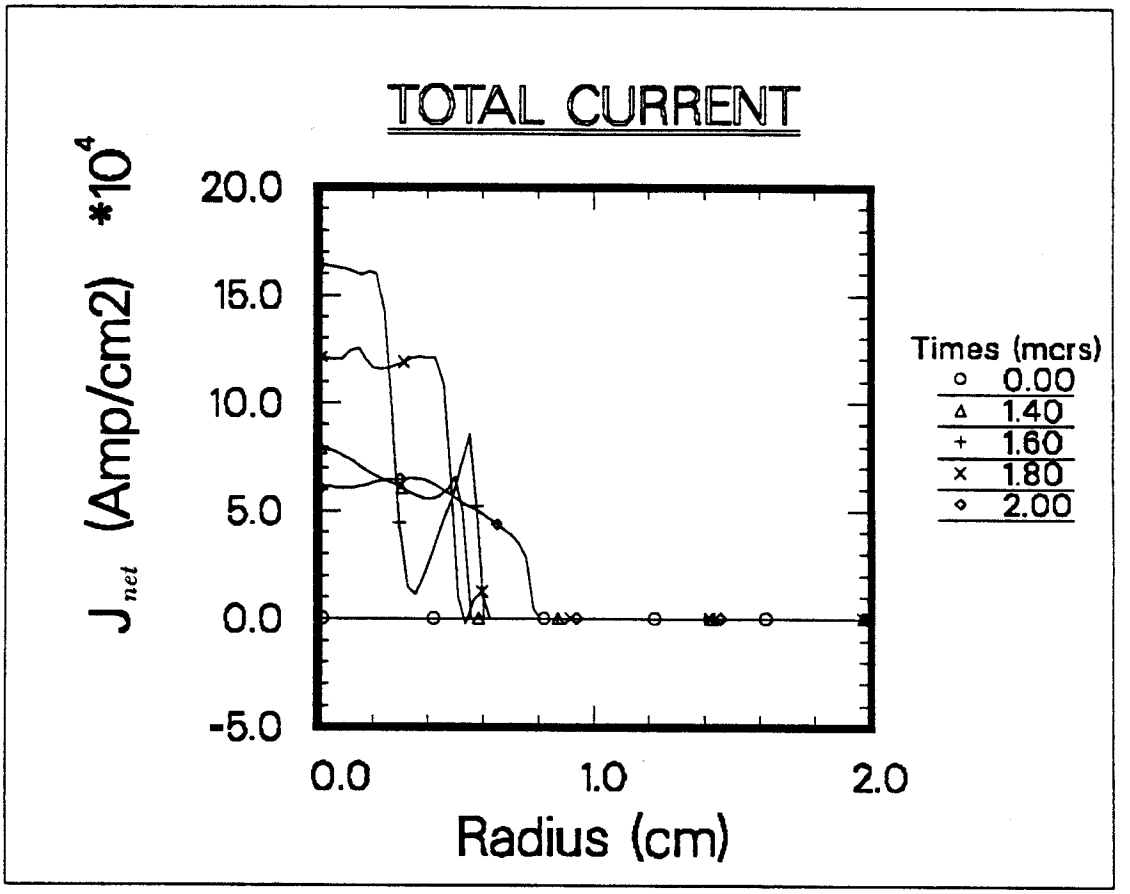

Figure 5.34: Channel current density profiles for helium channel subject to the discharge current in Figure 4.1 and beam injection at 1.8 μs.

whereas the inductive field work and collisional energy gain count for a lot less. An account for the collisional energy, return current joule heating and inductive field work from the beam point of view is given in the next section to clarify the loss better.

The elevated temperature and the Lorentz force acting on the channel by the return current push the gas mass radially outward to velocities of $10^6 cm/sec$, causing an expansion that overcomes the pinching effects caused earlier by the magnetic force. The beam injection adds no significant radiation loss to what is already lost without it. Consequently, the radiation loss and its effects are almost trivial for helium, confirming the idea that it radiates less under current circumstances of plasma channel designs.

5.3.3 Collisional Loss

The plasma channels must be capable of confining the minimum required amount of ion beam power. The power loss that the beam suffers through the collisions with plasma ions and electrons is an important issue. The plasma energy equation in Chapter 3 involves a collisional heat source S_{col} that needs to be calculated in the simulations. Within the framework of the plasma kinetic theory, the energy loss rate for a beam particle α, with energy $\epsilon = (m_\alpha/2)v_\alpha^2$, through collisions with a background gas β is

$$\frac{d}{dt}\epsilon = -\nu_\epsilon^{\alpha/\beta} \cdot \epsilon. \tag{5.6}$$

Here ν_ϵ is the collision frequency given as

$$\nu_\epsilon^{\alpha/\beta} = 2[(\frac{m_\alpha}{m_\beta}\psi(x^{\alpha/\beta}) - \psi'(x^{\alpha/\beta})]\nu_0^{\alpha/\beta}$$

where

$$\nu_0^{\alpha/\beta} = \frac{4\pi e_\alpha^2 e_\beta^2 \lambda_{\alpha\beta} n_\beta}{m_\alpha^2 v_\alpha^3},$$

$$x^{\alpha/\beta} = \frac{m_\beta v_\alpha^2}{2kT_\beta} = \frac{m_\beta v_\alpha^2}{m_\beta v_\beta^2} = \frac{v_\alpha^2}{v_\beta^2},$$

$$\psi(x) = \frac{2}{\sqrt{\pi}}\int_0^x dt\, t^{1/2}e^{-t}, \quad \psi'(x) = \frac{d\psi}{dx}.$$

Also $\lambda_{\alpha\beta} = ln\Lambda_{\alpha\beta}$ is the Coulomb logarithm and $e_\alpha = Z_\alpha e, e_\beta = Z_\beta e$.

Due to the ratio m_α/m_β, the energy loss rate is the greatest for collision of beam ions with discharge electrons. Also note that 30 MeV ions are fast compared to the background electrons implying that $x \gg 1$. For $x \gg 1$, $\psi(x)$ and $\psi'(x)$ are easily expanded as [81]

$$\psi(x) = 1 - \frac{2\sqrt{x}}{\sqrt{\pi}}e^{-x}(1 + \frac{1}{2x} - ..)$$

$$\psi'(x) = \frac{2}{\sqrt{\pi}}\sqrt{x}e^{-x}$$

Utilizing only the lowest order of these expansions, we find

$$\nu_\epsilon^{\alpha/\beta} = 2[\frac{m_\alpha}{m_\beta}(1 - 2\sqrt{\frac{x}{\pi}}e^{-x})]\nu_0^{\alpha/\beta}.$$

Therefore the energy loss rate $\dot{\epsilon}$ is

$$\dot{\epsilon} = -\frac{m_\alpha}{2}v_\alpha^2 \cdot 2[\frac{m_\alpha}{m_\beta}(1 - \frac{2}{\pi}(\frac{v_\alpha}{v_\beta}\ e^{-v_\alpha^2/v_\beta^2})]\nu_0^{\alpha/\beta}. \tag{5.7}$$

and the total energy loss rate per volume is $n_\alpha \cdot \dot{\epsilon}$ where n_α is beam number density. This energy is a gain for the plasma and in fact is what we have written as S_{col} in the plasma energy equation in Chapter 3. Thus,

$$S_{col} = -n_\alpha \cdot \dot{\epsilon}. \tag{5.8}$$

LIBRA designs, as mentioned before, require 30 MeV Li^{+3} particles transported in helium gas for 6.6 meters. As the power flow diagram in Figure 5.30 shows, the beam carries a current of $\sim$ 300 kA at the channel entrance corresponding to a beam number density of 10^{15} per cm^3. For such conditions, the energy loss per cm in the channel is 0.01 % but is higher for higher plasma densities. It amounts to 10 % for $n_p = 3.5 \times 10^{22} cm^{-3}$. Therefore both current neutralization and collisional energy loss do not seem to be a major concern for current LIBRA channel designs.

5.3.4 Ohmic and Inductive Losses

Another major part of the energy loss for ion beams is considered to be due to the return current [77]. The return current is produced by the beam current in the plasma and whatever energy is gained through the return current by the plasma is taken out of the beam energy pool. The return current $\mathbf{J}_r$ is included in our model equations in Chapter 3 as part of the plasma current $\mathbf{J}_p$ which follows

$$\mathbf{J}_p = \mathbf{J}_r + \mathbf{J}_d$$

Note that the electromagnetic energy term in the plasma energy equation Eq.3.10 is $\mathbf{E} \cdot \mathbf{J}$ where $\mathbf{E}$ and $\mathbf{J}$ are measured in the laboratory frame. This term counts for the Joulean dissipation $\mathbf{E}' \cdot \mathbf{J}'$, plus an additional work term

$$\mathbf{u} \cdot (\rho_e \mathbf{E} + \frac{1}{c} \mathbf{J} \times \mathbf{B})$$

due to the inductive electric fields. Here ρ_e (space charge) may be neglected in the plasma. So, altogether again, we write

$$\mathbf{E} \cdot \mathbf{J} = \mathbf{E}' \cdot \mathbf{J}' + \mathbf{u} \cdot (\frac{1}{c} \mathbf{J} \times \mathbf{B}).$$

or

$$\mathbf{E} \cdot \mathbf{J} = [\mathbf{E}' - \frac{1}{c} (\mathbf{u} \times \mathbf{B})] \cdot \mathbf{J}.$$

Here $\mathbf{J}' = \mathbf{J} - \rho_e \mathbf{u}$ is the plasma current density in the fluid frame and is taken as equal to $\mathbf{J}$. The laboratory and fluid frame electric fields $\mathbf{E}, \mathbf{E}'$ are the same as $\mathbf{E}_l, \mathbf{E}_f$ given in Chapter 3 with $\mathbf{E} = \mathbf{E}' - \frac{1}{c} \mathbf{u} \times \mathbf{B}$.

So, the energy loss consists of the ohmic term and the inductive term. It is clear that the inductive term depends on the radial hydromotion of the plasma and the azimuthal magnetic field. It becomes significant for an expanding channel (high radial velocity u) that leaves behind a low density rarefaction region in the channel where the beam is injected. A relatively expanding channel is achievable with less plasma density and it is a desirable situation from the collisional energy loss point of view. Because of the inverted dependence on the plasma density of the collisional and inductive

terms, there is an optimum channel density that plasma channel designers usually worry about [77] for efficient beam transport.

The simulations done with helium gas for LIBRA here do not indicate a large energy loss for the beam due either to the inductive electric field or to the ohmic heat. The plasma channel with an average radial velocity of $10^6 cm/sec$ is not expanding very fast. With a plasma current of $-0.4\ MA/cm^2$ and a magnetic field of $\sim$ 20 kG the inductive and ohmic losses are about $1J/cm$ and $10J/cm$. For a channel with the total length of 6 meters as for LIBRA, a linear relation yields these losses as 600 and 6000 Joules, fairly small compared to the total beam energy of $\sim 10^5 Joules$. Therefore the loss throughout the channel is about 6 % and if put together with the collisional losses in Section 5.3.3, the total loss comes up to 15 %.

5.4 An Optimized Channel

The discharge current used in our LIBRA simulations was illustrated before in Figure 4.1. The main goal for using a prepulse is to reduce the pinching effect of the second (main) pulse. The tendency for the channel to pinch instead of expand presents difficulties in meeting the density requirement. The usual expanding channels achieve a density reduction between 4 to 10 on axis, thereby reducing the collisional energy losses within the channel while still providing a high enough neutral background gas density in the

reactor chamber to attenuate the soft x-rays produced by the ICF target.

The main discharge current pulse is usually high enough to pinch the plasma and this problem is overcome, as Freeman explains [10], by using the "two-stage" drive for current, being a reference for LIBRA designs. The first pulse is aimed to heat the central region and the channel expands after that, if there is time, Δt, for it before the main pulse comes along. As mentioned earlier, there are competing events in the channel dynamics. If one wants an expanding channel, he/she should allow sometime (several μs) to pass between the pulses. On the other hand, the magnetic field peak value decreases for expanding channels, $B_c \propto \frac{1}{r_c}$, resulting in a relation as $B_c \propto \frac{1}{\Delta t}$. Thus, a smaller Δt may be wanted for higher magnetic fields.

Seeking a high enough magnetic field (27 kG) at $r_c = 0.5$ cm has been the primary goal for current LIBRA channel designs. The difficulties led to a *time delay*, Δt, of zero. Fortunately, the chosen gas (helium) is good at expanding due to its high pressure which lessens the pinching caused by the magnetic force. Simulations for LIBRA with ARMHD were presented before in Sections 5.1 and 5.2. The magnetic field prior to beam injection at $r_c = 0.5$ cm is 35 kG for helium. This value is higher than what is needed to confine the ions from the LIBRA diode design. An immediate question is if we could meet the requirement with less current. The answer is yes and the simulation presented in Figure 5.35 with 70 kA discharge current seems to be showing that. Obtaining the requirement with lower discharge voltage is

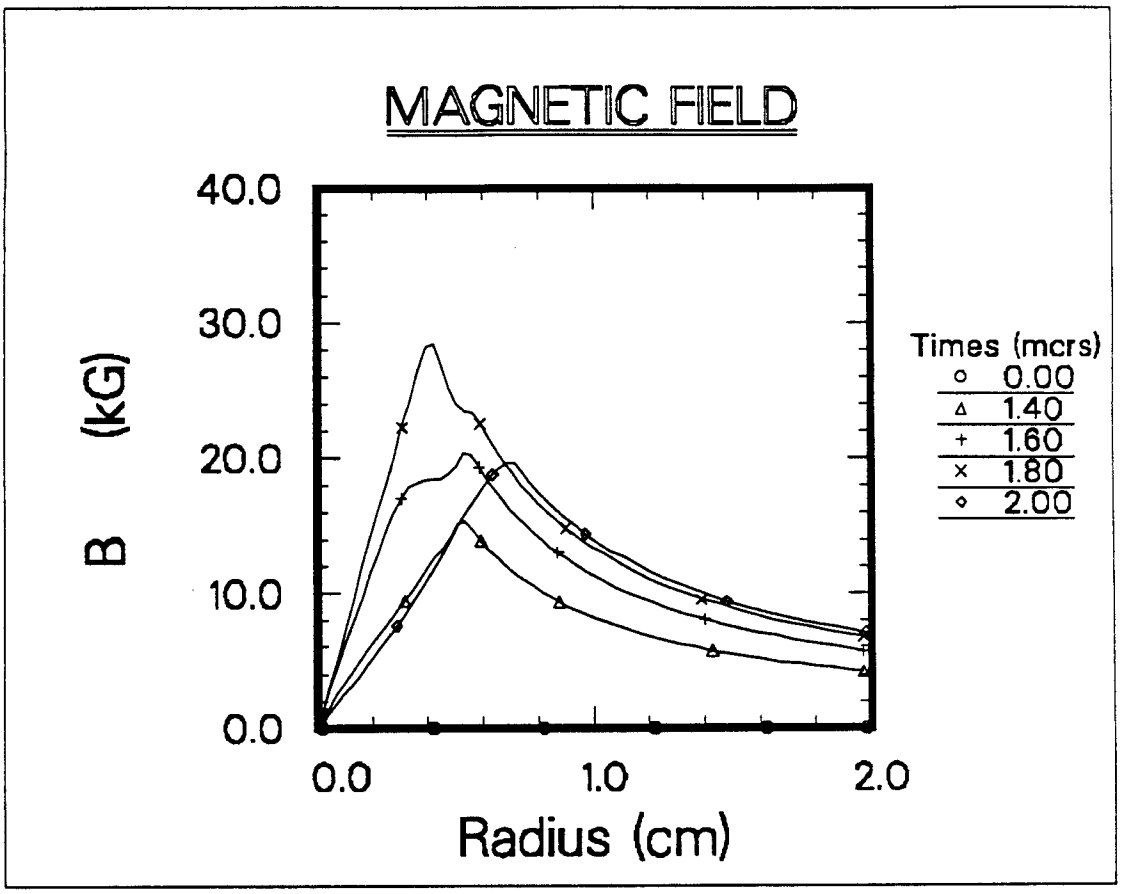

Figure 5.35: Magnetic field profiles for helium channel subject to the discharge current of 70 kA and beam injection at 1.8 μs.

certainly significant for reactor applications since there is less risk involved in the breakdown of the high voltage to the reactor chamber [82].

One drawback with helium is that it is not as effective as argon and nitrogen at attenuating the X-rays coming from the target explosion. It is therefore worth looking for an alternative channel for LIBRA with argon and nitrogen. Previous ARMHD code simulations with argon show magnetic field values of 22-26.5 kG at channel radii of 0.7-0.85 cm. An improvement could be made to acheive the 27 kG at 0.5 cm by increasing the discharge current. One problem with argon, though, is that it goes through pinching at times before beam injection. This problem exists with helium too but it does not cause a significant density increase in the center region. The pinching for argon is worse, causing problems with the density requirement. This is all due to the zero time delay factor and could be eliminated by changing the current profile and rising times completely. Nevertheless, we will not do that here and instead will put the effort in checking the possibility for nitrogen channels. Just as helium and argon, nitrogen suffers too from the pinching but it seems to be much less compared to argon. It is much easier to improve the conditions for a nitrogen channel: we get a magnetic field of 30 kG at radius 0.5 cm.

As opposed to early LIBRA calculations done with ZPINCH [78], simulations we have done here prove both argon and nitrogen acceptable for creating high enough magnetic fields. One important fact that led to this is that,

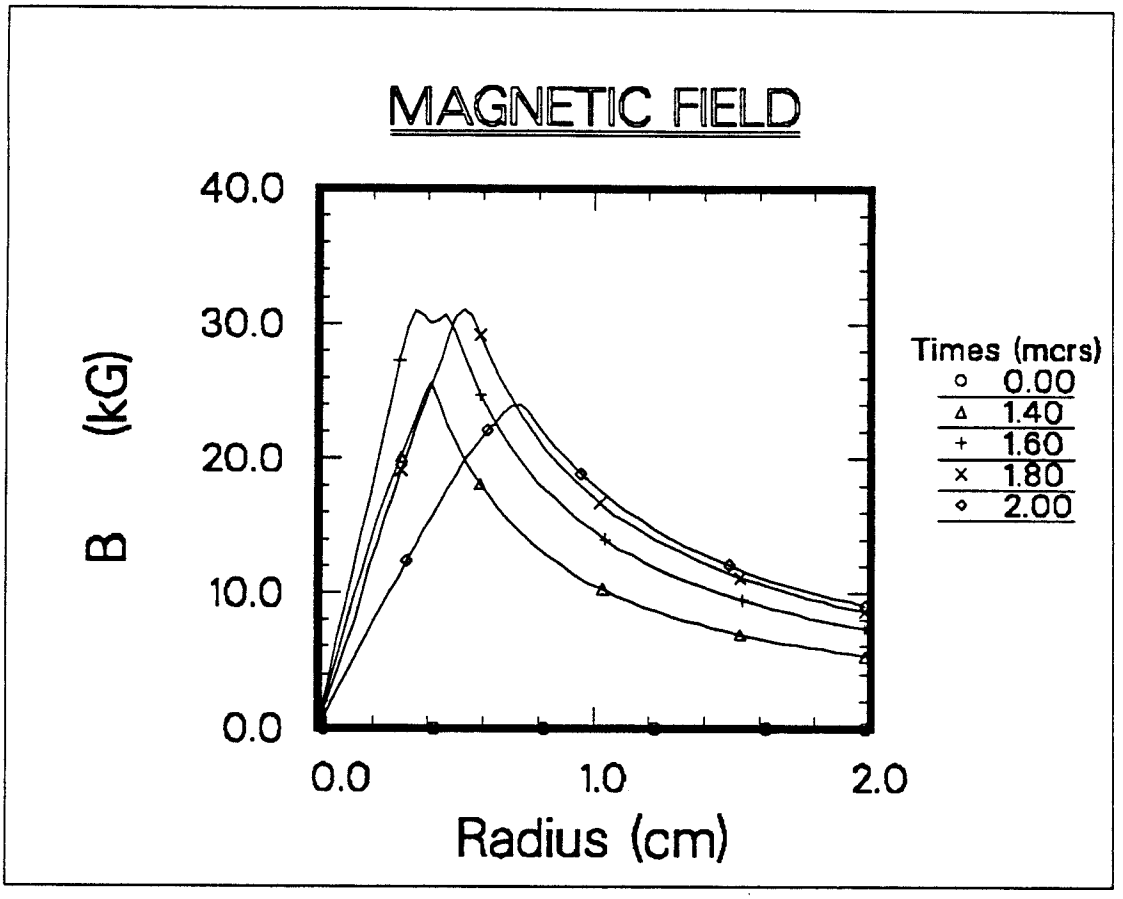

Figure 5.36: Magnetic field profiles for nitrogen channel with 20 group continuum opacity. The channel is subject to the discharge current of 90 kA and a beam injection at 1.8 μs.

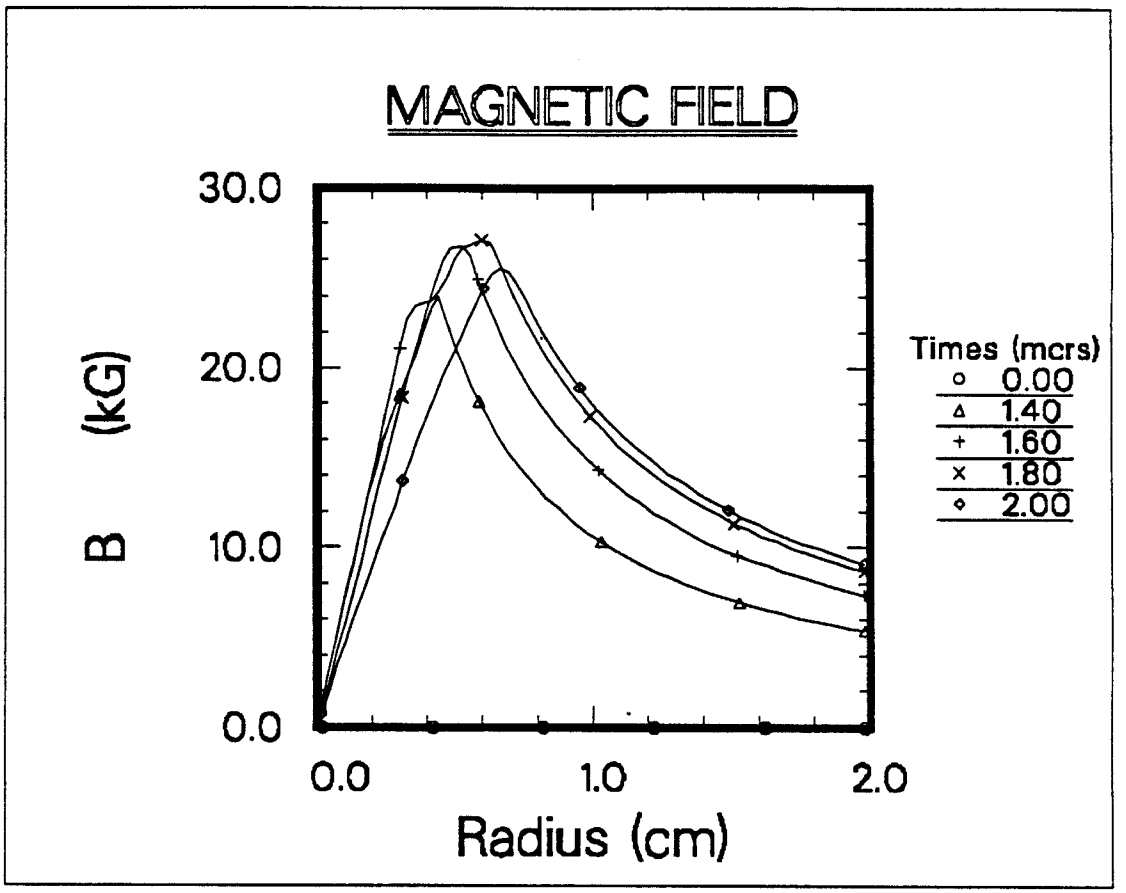

Figure 5.37: Magnetic field profiles for nitrogen channel with 160 group continuum+lines opacity. The channel is subject to the discharge current of 90 kA and a beam injection at 1.8 μs.

by using a more accurate model, ARMHD corrected the **overestimations** done by ZPINCH regarding the radial radiative transfer in the channel. To overcome the problem of pinching for nitrogen, we suggest lowering the first pulse. As mentioned earlier, the first pulse has been originally considered to heat up the channel for a following expansion, and the higher this pulse is the more the channel expands. Nevertheless, the situation here, for a *time delay* of zero, turns out to be the other way around: there is no time for the channel to expand, and the higher the first pulse is the higher the magnetic field is due to that pulse, resulting in a channel to be pinched more easily with the following main pulse. Not surprisingly, simulations with a 0.5 kA first and 90 kA main pulse reduces the pinching effects to where the nitrogen stands as a candidate for channels. The results are illustrated in Figures 5.36-37. They are done by working with two different opacity group calculations, 20-group continuum and 160-group continuum+lines, to see how much line transport is important for nitrogen. A comparison for magnetic field, channel radius and axis temperature is given in Table 5.5. These results also indicate to us that lines play a non-trivial role for nitrogen.

The beam injection of $\sim$ 400 kA brings high current neutralization and relatively insignificant collisional energy losses of 0.004%, return current losses of 0.02 % per cm for nitrogen channels. In LIBRA designs, again the linear relation yields a total energy loss of 14 % for nitrogen channels.

In conclusion, we have been able to create the required helium channels

Table 5.5: Simulation results vs the number of opacity groups (nitrogen).

Case	# of opacity groups	Peak B-Field value (kG)	Channel radius (cm)	Temperature at center (eV)
continuum 0	20	31	0.56	9.3
cont.+ lines 1	160	27.5	0.58	8.2

with 30 % less discharge current. The same channel conditions can be created with nitrogen gas, giving an alternative to helium. Argon channels give high magnetic fields but also introduce problems for density requirements which may be overcome with some effort. Overall, there seems to be no serius problem with beam energy losses and current neutralization for any of these gases within the frame of ARMHD model.

Chapter 6

Conclusion

A computational model has been developed to study z-pinch plasma channels and ion beam propagation in the magnetohydrodynamic approximation. It has proven to be very robust so far, although it may require relatively small time steps for some highly unsteady problems because of the stability condition for the explicitly solved equations. Some of the model's best features are :

- **Adaptive Gridding** : The grid points follow high gradients that occur in the solution of PDEs for the purpose of better resolution (accuracy) and minimizing the number of mesh points. The redistribution of mesh points is not like a local grid refinement nor a periodic rezoning as used in *ad hoc* ways with eulerian and lagrangian schemes. It is quite general and set up for multigradient problems.

- **Diverse Applicability** : It can be used for one dimensional compresible flow in planar, cylindrical and spherical geometries. In addition to the z-pinch plasma problem, it could be applied to microfireball simulations in ICF target chambers.

- **RHD Capability** : The model equations include radiative transfer coupled to the plasma and the solution for the radiation field is found by a radiation transfer equation using a multigroup discrete ordinate S_N method. Opacities are obtained from an atomic physics code IONMIX [66].

- **MHD Capabilty** : Single-fluid MHD equations and ion beam injection physics is used to model the magnetic properties of the plasma which is subject to a discharge current and beam injection in the axial direction.

- **Fast response time** : The code is mostly vectorized and it takes several minutes to run the simulations described in early chapters on a CRAY X-MP/48 supercomputer.

The applications of our computational model ARMHD to the Light Ion Beam Fusion Reactor study LIBRA has produced the following results :

- Adaptive gridding has given us a finer mesh distribution where needed in the channel to resolve the magnetic field profile, when compared to a lagrangian scheme using the same number of mesh points.

- The correct description of the radiation transfer phenomena in the channel is not diffusion but rather anisotropic transport. Thus, ARMHD treats the thin plasma more accurately than the commonly used diffusion approximation.

- Multigroup radiation transfer methods are highly dependent on the group structure defined for opacity group averaging. Lines in the absorption and emission spectrums are so narrow that they require many numbers of groups (hundreds) to allow a good averaging over the whole spectrum. A coarse group structure leads to overestimated absorption and emission coefficients. On the other hand, using many points requires a lot of computing time for the time-dependent solution of the radiation field by the multigroup S_N method. Simulations with 160 opacity groups required roughly 40 minutes on the CRAY X-MP/48 computer. The outcome is such that the line transport in the thin channel plasma is important and should be treated well. Overestimation of absorption and emission coefficients leads to a net transfer of energy from the channel center to the cold surrounding gas and therefore creates a premature expansion, called a radiation driven expansion (RDE). This is identical to the RDE phenomena seen with diffusion calculations. More accurate results require more groups, meaning higher cost. Therefore a new way to avoid the difficulties of group averaging with the lines should be studied. One way of doing this, as MacFarlane

and Moses suggested, is that the line transport can be done separately to be combined later with the multigroup S_N treatment of continuum transport for the total answer.

- Argon and nitrogen channels are feasible for LIBRA in terms of obtaining the required magnetic field to confine the ion beam. These gases were ruled out in favor of helium by early calculations using a radiative diffusion model. Further improvements can be made for argon by changing the timing of the discharge current pulses to satisfy the density requirement too. Nitrogen, on the other hand, is as good as helium as a candidate for efficient beam transport in LIBRA. One drawback with helium is that it is not as effective as argon and nitrogen at attenuating the X-rays coming from the target explosion.

- Beam energy losses for both helium and nitrogen are about 15 %. Most of this loss is due to collisons with the background plasma and ohmic heating by the return current. The loss through inductive electric fields seems less because the channel dynamics leads to either a slow expansion or a pinching which do not let high inductive fields be created.

- The magnetic flux due to the beam current, $\sim 0.5MA$, of 30 MeV lithium ions gets cancelled successfully by the return current produced in the highly conductive plasma.

The idea behind creating the ARMHD computer code for the z-pinch plasma and ion beam propagation research was basically due to the desire to achieve more accuracy in such a non-linear and unsteady problem. Although many questions have been answered, effort is still needed to further improve both the numerics and physics of the computational model. Below is the list of points for further development in these areas.

- The multigroup radiation transfer depends on the number of groups. As an alternative to using many groups, which raises the cost of the computations, a separate treatment of lines could be done to associate later with the multigroup treatment of the continuum radiation. This issue has already been taken up by colleagues at UW-Madison [83].

- The magnetohydrodynamics equations used in ARMHD are for single-fluid plasmas in which ions and electrons are not distinguished. A more elaborate investigation perhaps requires the distinction be made for ions and electrons. The electrons and ions would then have different sets of equations for continuity, momentum and energy. A simplifying alternative is to assume the ions and electrons move together as a fluid (i.e. no charge separation) but that they are allowed to have different temperatures.Thus, further study in developing the two-fluid MHD equations is necessary.

- The simplicity of the donor cell differencing method has helped create a scheme without much difficulty. The donor cell differencing is first order accurate but as Bartel states [20] it works well with the adaptive gridding. It is better than second order accurate MacCormack and Leonard's methods for test problems. Nevertheless, it is known to be a diffusive scheme [18], so much that it does not really need an artificial viscosity term to smear out the shock fronts. Although it is successful in capturing the high gradient regions, shocks and contact discontinuities, it may be questioned for its performance in mild gradient regions, such as rarefaction fans. Therefore there is need for research and improvement to be done on the numerical method as accuracy issues are raised.

Bibliography

[1] G.A.Moses, et al., "LIBRA - A Light Ion Beam Fusion Conceptual Reactor Design," University of Wisconsin Fusion Engineering Program Report UWFDM-800, May 1989.

[2] J.J.Duderstadt, G.A.Moses, *Inertial Confinement Fusion*, John Wiley, N.Y., 1982.

[3] G.Yonas, "Particle Beam Fusion," Bull.Am.Phys.Soc 21, 1972, p.1102.

[4] D.Bohne, et al., "HIBALL - A Conceptual Design of a Heavy-Ion Driven Inertial Confinement Fusion Power Plant," *Nucl. Engr. and Design*, 73, 195 (1982).

[5] G.A.Moses, et al., "LIBRA - A Light Ion Beam Fusion Conceptual Reactor Design," Proceedings of the Beams '88 Conference, July 1988, Karlsruhe, FRG.

[6] "Preliminary Design of Light Ion Beam Fusion Reactors, UTLIB (1) & ADLIB-1," University of Tokyo Nuclear Engineering Research Labora-

tory UTNL-R-0135 (1982).

[7] K. Nui and S. Kawata, "Proposal of Power Plant by Light Ion Beam Fusion," *Fusion Technology*, 11, 365 (1987).

[8] "Light Ion System Analysis and Design - Phase I: Engineering Test Reactor Goal Specification," Research project 1527, Electric Power Research Institute (April 1982), no author.

[9] G.A.Moses, et al., "Overview of The LIBRA Light Ion Beam Fusion Conceptual Reactor Design," Proceedings of the Beams '88 Conference, July 1988, Karlsruhe, FRG.

[10] J.R.Freeman, L.Baker, D.L.Cook, "Plasma Channels for Intense LIB Reactors," Nuc.Fusion 22, No.3, 383 (1982).

[11] J.J.Watrous, G.A.Moses, R.R.Peterson, "Z-PINCH– A Multifrequency Radiative Transfer Magnetohydrodynamics Computer Code," University of Wisconsin Fusion Engineering Program Report UWFDM-584, June 1984.

[12] G.A.Moses, "ION - A Code to Compute Ion Trajectories in Z-Pinch Plasma Channels," University of Wisconsin Fusion Engineering Program Report UWFDM-712, Jan. 1986.

[13] R.R.Peterson, "WINDOW - A Code to Compute Ion Beam Power Constraints," Fusion Power Associates Report FPA-84-6 (1984).

[14] J.J.Watrous, "Numerical and Theoretical Investigations of Z-Pinch Plasma Channels for LIB Inertial Confinement Fusion," Ph.D Thesis, University of Wisconsin, 1986.

[15] G.A.Moses, R.R.Peterson, T.J.McCarville, "MF-FIRE–A Multifrequency Radiative Transfer Hydrodynamics Code," University of Wisconsin Fusion Engineering Program Report UWFDM-458, Dec.1982.

[16] B.Badger, "Light Ion Beam Fusion Target Development Facility Studies:Progress Report for the Period 1 Nov.1986 to 31 Dec.1987," University of Wisconsin Fusion Engineering Program Report UWFDM-752, Jan.1988.

[17] G.A.Moses, R.R.Peterson, *Private Communication*, Dec.1987.

[18] E.S.Oran and J.P.Boris, *Numerical Simulation of Reactive Flow*, Elsevier, N.Y., 1987.

[19] H.A.Dwyer, "Grid Adaption for Problems in Fluid Dynamics,"AIAA J. 22, No.12, 1984, p.1705.

[20] T.J.Bartel, "Adaptive Mesh Techniques for Unsteady Multi-Gradient Problems in Computational Fluid Dynamics," Ph.D Thesis, Univeristy of Wisconsin Fusion Engineering Program Report UWFDM-720, Jan.1987.

[21] Meek and Craggs, *Electrical Breakdown of Gases*, Clarendon Press, Oxford, 1953.

[22] NRL Plasma Radiation Branch, "Advanced Concepts Theory Annual Report 1984," NRL Memorandum Report 5590, June 1985.

[23] P.A.Miller, R.I.Butler, M.Cowan, "Propagation of Pinched Electron Beams for Pellet Fusion," Phys.rev.Lett.39, No.2, July 1977, p.92.

[24] J.R.Vaill, D.A.Tidman, T.D.Wilkerson, D.W.Koopman, "Propagation of High Voltage Streamers Along Laser Induced Ionization Trails," Appl.Phys. Lett. 17, No.1, July 1970, p.20.

[25] D.W.Koopman, T.D.Wilkerson, "Channeling of an Ionizing Electrical Streamer by a Laser beam," J.Appl.Phys. 42, No.5, April 1971, p.1883.

[26] D.W.Koopman, K.A.Saum, "Formation and Guiding of High Velocity Electrical Streamers by Laser Induced Ionization," J.Appl.Phys. 44, No.12, Dec.1973, p.5328.

[27] K.A.Saum, D.W.Koopman, "Discharge Guided by Laser Induced Rarefaction Channels," Phys.Fluids 15, No.17, Nov.1972, p.2077.

[28] R.M.Measures, "Electron Density and Temperature Elevation of Potassium Seeded Plasma by Laser Resonance Pumping," J.Quant.Spect. Radiative Transfer 10, p.107.

[29] R.M.Measures, N.Drewell, P.Cardinal, "Electron-and Ion- Beam Transportation Channel formation by Laser Ionization Based on Resonance saturation – LIBORS," J.Appl.Phys. 50, No.4, April 1979, p.2662.

[30] R.S.Pease, "Equilibrium Characteristics of a Pinched gas Discharge Cooled by Bremsstrahlung Radiation," Proc.Phys.Soc., B70, 445, 1957, p.11.

[31] C.G.Falthammer, "Stationary State of a High-Temperature Gas-Insulated Plasma Column," Phys. Fluids 4, No.9, Sept. 1961, p.1145.

[32] D.W.Scudder, "Steady State radial Heat Conduction in a Z-Pinch," Phys. Fluids 26, No.5, may 1983, p.1330.

[33] S.I.Braginskii, "The behavior of a Completely Ionized Plasma in a Strong Magnetic Field," Sov. Phys. JETP 6 (33), No.3, March 1958, p.494.

[34] M.Kruskal, M.Sckwarzchild, "Some Instabilities of a Completely Ionized Plasma," Proc. Phys. Soc. B70, 1957, p.31.

[35] R.J.Tayler, "Hydrodynamic Instabilities of an Ideally Conducting Plasma," Proc. Roy. Soc. a223, 1954, p.348.

[36] W.M.Mannheimer, M.Lampe, J.P.Boris, "Effect of a Surrounding Gas on Magnetohydrodynamic Instabilities ia a Z-Pinch,' Phys. Fluids 16, No.7, July 1973, p.1126.

[37] J.Killeen, B.A.Lippmann, "Circuit Dynamics of the Pinch," J. Appl.Phys. 31, No.9, Sept. 1974, p.1549.

[38] W.M.Mannheimer, "Energy Input into a Gas-Enclosed Z-Pinch," Phys. Fluids 17, No.9, Sept. 1974, p.1767.

[39] P.F.Ottinger, D.Mosher, S.A.Goldstein, "Propagation of Intense Ion Beams in Straight and Tapered Z-Discharge Channels," Phys. Fluids 23, No.5, May 1980, p.909.

[40] P.F.Ottinger, D.Mosher, S.A.Goldstein, "Microstability of a Focused Ion Beam Propagating Through a Z-Pinch Plasma," Phys. Fluids 22, No.2, Feb. 1979, p.332.

[41] P.F.Ottinger, D.Mosher, S.A.Goldstein, "Electromagnetic Instabilities in a Focused Ion Beam Propagating Through a Z-Discharge Plasma,"Phys. Fluids 24, No.1, Jan. 1981, p.164.

[42] A.Mankofsky, R.N.Sudan, "Numerical Simulation of Ion beam Propagation in Z-Pinch Plasma Channels," Nucl. Fusion 24, 1984, p.827.

[43] A.Mankofsky, "Numerical Simulation of Ion Rings and Ion Beam Propagation," Ph.D Thesis, Cornell University, August 1982.

[44] P.A.Miller, "REB Propagation and Combination in Plasma Channels," Proc. Second Int. Top. Conf. High-Power Electron and Ion Beams, Ithaca, N.Y., 1977, p.393.

[45] J.N.Olsen, "Laser-Initiated Channels for Ion Transport: CO_2-Laser Absorption and Heating of NH_3 and C_2H_4 Gases," J.Appl.Phys. 52, No.5, May 1981, p.3279.

[46] J.N.Olsen, "Laser-Initiated Channels for Ion Transport: Breakdown and Channel Evolution,"J.Appl.Phys. 52, No. 5, May 1981, p.3286.

[47] D.G.Colombant, S.A.Goldstein, D.Mosher, "Hydrodynamic Response of Plasma Channels to Propagating Ion Beams," Phys.Rev.Lett. 45, No.15, Oct. 13 1980, p.1253.

[48] J.F.Thompson, "A Survey of Dynamically-Adaptive Grids in the Numerical Solution of Partial Differential Equations," AIAA-84-1606, 1984.

[49] J.F.Thompson, Z.U.A.Warsi, C.W.Mastin, *Numerical Grid Generation*, North-Holland, 1985.

[50] P.R.Eiseman, "High Level Continuity for Coordinate Generation with Precise Controls," J. Comp. Phys. 47, 1982, p.352.

[51] P.R.Eiseman, "Alternating Direction Adaptive Grid Generation," AIAA J. 23, No.4, 1985, p.551.

[52] H.A.Dwyer, "A Discussion of Some Criteria for Use of Adaptive Gridding" in *Adaptive Computational Methods For Partial Differential Equations*, Edt: I. Babuska, SIAM, 1983.

[53] H.A.Dwyer, "Grid Adaption for Problems with Separation Cell Reynolds Number, Shock-Boundary Layer Interaction, and Accuracy," AIAA-83-0449, 1983.

[54] D.A.Anderson, "Adaptive Mesh Schemes Based on Grid Speeds,"AIAA 83-1931, 1983.

[55] D.A.Anderson, "Application of Adaptive Grids to Transient Problems" in *Adaptive Computational Methods for Partial Differential Equations*, Edt: I.Babuska, SIAM, 1983.

[56] D.A.Anderson, M.M.Rai, "The Use of Solution Adaptive Grids in Solving Partial Differential Systems" in *Numerical Grid Generation*,Edt: J.F.Thompson, Elseiver Science, 1982.

[57] R.W.MacCormack, "The Effect of Viscosity in Hyper-Velocity Impact Cratering," AIAA-69-354, 1969.

[58] R.W.MacCormack, "An Efficient Numerical Method for Solving the Time-Dependent Compressible Navier-Stokes Equation at High Reynolds," NASA TM X-73, 1976, p.129.

[59] R.W.MacCormack, "A Numerical Method for Solving the Equations for Compressible Viscous Flow," AIAA J. 20, No.9, 1982, p.1275.

[60] R.W.MacCormack, "Current Status of Numerical Solutions of the Navier-Stokes Equations," AIAA-85-0032, 1985.

[61] B.P.Leonard, "A Stable and Accurate Convective Modelling Procedure Based on Quadratic Upstream Interpolation," Comp. Meth. in Appl. Mech, and Engr. 19, 1979, p.68.

[62] G.C.Pomraning, *The Equations of Radiation Hydrodynamics*, Pergamon Press, 1973.

[63] D.Mihalas and B.W.Mihalas, *Foundations of Radiation Hydrodynamics*, Oxford University Press, 1984.

[64] D.Mihalas, *Stellar Atmospheres*, W.H.Freeman and Company, N.Y. 1978.

[65] R.R.Peterson, G.A.Moses, "MIXERG- An Equation of State and Opacity Computer Code," Comp. Phys. Com. 28, 1983, p.405.

[66] J.J.MacFarlane, "IONMIX- A Code for Computing the Equation of State and Radiative Properties of LTE and Non-LTE Plasmas," University of Wisconsin Fusion Engineering Program Report UWFDM-750, Dec. 1987.

[67] W.F.Hughes, F.J.Young, *The Electromagnetodynamics of Fluids*, John Wiley, N.Y. 1966.

[68] R.D.Richtmyer, K.W.Morton, *Difference Methods for Initial-Value Problems*, Interscience, 1967

[69] P.J.Roache, *Computational Fluid Dynamics*, Hermosa 1972.

[70] E.E.Lewis, W.F.Miller,Jr., *Computational Methods of Neutron Transport*, Wiley-Interscience 1984.

[71] J.L.Anderson, S.Presier, E.L.Rubin, "Conservative Form of the Equations of Hydrodynamics in Curvilinear Coordinates," J. Comp. Phys. 2, 1968, p.279.

[72] D.R.Nickolson, *Introduction to Plasma Theory*, John Wiley & Sons, 1983.

[73] J.C.Strikwerda, *Finite Difference Schemes and Partial Differential Equations*, Wadsworth & Brooks/Cole Advanced Books & Software, Pacific Grove, CA 1989.

[74] S.V.Dresvin,*Physics and Technology of Low Temperature Plasmas*, Iowa State University Press, Ames, IA (1977).

[75] L. Spitzer, *Physics of Fully Ionized Gases*, Second Edition, Interscience Publishers, N.Y., 1962 (144).

[76] K.A.Winkler, M.L.Norman, *Astrophysical Radiation Hydrodynamics*, D.Reidel Publishing Com., Dordrecht, Holland 1982.

[77] P.F.Ottinger, et al., "Constraints on Transportable Ion Beam Power," NRL Memorandum Report 4948, Nov. 12, 1982.

[78] R.R.Peterson and G.A.Moses, "Plasma Channels for The Propagation of Ion Beams in LIBRA," Proceedings of the Beams '88 Conference, July 1988, Karlsruhe, FRG.

[79] J.J.MacFarlane, *Private Communication*, Univ. fo Wisconsin - Madison, June 1989.

[80] R.V.Lovelace and R.N.Sudan, *Phys. Rev. Lett.*, 27 1971 (1256).

[81] J.D.Callen, *Class Notes*, Univ. of Wisconsin-Madison.

[82] R.R.Peterson, *Private Communication*, Univ. of Wisconsin-Madison.

[83] J.J.MacFarlane, P.Wang, O.Yasar and G.A.Moses, "Non-LTE Radiation from Microfireballs Created by ICF Target Explosions," Presented at the APS Plasma Physics Meeting, Anaheim CA, Nov. 1989.